Title
Vortex Wake of Coaxial Rotors in Hover

Author
Konus, Mehmet Fatih

Publication Date
2017

Peer reviewed|Thesis/dissertation

Vortex Wake of Coaxial Rotors in Hover

By

Mehmet Fatih Konus

A dissertation submitted in partial satisfaction of the

requirements for the degree of

Doctor of Philosophy

in

Engineering - Mechanical Engineering

in the

Graduate Division

of the

University of California, Berkeley

Committee in Charge:

Professor Ömer Savaş, Chair
Professor Philip Marcus
Professor Lin Lin

Fall 2017

Vortex Wake of Coaxial Rotors in Hover

Abstract

Vortex Wake of Coaxial Rotors in Hover

by

Mehmet Fatih Konus

Doctor of Philosophy in Engineering-Mechanical Engineering

University of California at Berkeley

Professor Ömer Savaş, Chair

An extensive sets of experiments are carried out regarding the stability characteristics of helical vortex filaments off a coaxial rotor model. A coaxial rotor model consisting of two 26-cm (10.25-in) diameter counter-rotating rotors with a root cut-out of 3.2 cm (25%) is employed in these experiments in one- and two-bladed configurations. Axial rotor separation varied from 25% of the rotor radius to one rotor radius. Rotor speed ranged from 2 to 8 rps at each rotor spacing. Dye flow visualization, particle flow visualization and particle image velocimetry are employed in order to take measurements of the flow field. For one-bladed tests, helical tip vortex filament trailed from the lower rotor blade is observed to develop strong deformations soon after its formation at the rotor spacing of a quarter rotor radius as opposed to that of upper rotor. This deformation is less pronounced at the rotor spacing of $0.8R$. Upper and lower rotor vortices are seen to develop long-wave vortex pairing instabilities where they orbit around each other as they travel downstream, particularly at smaller rotor spacing, which is also confirmed in PIV results. Successive turns of the upper rotor helices appear to be stable as opposed to unstable nature of lower rotor helix in both rotor separations. At $H/R = 0.8$, the upper rotor wake contraction is markedly higher than that of the lower rotor. Vortex filaments develop short-wave instabilities at 2 & 4 rps just immediately after their inceptions in both rotor separations. In two-bladed configurations, in all cases tip vortices trailed from the lower rotor experience extreme distortions, resulting in the loss of their orderly helical shapes, which is a clear manifestation of the effect of the upper rotor on the lower one. At smaller rotor spacings up to 50% radius, lower rotor filaments develop long-wave vortex pairing instabilities in similar ways to what is found in single rotor wakes although they differ to the extent lower vortex filaments undergo deformations. At this rotor spacing range, upper rotor filaments does not have sufficient space between the rotors to develop mutual interactions before they reach the plane of the lower rotor and interact with lower rotor blades, i.e. interrotor blade-vortex interactions (BVIs). As the rotor spacing is further increased up to a rotor radius, upper rotor filaments are seen to develop long-wave pairing instabilities similar to what is observed in the wakes of single rotor runs. As in the one-bladed configurations, upper rotor filaments possess a more stable nature whereas those from lower rotor becomes unstable within first rotor revolution beneath the lower rotor. At rotor spacing of 50% radius, hairpin vortices are observed to form beneath the lower rotor during the long-wave instability mode developed by the lower rotor filaments where streamwise elongation of the vortex filament from a particular blade of the lower rotor in each rotor revolution is observed. At other rotor spacings, similar deformation of the vortex filaments in the streamwise direction is seen to occur however distinct hairpin vortex structures are only seen at the rotor spacing of $0.5R$. Upper rotor wakes contract to more inward than those of the lower rotor wakes for all the rotor separation distances tested, which is also confirmed from the PIV measurements and particle visualization results. Increasing rotor spacing changes the wake contraction of the upper rotor at the plane of the lower rotor where it reaches a more fully-developed state towards the rotor spacing of one radius. This is further confirmed from the streamline patterns from the PIV results. Regardless of the rotor spacing, short-wave instabilities formed along the helical filaments at 2 & 4 rps cases from their generation whereas at 6 & 8 rps filaments are only observed to develop these types of instabilities long after their formation and not in an explicit manner since they become superimposed with long-wave instability mode where filaments develop strong distortions beneath the lower rotor.

Contents

List of Tables

List of Figures

List of Symbols

b	separation between straight vortex filaments
c	blade chord, 1.9 cm
d	distance between rectilinear vortex pair
d_1	distance from rectilinear vortex 1 to vortex pair centroid y_c
d_2	distance from rectilinear vortex 2 to vortex pair centroid y_c
k	dimensionless pitch of the helix
ℓ	blade span
li	successive lower rotor vortex filaments, i=1, 2, ...
n	wave number
r, x	polar coordinate system
r_w	wake radius
t	time
$\underline{\mathbf{u}}$	velocity field from PIV measurements
ui	successive upper rotor vortex filaments, i=1, 2, ...
V_{tip}	rotor speed at the blade tip, $2\pi NR = \Omega R$
x, y, z	right-handed rectangular coordinate system
y_c	centroid of the rectilinear vortex pair
A_Γ	integration area used in tip vortex circulation estimation
D	rotor diameter, 2R, 26 cm
H	dimensional axial distance between coaxial rotors
H/R	non-dimensional axial distance between coaxial rotors
L	axial distance between successive turns of helices
N	rotor rotational speed, Hz (rev/s)
R	rotor radius, 13 cm
Re_c	chord-based Reynolds number, cV_{tip}/ν
Re_Γ	tip vortex circulation-based Reynolds number, Γ/ν
V_1	induced velocity at the center of vortex 1 due to vortex 2
V_2	induced velocity at the center of vortex 2 due to vortex 1
$\tan\alpha$	pitch of a helix
θ	rotor collective angle, 13.5°
λ	wavelength
ν	kinematic viscosity of water, 0.01 cm^2/s
σ	rotor solidity
	wake azimuth in radians
$\omega(x, y)$	vorticity field
Γ	tip vortex circulation
Γ_i	circulations of rectilinear vortex i $(i = 1, 2)$
Ω	rotor speed in radians, $2\pi N$

Acknowledgements

"...Whoever is the cause of another's becoming powerful will come to ruin himself, because that power is created by him through either his industriousness or his force, and both of these qualities are suspect to the one who has become powerful." [1]

I embarked upon this interesting and formidable journey in August 9, 2012. I am grateful that I had this once-in-a-lifetime opportunity to pursue a doctoral degree at the University of California, Berkeley. I would like to express my sincere gratitude to those who supported me and made this journey possible, easier, enjoyable and endurable for me. I am grateful to my research advisor Professor Ömer Savaş for what he has taught me during my PhD studies. He has been a great mentor to me. I have learned valuable lessons from him, which will help and guide me in my future endeavors. I am also thankful to Prof. Philip Marcus and Prof. Lin Lin for serving as my committee members as well as their valuable insights and time into my dissertation.

I am thankful to all my fellow lab mates, Rachael Elizabeth Hager, Eric Ibarra, Daniel Joseph Grieb, Benjamin Keyser, Onur Recep Bilgi, Onur Kaltakci, and Jocelyn Bale-Glickman for their help during my experiments. I spent valuable and memorable times with them throughout my stay at Fluid Mechanics Lab and had stimulating discussions. I am also thankful to Ercan Degirmenci and his family for his help, valuable insights, and guidance. This thesis would not have been possible without the valuable help of Jesse Lopez, Dennis Lee and other members of Mechanical Engineering Machine Shop at the University of California, Berkeley. I am thankful to Turkish Military Academy for their support. I also would like to offer my deepest gratitude to Donna Craig on behalf of the Department of Mechanical Engineering for their support in my final year at the university.

Last but not the least, I am grateful to my dear wife Elif for her endless love and understanding. She had to bear with me during my endless and stressful studies. She was always there supporting and standing by me through those good and bad times. I would also like to thank our families for their support and encouragement.

[1] Niccolo Machiavavelli, *The Prince and Other Writings*, New York, Barnes and Nobles Classics, 2003, p.16

Chapter 1

Introduction

1.1 Historical background

The concept of coaxial rotors, rotorcraft with two counter-rotating rotors mounted a distance apart on a single axis, is not new. In 1754, Mikhail Vassilyevich Lomonossov, a Russian inventor, was able to get his small coaxial rotor model, which he named 'aerodynamic machine', fly for a few seconds [1, 2]. In 1859, the first ever helicopter patent was granted to Henry Bright for his coaxial rotor design [3]. There were numerous attempts to build coaxial helicopters in the first half of the 20th century. However, none of them was able to go into mass production. Kamov Design Bureau, a Russian helicopter company, has pioneered the design and mass production of the coaxial helicopters as we know them today [4, 5]. In 1970s, Sikorsky Aircraft developed the Advancing Blade Concept (ABC) helicopter, which consisted of two counter-rotating rigid coaxial rotors [6]. It was aimed to increase the maximum speed by utilizing the higher lift capabilities of the advancing blades. The ABC helicopter never saw mass production. In 2005, Sikorsky Aircraft announced that it would begin the development of X2 Technology Demonstrator [7], a coaxial helicopter that would also utilize the advancing blade concept. Based on the X2 Technology Demonstrator, Sikorsky Aircraft launched the S-97 Raider program, which is still under development. The coaxial rotor concept has recently emerged in uninhabited aerial vehicle (UAV, a.k.a drone) designs, too. A Chinese company introduced the Ehang 184 [8], an autonomous transport drone with 8 coaxial propellers mounted on four arms aimed to carry one passenger. DARPA has been developing an autonomous drone with coaxial propellers, dubbed TERN [9], that will be able to take off and land vertically, i.e. launched in rotary-wing configuration, and transition to fixed-wing flight once airborne. These recent developments in rotary-wing UAVs and high-speed rotorcraft have led to a resurgence of interest in the research of coaxial rotor configurations. In Figures 1.1 and 1.2 are shown the aforementioned coaxial rotor concepts.

1.2 Motivation and Problem Statement

All rotorcraft vehicles, whether it be in single, coaxial or tandem rotor configuration, trail helix-shaped vortex filaments as the rotor blades turn, creating a highly three-dimensional and unsteady wake structure [14]. These vortices, trailed from the tips of the blades, create a nonuniform inflow distribution over the rotor disk and continue to affect this distribution as they trail downstream [15]. This nonuniform inflow distribution, i.e. the flow induced through the rotor disk by the action of the turning of the blades, is an important parameter for accurately calculating the power and torque coefficients of the rotor, which

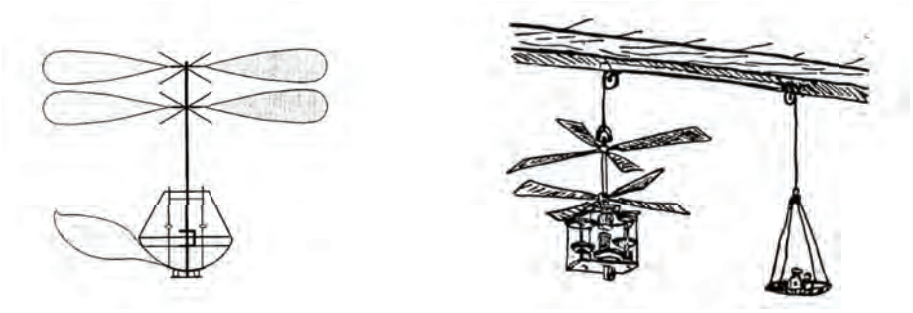

(a) First patented coaxial rotor design (b) Lomonossov's aerodynamic machine

Figure 1.1: (a) First patented coaxial rotor design [3], (b) Lomonossov's aerodynamic machine [1]

(a) Kamov Ka-52 Alligator coaxial helicopter (b) Sikorsky S-69 ABC Helicopter (c) DARPA TERN

(d) Ehang 184 autonomous transport drone (e) Sikorsky S-97 Raider

Figure 1.2: (a) Kamov Ka-52 Alligator [10], (b) Sikorsky Aircraft's Advancing Blade Concept (ABC) coaxial helicopter [11], (c) DARPA TERN in its phase 3 [9], (d) Ehang 184 autonomous transport aerial vehicle [12], and (e) Sikorsky S-97 Raider [13].

are essential in rotor performance calculations. The characteristics of this inflow is largely affected by the geometry of the wake and the behavior of the vortices below the rotor. Therefore, the significance of these tip vortices lies in the fact that their stability characteristics (e.g. interactions with each other, vortex perturbations, vortex bursting or break down etc.), strengths, and locations in the rotor wake affect the aerodynamic loads acting on the blades of the rotor as well as its performance, vibration, and acoustic characteristics. To this end, a great deal of emphasis has been placed on the investigation of the wake vortex instabilities. However, these studies (mostly theoretical, numerical, and experimental) concentrated heavily on the single rotor configurations. As stated earlier, the rotor wakes are comprised of highly complex unsteady vortical flows. The coaxial rotors trail vortices from each of the counter-rotating rotors, forming two different wakes below the rotors. The wakes of the coaxial rotors interact with each other, generating a more complicated flow field than what is found in a single-rotor system. The presence of the second rotor triggers these mutual interactions between two rotors (upper and lower rotors) that affect the wake geometry and performance of the coaxial system. Some of these rotor-on-rotor interactions are, but not limited to, mutually induced effects of vortices from one rotor on those of the other one and the blade-vortex interactions (BVIs) between the vortices from the upper rotor and the blades of the lower rotor. Axial separation distance between the upper and lower rotors and different rotor rotational speeds influence the strength and degree of these interactions. In this dissertation, it is intended to experimentally investigate the stability of helical vortex filaments trailed from a hovering coaxial rotor configuration having both one and two blades per rotor and mounted at varying separation distances from each other. There is a scarcity of flow visualization studies of coaxial rotor configurations. Therefore, it is also intended to provide flow visualizations of helical vortices and rotor wakes that are present below coaxial rotors. In addition to the flow (i.e. dye) visualization study of the stability characteristics of the helical filaments, 2-D Particle Image Velocimetry (PIV) measurements are taken for quantitative flow analysis, i.e. velocity and vorticity fields are constructed from those data sets. Two sets of data are recorded for each PIV experiment, one with short-exposure for PIV purposes and one with long exposure for particle flow visualization.

1.3 Literature review

In this section, relevant research for the current study will be summarized. First, a review of the instability types that are found on rotor wakes will be presented. Second, the research on the stability of helical vortex filaments of single rotor configurations will be reviewed. Finally, relevant research on coaxial rotors will be summarized.

1.3.1 Instability modes of helical filaments

Widnall [16] theoretically investigated the stability of a helical vortex filament to small sinusoidal displacements of its center-line, which corresponds to a helical filament trailed from a one-bladed rotor, and has reported three modes of instability mechanisms that occur on tip vortex filaments: (i) a very short-wave instability mode, (ii) a long-wave, or low wave-number, instability mode, and (iii) a mutual-inductance instability mode.

Short-wave instability

The short-wave instability mode is recognizable as small *smooth-sinous-wave-type* perturbations along a helical vortex filament as observed by Sullivan [17]. They result from the self-induced motion of a curved filament and an external strain field induced by a neighboring vortex [18]. In Widnall [16] short-wave

instability mode is given in terms of the the relation where the number of waves per cycle of the helix is greater than the inverse of the helix pitch. Widnall [19] reported that for the stability of a straight vortex pair, e.g. as found in fixed-wing aircraft wake, the short-wave limit is when $\lambda/b < 1$, where λ is the wavelength and b is the separation distance between the straight vortex filaments. In Wang [20], for co-rotating straight vortex filaments, short-wave is defined in the way that wavelength is comparable to or smaller than the vortex core size. Similarly, in rotor wakes, short-wave instability can be characterized as the ratio of wavelength of the perturbations along the filament to the wake radius [21], i.e. $\lambda/r_w < 1$, where r_w is the wake radius. It can also be given as the number of waves per pitch of the helices, i.e. $2\pi r_w/\lambda > 1$. The disturbances in short-wave instability mode grow in amplitude at greater downstream distances in the rotor wake [22]. This type of instability mode is also referred as the *elliptic*, or *bending instability* due to the elliptic streamlines in the vortex core caused by the external strain field of a neighboring vortex and has wavelengths on the order of vortex core diameter [23]. A comprehensive review on elliptical instabilities is given in Ref. [24].

Long-wave instability

In the context of Ref. [16], the long-wave instability is defined as the low wave-number instability. It differs from the short-wave instability in terms of number of waves formed in one turn of the helical filament. In this instability mode, the number of waves per cycle of the helix is less than the inverse of the helix pitch. In Ref. [19], for a straight vortex pair, while the short-wave limit is given as $\lambda/b < 1$, long-wave limit is $\lambda/b \approx 8$. For co-rotating straight vortex filaments, Wang [20] defined the long-wave in the way that wavelength is large compared to the vortex core size. A well-known long-wave instability mode is the Crow instability [25], which is observed on the trailing vortices of a fixed-wing aircraft. During the long-wave Crow instability, also referred as the long-wave vortex pair instability, the counter-rotating vortices are displaced as a whole and their disturbance amplitude increases until the the vortices touch each other, which results in the formation of vortex rings and subsequent decay of the vortex pair. In the helicopter and propeller literature, long-wave instability is generally used in conjunction with the mutual inductance instability mode, which will be described subsequently. This is due to the reason that, in practice, it is rather difficult to distinguish between different instability modes since they are superimposed and affect each other mutually.

Mutual inductance instability

Third instability mode that is reported in Widnall [16] is the mutual inductance instability, which is found to appear when the successive turns of the helices pass within a helix radius. This type of instability stems from the mutual interactions between different helical filaments (for multi-bladed rotors) and/or the adjacent turns of a helical filament (for single-bladed rotors). The strength of the mutual interactions between the neighboring portions of the helical filaments is affected by changes in the helix pitch. The rotors with higher number of blades will have smaller axial spacing between the successive turns of the filaments, which, in turn, will bring about stronger mutual interactions between the vortex filaments. Mutual induction between the neighboring vortex filaments may lead to rolling-up of these filaments around one another and subsequent *leapfrogging* of the vortices, which is also called as vortex-pairing instability. In leapfrogging process, mutual interactions between the adjacent turns of the filaments cause the rearward helix to pass through the forward helix, resulting in a decrease in the diameter of the former and an increase in the diameter of the latter [26]. This phenomenon is akin to the leapfrogging of the coaxial vortex rings, which are shed off in quick succession [27]. This process may continue with the reversal of the roles between the helical filaments until both vortex vortices merge into a single vortex or become unstable and break down.

Following simplified analogy illustrates the mutual interactions between a rectilinear vortex pair and helps explaining the spiraling of adjacent rotor tip vortices around each other. Consider two co-rotating

infinite parallel rectilinear vortices with arbitrary circulations Γ_1 and Γ_2 as shown in In Figure 1.3. The distance between the vortex pair is given as $d = d_1 + d_2$. The velocity induced at the center of vortex 2 due to the vortex 1 is $V_2 = \Gamma_1/2\pi d$. Similarly, the velocity induced at the center of vortex 1 due to the vortex 2 is $V_1 = \Gamma_2/2\pi d$. The centroid of the vortex pair lies a distance $y_c = \Gamma_1 d/(\Gamma_1 + \Gamma_2)$ from vortex 2 and the vortices orbit about this centroid in circular paths at a constant angular velocity of $(\Gamma_1 + \Gamma_2)/(2\pi d^2)$. A comprehensive review on the counter-rotating and corotating vortex pairs instabilities (merging, Crow instability, elliptic instability) is given in [23].

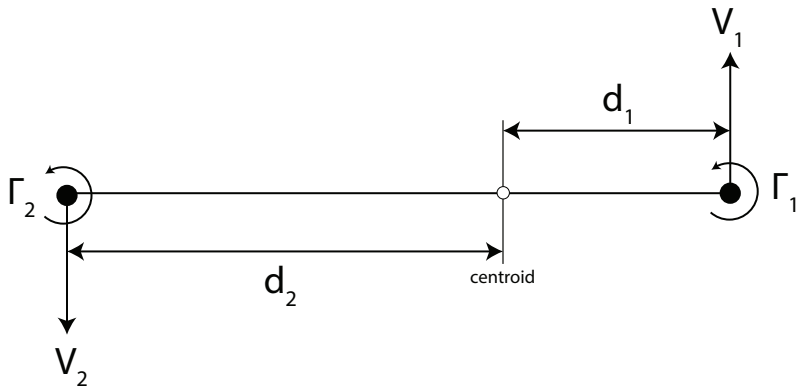

Figure 1.3: Rectilinear vortices

In subsequent discussions of the present study, long-wave instability and mutual inductance instability modes will be referred together as *long-wave pairing instability* or *leapfrogging* of the helical filaments.

1.3.2 Stability of helical filaments of single rotor configurations

Vortex wake instability of rotorcraft vehicles in single rotor configuration, also referred as conventional rotors, is well-studied. Landgrebe [28] noted that the rotor vortex wake has two primary components, one of which being the strong tip vortices coming off the tips of each blade and the other one is vortex sheet trailing from the inboard sections of the blades as shown in Figure 2 therein. This rotor vortex wake becomes unstable in the far-wake region (generally within a few rotor revolutions), manifesting itself in the form of axial oscillations in the tip vortex location, which is also known as vortex wandering. Okulov [29] investigated the linear stability of multiple helical vortex filaments as a vortex system and noted that as the pitch of the helical vortices decreases the vortex system is more likely to be unstable even for fewer number of vortices in the vortex array. Okulov [30] further extended the study in Ref. [29] by embedding an array of N-helical filaments into a assigned vorticity field (Rankine, Gaussian, and Scully) due to vortex sheet trailed from the inboard section of the blades, root vortices and the rotor hub. It is concluded that the stability of the tip vortices largely depends on the type of the prescribed vorticity field as well as its radial extent. Representing the far wake of the rotor as a combination of N helical tip vortices and the root vortex leads to unconditionally unstable vortex system. However, assigning a vorticity field into the vortex model may result in a stable vortex system in the far wake. The stability studies given in Refs. [28–30] can be considered as the stability of multiple helices as a vortex system. The stability issue also manifests itself as development of vortex filament instabilities [16]. As mentioned earlier, Widnall [16] investigated the stability characteristics of a single helical vortex filament to sinusoidal perturbations of its centerline. Three modes of instability have been reported: (1) a very-short wave instability, which is characteristics of all curved vortex filaments, (2) a long-wave or low wave-number instability mode, and (3) mutual inductance instability (rolling up of vortices around one another). As the helix pitch decreases, the neighboring turns of

the filaments get closer to each other, resulting in stronger interactions and a mutual inductance instability mode. Vortex core size, which is defined as the ratio of vortex core diameter to helix radius, is also an important parameter in terms of stability considerations. While the amplification rate of the long-wave mode is found to increase with decreasing vortex core size, the mutual inductance mode tends to weaken with decreasing core size. Sullivan [17] experimentally observed a wave-like structure on the helical tip vortex, a smooth sinuous wave-type instability. Gupta and Loewy [31, 32] theoretically investigated the stability of centerline displacements of single and multiple-helix vortex systems. For a single helix, i.e. one-bladed rotor, it was found that the single helix is unstable for all wave number modes except $n = 0, 1$, where $n = 0$ corresponds to the dilatational mode, a uniform expansion in radial direction. For the case of multi-bladed rotors, it was noted that as the helical pitch decreases, instability tends to grow due to consequent strong interaction between the adjacent helical vortices. Similarly, decreasing vortex core size accentuates the instability since higher induced velocity results from smaller core sizes for the case of a single helix. For a multiple helical vortex system, however, the stability is less likely to be affected by the variation in vortex core size. The maximum divergence rates in the unstable modes increase with decreasing helical pitch and increasing number of blades, and decrease with increasing wave numbers in one turn of the helix. In Fig. 7 of Leishman [22], two types of short-wave, or bending, instabilities are shown. One is the smooth sinuous wave-type instability that grows in amplitude as the wake age gets older. The second type of instability shown is the helical or corkscrew type instability that is quite common in the wake of the highly loaded propellers. There are a number of factors that affect the onset of short-wave perturbations in rotor wakes, which are number of blades, rotor rotational speed, and operating conditions. Another instability type that is observed on rotorcraft wakes is the vortex-pairing instability, or long-wave pairing instability as stated earlier. The vortex pairing instability differs from the mutual induction instability in the sense that the circulation of each filament in the former is not necessarily the same as in the latter [16]. Tangler et al. [33] conducted a schlieren experiment in order to investigate the effect of number of blades, collective pitch, and tip speed on the vortex stability of propellers and rotors. It was observed that due to the strong interaction between two tip vortices shed from the adjacent blades,these vortices started to spiral around the common centroid of vorticity, and consequently either destructing each other or merging into a single diffuse vortex. This phenomenon was both observed in two-bladed and four-bladed configurations of propellers and rotors. Increasing the number of blades or decreasing the collective pitch had the corresponding effect of reduced axial spacing between the tip vortices, resulting in increased angular velocity about the common centroid of vorticity and more unstable condition leading to diffusion of vortices sooner than that of the fewer bladed or higher collective angle cases. The authors compared this type of large scale interactions between the adjacent vortices, also referred as pairing of adjacent vortices in the text, to the mutual induction instability mode reported by Widnall [16].The pairing of adjacent tip vortices resulted in asymmetric vortex wakes, which is more pronounced in the case of highly-loaded propellers in hovering flight. It was also noted that the along vortex filament exists small random sinusoidal fluctuations, i.e. a short-wave instability mode. Caradonna et al. [34] observed a vortex-pairing instability where adjacent helical vortices start to roll up around each other and lose their individual identities by merging into a single vortex. Collective angle and the climb speed, which determine the spacing between adjacent helical filaments, affect the location of the vortex merger. Larger collective angles and higher climb speeds, hence larger spacing between the adjacent helices, will delay vortex-merging farther downstream. In a flow visualization experiment of a two-bladed rotor performed by Muller [35], the vortex-pairing phenomena can be clearly seen as given in Figure 12 therein even though it was not discussed by the author. Vortex-pairing instability is also observed in subwing rotor tip shapes. Flow visualization experiments of a single-bladed rotor (Refs. [36,37]) revealed that subwing rotor tip shape sheds two vortices, one from the subwing and the other from the main blade tip. It was observed that the secondary vortex trailed from the subwing orbits around the blade tip vortex and consequently both vortices merge into a single diffuse vortex before the second turn of the blade (see Fig. 12 in Ref. [37]). Jain and Conlisk [38] numerically computed the wake of a two-bladed rotor and noted the strong interaction between the tip vortices, which was previously observed experimentally. In a process similar to leapfrogging of two coaxial vortex rings (Ref. [27]), two trailed tip vortices intrinsically commence spiraling around each other and merge into a single vortex in one and one-half rotor cycles. The vortex-pairing instability appears to be akin to the pairing of the straight vortex filaments similar to the wing-tip vortices of the fixed-wing

airplanes [39, 40]. Ohanian et al. [21] performed a flow visualization study of the instability characteristics of the helical vortex filaments of a three-bladed hovering rotorcraft model. It is observed that within two revolutions, two of the three helical filaments interact with each other and merge together. The merging process, which is referred as long-wave pairing instability and leapfrogging by the authors, is completed in about three revolutions following merging of the third vortex with the other merged vortex pair, culminating in a single diffuse turbulent vortex. It is also noted that the rotor speed affect the merger location in the way that higher rotor speeds correspond to a greater downstream distance for the vortex merger. Flow visualization images therein also reveals the short-wave instabilities on the helical vortex filaments. It is noted that these short-wave instabilities grow rapidly in amplitude as the merging of the vortices become imminent.

1.3.3 Research on coaxial rotor configurations

The research conducted on the aerodynamics of the coaxial helicopters in the second half of the last century was summarized by Coleman [3]. This survey includes the previous research done in the United States, Russia, Japan, Germany, and United Kingdom. It gives a comprehensive list of relevant citations on performance issues, measured wake flow characteristics, and possible methods of performance analysis. Important findings from some of the cited researches from this survey as well as from more recent studies will be summarized in this section. Previous research on coaxial rotors will be summarized under two headings, one of which is the wake characteristics, and the other one is the thrust (performance) measurements of the coaxial rotors.

Wake characteristics

The first known flow visualization study of coaxial rotor configurations was done by Taylor [41] in Langley full-scale tunnel in 1950. A balsa-dust technique was employed to visualize the air-flow patterns of a two-bladed coaxial rotor configuration along with single and bi-axial rotors. A flow visualization video from these experiments can be found in Ref. [42]. In the experiments, non-dimensional axial rotor spacing between the coaxial rotors, defined as H/R where H is the dimensional axial distance between the rotors and R is the rotor disk radius, was 35% of the rotor radius, Reynolds number evaluated at the blade tip was 110,000, solidity of the system was 0.08, and the collective angle was set to 14°. It was noted that the tip vortices trailed from the upper and lower rotors did not either merge or cancel each other, instead they retained their individual identities as they travel downwards in the rotor wake, unlike reported in later researches which will be discussed shortly. It was also suggested that the wake of the upper rotor should be taken into account when considering the blade bending moments in the lower rotor. In Cheney [6], the results of the hover testing of the Advancing Blade Concept (ABC) helicopter is given. The ABC helicopter, also known as Sikorsky S-69, was a three-bladed (per rotor) coaxial rotor with rotor spacing of $H/R = 0.138$ and rotor solidity of 0.127. Smoke visualization results of the ABC coaxial helicopter revealed that the vortices trailed from the upper rotor traveled at a faster rate than those from the lower rotor and the wake contraction ratio of the upper rotor was larger than that of the lower rotor. Moreover, at downstream distances, the vortices from both rotors interacted mutually with each other, attempting to roll up around each other to form larger diffuse vortices. A flow visualization image is given in Figure 6 of this reference. Andrew [43] obtained wake measurements of coaxial rotors separated a quarter of rotor radius apart and found that due to the mutual interactions between the coaxial rotors, upper rotor and lower rotor wake contraction ratios were greater and smaller than that of the single rotor, respectively. Numerical results from Nagashima and Nakanishi [44] showed that varying the separation between the rotors altered the wake geometry of coaxial rotors. Akimov et al. [45] conducted a smoke visualization study of the tip vortex structure of a full-scale Kamov Ka-32 coaxial helicopter in hover and level flight. A visualization photo of the coaxial rotor wake is given in Fig. 6 therein. Each of the rotors was 3-bladed and the overall rotor solidity (upper and lower rotor together)

was 0.119. Axial rotor spacing was $0.189R$, where R is the rotor disk radius. Within a rotor revolution (at about 240° azimuth), the wakes of the upper and lower rotors were measured to contract to $0.85R$ and $0.91R$, respectively. In a numerical study of two two-bladed coaxial rotors separated $0.19R$ apart, Kim and Brown [46, 47] found that the tip vortices from both rotors in coaxial configuration in hover, particularly upper rotor vortices, traveled downstream at a faster rate when compared to their axial convection rates in isolated single rotor configurations of both rotors due to increased overall thrust, and hence increased rate of transfer of momentum into the wake. When compared to axial convection rates of the vortices from the equivalent single rotor configuration, i.e. the single rotor having the equal number of geometrically identical blades with the coaxial rotors, however, upper rotor and lower rotor tip vortices traveled at a faster and slower rate, respectively, than the axial convection rate of the vortices from equivalent single rotor configuration. Lower rotor of the coaxial system showed a slower radial contraction compared to when operated in isolation. Due to mutual interactions between the tip vortices of each rotor, they tended to merge to form larger vortex structures downstream of the wake.

Thrust characteristics (Performance)

Experimental hover performance measurements of two two-bladed coaxial rotors with different airfoil thickness and chord variations on the blade, and rotor spacings of $H/R = 0.16$ and $H/R = 0.19$ was carried out by Harrington in 1951 [48]. It was noted that the hover performance of the coaxial rotors between these rotor spacings can be predicted using a single rotor of the same solidity, i.e. four-bladed rotor in this case. Experimental and theoretical results in Andrew [43] revealed that the coaxial rotor produced more thrust than its equivalent single rotor for the same amount of power expended in hover.This is owing to the fact that the induced power consumption of the coaxial rotor was about 5% less than that of the equivalent single rotor. Nagashima and Nakanishi [44] numerically studied the hover performance of coaxial rotors and showed that the mutual interaction effects of the upper rotor wake on the outer portions of the lower rotor, i.e. outside regions of contracted upper rotor wake, which changes with changing the rotor spacing, could affect the optimum hover performance of the system. McAlister et al. [49] conducted hover performance measurements of a 3-bladed coaxial rotor with varying rotor spacings, which ranged from 0.2 to $1.6R$, in and out of ground effect. They found that the separation distance between the rotors seemed to play little role collectively when the rotors were employed in coaxial configuration and operated out of ground effect. However, each rotor showed variations in its performance as the rotor spacing is varied compared to when the rotors were operated in complete isolation. They only tested one rotor spacing ($H/R = 0.2$) in ground effect tests. Kim and Brown [46, 47] compared the hover performance of the coaxial and conventional rotors and noted that the coaxial rotors in hover consume less induced power than its equivalent single rotor. Leishman and Syal [50] developed a figure of merit definition for coaxial rotors using the classical momentum theory. It is shown that the maximum efficiency, i.e. figure of merit of a coaxial rotor configuration, occurs at a rotor axial spacing such that the lower rotor operates under the fully developed slipstream of the upper rotor. An optimum coaxial rotor with maximum efficiency will require different blade twist distributions and planform shapes on both the upper and lower rotors [51]. Lei et al. [52] conducted experiments to measure the effect of axial rotor spacing ($0.32R-0.75R$) on the aerodynamic performance of a small scale coaxial rotor (Micro Air Vehicle-MAV) and found that the system thrust increased until an intermediate spacing, from which it started to decrease and approach a constant value for larger spacings. Ramasamy [53] conducted comprehensive experiments in order to measure the hover performance of coaxial rotors along with single and tandem rotor configurations. The axial separation distances between the upper and lower rotors were varied between $0.1R$ and $3R$ to measure and compare the thrust and torque of both rotors at different rotor spacings. In the study, three distinct regions have been identified for the performance of the coaxial rotor at different separation distances. In the first region, which is given as $H/R > 1.5$, the overall performance of the coaxial rotors as well as the performance of rotors separately, showed no difference to the changes in axial separation distances. In region 2, where $0.4 < H/R < 1.5$, while the figure of merit of the upper rotor decreased with decreasing H/R, that of the lower rotor increased, resulting in unchanged efficiency of the coaxial system as a whole. In the third region, in which $H/R < 0.4$, the upper rotor's figure of merit

decreased rapidly while lower rotor figure of merit increased greatly. Unlike the region 2, however, the overall coaxial rotor efficiency decreased, which is indicative of the adverse effect lower rotor induces on the upper rotor performance when their separation is significantly reduced. Yoon et al. [8] numerically investigated the performance of the torque-balanced coaxial rotors and noted that the overall thrust increased for a torque-balanced system when the rotor spacing was decreased below half a rotor disk radius. The rate at lower rotor thrust increased was greater than the rate at which upper rotor thrust decreased.

1.4 Current research

Comprehensive sets of experiments have been conducted where two rotors operated in coaxial configuration were employed. To this end, a coaxial rotor drive system was designed using that of an existing single rotor model in SolidWorks environment. In order to take measurements at different axial rotor separations, a number of disk spacers (9 in total) were designed with rotor spacings ranging from 25% of the rotor radius to one rotor radius. The way these disk spacers were designed made it easier to remove and replace them with another one between the tests at different rotor separations. Also, at a specific rotor separation when the coaxial rotors were fitted with one of the disk spacers, measurement were taken at four different rotor speeds of 2, 4, 6 & 8 rps. In addition to coaxial rotor experiments, single rotor measurements were also carried out in order to serve as baseline flow characteristics when comparing with that of the coaxial rotor tests. Rotors in single and coaxial configurations were tested having two different number of blades, i.e. one- and two-bladed rotors. In two-bladed configurations, measurements were recorded at all rotor spacings available. In one-bladed configuration, however, measurements were only taken at two different rotor spacings out of nine in total. In both cases, data in single rotor configuration was also captured. The main objective of this dissertation is to investigate wake and stability characteristics of helical filaments trailed from a coaxial rotor. This was done through flow visualization of the flow field by recording a number of images at each rotor separation and speed. In addition to flow visualization experiments, which was done by injecting fluorescent dye into the flow medium, particle image velocimetry (PIV) measurements were also taken where particles were introduced into the flow field which were then illuminated through a laser to capture images. Moreover, another type of flow visualization experiments were carried out using PIV particles, i.e. particle flow visualization. These measurements were also recorded at each rotor separation and speed in the same way as it was done in dye visualization tests.

1.4.1 Objective of the current study

The main objective of this experimental research is to investigate the stability characteristics of helical filaments trailed from a coaxial rotor having both one and two blades per rotor and compare the results with that of single rotor configurations. This is an important issue in consideration of the rotor performance. Presence of second rotor introduces more complexities into the flow field compared to the wake of a single rotor. Interactions between helical filaments of the same rotor and the different rotors as well as interactions of helical filaments from one rotor with the blades of the other rotor largely affect these stability and wake characteristics of coaxial rotor filaments. Effect of coaxial rotor parameters, rotor spacing and rotor speed, on these stability and wake characteristics of the helical filaments is investigated through flow visualization images and PIV measurements.

Experimental research on coaxial rotor wakes has not garnered much attention partly due to coaxial rotors being mostly designed by Russian companies and wider usage of single rotor configurations in both civilian and military roles. To this end, it is also intended in this dissertation to provide a comprehensive flow (dye) visualization data set where a series of flow images are present at different rotor spacings and speeds as well as different number of blades in order to serve as accurate experimental flow models for future

coaxial rotor designs and calculations.

1.4.2 Organization of dissertation

This dissertation consists of six chapters. Chapter 1 introduces a brief historical development of coaxial rotors with photos of past, current and proposed coaxial rotors, comprehensive literature review from a number of relevant publications on the stability characteristics of helical filaments trailed from single rotor configurations, and the wake and thrust characteristics of coaxial rotors. Chapter 2 presents the experimental setup and instrumentation employed in this study where the experimental procedure is explained in detail. Specifications of the coaxial rotor model assembly are provided along with the design phase of the rotor model. Both images of SolidWorks and actual rotor assemblies are shown. Chapter 3 presents the results of the experiments conducted with one-bladed rotors employed both in single and coaxial configurations. First, flow conditions are given where two types of definitions of Reynolds numbers and the procedure how the circulation-based Re number is estimated is introduced. Then, results of single rotor measurements are introduced followed by coaxial rotor measurements at two different axial rotor separations in three consecutive sections. In each of these three sections, first, flow images at each rotor speed of 2, 4, 6 & 8 rps along with their corresponding time- and phase-averaged images are introduced. Second, a number of images that show the wake vortex evolution of the wakes beneath the rotors are provided at 4 & 8 rps. Observations regarding the characteristics of the flow field is presented based on these images. Vortex instabilities are investigated and discussed in detail. Third, vortex trajectories and xt diagrams are provided. Wake contraction ratios in each case are presented. Finally, each section is concluded by the results of PIV measurements where instantaneous and average velocity and vorticity fields are shown along with particle visualization images. Chapter 4 presents the results of the experiments conducted with two-bladed rotors employed both in single and coaxial configurations. Presentation is done in the same way as in Chapter 3, only difference being in the higher number of rotor separations tested in two-bladed runs. Chapter 5 presents the comparison of the results discussed in Chapters 3 & 4. Chapter 6 concluded the findings and implications of this dissertation. In Appendix A is provided flow visualization images at 2, 4 & 6 rps along with results of processed-PIV images at 2, 4 & 6 rps. SolidWorks drawings of the parts of coaxial rotor are presented in Appendix B.

Chapter 2

Experimental Setup and Instrumentation

2.1 Introduction

The following chapter describes the instrumentation, setup and testing procedures of the experiments performed for the purpose of the current study. First, the coaxial rotor model, including the design phase, will be introduced. Second, the range of the experiments, i.e. range of rotor rotational speeds, and the axial separation distances between the upper and lower rotors will be presented. Third, details of the flow visualization runs will be given. Particle Image Velocimetry (PIV) experiments will follow in the last section.

2.2 Coaxial Rotor Model Assembly

For the purposes of the experimental studies to be described here, the drive system of a three-bladed single rotor assembly that were employed in previous studies (Refs. [21, 54–56] has been converted into that of a coaxial rotor model, which was designed to have provision for varying the axial rotor spacing. The necessary parts for the coaxial rotor model were designed in SolidWorks environment and constructed in the University of California, Berkeley Mechanical Engineering Machine Shop. The parts that were designed and built are: two horizontal concentric hollow cylindrical shafts on which upper and lower rotors of the coaxial system were fixed, two rectangular rotor hubs, each of which were designed to accommodate two blades at most, and nine disk spacers that were utilized to vary the axial rotor spacing between the upper and lower rotors of the coaxial system. The disk spacers were designed in such a way that for each rotor separation distance to be tested, they can easily be removed and replaced by another one. These disk spacers serve as connectors between the shaft and the hub of the lower rotor. The SolidWorks assembly of the coaxial rotor model is shown in Figure 2.1, and the detailed SolidWorks drawings and the photos of the individual parts are provided in the Appendix B.

The coaxial rotor model consisted of two 26-cm (10.25-in) diameter counter-rotating rotors with a root cut-out of 3.2 cm (25%). The coaxial rotors were driven by a digitally-controlled 25,000 steps/rev microstepper motor, which was coupled to the rotor through a 90° gearbox consisting of three identical 18-teeth spiral bevel gears, which turn the upper rotor clockwise and the lower rotor counterclockwise. The

motor allows for precise control of both the rotor's azimuthal position and rotational velocity. The motor was mounted atop an 89-cm vertical shaft and drove two horizontal counter-rotating shafts onto which the coaxial rotors were fixed. The horizontal shaft on which the upper rotor was fixed (outer shaft) was a 18.8 cm (7.4-in) with a 1.27-cm (0.5-in) outer diameter while the shaft that rotates the lower rotor (inner shaft) had a 30.5 cm (12-in) length with outer diameter of 0.95 cm (0.375 in). Just beneath the motor was a 2.5 cm thick rectangular mounting plate that supported the model assembly and accommodated a pair of flexures instrumented with 120 ohm strain gage bridges in order to measure rotor thrust. Figure 2.2 shows photographs of the coaxial rotor assembly, upper and lower rotor blades, the end view of counter-rotating blades, and the dye injection tubes between the rotor hubs and the blades.

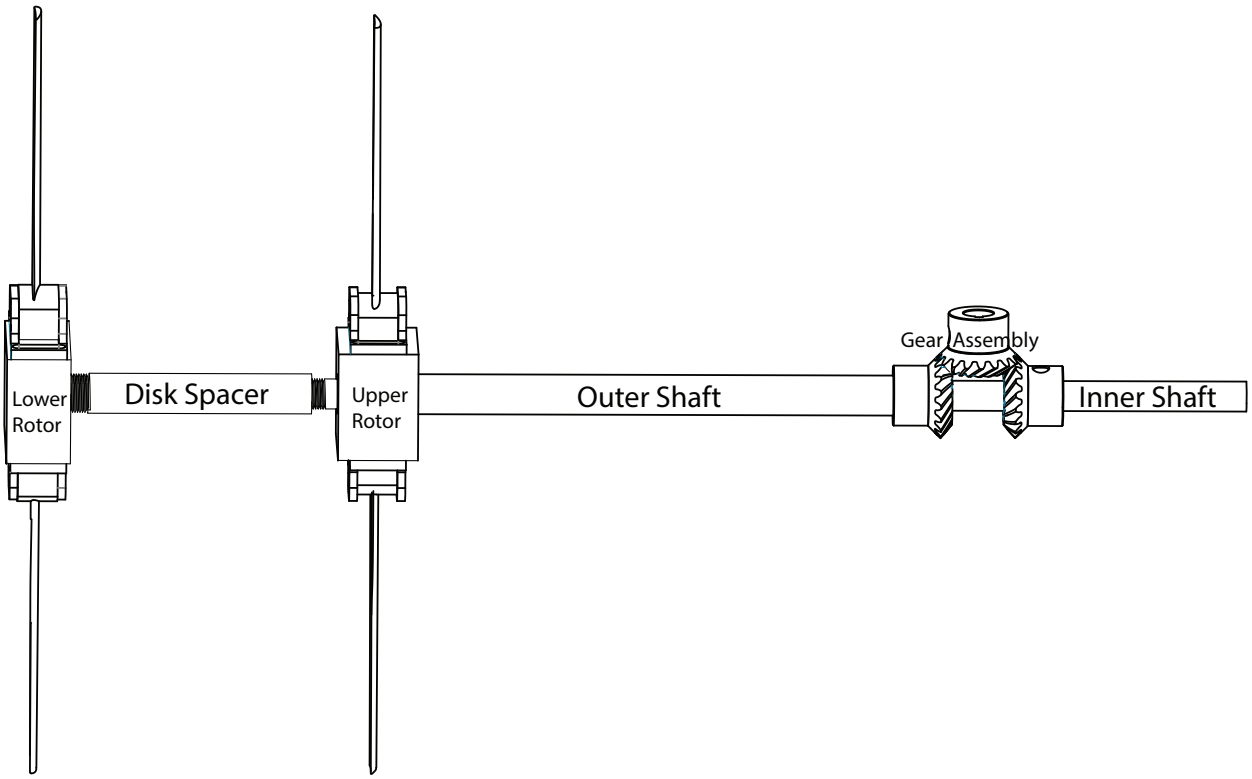

Figure 2.1: SolidWorks assembly of the coaxial rotor model

Each of the untapered blades, which were molded from carbon fiber reinforced plastic, measure $l = 9.5$ cm long with a chord length of $c = 1.9$ cm. Hence the solidity ratio is $\sigma = 2 \times cl/\pi R^2 = 0.068$ for a two-bladed single rotor and $2\sigma = 0.136$ when in coaxial configuration, where the actual blade area is used. The blades have a twist of approximately 5°. Blade profiles at the tip and root are made up of a modified ARAD-10, and a modified ARAD-13, respectively. The detailed rotor properties are shown in Table 2.1. For flow visualization purposes, the cores of the blade-tip vortices are rendered visible by injecting dye/air into the flow from the blade tips through 0.036-cm inner diameter stainless steel tubes inserted along each blade's span. The airfoil modifications include a chord wise linear thickness increase which thickened the trailing edge and provide more room for the injection tubes. In addition, the aft camber of the root airfoil is increased. The collective angle was manually set to $\theta = 13.5°$ using the reference surfaces machined at the roots of blades and using a digital inclinometer with $\pm 0.1°$ resolution. The uncertainty in angle measurements was less than $\pm 0.5°$.

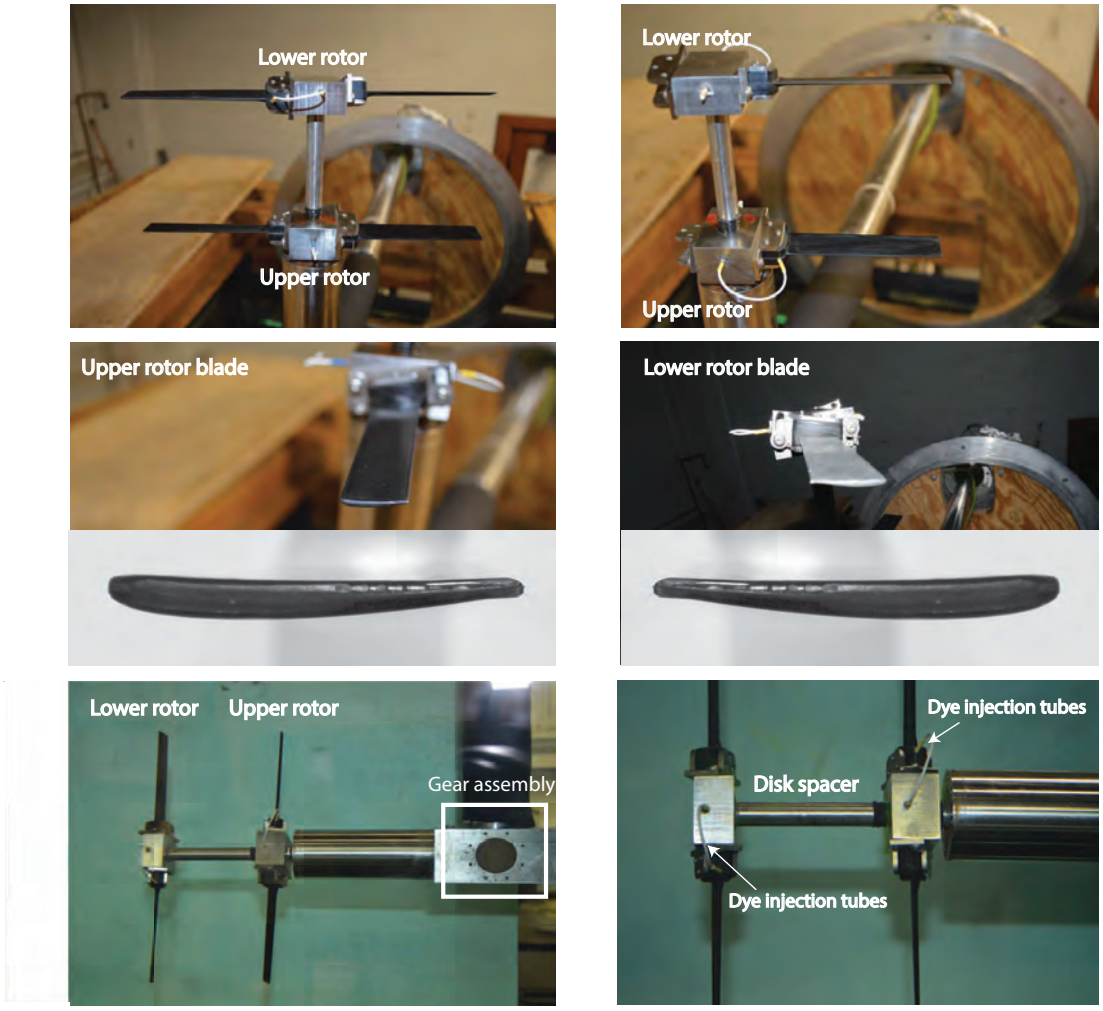

Figure 2.2: Coaxial rotor model assembly with axial rotor spacing of $H/R = 0.8$: two-bladed (top-left) and one-bladed (top-right), upper rotor blade (middle-left), lower rotor blade (middle-right), location of gearbox (bottom-left), and closer view of disk spacer (spacer 7) and the dye injection tubes between the hubs and the blades (bottom-right).

Number of blades per each rotor	1-2
Rotor disk radius	0.13 m
Blade chord	0.019 m
Overall solidity	0.136
Twist	-5°
Airfoil (tip and root profiles)	ARAD-10, ARAD-13
Collective angle	13.5°

Table 2.1: Properties of the test rotors in this study.

In order to investigate the effects of axial rotor spacing on the stability characteristics of the helical filaments off a coaxial rotor model, nine removable disk spacers with varying axial rotor separation distances were designed and built. The non-dimensional rotor separation distance, H/R, is defined as the ratio of the axial rotor separation distance H to the rotor radius R. H/R will also be referred as spacer to disk ratio. H is measured from the center of upper rotor hub to the center of lower rotor hub in the axial direction. All removable disk spacers were numbered from 1 to 9 for ease of describing the experiments while discussing the results. Ascending order of numbers from spacer-1 to spacer-9 corresponds to an increment in the nondimensional rotor spacing from $H/R = 0.25$ to $H/R = 1$. Details of this numbering of the removable disk spacers with their corresponding rotor spacings are given in Table 2.2.

Spacer No	H/R
Spacer-1	0.25
Spacer-2	0.375
Spacer-3	0.41
Spacer-4	0.5
Spacer-5	0.625
Spacer-6	0.75
Spacer-7	0.8
Spacer-8	0.875
Spacer-9	1

Table 2.2: Range of non-dimensional rotor separation distances employed in the experiments

2.3 Range of experiments

All experiments were performed in a 1.2 m wide, 2.4 m long, and 1.2 m deep stationary glass water tank at a water level of about 105 cm in the Fluid Mechanics Lab (FML) at University of California, Berkeley. The coaxial rotor centerline stood 67 cm off the floor and the upper rotor disk 80 cm off the end wall. The time intervals between the sequential runs were set to be minimum 7 minutes in order for the flow field in the tank to be free of the disturbances (e.g. recirculation effects) from the preceding test. Data were taken in both one-bladed and two-bladed coaxial rotor configurations. Two-bladed runs were carried out using all of the available spacers. However, measurements for one-bladed runs were only recorded for spacer-1 and spacer-7 cases. Table 2.3 and Table 2.4 show the range of experiments conducted with the two-bladed and one-bladed coaxial rotor configurations, respectively. Experiments in the single rotor configuration (both one- and two-bladed) were also carried out as reference by removing the lower rotor. The tests at a specified spacer number as given in both tables were carried out at the rotor rotational speeds (N) of 2, 4, 6, and 8 revolutions per second (rps). The rotor speed was controlled independently through a C-code running on a

Windows XP workstation.

Two-Bladed Tests											
	Spacer No	1	2	3	4	5	6	7	8	9	Single Rotor
	H/R	0.25	0.375	0.41	0.5	0.625	0.75	0.8	0.875	1.0	-
Rotor Speed	2 rps	1	5	9	13	17	21	25	29	33	37
	4 rps	2	6	10	14	18	22	26	30	34	38
	6 rps	3	7	11	15	19	23	27	31	35	39
	8 rps	4	8	12	16	20	24	28	32	36	40

Table 2.3: Range of experiments for two-bladed single and coaxial rotor configurations: numerical entries in the table indicate test numbers at the specified speed and H/R ratios. The rightmost column shows the test numbers for the single rotor configuration.

One-Bladed Tests				
	Spacer No	1	7	Single Rotor
	H/R	0.25	0.8	-
Rotor Speed	2 rps	41	45	49
	4 rps	42	46	50
	6 rps	43	47	51
	8 rps	44	48	52

Table 2.4: Range of experiments for one-bladed single and coaxial rotor configurations: numerical entries in the table indicate test numbers at the specified speed and H/R ratios. The rightmost column shows the test numbers for the single rotor configuration.

2.4 Flow visualization (FV)

Helical filaments from both rotors were visualized by releasing a solution of fluorescent sodium salt dye (Sigma Chemical Company, No. F-6377) at a concentration of 0.2 g/ℓ from the blade tips in a direction tangential to the blade path into the vortex cores. The dye was supplied to the dye reservoir at the base of the vertical shaft through thin, flexible plastic tubing. The dye reservoir was directly connected to the rotor dye tubes through the horizontal drive shafts and rotor hubs. External pressure was supplied to the dye in order to achieve clear visualization of the flow. Every effort was made to ensure that the injection velocity of the fluid did not alter the flow at the rotor tip (i.e., the fluid was merely leaked out at the same speed as the rotor, giving it no total velocity with respect to the surrounding fluid). The dye is delivered to the blade tips for flow visualization purposes through the hollow inner shaft. The upper rotor hub is designed to have a dye chamber in order to transfer the dye from the inner shaft to the upper rotor blades.The dye that is forced to the inner shaft is first transferred to the dye chamber in the hub of the upper rotor through circular holes drilled on both shafts, then to the surface of the hub through the holes drilled from the dye chamber. Finally, silicon rubber tubing is used to deliver the dye from the surface to the blades. Similarly, the lower rotor hub is designed in the same way to deliver the dye to the lower rotor blade tips. The dye inside the inner shaft is transferred to the dye chamber in the lower rotor hub through disk spacers that connect the lower hub to the inner shaft. Once the dye reached the chamber, it is delivered to the lower rotor blade tips in the same way as it is done in the upper rotor.

The flow field was illuminated with a 10-Watt CW Krypton-ion laser (American Laser Corporation) from which a 6-Watt beam was directed through two negative lenses to create a volumetric laser light shell.

A 1280 × 1024 pixel IDT Motion Pro X3-S1 camera with a maximum frame rate up to 1040 frames per second (fps) was used for image acquisition. The camera was fitted with a Canon 50-mm lens with 1.4 f-number and operated in continuous mode. The imaging rate was adjusted for different rotor speeds. For each set of experiments (at a specified spacer and rotor rotational speed), 18 images were recorded in each rotor revolution, which correspond to a 20°-difference between the consecutive images. Image acquisition continued for 25 rotor revolutions with a total of 450 recorded images. Acquired images are both recorded in video (.avi) and image (.tif) formats. Image recording started just after the starting vortex, which is formed by the filaments that come off the upper and lower rotors following the coaxial rotor start, left the imaging window (region of interest). Image acquisition details of the flow visualization runs are provided in Table 2.5. Camera (image acquistion), laser (illumination), and the motor are operated independently. Camera and the laser were controlled manually while the motor was controlled digitally.

Acquisition Details					
Speed	Revolutions	Frames/Rev	Total Frames	Framing Rate	Exposure (μs)
2 rps	25	18	450	36	6941
4 rps	25	18	450	72	6941
6 rps	25	18	450	108	6941
8 rps	25	18	450	144	6941

Table 2.5: Image acquistion details of flow visualization experiments.

2.5 Particle image velocimetry (PIV)

The water tank was seeded with silver-coated hollow ceramic spheres (Potters Industries Inc. AGSL 150-16TRD) with an average diameter of 100 μm and specific gravity of 0.9 for both particle flow visualization and PIV purposes. The large particle size enhances the light-scattering property of the particles. The same laser and camera setting was employed as in flow visualization runs. The imaging rate was adjusted for different rotor speeds. At a specified rotor speed and spacer, one set of data was recorded with short exposure for PIV purposes and one set of data was recorded with long exposure for particle flow visualization. For each experiment of PIV runs, 60 images were taken in each rotor revolution. Image acquisition continued for 50 rotor revolutions with a total of 3000 recorded images. Image acquisition of particle visualization runs was done in the same way as in the case of dye visualization experiments. Image acquisition details of the PIV and particle flow visualization runs are provided in Table 2.6.

Acquisition Details						
Speed	Revolutions	Frames/Rev	Total Frames	Framing Rate	Image separation (μs)	Exposure (μs)
2 rps	25	120	3000	240	4167	2080
2 rps	25	18	450	36	27778	6941
4 rps	50	60	3000	240	4167	2080
4 rps	25	18	450	72	13889	6941
6 rps	50	60	3000	360	2778	2080
6 rps	25	18	450	108	9260	6941
8 rps	50	60	3000	480	2083	2080
8 rps	25	18	450	144	6944	6941

Table 2.6: Image acquistion details for PIV experiments.

PIV data processing was performed on successive image pairs using the wall-adaptive Lagrangian parcel tracking algorithm (WALPT) (Refs. [39,57,58]) developed at UC Berkeley, an inhouse package. This algorithm utilizes interrogation windows that are advected and deformed according to the local velocity and velocity gradient fields, improving the quality of the data in regions of strong deformation. The algorithm outputs two-dimensional velocity field and its gradient tensor, which is computed spectrally. A total of 2999 image pairs were processed. The dimensions of the output files were 157 bin $\times$ 127 bin. A list of the parameters that were used in WALPT processing is provided in Appendix A. Post processing was done using several routines written in IDL. Average velocity and vorticity fields were constructed from the instantaneous velocity and velocity gradient fields. Accuracy studies on our WALPT algorithm carried out by Ortega (Ref. [58]) on synthetic vortex filaments of Gaussian vorticity profiles showed that the algorithm extracted the prescribed velocity and vorticity fields within 5% and 3%, respectively, as determined by the standard deviations of overall fields. These numbers, however, are presented for guidance only, since the actual flow fields have inherent uncertainties, out-of-plane motion being of the main ones. Further discussion may be found in Ortega (Ref. [58]) and the references therein.

Chapter 3

Stability Characteristics of Helical Filaments off a One-Bladed Coaxial Rotor

3.1 Introduction

In this chapter, findings of the sets of experiments carried out in order to investigate the stability characteristics of helical vortex filaments trailed from one-bladed rotors, both in single and coaxial configurations, will be presented and discussed. The range of these one-bladed rotor experiments were discussed in detail in Chapter 2 and shown in Table 2.4. Each experiment is assigned a numerical entry as given in the table. The numbers from 41-44 indicate the tests conducted when the coaxial rotor is fitted with spacer 1, which is designed to have a non-dimensional axial rotor separation distance of $H/R = 0.25$, at the rotor rotational speeds (N) of 2-8 revolutions per second, respectively. Similarly, the numbers 45-48 indicate the sets of experiments performed when the coaxial rotor is fitted with spacer 7 with $H/R = 0.8$. In addition to the one-bladed coaxial rotor experiments in two different rotor spacings, measurements were also taken when the one-bladed rotor was operated in single rotor configuration for comparison purposes. These experiments, also conducted at 2-8 rps, are indicated with numbers from 49-52, which is given on the rightmost column of the Table 2.4.

3.2 Flow conditions

Two definitions of Reynolds number will be used when discussing the vortex filament interactions in this study. First is the chord-based Reynolds number, which is defined as

$$Re_c = \frac{cV_{tip}}{\nu} \tag{3.1}$$

where c is the blade chord, $V_{tip} = 2\pi NR$ is the rotor speed at the blade tips, and $\nu = 0.01\ cm^2/s$ is the kinematic viscosity of water at $20°C$. Rotor rotational speeds (N) of 2-8 rev/s correspond to rotor tip speeds (V_{tip}) of 1.6-6.5 m/s, which give the chord-based Reynolds number in the range $Re_c = 3.1 \times 10^4 - 1.2 \times 10^5$.

Second, a more useful measure of the Reynolds number is provided based on the vortex filament circulation Γ, Re_Γ, which is defined as

$$Re_\Gamma = \frac{\Gamma}{\nu} \tag{3.2}$$

The filament circulation Γ used in Eq. 3.2 is extracted from the PIV measurements, which is explained in Chapter 2, by an integration in the vorticity field $\omega(x, y)$

$$\Gamma = \int_{A_\Gamma} \omega(x, y) dA \tag{3.3}$$

where the area A_Γ is bounded by a rectangular contour as marked in Fig. 3.1. This is done in a similar way as reported in Konus and Savas [54]. In the figure is shown the result of instantaneous vorticity field from PIV measurements of a single-bladed coaxial rotor fitted with spacer 7, which is logged as the test number 48 in Table 2.4. Two rectangular contours, marked 1 and 2, are shown in the figure, which are used as integration contours in tip vortex circulation estimation. Also in the figure is marked the positions of upper and lower rotors. The contours 1 and 2 are used to estimate the circulation around a tip vortex trailed from the upper rotor and lower rotor, respectively. Vorticity integral was carried out for 15 consecutive rotor revolutions in each of which a single frame was arbitrarily chosen to estimate the magnitude of the circulation (there are 60 PIV frames in each revolution). Azimuths of the rotor blades was the same in each frame used for the contour integral. The ultimate circulation value for a given run (e.g. test no 48) was found by averaging all 2×15 estimates and was rendered dimensionless by the kinematic viscosity of the water, which gives the circulation-based Reynolds number, Re_Γ. For each run to be discussed in this chapter, vortex filament circulation-based Re numbers are presented in Table 3.1 along with their standard deviations. The integration area A_Γ around a tip vortex contains 10×11 measurement points for rotor rotational speeds of 4, 6 & 8 rps in each case while it contains 8×9 measurement points for experiments conducted at the rotor rotational speed of 2 rps.

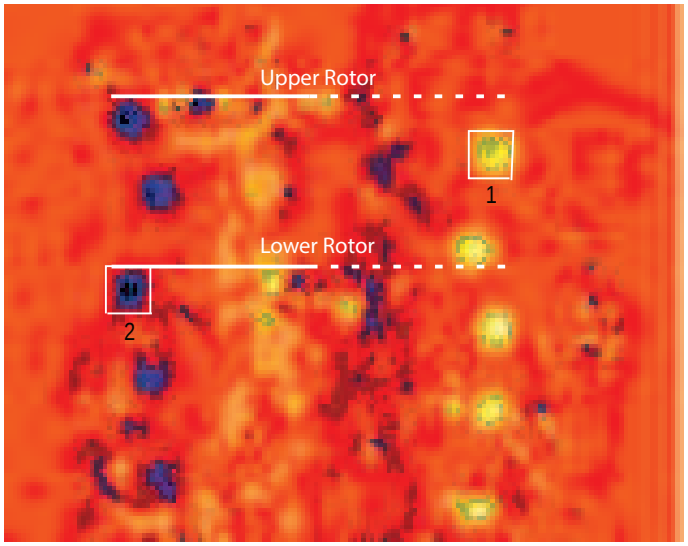

Figure 3.1: Integration contours utilized to estimate circulation around a tip vortex is drawn over instantaneous vorticity field from PIV measurements of one-bladed coaxial rotor fitted with spacer-7 (test no:48)

Circulation-based Re numbers (Re_Γ)			
Spacer No	1	7	Single Rotor
H/R	0.25	0.8	-
2 rps-Re_Γ	10500 ±900	10800 ±2000	11400 ±500
4 rps-Re_Γ	22000 ±1600	23900 ±500	23600 ±1000
6 rps-Re_Γ	45100 ±2300	50200 ±1300	50800 ±1100
8 rps-Re_Γ	43200 ±2200	49000 ±1900	47200 ±1800

Table 3.1: Circulation-based Reynolds numbers along with their standard deviations for each of the numeric entries that were given in Table 2.4.

3.3 Single rotor experiments

3.3.1 Flow images

Figure 3.2 shows the flow visualization images from the experiments conducted at the rotor rotational speeds of 2-8 rps, which correspond to test numbers of 49-52 in Table 2.4, for a one-bladed rotor operated in single rotor configuration. These measurements serve as reference in order to compare the results with that of coaxial rotor experiments as well as that of the theoretical study of Widnall [16] and the others. In the left column of the figure is given sample visualization images taken at an instant of the flows at all rotor speeds, in which the first row shows the images at the fastest rotor speed (8 rps) and the last row is from the test conducted at the slowest rotor speed (2 rps). Second and third rows shows the flow images taken at intermediate rotor speeds, i.e. when $N = 6$ & 4, respectively. In the middle column is provided the corresponding time-averaged images of the flows given in the left column. Averages were taken over 450 images, which correspond to a total of 25 rotor revolutions in each case. The right column shows the phase-averaged images which are locally contrast and brightness-enhanced. In each of the sample flow images given on the left is seen a single helical filament as it comes off the rotor blade tip and travels downstream of the rotor wake. Time-averaged images clearly show the expected axisymmetry of the rotor wake. The tip vortex circulation-based Reynolds numbers are provided on the rightmost column of Table 3.1 along with their standard deviation and estimated to be about 11400 for 2 rps, 23600 for 4 rps, 50800 for 6 rps, and 47200 for 8 rps cases.

Figure 3.3 shows the evolution of the single-bladed rotor wake during one complete rotor revolution at 8 rps. The images are numbered 1 to 18, which are shown on the top left of each image, and are 20° apart, which is the difference in the azimuths of the rotor in sequential images. Time separation between the successive images is about 6.94 ms. Successive turns of the filament are distinct and can be tracked up to the downstream distance of one rotor diameter. The vortex filament is seen to be fairly stable in the sequential images given in the figure.

3.3.2 Vortex instabilities and wake geometry

Vortex instabilities

Pitch of the helix (in radians) is defined as $\tan\alpha = L/R$ where L is the axial distance between the successive turns of the helical filament and R is the rotor radius. In dimensionless form, pitch can also be defined as $k = L/(2\pi R)$ where k is the dimensionless pitch of the helix. In subsequent discussions, unless stated otherwise, pitch of the helix will be given in dimensional form, i.e. in radians. In all cases ($N = 2 - 8$ rps), pitch of the helical filaments is about 0.27 radians (15°) in first turn and about 0.43 radians (25°) in second complete turn of the helix. These values are close to those reported in Widnall [16] in which mutual-inductance mode starts to appear (i.e., when $\tan\alpha \leq 0.3$).

At 2 & 4 rps, each filament develops short-wave instabilities just from their inception. At 6 & 8 rps, however, short-wave instabilities are not distinct in the first few turns of the rotor blade. In addition to the short-wave instabilities, in all cases successive turns of the vortex filament develop long-wave pairing instabilities, in which adjacent portions of the filament interact by orbiting around one another. Also, at downstream distances adjacent turns of the filament attempt to leapfrog one another, whereby the trailing turn of the helix accelerates and shrinks in size while the leading turn of the helix expand outward and slows down. This is seen in successive images provided in Figure 3.3. In Appendix A, rest of the evolution images of vortex wake for this one-bladed single rotor during one complete rotor revolution at 6, 4 & 2 rps are provided in Figures A.1, A.1, and A.1, respectively.

Wake contraction and xt diagram

In Figure 3.4 is shown trajectory of the tip vortex trailed from the single blade, which give the wake contraction ratios of single-bladed rotor in terms of rotor radius at all rotor speeds. Also, non-dimensional axial and radial locations of the tip vortex against the wake azimuths at all rotor speeds are plotted. The position data of the wake (both axial and radial) are extracted from a sequence of images following the vortex filament. The uncertainties in the position data are typically a few pixels. In all speeds, the rotor wake contracts to about 75% of the rotor radius, which is slightly higher than the value of 0.71R from the momentum theory and slightly lower than the commonly accepted value of 0.78R (Leishman [15]) for multi-bladed rotorcrafts. One of the reasons for the lower value than the commonly accepted wake contraction ratio is due to the fact that after the first blade passage the rate of axial displacement of the tip vortices increases with a corresponding decrement in radial contraction (Landgrebe [28]) as can be clearly seen in Fig 3.4-b. As it is clear in the figure, before and after the first blade passage, axial transport velocity assumes a constant value, the latter having a higher value than the former. For one-bladed rotor, this happens when the wake azimuth is $\psi = 360°$. For multi-bladed rotors, this occurs when $\psi \leq 180°$, which results in smaller wake contraction than the single-bladed case. Within two rotor revolutions, the helical filament travels to a distance of about a rotor radius beneath the rotor.

Particle Image Velocimetry (PIV)

Figure 3.5 shows PIV measurements at 8 rps for the corresponding one-bladed single rotor when talking about the dye visualization images. Instantaneous fields are presented on the left and the average fields on the right. In frame (a) in the first row, an instant of particle flow visualization is shown where PIV particles are used to visualize the flow. In frame (b) is given averaged flow picture. The average image in frame (b) is constructed by superposing 36 successive images which correspond to two complete rotor revolutions not necessarily beginning from the image shown in frame (a). In row 2 is given instantaneous and average

vorticity fields. Streamlines drawn over instantaneous and average vorticity fields are shown in third row. Streamlines in frames (e) of row 3 are drawn in a moving reference frame to highlight the individual vortices. In fourth row is given instantaneous and average speeds, over which streamlines are drawn. Average images in frames (d), (f), and (h) are constructed by superposing PIV results of 2999 successive processed image pairs captured during 50 rotor revolutions. The position of the one-bladed single rotor disk is marked in frame (d) in second row. The average images shown on the right also confirm the axisymmetry of the single rotor wake. The mean streamline patterns in frames (f) and (h) show the entrainment of the ambient fluid into the wake. Individual vortices are identifiable in the instantaneous fields shown on the left. In Appendix A, rest of the PIV results at 6, 4 & 2 rps are provided in Figures A.2, A.4, and A.6, respectively.

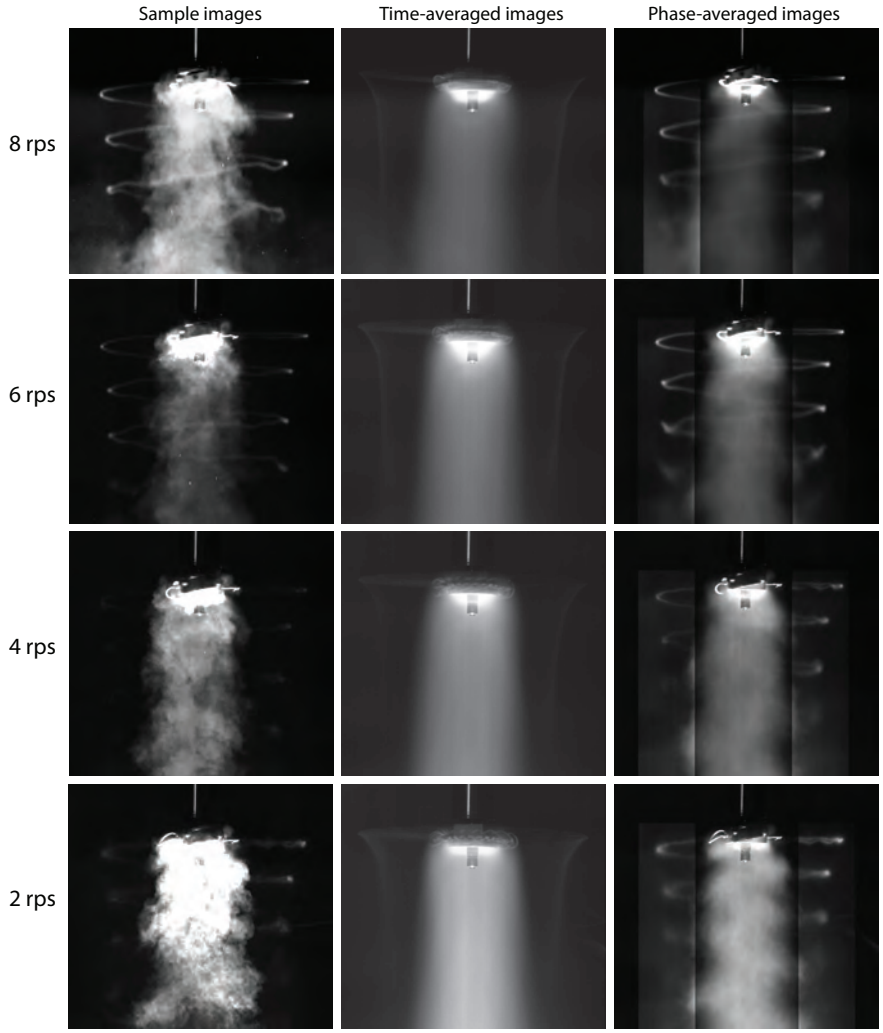

Figure 3.2: One-bladed single rotor: Flow visualization images at 8 rps (first row), 6 rps (second row), 4 rps (third row) & 2 rps (fourth row) Left column shows instantaneous flow images, the middle column shows the averaged flow fields, and the right column shows the phase-averaged images. The images on the right are locally contrast and brightness-enhanced.

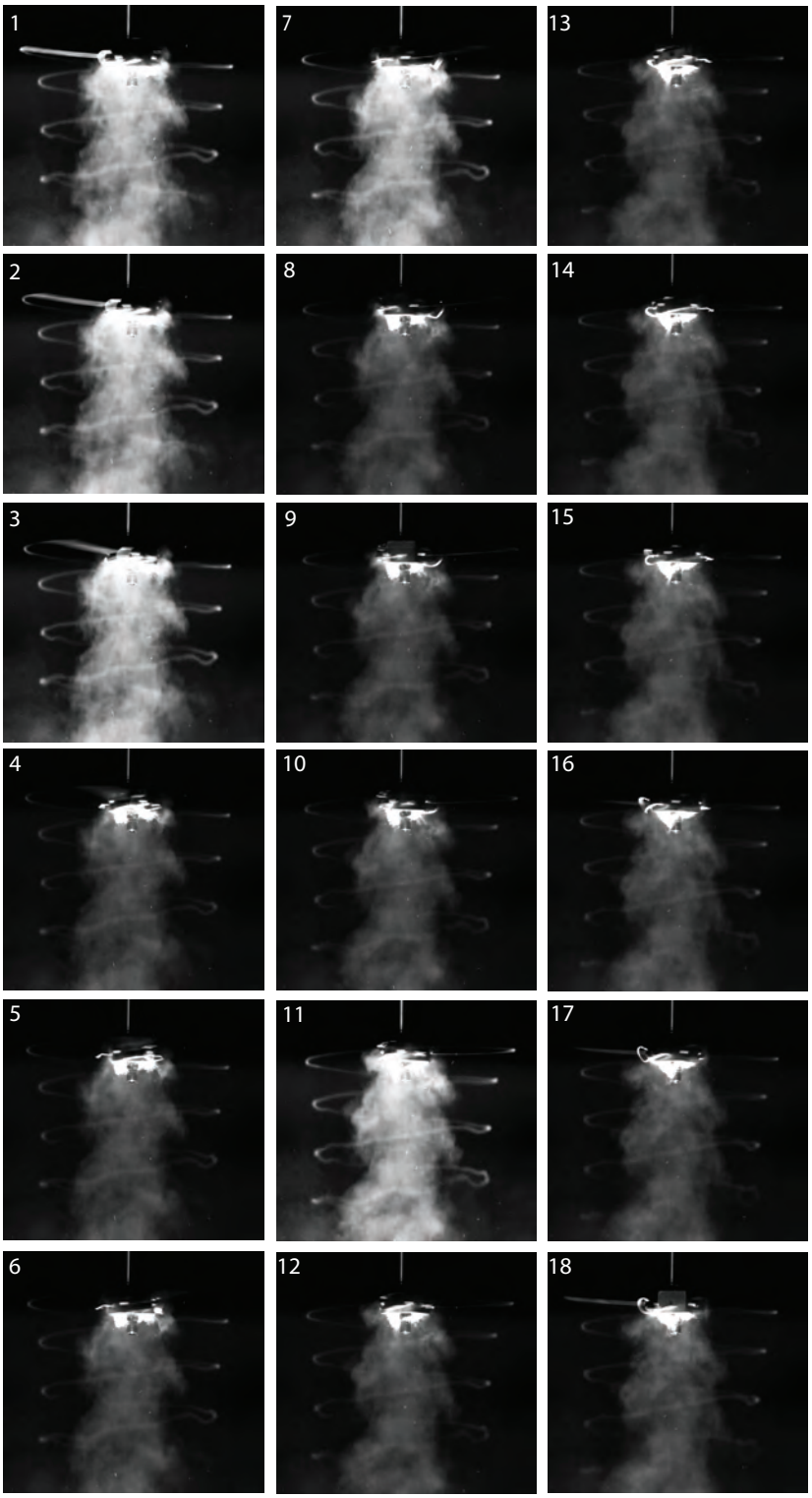

Figure 3.3: Vortex wake evolution of the one-bladed single rotor during one complete rotor revolution at 8 rps. Images are 20° ($\pi/9$ rad) apart. Time separation between successive images is 6.94 ms.

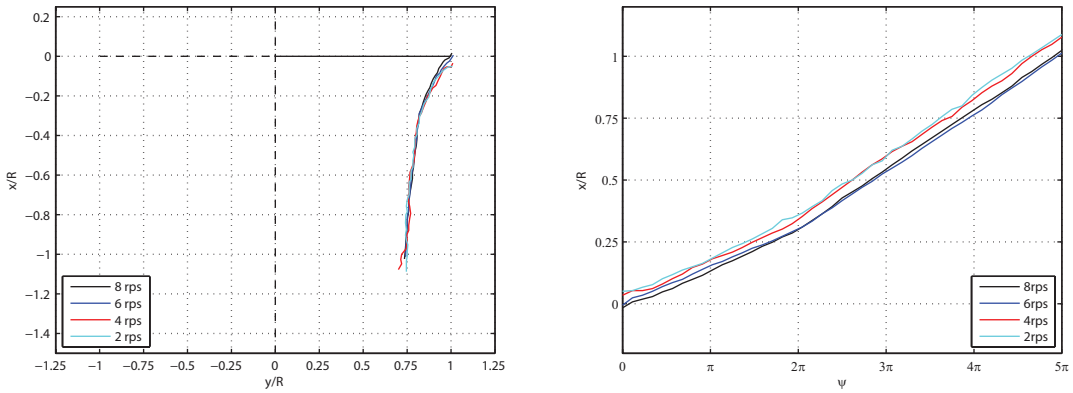

Figure 3.4: Trajectory of the helical filament trailed from one-bladed single rotor is shown. Right: spatial position of the tip vortex showing wake contraction. Left: xt diagram of the vortex filament at all speeds ($\psi = \Omega t$).

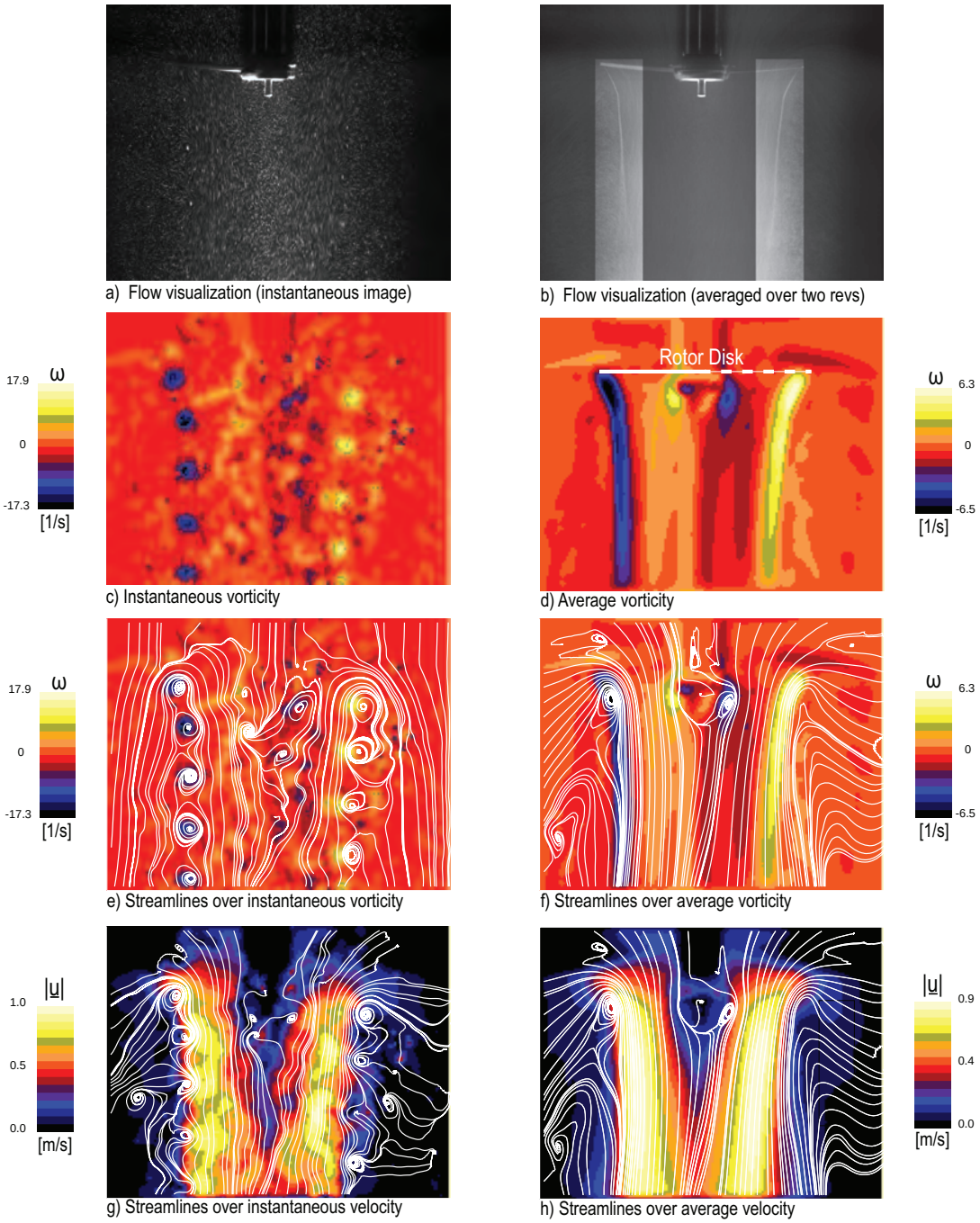

Figure 3.5: Flow field of a one-bladed single rotor at $N = 8$ rps. First row (a,b): particle flow visualization. Average field in frame (b) is locally brightness- and contrast-enhanced to highlight the wake contraction. In rows 2-4 are shown PIV measurements. Second row (c,d): vorticity fields. Third row (e,f): streamlines over vorticity. Fourth row (g,h): streamlines over speed. Streamlines in frame (e) are drawn from a moving reference frame and streamlines in frames (f-h) are drawn from a stationary reference frame.

3.4 Coaxial rotor with axial spacing of H/R=0.25

3.4.1 Flow images

Figure 3.6 shows the flow visualization images from the experiments conducted at the rotor rotational speeds of 2-8 rps, which correspond to test numbers of 41-44 in Table 2.4, for one-bladed rotors operated in coaxial configuration. The data is presented in the same order as in the Fig. 3.2 of single rotor runs. Coaxial rotors are fitted with spacer-1 (see Table 2.2 for numbering details), in which the rotors are spaced at 25% of the rotor radius. This is the shortest separation distance between the coaxial rotors employed in this study. This value is also the closest to those of the some of the full-scale helicopters, such as Russian Kamov-32 ($H/R = 0.189$) and Sikorsky ABC helicopter ($H/R = 0.138$). First obvious pattern to be observed from these images is that the lower rotor filament experiences strong deformation soon after its generation as opposed to the filaments trailed from single rotor configuration which is given in Figure 3.6. This feature is clearly visible at all rotor speeds. Time-averaged images on the middle are clear manifestation of the expected well-defined mean behavior of the rotor wakes. Note the difference in the radial contractions of the upper and lower rotor wakes, where the former is markedly higher than the latter. Phase-averaged flow images shown on the right are indicative of the persistence of the flow pattern throughout each particular runs.The tip vortex circulation-based Reynolds numbers are provided on the second column of Table 3.1 along with their standard deviation and estimated to be about 10500 for 2 rps, 22000 for 4 rps, 45100 for 6 rps, and 43200 for 8 rps cases. As given before, chord-based Reynolds numbers are computed to be between 31000-120000 at the rotor speeds of 2-8 rps.

Figure 3.7 shows the vortex wake evolution of the one-bladed coaxial rotors at this rotor spacing at 8 rps, where 18 sequential images are presented. Image representation is similar to those in Figure 3.3. The vortex filaments in the wake beneath the rotors are somewhat distinct up to about a rotor radius beneath the lower rotor. At 2 rps where the viscous effects are dominant, this value is within 50% of the rotor radius.

3.4.2 Vortex instabilities and wake geometry

Long-wave instability mode

Vortex filaments from both rotors develop long-wave pairing instabilities in which they orbit around each other as they travel downstream. As the upper rotor filament travels downstream through the lower rotor, turning blade of the lower rotor cut through the upper vortex, resulting in interrotor blade-vortex interactions (BVIs) ([22, 47]), an interaction that takes place between the vortices and blades of different rotors. Shorty after leapfrogging of upper vortex through lower vortex, which is completed in about one rotor revolution (2π rad), and its interaction between the lower rotor blade, upper vortex becomes diffuse and its subsequent location becomes difficult to trace. Also, the adjacent turns of the lower helix start to spiral around each other following the passage of the turns of the upper helix. This is followed by the nonuniform acceleration of these neighboring turns in the streamwise direction, resulting in elongation of the vortex. These long-wave instability characteristics and streamwise stretching of the lower rotor vortex are discernible in the successive images given in Figure 3.7 (see image 10, for example). Two vortices trailed from the upper and lower rotors of the coaxial rotor set exhibit repeatable long-wave pairing instability characteristics throughout the entire duration of the runs. Note the stable nature of the upper rotor vortex as opposed to more unstable nature of the lower rotor vortex. The lower rotor seems to have a stabilizing effect on the upper rotor filament while the upper rotor appears to destabilize the helical filament trailed from the lower rotor, resulting in strong distortions soon after its formation. At other rotor speeds, similar long-wave instability patterns are at play, however due to the more diffuse nature of the flow the filaments

cannot be tracked at farther downstream distances, which is clear in the flow images in Figure 3.6.

In all cases ($N = 2-8$ rps), pitch of the successive helices trailed from lower and upper rotors is about 0.22 rad (12.6°) and 0.5 rad (28.6°) in first complete turn, respectively. Filaments cannot be tracked after their first complete turn due to strong mutual interactions between them and viscous diffusion, particularly for those at lower rotor speeds. Weakness of mutual inductance between the adjacent turns of the upper rotor filament, if any, can be attributed to its higher helix pitch compared to that of lower rotor and also that given in Widnall [16] where the value $\tan\alpha > 0.3$ is documented to be critical in terms of initiation of mutual interactions between the adjacent portions of the helices. In Appendix A, rest of the evolution images of vortex wake at the same rotor spacing during one complete rotor revolution at 6, 4 & 2 rps are provided in Figures A.7, A.9, and A.11, respectively.

Short-wave instabilities

Flow images from 2 and 4 rps tests reveal that, similar to single rotor cases, vortex filaments from both rotors develop short-wave instabilities immediately after their formation. However, the wavelengths of these shortwaves appear to be shorter in lower rotor filament (ultra short-waves), particularly at 2 rps. At 6 & 8 rps, short-wave instabilities does not develop from the generation of filaments as opposed to slower rotation rates and extremely difficult to identify independently since the helical filaments, particularly the one from the lower rotor, lose their orderly shapes in a very short time after their formation following strong mutual interactions between the closely spaced rotors.

Wake contraction and xt diagram

Figure 3.8 shows the contraction and axial convection rates of the tip vortices from both rotors at all rotor speeds. Data representation is similar to that of single rotor wake in Figure 3.4. The locations of the centers of both rotor hubs are marked in the left plot of the figure where the axial separation of the rotors ($H/R = 0.25$) is also shown. Note the markedly higher axial convection rate of the upper rotor filaments compared to those of lower rotor filaments at all speeds. The vortices could be tracked up to 1.5 rotor revolutions (540° wake azimuth) below the rotors for 4-8 rps. For 2 rps, however, tip vortex from upper rotor could only be tracked up to half a rotor revolution. As given on the right part of the figure, lower vortex experiences an increment in its axial speed after the first blade passage ($\psi = 360°$) while the upper tip vortex speed slightly decreases. Upper wake contraction ceases and reaches a constant value after passing of the upper vortex through the lower vortex. Upper rotor wake contracts to about 77% of the rotor radius. Lower rotor wake contraction is about 80% of the rotor radius. Note that the contraction ratios of the both rotor wakes are close to each other, which is the result of the interactions between the vortices from different rotors.

Particle Image Velocimetry (PIV)

Figure 3.9 shows the results of corresponding PIV measurements. Data representation is similar to those provided in Figure 3.5. Positions of the upper and lower rotors are marked in frame (d), where the close separation of the rotors is seen. Orbiting of the upper and lower rotor vortices around one another was vivid in the videos of both particle visualization (a sample frame is shown in (a)) and processed PIV image pairs (sample frame in (c)). Note the expansion in the wake beneath the lower rotor as seen in frames (c) and (d). Curvature in the mean streamline pattern at the plane of the lower rotor implies that the upper wake is still developing. In Appendix A, rest of the PIV results at 6, 4 & 2 rps are provided in Figures A.8, A.10, and A.12, respectively.

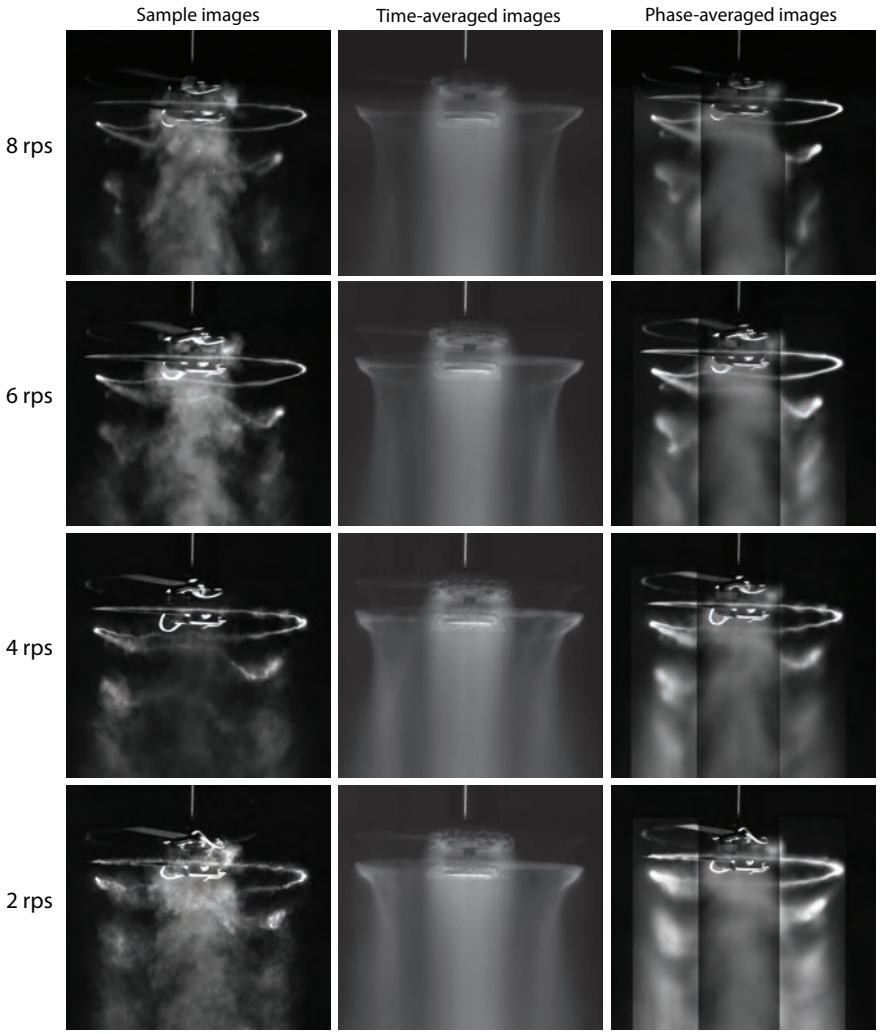

Figure 3.6: One-bladed coaxial rotor (spacer1), $H/R = 0.25$: Flow visualization images at 8 rps (first row), 6 rps (second row), 4 rps (third row) & 2 rps (fourth row). Left column shows instantaneous flow images, the middle column shows the averaged flow fields, and the right column shows the phase-averaged images. The images on the right are locally contrast and brightness-enhanced.

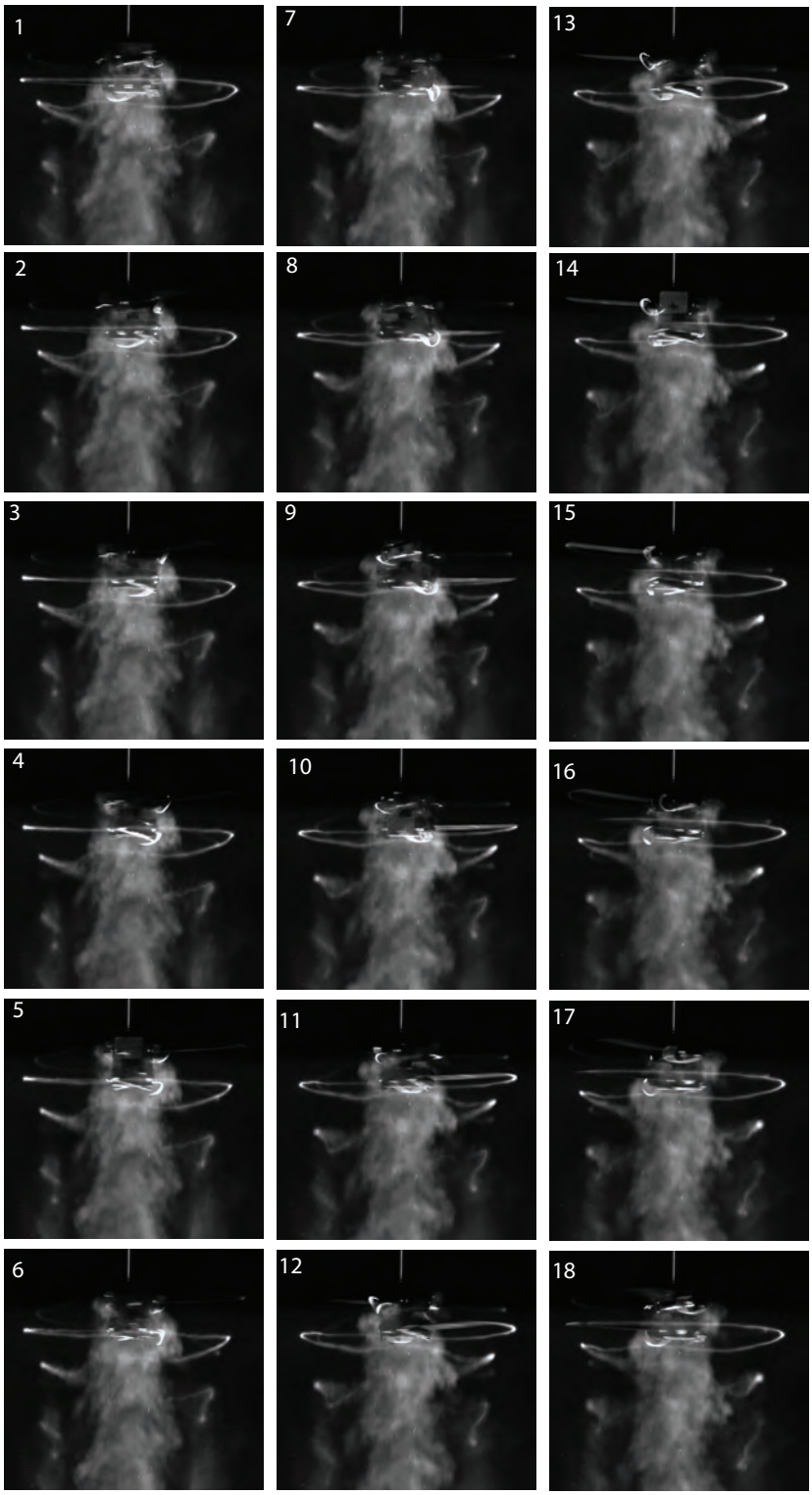

Figure 3.7: Vortex wake evolution of the one-bladed coaxial rotors with axial spacing of H/R=0.25 during one complete rotor revolution at 8 rps. Images are 20° ($\pi/9$ rad) apart. Time separation between successive images is 6.94 ms.

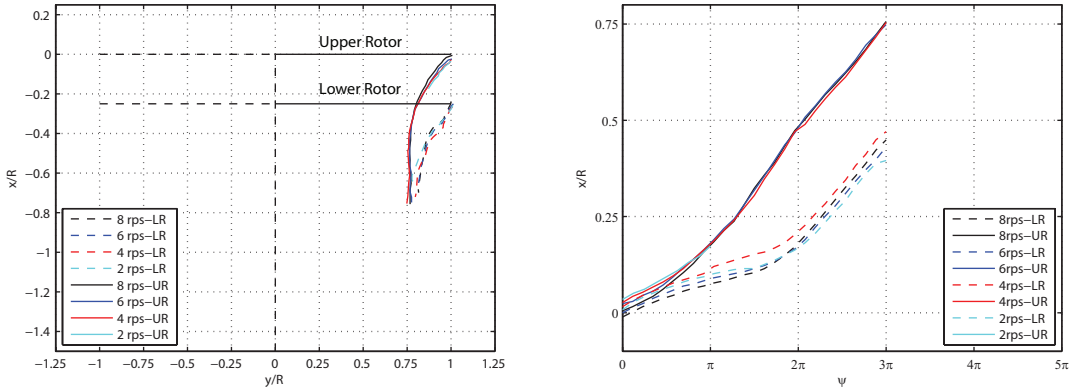

Figure 3.8: Trajectories of helical filaments trailed from coaxial rotor spaced at 25% of the rotor radius as well as those from the single rotor are shown. Right: spatial positions of tip vortices showing wake contraction. Left: xt diagram of the vortex filaments at all speeds ($\psi = \Omega t$).

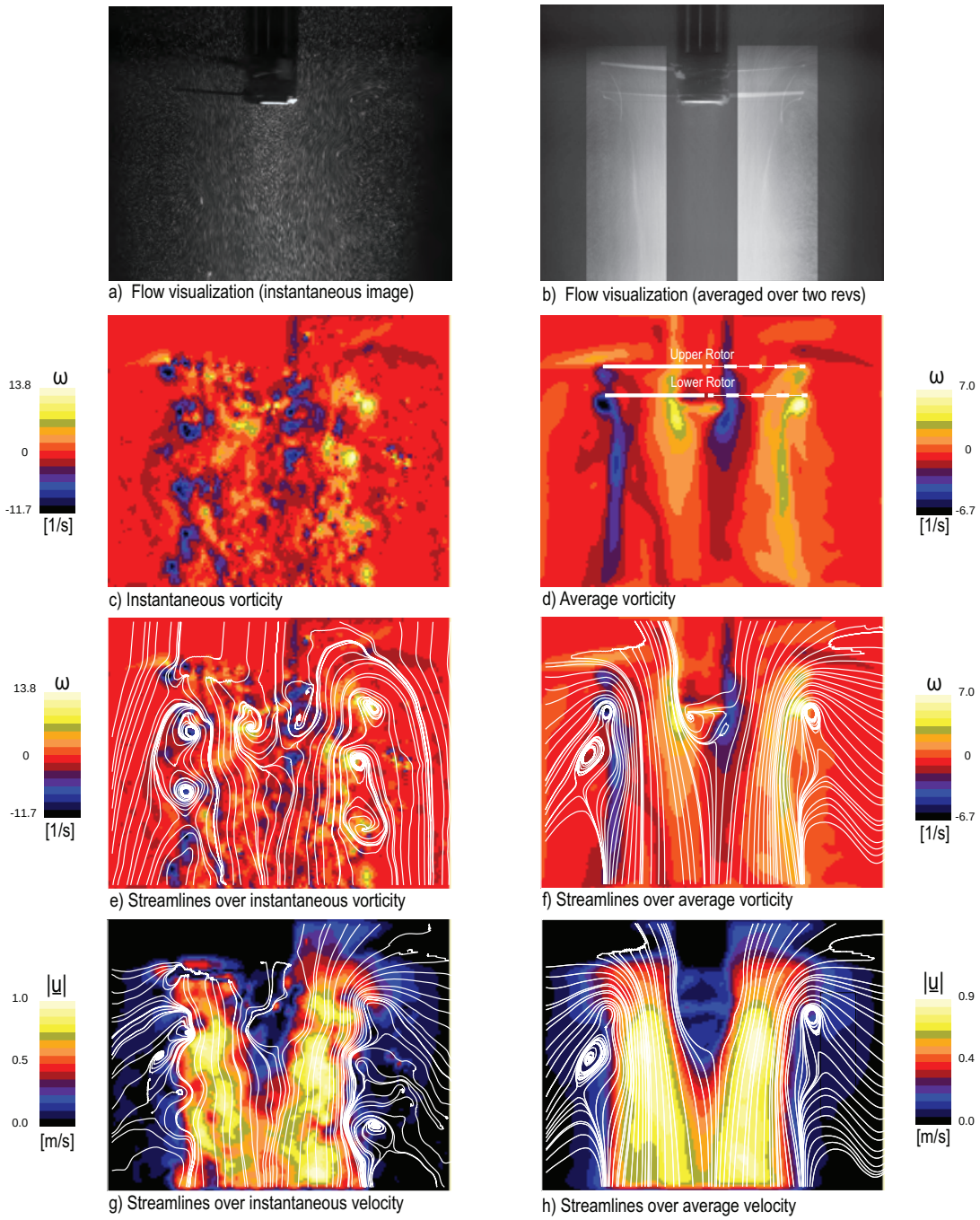

Figure 3.9: Flow field of a one-bladed coaxial rotor with rotor spacing of 25% of the rotor radius at $N = 8$ rps. First row (a,b): particle flow visualization. Average field in frame (b) is locally brightness- and contrast-enhanced to highlight the wake contraction. In rows 2-4 are shown PIV measurements. Second row (c,d): vorticity fields. Third row (e,f): streamlines over vorticity. Fourth row (g,h): streamlines over speed. Streamlines in frame (e) are drawn from a moving reference frame and streamlines in frames (f-h) are drawn from a stationary reference frame.

3.5 Coaxial rotor with axial spacing of H/R=0.8

3.5.1 Flow images

Figure 3.10 shows the flow visualization images from the experiments conducted at the rotor rotational speeds of 2-8 rps, which correspond to test numbers of 45-49 in Table 2.4, for one-bladed rotors operated in coaxial configuration. The data presentation is similar to those in Figure 3.2 of single rotor runs. Coaxial rotors are fitted with spacer-7, in which the rotors are spaced at 80% of the rotor radius. Axial separation is more than thrice compared to previous case where rotors are spaced at a quarter radius (spacer-1). Since the rotors are mounted at a greater distance than spacer-1 tests, helical vortex filament trailed from the lower rotor maintains its orderly helical shape for about 2 rotor revolutions before the filament from the upper rotor reach the plane of the lower rotor. Subsequently, mutual interactions between both filaments grow stronger and instigate long-wave pairing instability. Moreover, due to the greater distance between the rotors, upper rotor wake contracts more inward and impinges on a smaller cross-sectional area at the inner part of the lower disk than the closely-spaced rotors before it passes through the lower rotor filament, after which the upper filament ceases to contract. Therefore, for closely-spaced rotors (spacer-1) the wake contraction of upper rotor is smaller than that of the widely-spaced rotors (spacer-7) at the plane of the lower rotor. This is observed in all rotor speeds and can be compared from the mean data provided in Figures 3.6 & 3.10. Note also the higher wake contraction rate of the upper rotor as opposed to that of the lower rotor, which is smaller. The phase-averaged images provided on the right of the figure well represents that the flow pattern is persistent throughout the length of the tests. The tip vortex circulation-based Reynolds numbers are provided on the third column of Table 3.1 along with their standard deviation and estimated to be about 10800 for 2 rps, 23900 for 4 rps, 50200 for 6 rps, and 49000 for 8 rps cases. Figure 3.11 shows the vortex wake evolution of the one-bladed coaxial rotors at this rotor spacing at 8 rps. Image representation is similar to those in Figures 3.3 & 3.7. Note the more stable nature of the wake beneath the lower rotor as opposed to those of previous case.

3.5.2 Vortex instabilities and wake geometry

Long-wave instability mode

From the sequential images given in Figure 3.11, the pitch of the upper and lower rotor helices is different, where that of the former is higher than that of the lower. Smaller separation between the successive turns of the lower rotor helix leads to strong interactions. In all cases ($N = 2 - 8$ rps), pitch of the helical filaments trailed from both rotors is about 0.26 rad (14.9°) in first complete turn. Pitch increases to 0.37 rad (21.2°) for lower rotor and 0.5 rad (28.6°) for upper rotor in second complete turn of the helices. Within the wake beneath the lower rotor, the mutual interactions between the adjacent turns of lower filament becomes pronounced where neighboring portions of the lower rotor helix develops long-wave type perturbations in which they spiral around each other.Turns of upper helix is very stable from its inception as to the point where it reaches to the vicinity of the lower rotor and interact with the lower rotor blade. Subsequently, the upper vortex becomes diffuse in the wake beneath the lower rotor (see image 8 in Figure 3.11). A comparison of the images from spacer 1 and spacer 7 experiments, where the coaxial rotors are spaced at 25% and 80% of the rotor radius, respectively, reveals that the lower rotor vortex of the former case experiences stronger deformation than that of the latter case, which is readily seen from the sequential images of Figures 3.7 & 3.7. In Appendix A, rest of the evolution images of vortex wake at the same rotor spacing during one complete rotor revolution at 6, 4 & 2 rps are provided in Figures A.13, A.15, and A.17, respectively.

Short-wave instabilities

When rotor speed is 4 rps, upper filament develops short-wave instabilities just from its inception as well as lower filament. Amplitudes of these short-waves appear to small compared to those found on lower filament and do not grow in magnitude as the upper filament travels downstream of the wake. However, amplitudes of these short-waves developed along the lower filament increase at older wake ages. Results of experiments carried out at 2 rps shows similar attributes as in the 4 rps, only difference being the shorter wavelength (ultra short waves) on lower filament in the former case.

Wake contraction and xt diagram

Figure 3.12 shows the wake contraction and axial convection rates of the tip vortices from both rotors at all rotor speeds. Data representation is similar to those given in Figure 3.4. The locations of the centers of both rotor hubs are marked on the left of the figure where the axial separation of the rotors ($H/R = 0.8$) is also shown. The individual vortices could be tracked up to about 2.5 rotor revolutions (900° wake azimuth) below the rotors. From the average images given in Figure 3.10, the upper rotor wake contraction is found to be about 70% of the rotor radius and lower rotor wake contraction about 90% of the rotor radius, which are markedly greater compared to that of the upper rotor. Similar to before, the tip vortex from upper vortex traveled at a faster rate than the tip vortex from the lower rotor in axial direction, which can be seen from the xt diagram given on the right.

Particle Image Velocimetry (PIV)

Figure 3.13 shows the results of corresponding PIV measurements. Data representation is similar to those provided in Figures 3.5 & 3.9. Positions of the upper and lower rotors are marked in frame (d), where the large separation of the rotors is seen. As opposed to spacer 1 case where the rotor separation is the smallest, individual successive vortices from both rotors are easily identifiable in frame (c). Double tube structure of the rotor wakes is seen in average vorticity field in frame (d). A close investigation of the PIV videos from both cases (Spacer 1 & 7) reveals that the upper and lower rotor vortices does not exhibit a clear orbiting behavior in the latter as in the case of the former. Mean streamline pattern in frames (f) and (h) shows that the upper rotor wake approaches a more fully-developed state than the spacer 1 case as expected due to the larger separation of the rotors where upper rotor wake has sufficient time and space to contract. It becomes difficult to track upper vortices following their interaction with the lower rotor blade. Subsequently, the wakes from both rotors become coalesced beneath the lower rotor as seen in frame (d). In Appendix A, rest of the PIV results at 6, 4 & 2 rps are provided in Figures A.14, A.16, and A.18, respectively.

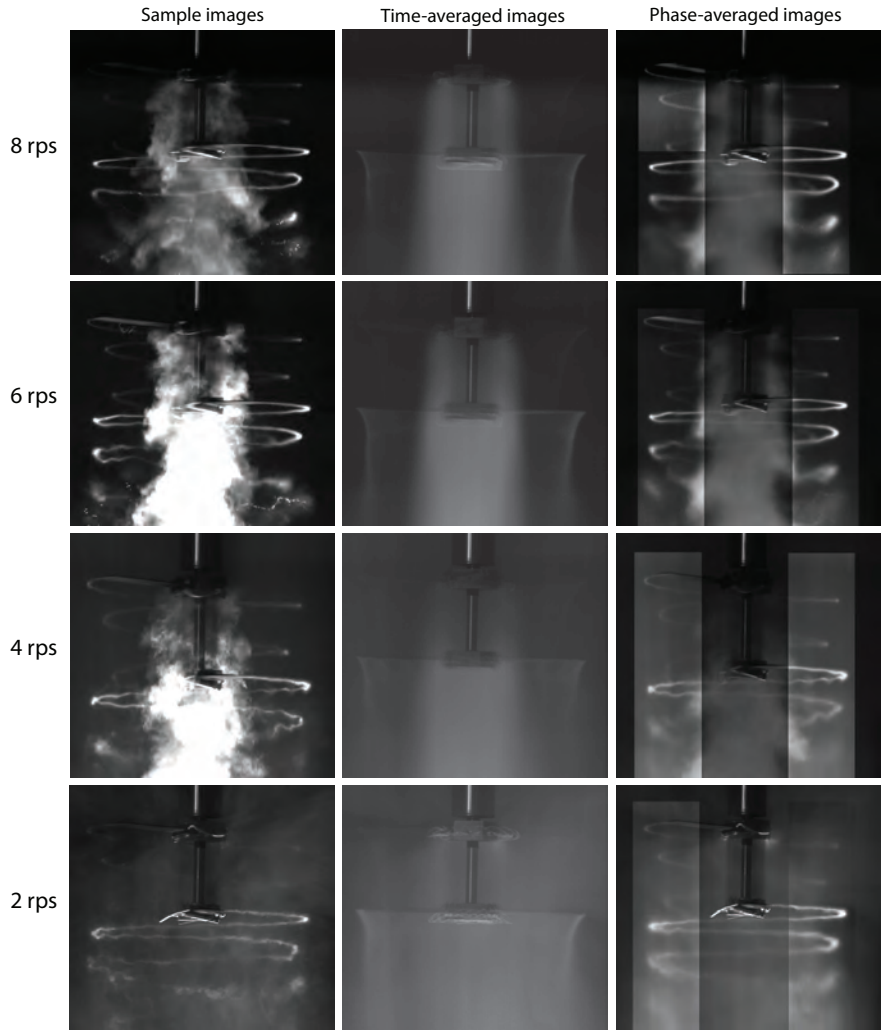

Figure 3.10: One-bladed coaxial rotor (spacer7), $H/R = 0.8$: Flow visualization images at 8 rps (first row), 6 rps (second row), 4 rps (third row) & 2 rps (fourth row). Left column shows instantaneous flow images, the middle column shows the averaged flow fields, and the right column shows the phase-averaged images. The images on the right are locally contrast and brightness-enhanced.

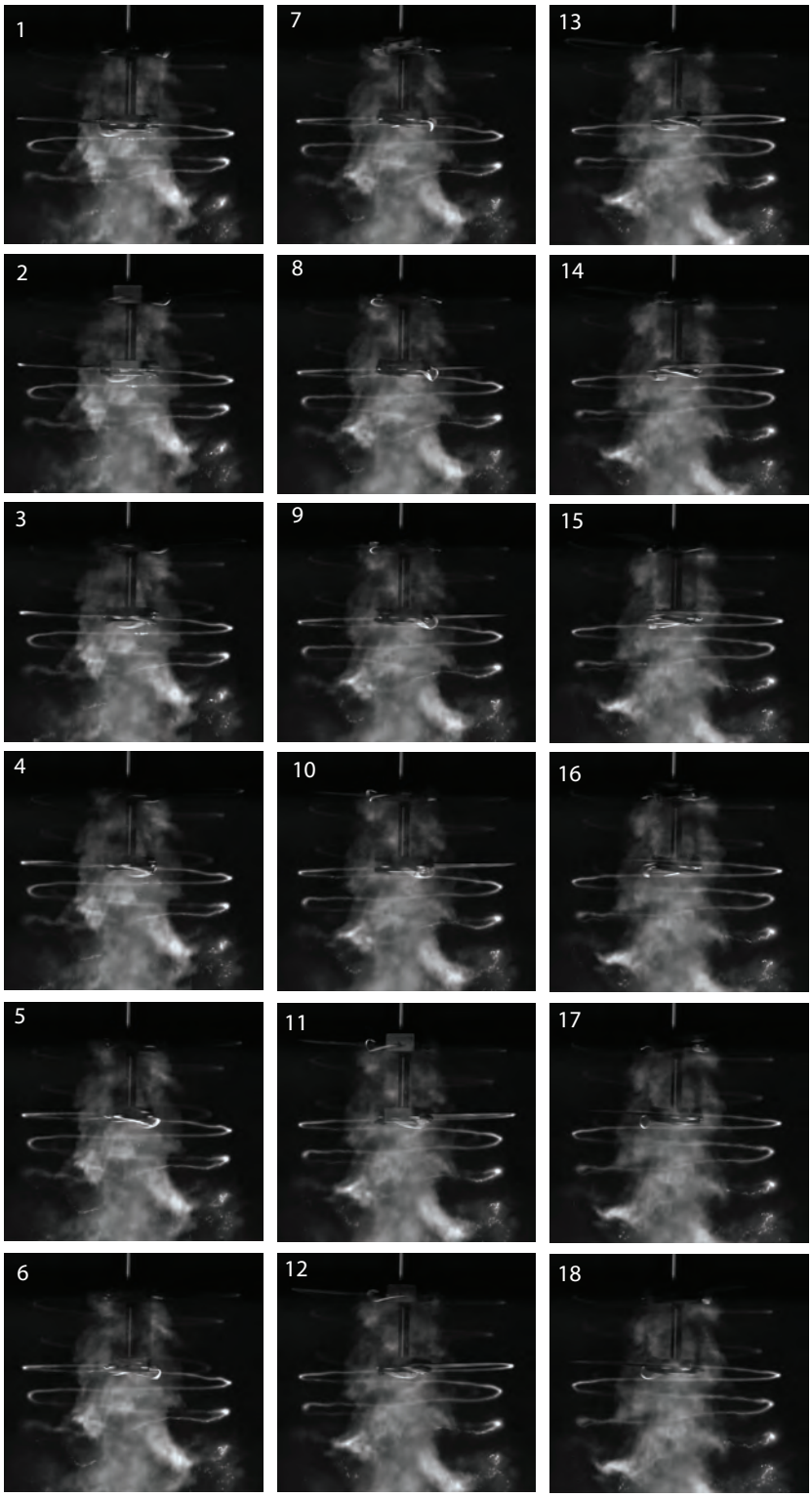

Figure 3.11: Vortex wake evolution of the one-bladed coaxial rotors with axial spacing of H/R=0.8 during one complete rotor revolution at 8 rps. Images are 20° ($\pi/9$ rad) apart. Time separation between successive images is 6.94 ms.

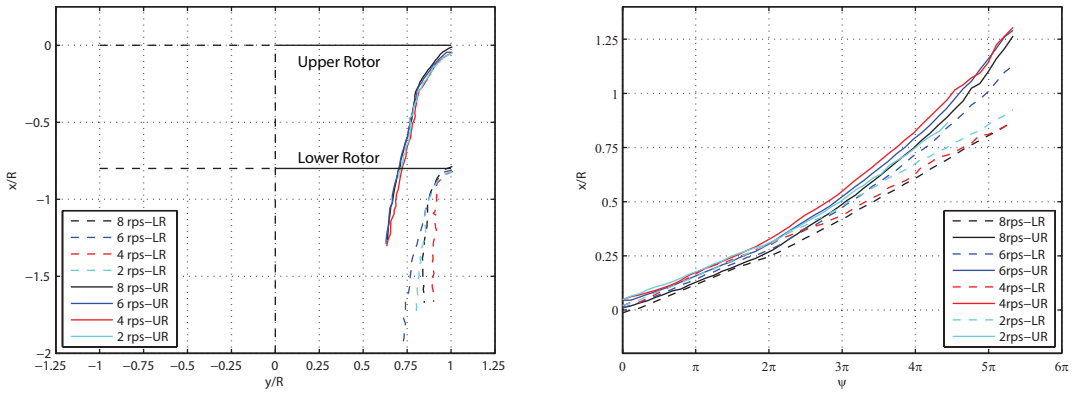

Figure 3.12: Trajectories of helical filaments trailed from coaxial rotor spaced at 80% of the rotor radius as well as those from the single rotor are shown. Right: spatial positions of tip vortices showing wake contraction. Left: xt diagram of the vortex filaments at 8 rps ($\psi = \Omega t$). Vortex labeling is similar to those in Figure 4.13

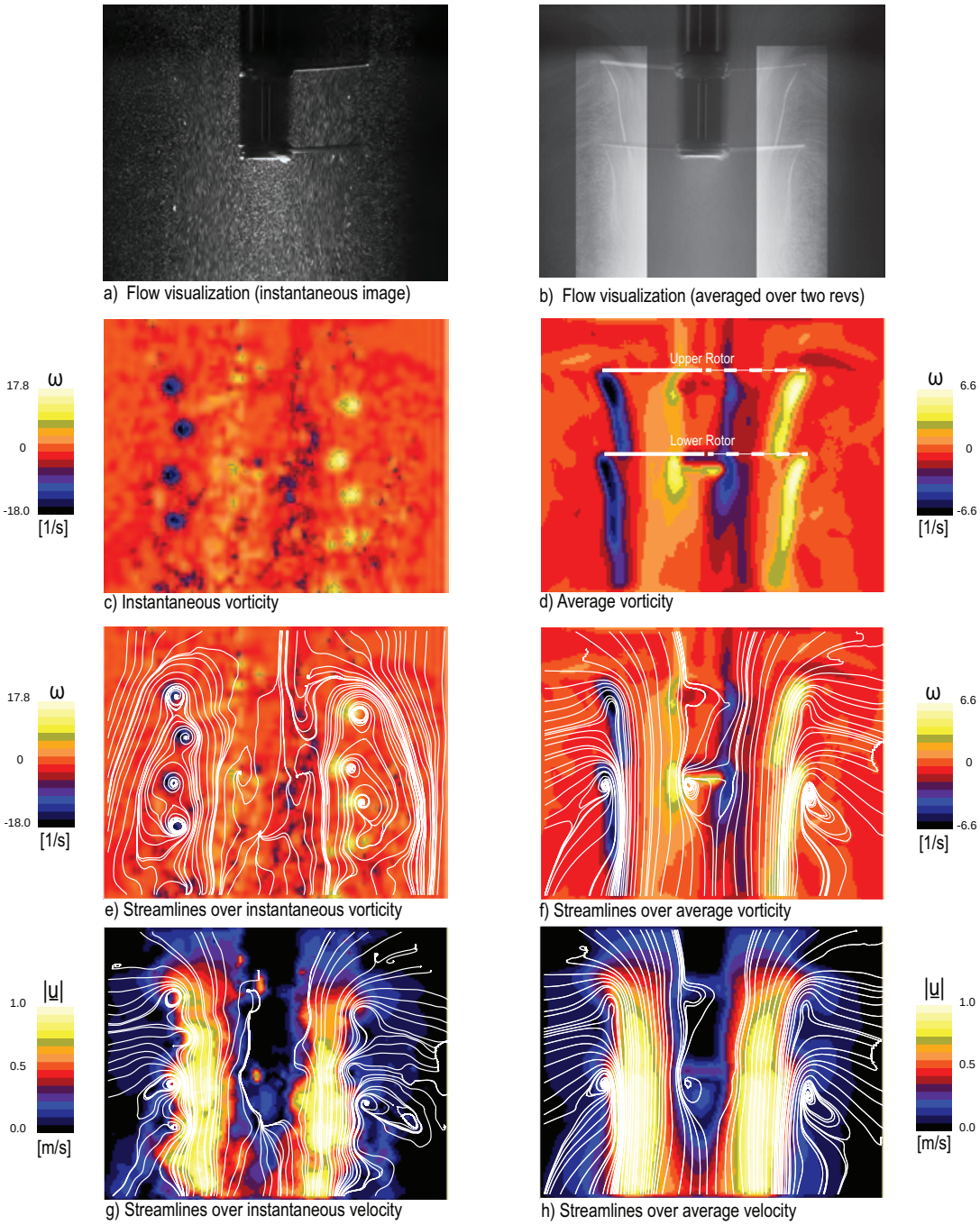

Figure 3.13: Flow field of a one-bladed coaxial rotor with rotor spacing of 80% of the rotor radius at $N = 8$ rps. First row (a,b): particle flow visualization. Average field in frame (b) is locally brightness- and contrast-enhanced to highlight the wake contraction. In rows 2-4 are shown PIV measurements. Second row (c,d): vorticity fields. Third row (e,f): streamlines over vorticity. Fourth row (g,h): streamlines over speed. Streamlines in frame (e) are drawn from a moving reference frame and streamlines in frames (f-h) are drawn from a stationary reference frame.

Chapter 4

Stability Characteristics of Helical Filaments off a Two-Bladed Coaxial Rotor

4.1 Introduction

In this chapter, findings of the sets of experiments carried out in order to investigate the stability characteristics of helical vortex filaments trailed from two-bladed rotors, both in single and coaxial configurations, will be presented and discussed. The range of these two-bladed rotor experiments were discussed in detail in Chapter 2 and shown in Table 2.3. Each experiment is assigned a numerical entry as given in the table as in the case of the one-bladed tests. Measurements were taken at nine different axial separation distances between the coaxial rotors which range from a quarter to one rotor radius. Adjusting the distance between the rotors was done by fitting the coaxial rotor set with the removable disk spacers for each H/R ratio. At each rotor separation distance, which is given by the numerical entries in each column in Table 2.3, experiments were conducted at rotor rotational speeds of 2-8 rps. In addition to the experiments conducted in coaxial rotor configuration, two-bladed single rotor measurements were performed in order to provide the baseline characteristics for further comparison with the coaxial rotor tests.

4.2 Flow conditions

As discussed in detail in the preceding chapter, two definitions of Reynolds numbers will be used when discussing the vortex filament interactions in this study. First is the chord-based Reynolds number, which is defined as

$$Re_c = \frac{cV_{tip}}{\nu} \tag{4.1}$$

where c is the blade chord, $V_{tip} = 2\pi NR$ is the rotor speed at the blade tips, and $\nu = 0.01\ cm^2/s$ is the kinematic viscosity of water at $20°C$. Rotor rotational speeds (N) of 2-8 rev/s correspond to rotor tip speeds (V_{tip}) of 1.6-6.5 m/s, which give the chord-based Reynolds number in the range $Re_c = 3.1 \times 10^4 - 1.2 \times 10^5$. At a specific rotational speed of the rotor, chord-based Reynolds numbers are identical for both one-bladed and two-bladed runs as well as for all rotor separation distances. Second, a more useful measure of the

Reynolds number is provided based on the vortex filament circulation Γ, Re_Γ, which is defined as

$$Re_\Gamma = \frac{\Gamma}{\nu} \tag{4.2}$$

Extraction of the filament circulation Γ as given in Eq. 4.2 is discussed thoroughly in the preceding chapter when discussing the one-bladed tests. Integration contours utilized to extract circulation around each tip vortex are shown in Figure 4.1 where these contours are numbered from 1 to 4 which correspond to tip vortices trailed from each one of the four blades. Also, locations of the upper and lower rotors are marked in the same figure. As in the case of one-bladed runs, the ultimate circulation values for each run were calculated by averaging all 4×15 estimates and was rendered dimensionless by the kinematic viscosity of the water, hence the circulation-based Reynolds number, Re_Γ. These estimated tip vortex circulation-based Re numbers along with their standard deviations are provided in Table 4.1.

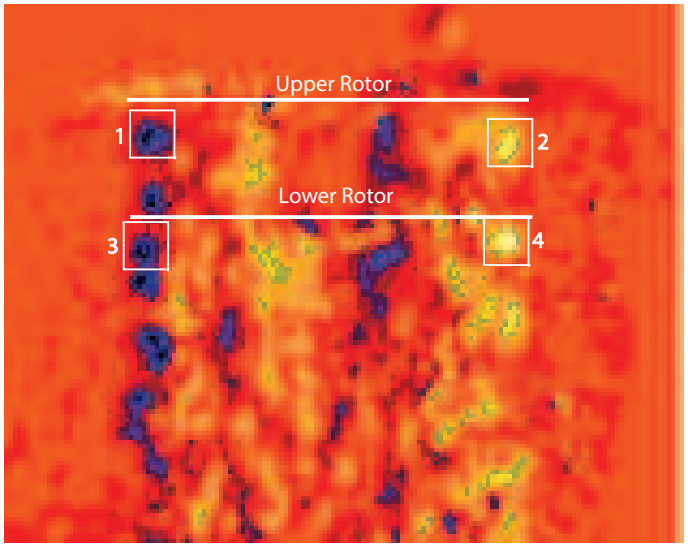

Figure 4.1: Integration contours utilized to estimate circulation around tip vortices are drawn over instantaneous vorticity field from PIV measurements of two-bladed coaxial rotor fitted with spacer-4, where $H/R = 0.5$ (test no:16).

Circulation-based Re numbers (Re_Γ)										
Spacer No	1	2	3	4	5	6	7	8	9	Single Rotor
H/R	0.25	0.375	0.41	0.5	0.625	0.75	0.8	0.875	1	-
2 rps-Re_Γ	8950 ±870	8950 ±1300	10600 ±810	10000 ±1100	9850 ±1300	8900 ±1400	8300 ±1600	8400 ±1250	8500 ±2000	10300 ±1200
4 rps-Re_Γ	16800 ±3700	15200 ±2200	19100 ±2200	18600 ±2000	17900 ±2900	16400 ±2500	14400 ±1500	15300 ±2500	15800 ±2600	17600 ±1600
6 rps-Re_Γ	34500 ±6450	31000 ±3300	34000 ±3800	34600 ±4800	40000 ±5900	34200 ±5200	33500 ±4000	33600 ±11400	27500 ±14800	38000 ±3800
8 rps-Re_Γ	34400 ±5000	30500 ±3550	31400 ±2600	31200 ±2950	38200 ±4800	33000 ±5400	33400 ±4250	27500 ±4500	29200 ±4550	32100 ±2400

Table 4.1: Circulation-based Reynolds numbers along with their standard deviations for each of the numeric entries that were given in Table 2.3.

4.3 Single rotor experiments

4.3.1 Flow images

Figure 4.2 shows the flow visualization images from the sets of experiments conducted at the rotor rotational speeds of 2-8 rps which are indicated in the rightmost column of Table 2.3 with the test numbers 37-40. A two-bladed hovering rotor in single configuration is employed in these experiments. Single-rotor measurements are intended to provide the baseline rotor characteristics when comparing with the coaxial rotor measurements. The lower rotor is removed from the coaxial rotor assembly, hence the upper rotor is operated in isolation in order to take measurements in single rotor configuration. In the figure is shown instantaneous (left column), time-averaged (middle column), and phase-averaged (right column) flow images from the experiments conducted at the rotor speeds of 8 (first row), 6 (second row), 4 (third row), and 2 (fourth row) rps. Instantaneous images on the left column were extracted from a video sequence recorded for a duration of 25 rotor revolutions for each rotor speed. 18 images were captured during a complete rotor revolution. These images show the two-bladed single rotor wake and individual helical filaments as they come off the blades and travel downstream. Adjacent helical filaments appear to develop long-wave pairing instabilities in all four cases. At 2 and 4 rps, both filaments develop short-wave instabilities just from their inception. Also, the right-handed rectangular (x, y, z) and polar (r,x) coordinate systems are defined in top left frame of the Figure 4.2 where the x-axis measures into the wake along the geometric centerline of the rotor. The average images provided on the middle column clearly shows the well-defined mean behavior of the wake of the single rotor configurations in which the wake is axisymmetric. These average images are constructed by superposing a total of 450 successive images not necessarily beginning from the instantaneous images that are shown on the left column. On the right column is given the phase-averaged images of the runs taken at each rotor speed. The periodicity of the flow pattern is taken into account while constructing phase-averaged images. In other words, the phase-averaged images are constructed by superimposing 13 images for 6 & 8 rps cases and 25 images for 2 & 4 rps cases beginning from the ones that are given in the left column and adding images that are taken at the same rotor azimuth in every two rotor revolutions for 6 & 8 rps and in every rotor revolution for 2 & 4 rps. This is done because a close investigation of the flow visualization data for this single rotor configuration reveals that the flow pattern exactly repeats itself in every two rotor revolutions when the rotor speed is 6 & 8 rps and in every rotor revolution for 2 & 4 rps cases although the vortex filaments show similar characteristics in each revolution. These phase-averaged images are also indicative of the fact that in each case the flow pattern is persistent throughout the entire duration of the runs. The tip vortex circulation-based Reynolds numbers are provided on the rightmost column of Table 4.1 along with their standard deviation and estimated to be about 10300 for 2 rps, 17600 for 4 rps, 38000 for 6 rps, and 32100 for 8 rps cases. The circulation values shown are rounded to three significant digits. As given before, chord-based Reynolds numbers are computed to be between 31000-120000 for rotor speeds of 2-8 rps, respectively. Lower values for circulation-based Reynolds numbers (Re_Γ) at 2 & 4 rps are indicative of the viscosity-dominated nature of the flow field, which is further confirmed by the flow images given in Figure 4.2.

Figure 4.3 provides 36 successive images that show the vortex wake evolution for the two-bladed single rotor during two complete rotor revolutions at 8 rps. The images are numbered 1 to 36, which are shown on the top left of each image, and are 20° apart, which is the difference in the azimuths of the rotor in sequential images. Time separation between the successive images is about 6.94 ms. In the figure adjacent vortex filaments from the two blades of the single rotor are labeled with odd and even numbers where odd numbers are used to refer to successive vortices from one of the two blades while the even numbers are used to identify the successive vortices from the other blade. In all the images in the figure, the filaments are distinct and can be tracked up to the downstream distance of $x/R < 1.5$ where x is a measure of the axial location of the filaments in the wake and R is the rotor disk radius. The evolution of the vortex wake and the development of the vortex instabilities can be clearly tracked from these sequential images provided in

the figure, which will be discussed in due course.

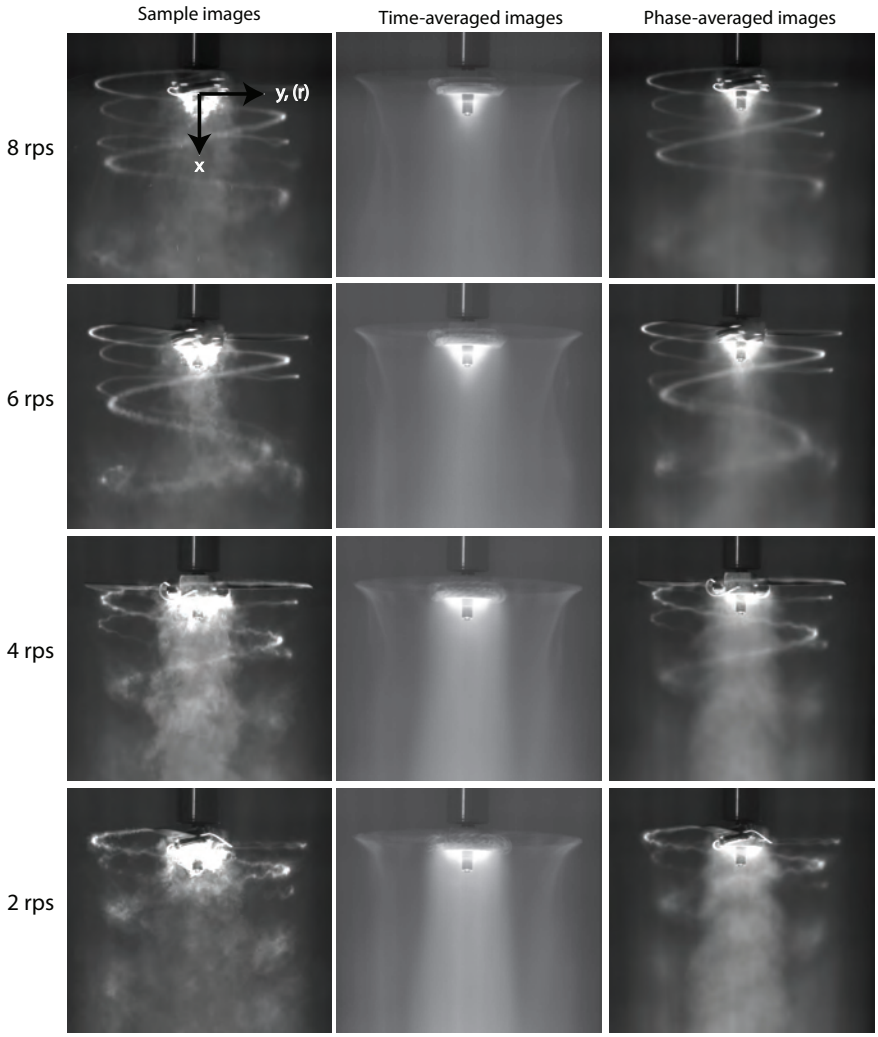

Figure 4.2: Two-bladed single rotor experiments where the upper rotor of the coaxial system was operated in isolation: Flow visualization images at 8 rps (first row), 6 rps (second row), 4 rps (third row), and 2 rps (fourth row) rps. Left column shows instantaneous flow images, the middle column shows the time-averaged flow fields, and the right column shows the phase-averaged images. The right-handed rectangular (x, y, z) and polar (r, x) coordinate systems are marked on top left frame.

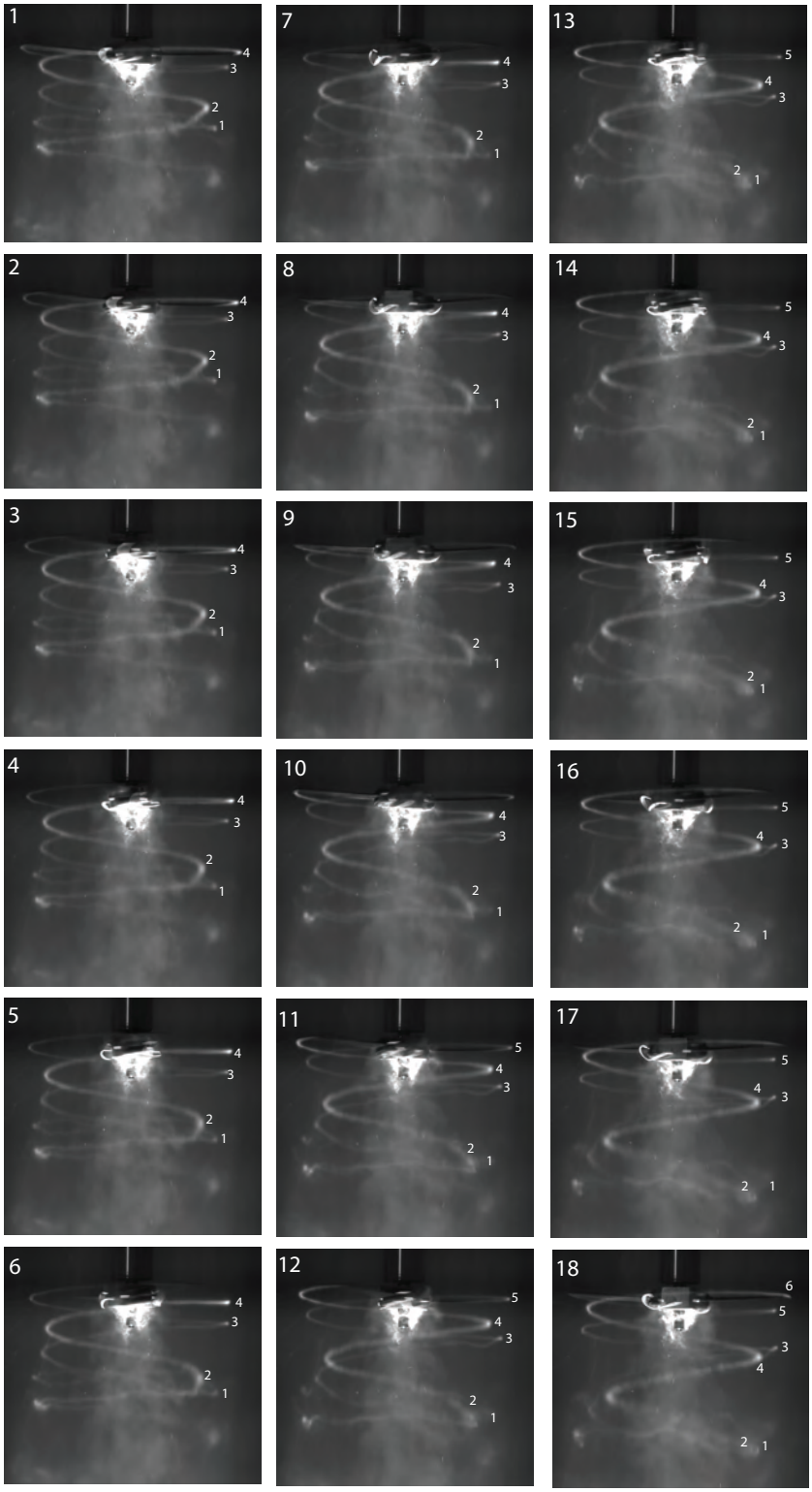

Figure 4.3: The first of two revolutions where the wake vortex evolution of the single rotor during two complete rotor revolutions at 8 rps is shown. Images are 20° ($\pi/9$ rad) apart. Time separation between successive images is 6.94 ms. Adjacent vortices are labeled with odd and even numbers. The odd numbers are used to refer to successive vortices from one of the two blades while the even numbers are used to identify the successive vortices from the other blade.

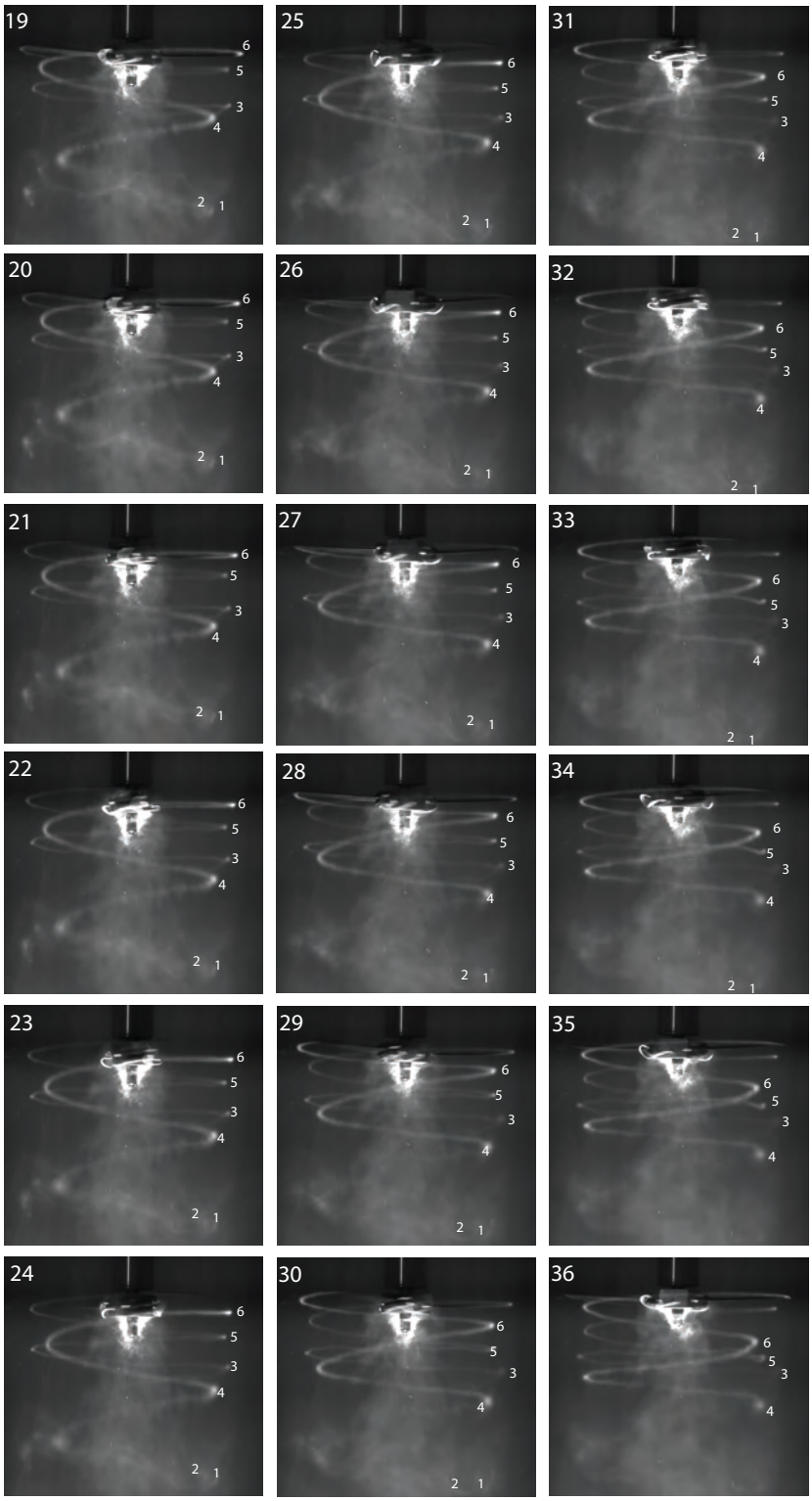

Figure 4.3: The second of two revolutions where the wake vortex evolution of the single rotor during two complete rotor revolutions at 8 rps is shown. Images are 20° ($\pi/9$ rad) apart. Time separation between successive images is 6.94 ms. Adjacent vortices are labeled with odd and even numbers. The odd numbers are used to refer to successive vortices from one of the two blades while the even numbers are used to identify the successive vortices from the other blade.

4.3.2 Vortex Instabilities and wake geometry

Long-wave instability mode

Adjacent helical filaments in the vortex wake develop long-wave pairing instabilities in which they orbit around one another. This interaction occurs following a mechanism similar to that documented in Caradonna et al. (Ref. [34]) where it is stated that the mode shape of this long-wave vortex pairing instability is dilatational mode. In this instability mode, turns of the first helix speed up and shrink in diameter as it leapfrogs through the turns of the second helix, which in turn experience an increase in its radius and a decrease in its speed. Also, Jain and Conlisk [38] suggested that due to the mutual interaction between the neighboring turns of the helical filaments, they undergo a process similar to leapfrogging of two coaxial vortex rings shed off in quick succession. As seen in top left image of Figure 4.3, the vortices 1 and 2 appear to be developing long-wave pairing instabilities. As the vortex 2 leapfrogs through the vortex 1, the adjacent portions of turn of the latter also interact where they start to spiral around each other, which is also visible in successive images in the figure. Moreover, the vortices 3 & 4 which are trailed one revolution after the formation of the vortices 1 & 2, respectively, also develop long-wave pairing instabilities which can be tracked from images 8-18 in the figure. However, long-wave instabilities developed by these two vortex pairs trailed in two consecutive rotor revolutions differ in the way that in the latter vortex 4 accelerates and shrinks in size as it leapfrogs through the decelerating and expanding vortex 3 as expected while in the former the vortex 1 appears not to be decelerating and expanding as opposed to the latter. Also, these two vortex pairs differ in the way that the adjacent portions of the turns of the helices 1 and 3 interact with each other within itself. As stated above, while the adjacent turns of vortex 1 orbit around each other, the same incident does not occur between those of the vortex 3. In the second part of Figure 4.3 where images 19-36 are shown from the second of two consecutive revolutions, a new vortex pair 5 & 6 is formed. They also exhibit long-wave pairing instability characteristics just like the vortex pair 1 & 2 which are formed two revolutions earlier. What is clearly visible from these images is that the vortex 3 decelerates and expands as opposed to vortex 5 which travels at a faster downward rate than the vortex 3. Also, the vortex 5 attempts to leapfrog through vortex 3 as seen in image 36 of the figure. During the leapfrogging processes, the vortex pairs do not reverse their roles, i.e. the odd numbered vortices always assume the role of leading (forward) vortex while the even numbered ones the role of the trailing (backward) vortex. Following leapfrogging processes, the vortices appear to merge to form bigger diffuse vortices in the far wake region. The flow pattern at 6 rps appears to be very similar to that at 8 rps. This is clearly visible in all flow images given in first row (for 8 rps) and second row (6 rps) of Figure 4.7. Flow data for 2 and 4 rps cases also reveal a similar leapfrogging effect between adjacent vortices although the helical filaments lose their individual identities earlier than 6 & 8 rps cases to coalesce into bigger vortices. At 2 rps, the vortices become extremely diffuse during their orbiting period within the first revolution and their subsequent locations become extremely difficult to trace as can be seen from the sample frame given in bottom left of Figure 4.7. For 4 rps case, the adjacent vortices merge to form a bigger diffuse vortex as they leapfrog through one another however at a farther downstream location than 2 rps case.

Short-wave instabilities

When rotor speed is 2-4 rps the helical filaments develop short-wave instabilities just from their inception, which is readily observed from sample flow images in Figure 4.2, a flow characteristic at these rotor speeds which is also observed in Ohanian *et al.* [21] for a three-bladed single rotor. Flow nature is highly viscous at 2 rps, which further make it extremely difficult to track the development of short-waves downstream of the flow. At these rotor speeds, the amplitude of these short waves appear not to be amplified significantly as the filaments travel farther downstream in the wake. At 6 & 8 rps, short-wave instabilities are seen to develop, however, locally and after a long time elapsed since the generation of the filaments. These features are visible in Figure 4.4 where sample flow images taken from each particular rotor speed are

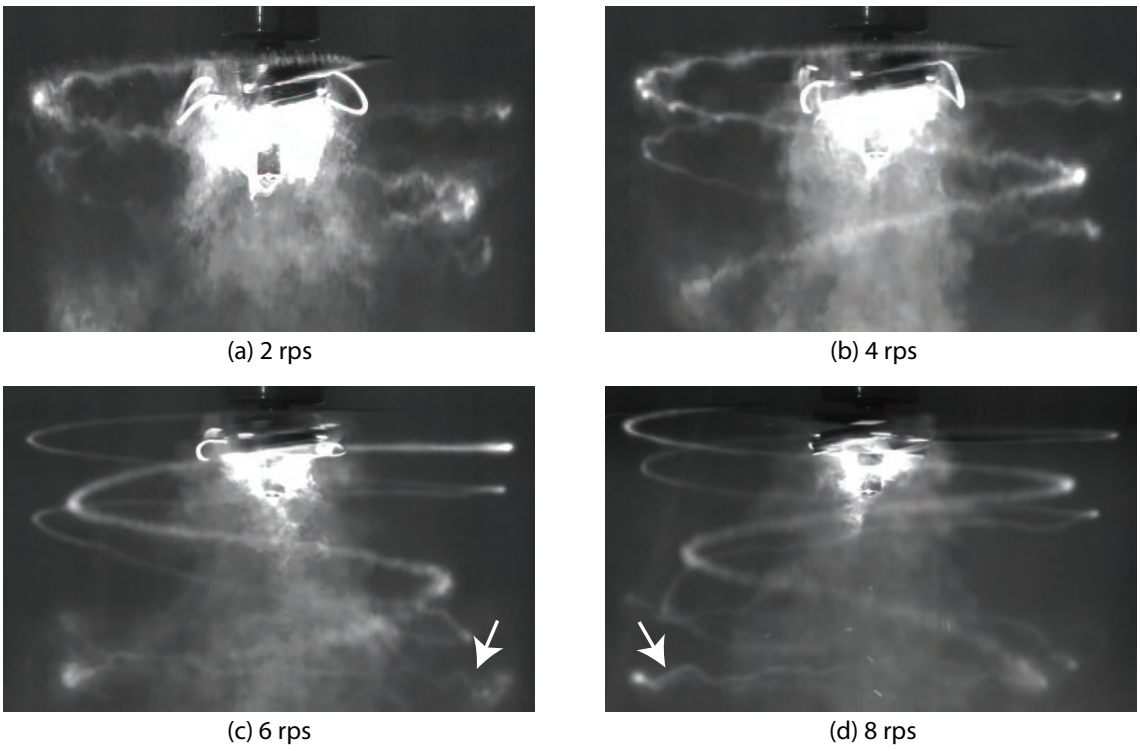

Figure 4.4: Sample flow images showing short-wave instabilities along the vortex filaments at all rotor speeds.

shown to reflect the development of the short-wave instabilities.

Wake contraction and xt diagram

Figure 4.5 shows the contraction and axial convection rates of the tip vortices at 8 rps. A sample xt diagram of the vortex trajectories is plotted on the right part of the figure where ψ denotes the wake age in terms of relative blade azimuth since the formation of the vortices. The position data are extracted from a sequence of images following an individual vortex filament. The uncertainties in the position data are typically a few pixels. The location of the center of the rotor hub is marked with solid black line on the left. In the figure, four individual vortex trajectories are shown in order to show that although the filaments exhibit similar characteristics in every rotor revolution, the flow pattern exactly repeats itself in every two rotor revolutions, which is discussed earlier. Vortex labeling is similar to those in Figure 4.3. xt diagram reveals that the leapfrogging process between vortex 1 & 2 takes place at a farther downstream location than that of vortex 3 & 4. The axial convection rates of the successive vortices from either of the blades is almost the same until the first blade passage ($\psi = \pi$), after which they travel downward at different rates. From the time-averaged image in Figure 4.2, wake contraction ratios are found to be about 0.85 (vortex 1) and 0.89 (vortex 3), which are higher than both the values of 0.707 from the classical momentum theory and the commonly accepted value of 0.78R (Leishman [15]). As noted in earlier studies (Landgrebe [28], Caradonnoa et al. [34]) and seen in the figure, the vortices do not contract monotonically, instead they start to expand during the long-wave instability mode, where they spiral around each other.

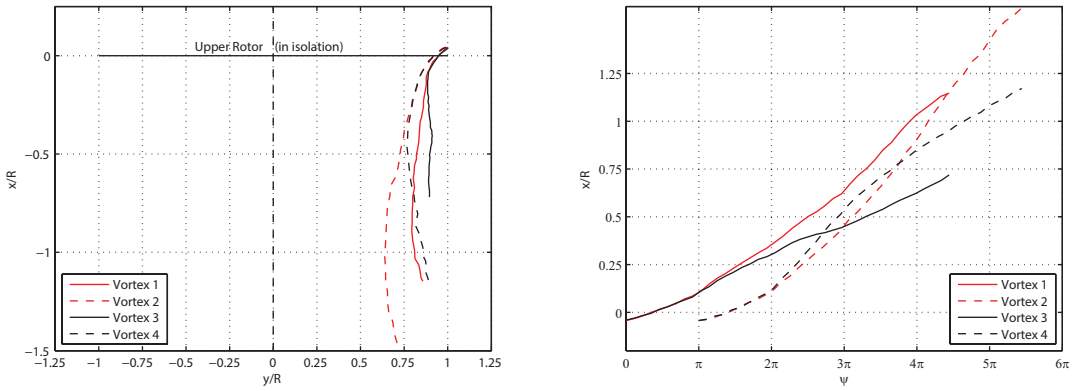

Figure 4.5: Trajectories of four helical filaments are shown during two successive rotor revolutions. Right: spatial positions of tip vortices showing wake contraction. Left: xt diagram of the vortex filaments at 8 rps ($\psi = \Omega t$). Vortex labeling is similar to those in Figure 4.3.

Particle Image Velocimetry (PIV)

Figure 4.6 shows PIV measurements at 8 rps for the aforementioned two-bladed single rotor when talking about the dye visualization images. Instantaneous fields are presented on the left and the average fields on the right. In frame (a) in the first row, an instant of particle flow visualization is shown where PIV particles are used to visualize the flow. In frame (b) is given averaged flow picture. The average image in frame (b) is constructed by superposing 36 successive images which correspond to two complete rotor revolutions not necessarily beginning from the image shown in frame (a). In row 2 is given instantaneous and average vorticity fields. Streamlines drawn over instantaneous and average vorticity fields are shown in third row. Streamlines in frames (e) of row 3 are drawn in a moving reference frame to highlight the individual vortices. In fourth row is given instantaneous and average speeds, over which streamlines are drawn. Average images in frames (d), (f), and (h) are constructed by superposing PIV results of 2999 successive processed image pairs captured during 50 rotor revolutions. The positions of the single rotor disk is marked in frame (d) in second row. The average images shown on the right also confirm the axisymmetry of the single rotor wake. The mean streamline patterns in frames (f) and (h) show the entrainment of the ambient fluid into the wake. Individual vortex filaments are identifiable in the instantaneous fields shown on the left. An assessment of the video sequences from both particle visualization and processed PIV image pairs reveal that the vortices trailed from the adjacent blades undergo long-wave pairing instability where they orbit around one another as observed during dye visualization runs.

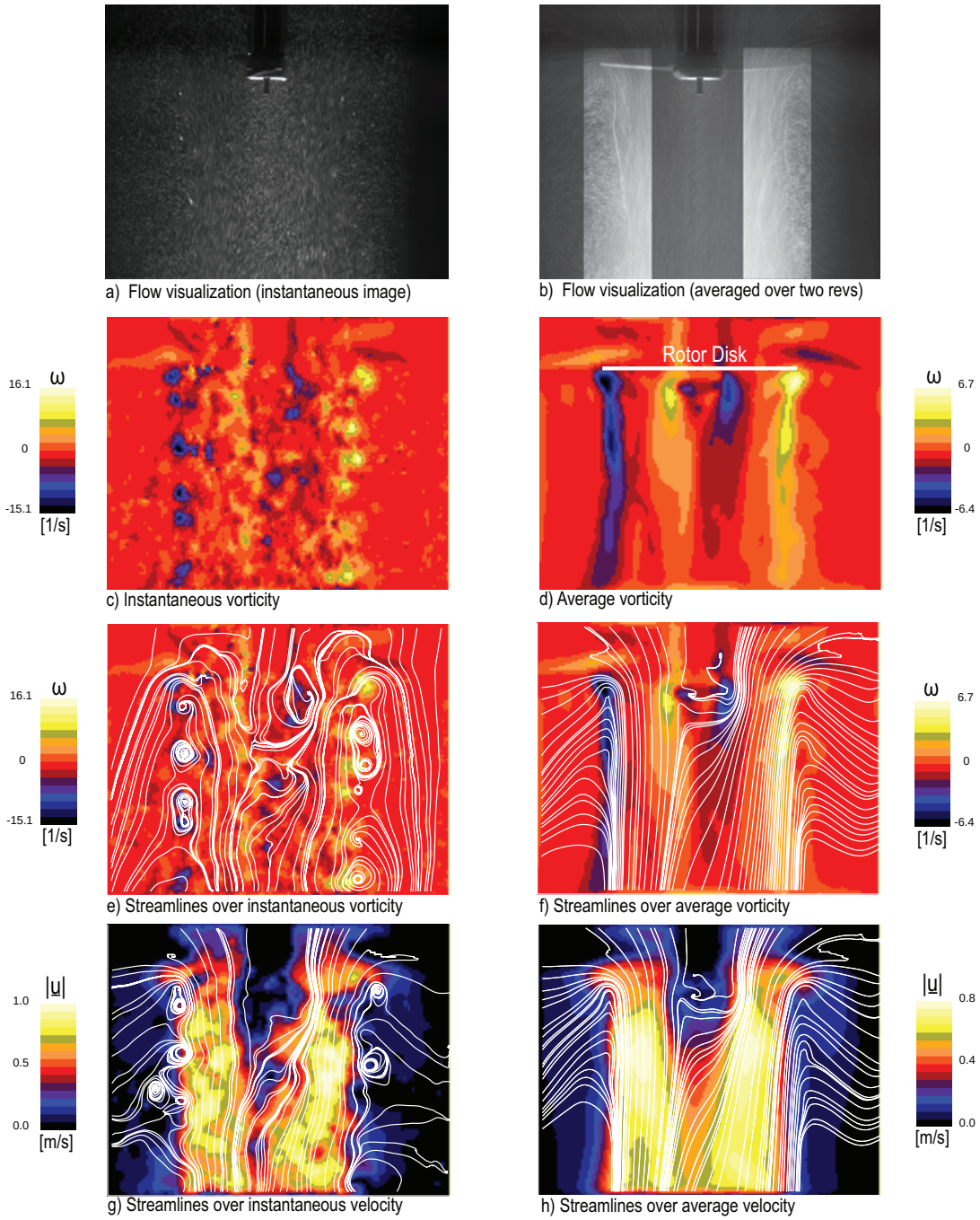

Figure 4.6: Flow field of a two-bladed single rotor at $N = 8$ rps. First row (a,b): particle flow visualization. In rows 2-4 are shown PIV measurements. Second row (c,d): vorticity fields. Third row (e,f): streamlines over vorticity. Fourth row (g,h): streamlines over speed. Streamlines in frame (e) are drawn from a moving reference frame and streamlines in frames (f-h) are drawn from a stationary reference frame.

4.4 Coaxial rotor with axial spacing of H/R=0.25

4.4.1 Flow images

Figure 4.7 shows the flow visualization images from the experiments conducted at the rotor rotational speeds of 2-8 rps which correspond to test numbers 1-4 in Table 2.3. A coaxial rotor having two blades per rotor was employed in the experiments. The rotors were spun in the opposite direction in which the upper rotor rotates clockwise while lower rotor rotates counterclockwise as shown in the images. Non-dimensional axial (vertical) separation distance between the coaxial rotors was set to $H/R = 0.25$ where H is the dimensional axial separation distance and R is the rotor disk radius. This is the shortest axial rotor spacing to have been tested between the coaxial rotors employed in this study. This value is also the closest to those of the some of the full-scale helicopters, such as Russian Kamov-32 ($H/R = 0.189$) and Sikorksy ABC helicopter ($H/R = 0.138$). The data representation in the figure is similar to that of single rotor experiments as discussed earlier. These images show the various details of the flow field of the coaxial rotor model where the rotors are closely separated. The centers of the blade tip vortices were rendered visible by injecting dye from each blade tip. The dye visualization images clearly show the intricate vortical nature of the flow which is highly unsteady and three dimensional. The pair-dynamics of the helices highlight the complexity of the internal vortical structure as contorted filaments in the instantaneous view and splitting paths in the average picture. Moreover, what is clear in the average views is the splitting paths followed by each helix which is another indication of intricacy of the vortical nature of the flow. These average pictures show the expected axisymmetry of the rotor wakes. Also what they show is that the wake of the upper rotor being ingested by the lower one, which results in the continual operation of the inner portions of the lower rotor under the influence of the upper rotor wake throughout the duration of each run. This has a profound affect on the inflow distribution of the entire coaxial rotor system. The average images of the coaxial rotors reveal the double tube structure formed by the wake of each rotor unlike the single rotor case where there is only one such tube structure. Phase-averaged images on the right column of the figure clearly manifest that the flow field beneath the lower rotor shows small variations during two successive revolutions and exact pattern repeats itself in every two rotor revolutions whereas the flow pattern at the interrotor region is persistent in every revolution. However, this observation is valid only for 6 & 8 rps flow images similar to what is observed during single rotor experiments. At 2 & 4 rps, however, the flow period is one rotor revolution. The tip vortex circulation-based Reynolds numbers at this rotor spacing are provided on the second column of Table 4.1 along with their standard deviation and estimated to be about 8950 for 2 rps, 16800 for 4 rps, 34500 for 6 rps, and 34400 for 8 rps cases. Difference in the values for smaller rotor speeds of 2 & 4 rps are manifest in the more diffuse nature of the vortices in the wake in the corresponding instantaneous flow images.

Figure 4.8 shows the vortex wake evolution beneath the coaxial rotors during two complete rotor revolutions at 8 rps. Data representation is similar to those of single rotor tests in Figure 4.3. In the figure adjacent vortex filaments from the two blades of the each rotor are labeled with odd and even numbers along with the letters 'u' for upper rotor and 'l' for lower rotor where odd numbers are used to refer to successive vortices from one of the two blades while the even numbers are used to identify the successive vortices from the other blade. This is shown in the figure where successive vortices of the upper and lower rotor are marked u1-u6 and l1-l6. The individual filaments inside the wake, particularly those from the lower rotor, are distinct to up to a rotor radius beneath the lower rotor where two successive turns of the helices at most can clearly be traced. This is less than that of the single rotor where three successive turns of the helices can be tracked in the wake. The filaments retain their individual identities in this region although they appear to have lost their orderly helical shapes, manifestation of strain experienced by the lower vortices.

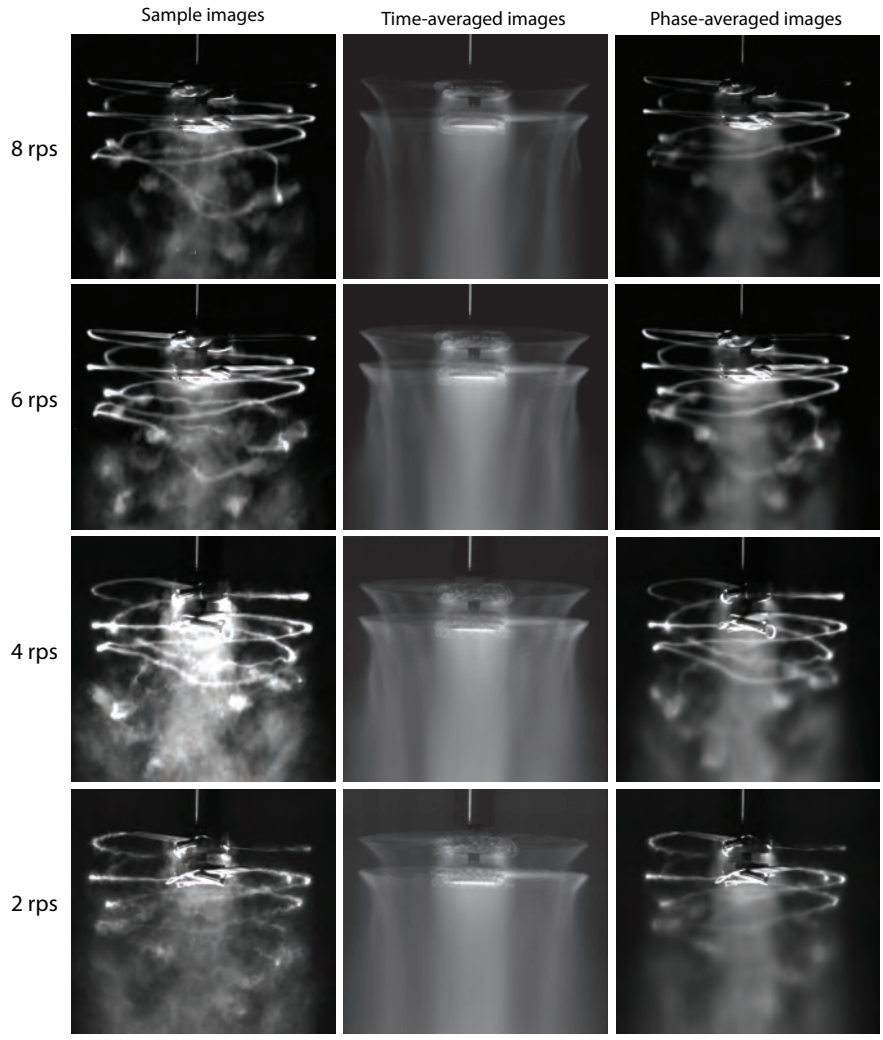

Figure 4.7: Two-bladed coaxial rotor with a rotor spacing of 25% of the rotor radius: Flow visualization images at 8 rps (first row), 6 rps (second row), 4 rps (third row) & 2 rps (fourth row). Left column shows instantaneous flow images, the middle column shows the time-averaged flow fields, and the right column shows the phase-averaged images.

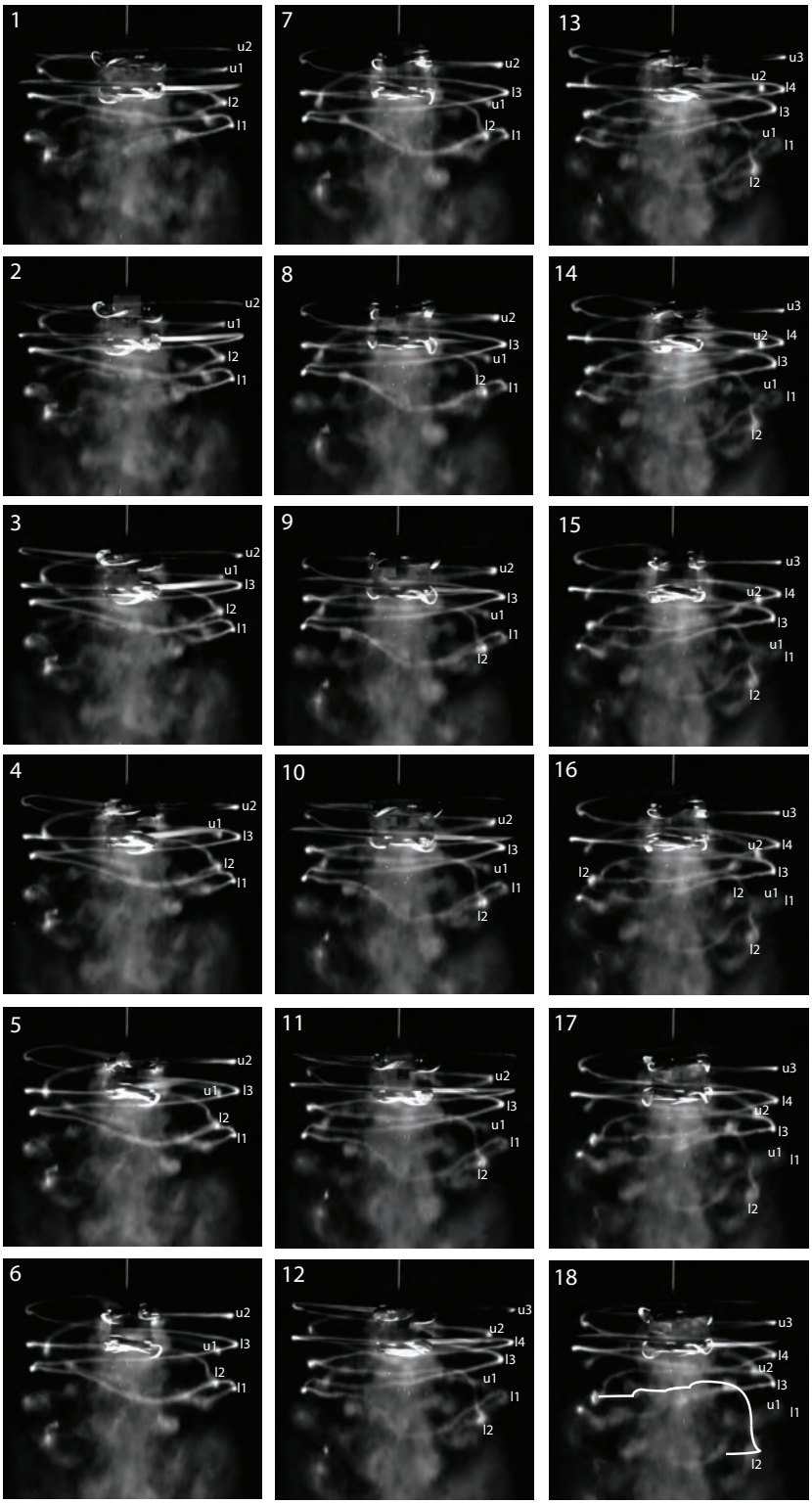

Figure 4.8: The first of two revolutions where vortex wake evolution of the coaxial rotors with axial spacing of H/R=0.25 during two complete rotor revolutions at 8 rps. Images are 20° ($\pi/9$ rad) apart. Time separation between successive images is 6.94 ms. Adjacent vortices are labeled with odd and even numbers. The odd numbers are used to refer to successive vortices from one of the two blades while the even numbers are used to identify the successive vortices from the other blade. The letters 'u' and 'l' denote the vortices trailed from upper and lower rotors, respectively.

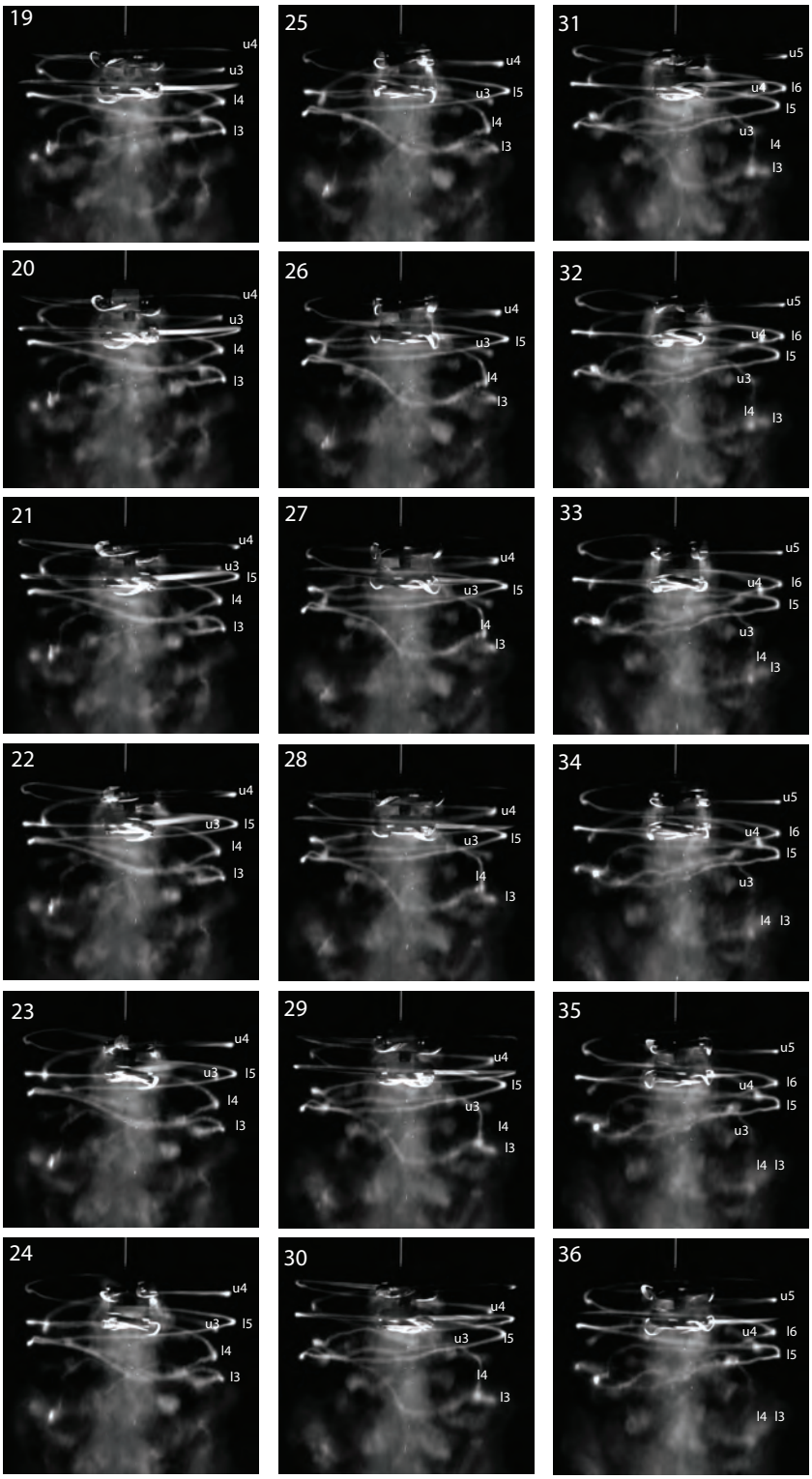

Figure 4.8: The second of two revolutions where the wake vortex evolution of the coaxial rotors with axial spacing of H/R=0.25 during two complete rotor revolution at 8 rps. Images are 20° ($\pi/9$ rad) apart. Time separation between successive images is 6.94 ms. Adjacent vortices are labeled with odd and even numbers. The odd numbers are used to refer to successive vortices from one of the two blades while the even numbers are used to identify the successive vortices from the other blade. The letters 'u' and 'l' denote the vortices trailed from upper and lower rotors, respectively.

4.4.2 Vortex Instabilities and wake geometry

Long-wave instability mode

The presence of the upper rotor brings about interesting flow features inside the wake beneath the lower rotor where all of the filaments develop strong mutual interactions with one another, resulting in extreme distortions in the orderly helical shape of the filaments, especially those from the lower rotor, within a rotor revolution. A comparison of the first frames in Fig. 4.3 and Fig. 4.8 reveals that the extent and strength of these interactions is more complicated and unusual than what is observed on the two-bladed single rotor tests in the current study as well as that is documented on multi-bladed single rotor experiments in the previous studies (cf. Caradonna et al. [34], Felli et al. [26], Ohanian et al. [21], Konus and Savas [54]). Since the rotors are closely separated with a rotor spacing of quarter radius, the upper rotor wake does not have sufficient time to be fully developed before it is ingested by the lower rotor. It takes only about half a rotor revolution for upper filaments to reach the plane of the lower rotor following their formation. At this rotor spacing, the effect of lower disk on the upper rotor is significant. Since the upper rotor here is the same with that employed in single rotor tests, it is readily seen that the interactions developed by the single rotor filaments (e.g. long-wave pairing instability) appear not to take place between the filaments of the upper rotor in the space between the upper and lower rotors, at least not in the same clear way and strength. As the upper rotor filaments travel downstream through the lower rotor, turning blades of the lower rotor cut through the helical filaments from the upper rotor, resulting in interrotor blade-vortex interactions (BVIs) ([22, 47]). This interrotor BVIs differ from that of the conventional, or single, rotor configurations in the sense that the interaction takes places between the trailed vortices and the blades of the different rotors as opposed to the classical BVIs where the interaction takes place within the same rotor blades and filaments. As seen in frames 16-18 in Fig. 4.8, the lower rotor blade cuts through the upper filament u2, resulting in separation of u2 from the rest of it lying above. Soon after the occurrence of this interrotor BVI, the separated upper filaments become diffuse and their subsequent locations in the wake become difficult to trace.

Passing of the upper rotor tip vortices through the plane of the lower rotor affect profoundly the interactions between the adjacent filaments of the lower rotor as well as between the adjacent portions of turns of each filament. As before, the lower rotor filaments exhibit long-wave pairing instability in which they orbit around each other while traveling downstream in the wake. This leapfrogging process of lower vortices l1 & l2 is seen throughout the sequential images in Fig. 4.8 and the same process is underway between l3 & l4 in the second part of the the same figure. Also, the adjacent portions of the turns of the lower filament 1 spiral around each other during this process. Although this long-wave instability is developed in a similar mechanism to that of the single rotor tests, it differs to the extent which adjacent lower rotor filaments undergo deformations and the shapes they are deformed to later in the wake. A comparison of Figures 4.3 and 4.8 sheds light into this difference. During this leapfrogging process, the portions of the lower vortices near the wake boundaries become elongated in the streamwise direction. This is seen in frame 18 in the figure where roughly the path of vortex l2 is drawn to highlight this stretching of the vortex. Noting the single rotor behavior of the adjacent filaments, it is easily inferred that the process leading to strong deformation of the lower rotor filaments, which is uncommon for single rotor configurations, is initiated by the passing of the upper vortices through the plane of the lower rotor and its induced effect on those filaments. The upper filaments appear not to develop a long-wave instability process with the lower rotor filaments where they would orbit around each other. This is mainly because when upper vortices reach the vicinity of the lower rotor they have already contracted more and more inward and increased its downward speed with an additional increase from the sucking effect from the lower rotor while the newly formed lower vortex is slowly contracting and traveling downstream (see images 1-10 in the figure). In about a distance of rotor radius beneath the lower rotor, the upper rotor vortices following their interaction with lower rotor blades merge with the parts of the lower rotor vortices (see in images 16-18 between the vortices u1 and l1, for instance). In the central part of the far wake region, the vortices coalesce into more diffuse and bigger vortices, losing

their individual identities. Flow field at 6 rps exhibits very similar characteristics with that at 8 rps, which can be observed from the images given in Figure 4.7. At 2 & 4 rps, the vortex filaments appear to develop long-wave instabilities in similar ways to that is seen at 6 & 8 rps, however the vortices become extremely diffuse, especially at 2 rps, earlier and become hard to follow. Also at 2 rps, the deformation of the vortices is not clearly visible due to this more diffuse nature of the flow field. In Appendix A, rest of the evolution images of vortex wake at the same rotor spacing of a quarter radius during one complete rotor revolution at 6, 4 & 2 rps are provided in Figures A.25, A.27, and A.29, respectively.

Short-wave instabilities

When the rotor speed is 2 & 4 rps, which yield lower Reynolds numbers ($3.1 - 6.2 \times 10^4$) another vortex instability mode becomes evident, which is a smooth sinuous wave type (also the short-wave and bending) instability, which result from the self-induced motion of a curved filament and an external strain field induced by neighboring vortices [18], develops along the filaments trailed from both lower and upper rotors immediately after their formation. The short waves formed along the filaments of upper rotor whose amplitudes appear to be comparatively smaller than those of the lower rotor cannot be tracked after about one-half rotor revolution since the wake of the upper rotor was ingested into the lower rotor shortly after their formation at this close rotor separation. The short-waves along the filaments of lower rotor grow rapidly in amplitude within one rotor revolution before eventually the rotor wakes become unstable in the far wake region. Figure 4.9 presents sample flow images at each rotor speed where the short-wave instabilities are clearly visible just from the beginning at 2 & 4 rps while at 6 & 8 rps the short waves are formed only locally (i.e. along just one vortex filament) at farther downstream distances. Frame (b) reveals the growing amplitude of short waves along lower rotor filaments at 4 rps. Also, amplitude of the waves later in the wake at 2 rps, which is shown in frame (a) of the same figure, is seemingly smaller than that is found to be at 4 rps. Note the strong stability of the upper rotor vortices at 6 and 8 rps images in frames (c) and (d) as opposed to lower rotor vortices. Also, the wavelengths of the short waves formed at 2 rps appear to be shorter (ultra short waves) than that at 4 rps. Evolution of short-wave instabilities was particularly vivid when viewed on video since the figure shows only an instant of the rotor wake. Throughout the entire length of the run at 4 rps case, the development of the short-wave instability pattern as seen in frame (b) of Figure 4.9 was persistent. Unlike 2 & 4 rps runs, the filaments do not develop any noticeable short-wave instabilities at the start of the rotor at the speeds of 6 & 8 rps. After a very short time elapsed, i.e. within a rotor revolution, the filaments from upper and lower rotors strongly interact with each other, undergo extreme strain, strong contortions and become entangled, resulting in long-wave pairing instabilities, which make it extremely difficult to track the development of short-wave instabilities which become superimposed with the long-wave instability of the filaments.

Wake contraction and xt diagram

Figure 4.10 shows the contraction and axial convection rates of the tip vortices from both rotors at 8 rps. Data representation is similar to that of single rotor wake in Figure 4.5. The locations of the centers of both rotor hubs are marked in the left plot of the figure where the axial separation of the rotors ($H/R = 0.25$) is also shown. Also, the vortices 3 and 4 from single rotor experiments are plotted for the sake of comparison with coaxial rotors. Vortex trajectories, both from upper and lower rotors, can be followed for only one rotor revolution since the close separation of the rotors and strong mutual interactions developed by the vortex filaments render the position data extraction extremely difficult. It is immediately obvious from the plot on the left of the figure that both of the upper rotor vortices u1 and u2 are convected downstream at a much faster rate than one of the vortices of both single (vortex 3 (SNG)) and lower rotors (vortex l1). As stated earlier, single rotor measurements are taken by operating the upper rotor in isolation. Both vortex 3 and vortex l1 is slowed down during the process when they exhibit leapfrogging effect with

adjacent vortices within the same rotor as discussed above in detail. Unlike observed in single rotor case, the upper rotor filaments do not show long-wave instability characteristics, which can be noted from the figure where both vortices travel and contract almost at the same speeds. The upper rotor vortices contract more inward than those from the lower rotor. The reasoning for this is given in the following: Consider a vortex just trailed from either of all rotor blades. This vortex experiences a net inward velocity induced by the other vortices that lay beneath it in the wake, which is governed by the Biot-Savart law (Batchelor [59]) which gives a kinematic relation between the vorticity and velocity field in a flow field. This inward induced velocity component causes this vortex to contract more and more inward as it travels downstream. After the formation of new vortices in subsequent rotor revolutions, this vortex also experiences an outward velocity component which is induced by the vortices that lay above it in the wake. This outward induced velocity component acts as a balancing agent to the inward velocity component (Brand et al. [60]). This balancing of two velocity components results in further cessation of the wake contraction and even an expansion in the wake boundary as noted by Landgrebe [28] and others. By the same token, the upper rotor filaments experience an inward radial velocity induced by the vortices both that resides in the space between the rotors (upper rotor filaments at older wake ages) and beneath the lower rotor (older upper rotor filaments plus lower rotor filaments) which is higher than that when the upper rotor would operate in isolation. Similarly, a newly formed lower rotor filament feels an outward radial velocity component induced by the upper rotor vortices that lay above the lower rotor plane. Therefore, it does not contract as more inward as that of the upper rotor. It is also important to note the induced effect of the same-rotor vortices on each other as in the case of leapfrogging through one another where an increase and decrease in the speeds of adjacent vortices occur, which results in different contraction and convection rates of adjacent vortices of the same rotor as can be seen from the different vortex trajectories plotted in the figure. From the average images in Figure 4.7, the wake contraction ratios for the upper and lower rotor wakes are estimated to be about 0.8 (at the plane of the lower rotor) and 0.9, respectively, the latter of which is very close to the value of 0.91 documented by Akimov et al. [45] and the former is smaller than the value of 0.85 also reported therein.

Particle Image Velocimetry (PIV)

Figure 4.11 shows the corresponding PIV measurements of at 8 rps where data representation is similar to those in Figure 4.6. The positions of the upper and lower rotors are marked in frame (d) in second row. Double tube structure formed by the wakes of the coaxial rotors is also visible in PIV results. The average data shows the expected axisymmetry of the rotor wakes. The mean streamline patterns in frames (f) and (h) show the entrainment of the ambient fluid into the wake. The average streamline patterns of the fluid ingested into the rotors in frames (f) and (h) show that the slipstream of the upper rotor has still curvature as it is intercepted by the lower rotor which support the dye visualization result that the upper rotor wake has not become the fully-developed yet when it reaches the vicinity of the lower rotor. Individual vortex filaments are identifiable up to a downstream distance of one rotor radius in the instantaneous fields shown on the left. The mean vorticity plot in frame (d) suggests that the lower rotor wake ceases contraction and starts to expand radially outward. This is the consequence of the leapfrogging process the vortices l2 and l1 manifest. In Appendix A, rest of the PIV results at this rotor spacing of a quarter radius at 6, 4 & 2 rps are provided in Figures A.26, A.28, and A.30, respectively.

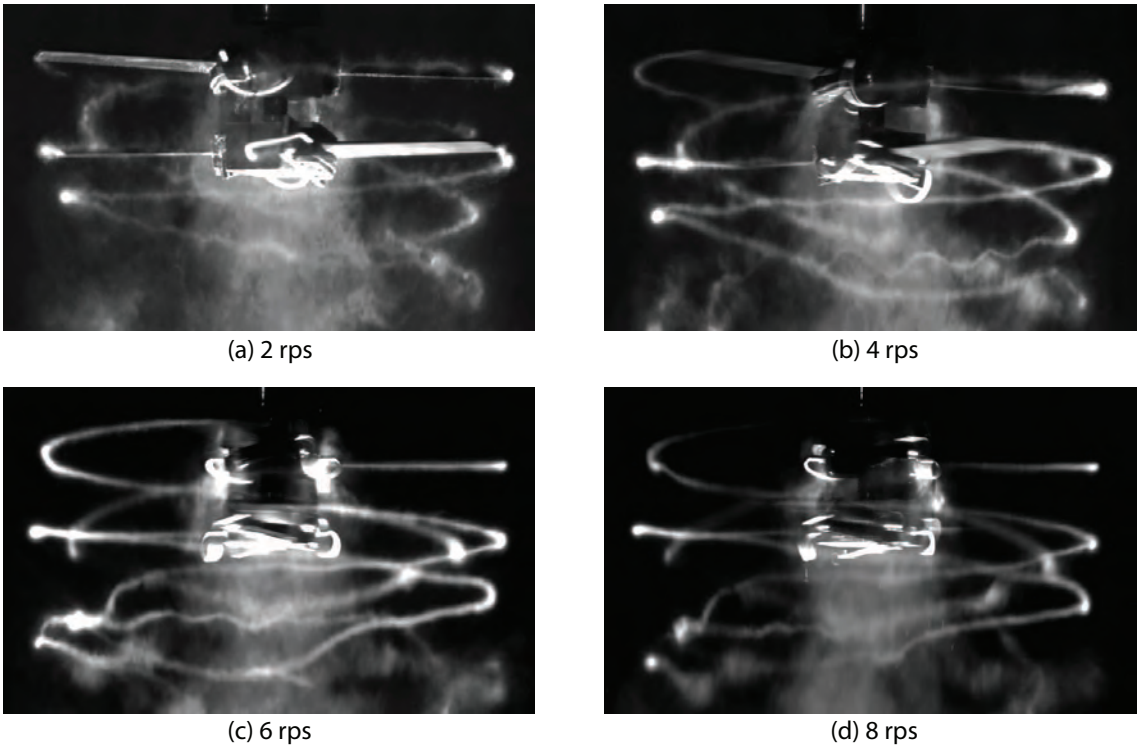

Figure 4.9: Sample flow images showing short-wave instabilities along the vortex filaments for all rotor speeds. Coaxial rotors are spaced at a quarter radius (Spacer 1).

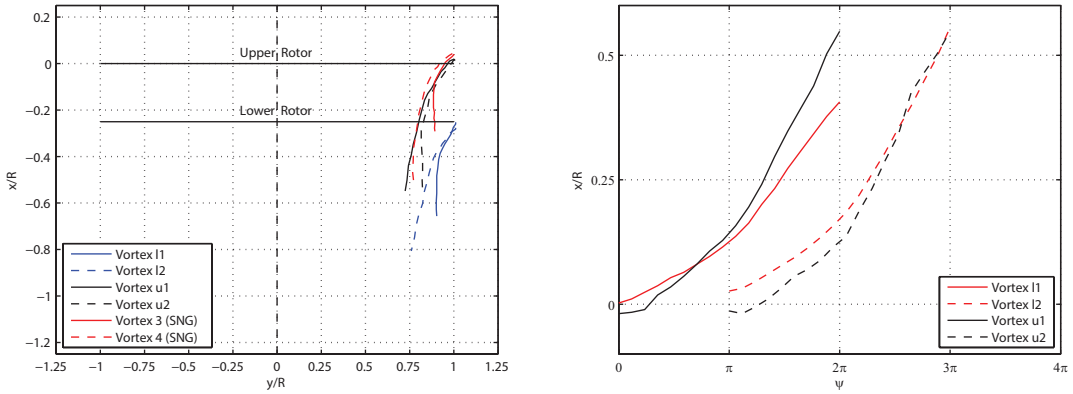

Figure 4.10: Trajectories of helical filaments trailed from coaxial rotor spaced at a quarter radius as well as those from the single rotor are shown. Right: spatial positions of tip vortices showing wake contraction. Left: xt diagram of the vortex filaments at 8 rps ($\psi = \Omega t$). Vortex labeling is similar to those in Figure 4.8

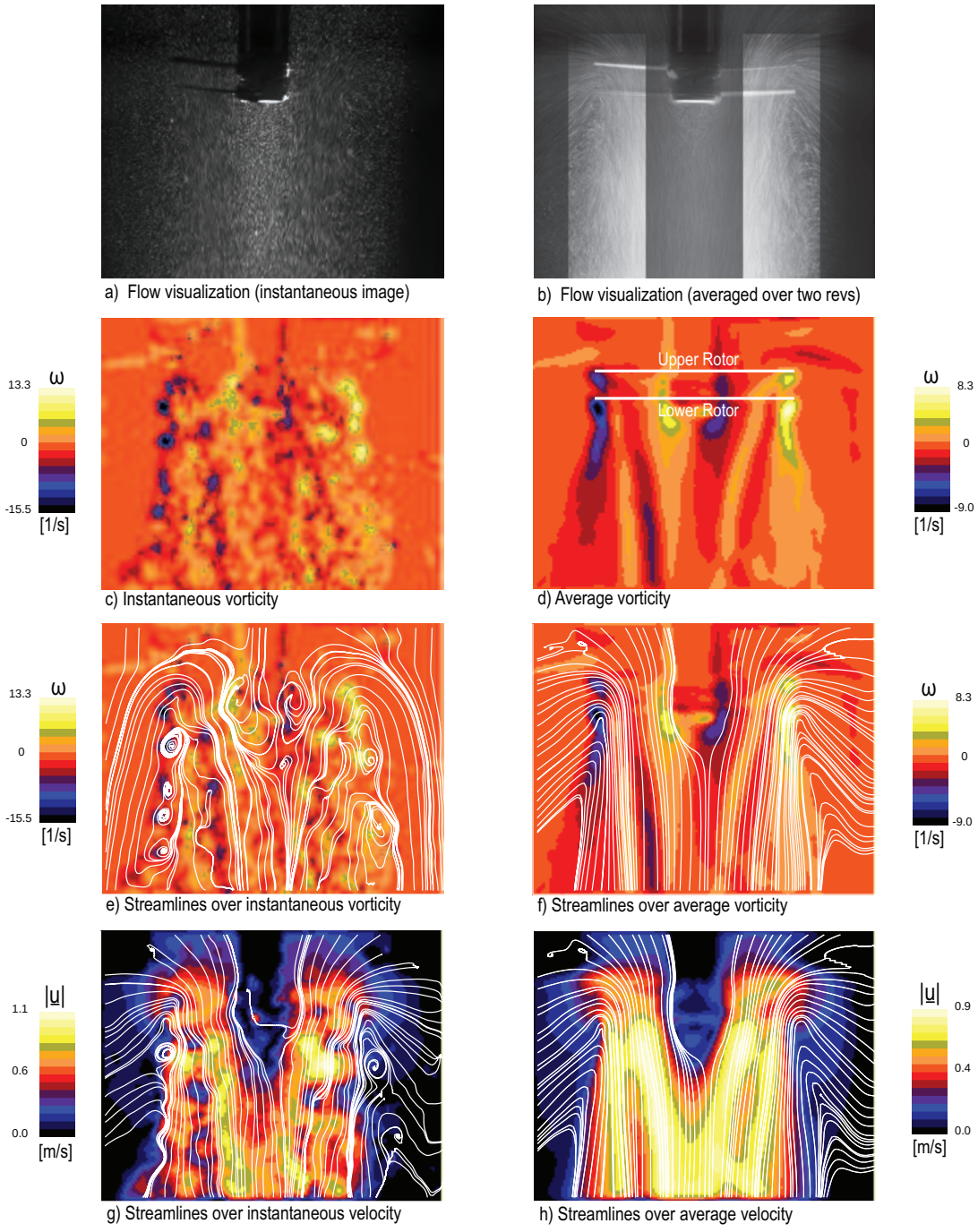

Figure 4.11: Flow field of a two-bladed coaxial rotor with rotor spacing of 25% of the rotor radius at $N = 8$ rps. First row (a,b): particle flow visualization. Average field in frame (b) is locally brightness- and contrast-enhanced to highlight the wake contraction of both rotors. In rows 2-4 are shown PIV measurements. Second row (c,d): vorticity fields. Third row (e,f): streamlines over vorticity. Fourth row (g,h): streamlines over speed. Streamlines in frame (e) are drawn from a moving reference frame and streamlines in frames (f-h) are drawn from a stationary reference frame.

4.5 Coaxial rotor with axial spacing of H/R=0.375

4.5.1 Flow images

Figure 4.12 shows the flow visualization photos from the experiments conducted at the rotor speeds of 2-8 rps which correspond to the test numbers 5-8 in Table 2.3. Data representation is similar to those in Figure 4.7. Axial spacing between the coaxial rotors is set to 37.5% of the rotor radius by fitting the coaxial rotor setup with spacer-2. The upper rotor wake is still developing and contracting radially inward when it reaches to the plane of lower rotor although the area where it impinges on the inner part of the lower rotor disk is less than that of the spacer-1 case, where $H/R = 0.25$. This is one of the consequences of the increased rotor spacing: to reduce the area, however small, where the contracted upper rotor wake goes through the inner part of the lower rotor until the upper rotor wake reaches the fully-developed state. Comparison of the time-averaged images on the middle column between Figures 4.7 and 4.12 shows this difference in the upper rotor wake contractions for these two cases. Also, what is observed from the time-averaged images here is that the splitting path of the upper rotor filaments start to become discernible. The tip vortex circulation-based Reynolds numbers at this rotor spacing are provided on the third column of Table 4.1 along with their standard deviation and estimated to be about 8950 for 2 rps, 15200 for 4 rps, 31000 for 6 rps, and 30500 for 8 rps cases. These values lay in the close range of the corresponding circulation based Re numbers for spacer 1 case where rotors spaced at a quarter radius.

In Figure 4.13 is given the consecutive flow images for this rotor spacing that show the evolution of the coaxial rotor wakes during one complete rotor revolution at 8 rps. Data representation is similar to those of Figure 4.8. The successive vortices from each of the rotors are labeled in a similar manner to the previous cases. The flow field characteristics appear to be very similar to those given in Figure 4.8 where the rotor spacing is a quarter of rotor radius. This is expected since the rotors in both cases are closely-spaced.

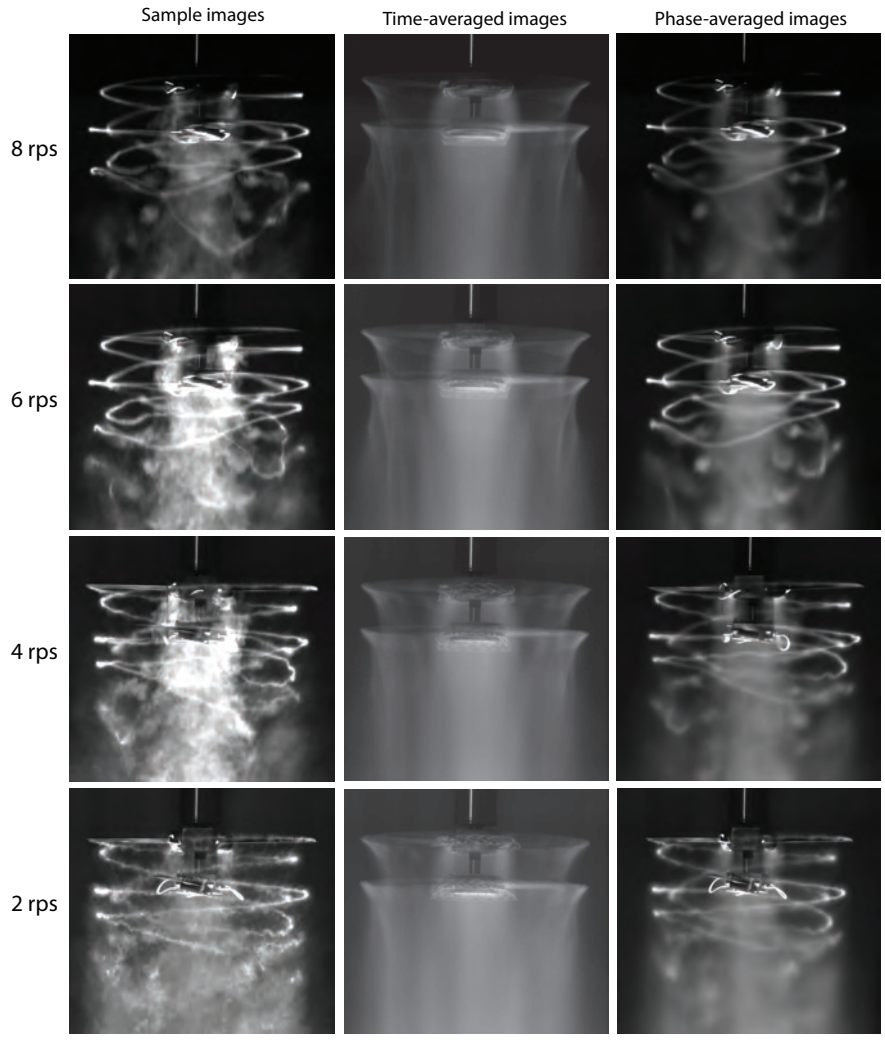

Figure 4.12: Two-bladed coaxial rotor (spacer2), $H/R = 0.375$: Flow visualization images at 8 rps (first row), 6 rps (second row), 4 rps (third row) & 2 rps (fourth row). Left column shows instantaneous flow images, the middle column shows the averaged flow fields, and the right column shows the phased-averaged images.

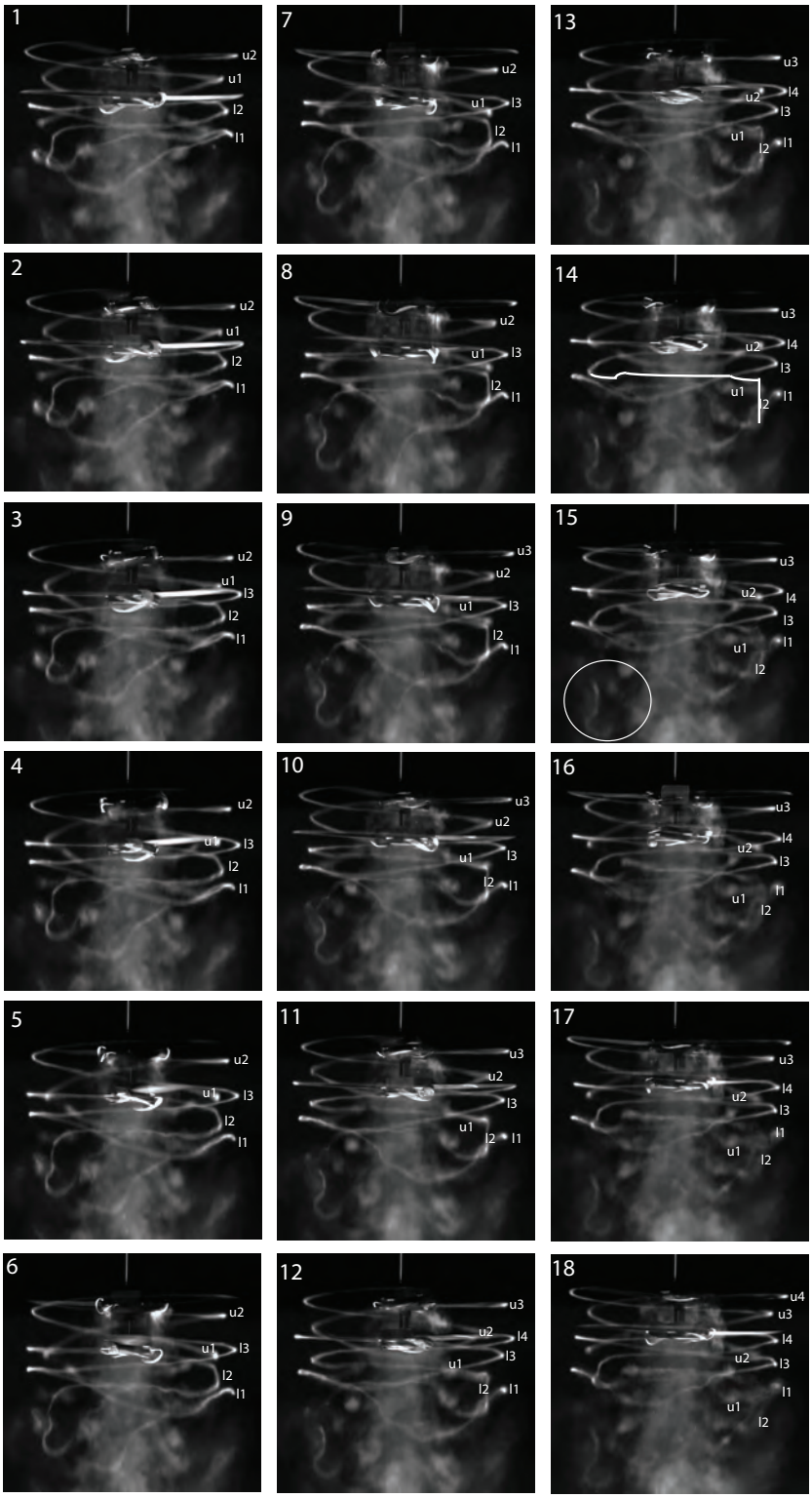

Figure 4.13: Vortex wake evolution of the coaxial rotors with axial spacing of H/R=0.375 during one complete rotor revolution at 8 rps. Images are 20° ($\pi/9$ rad) apart. Time separation between successive images is 6.94 ms. Adjacent vortices are labeled with odd and even numbers. The odd numbers are used to refer to successive vortices from one of the two blades while the even numbers are used to identify the successive vortices from the other blade.

4.5.2 Vortex Instabilities and wake geometry

Long-wave instability mode

Due to increased distance between the rotors, the upper rotor filaments travel 50% more in the space between the rotors as compared to spacer-1 case (i.e. $H/R = 0.25$) before they encounter the lower rotor blades and are cut through by them, which results in the separation of the upper filaments into three pieces and more diffuse vortex. The flow fields in two rotor spacing cases are almost identical to each other with only minor differences. In frame 14 in Figure 4.13, the shape the vortex l2 deforms to is shown. It is very similar to that is given in image 18 of Figure 4.8 which confirm the resemblance of these two flow fields. As before, the upper rotor filaments accentuate the mutual interactions between the lower rotor vortices just beneath the lower rotor in the near wake region, i.e. within one rotor revolution, resulting in strong contortions in the orderly helical shape of the lower rotor filaments. The lower rotor filaments manifest long-wave pairing instability characteristics where they orbit around each other in a similar leapfrogging process as discussed in detail above. This process is accompanied with the deformation and stretching of the vorticity which leads to the eventual formation of structures resembling a hairpin vortex with elongated legs in the streamwise direction. Formation of this vortex structure can be tracked from the sequential images in Figure 4.13 and one such structure is circled in frame 15 in the same figure. For the spacer 1 case where rotor spacing is of a quarter radius, a similar progress seems to be underway however it is not distinct as it is here. What can be inferred from the two cases discusses up to this point is that the lower rotor seems to have a stabilizing effect on the upper rotor filaments while the upper rotor filaments cause the lower ones to develop strong instabilities which lead to extreme strain and contortions as evident in the images provided. As before, the flow field characteristics show similarities at rotor speeds of 2-6 rps. However, the extent of the deformation experienced by the lower rotor filaments is markedly increased and more discernible at 6 & 8 rps as opposed to that at 2 & 4 rps where the viscous effects are more dominant. In Appendix A, rest of the evolution images of vortex wake at the same rotor spacing during one complete rotor revolution at 6, 4 & 2 rps are provided in Figures A.31, A.33, and A.35, respectively.

Short-wave instabilities

Figure 4.14 shows a flow image at each rotor speed where short-wave instabilities are seen. As before, at 2 & 4 rps short-waves inherently develop just from the start of the rotor, amplitudes of which grow in magnitude as the vortex age gets older. Frames (a) and (b) indicate these amplified short waves beneath the lower rotor. The amplitude of the short-waves formed along the upper rotor filaments appear to be small compared to those of the lower rotor vortices. At 6 & 8 rps, short waves are rarely seen to be formed at older wake ages just before lower rotor filaments exhibit unusual long-wave pairing instabilities where they deviate from orderly helical shapes and get elongated in the streamwise direction.

Wake contraction and xt diagram

Figure 4.15 shows the contraction and axial convection rates of the tip vortices from both rotors at 8 rps at the same rotor spacing. Data representation is similar to that shown in Figure 4.10. The observations made in the previous rotor spacing case is also valid here. The wake contraction ratios for the upper and lower rotor wakes are estimated to be about the same although the upper wake at the plane of the lower rotor is a little bit smaller as expected, albeit not easily discernible. The leapfrogging process between the lower rotor filaments is underway in the right part of the figure whereas the upper rotor filaments appear to be free of such interactions as discussed earlier. What can be inferred from both this and previous rotor spacing data is that the contraction ratio of the upper rotor wake is markedly greater than that of the single

and lower rotors, of which the wake of former also contracts more inward than that of the latter as also reported by Kim and Brown [47].

PIV

Figure 4.16 shows the corresponding PIV measurements of at 8 rps where data representation is similar to those in Figure 4.11. The positions of the upper and lower rotors are marked in frame (d) in second row. The average data shows similar features to that of the previous case where $H/R = 0.25$. The slipstream of the upper outer rotor has still curvature as it is ingested by the lower rotor suggesting the upper rotor wake is still developing as before. The wake does not appear to expand radially outward unlike before. A close investigation of the video sequence comprised of the processed PIV image pairs reveal that the lower vortices undergo long-wave pairing instability where they orbit around each other as observed in dye visualization runs. The tip vortices from the upper rotor is identifiable up to the point where they reach the vicinity of the lower rotor. At this point, they interact with the lower rotor blades, i.e. interrotor BVIs, after where it becomes extremely difficult to track these upper rotor tip vortices, a result also supporting dye visualization images. This is seen in frame (c) in the PIV results. In Appendix A, rest of the PIV results at this rotor spacing at 6, 4 & 2 rps are provided in Figures A.32, A.34, and A.36, respectively.

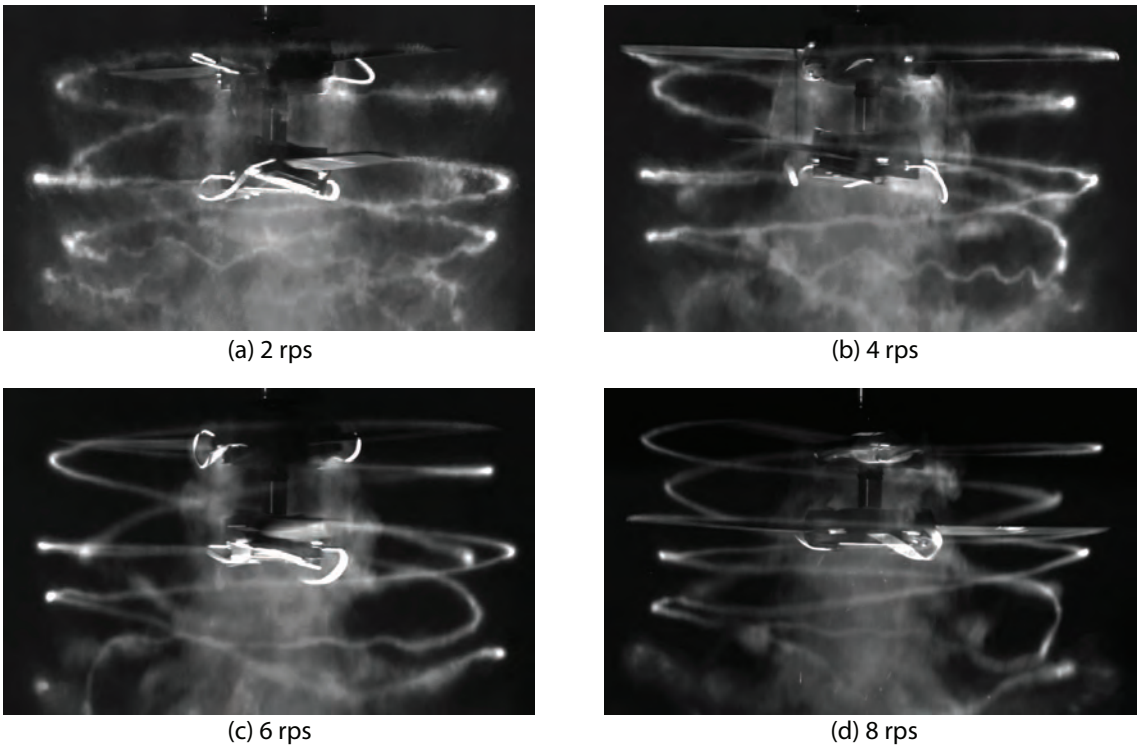

Figure 4.14: Sample flow images showing short-wave instabilities along the vortex filaments for all rotor speeds. Coaxial rotors are spaced at a 37.5% of the rotor radius (Spacer 2).

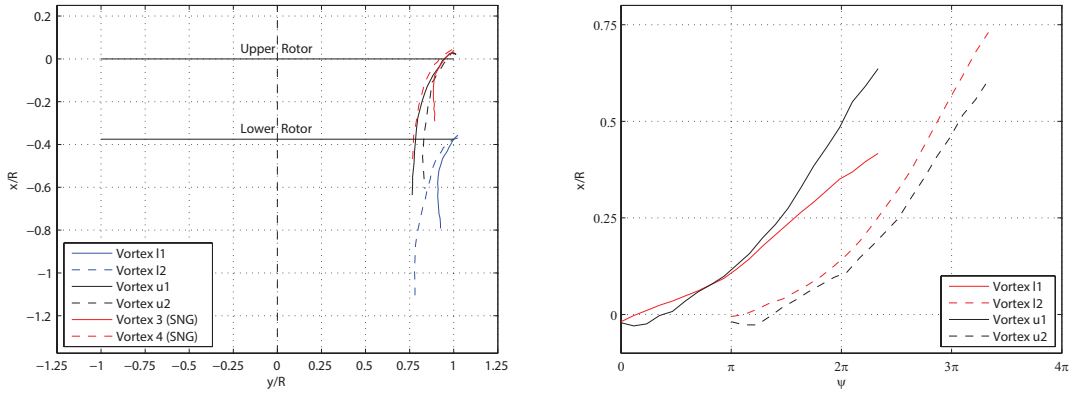

Figure 4.15: Trajectories of helical filaments trailed from coaxial rotor spaced at 37.5% of the rotor radius as well as those from the single rotor are shown. Right: spatial positions of tip vortices showing wake contraction. Left: xt diagram of the vortex filaments at 8 rps ($\psi = \Omega t$). Vortex labeling is similar to those in Figure 4.13

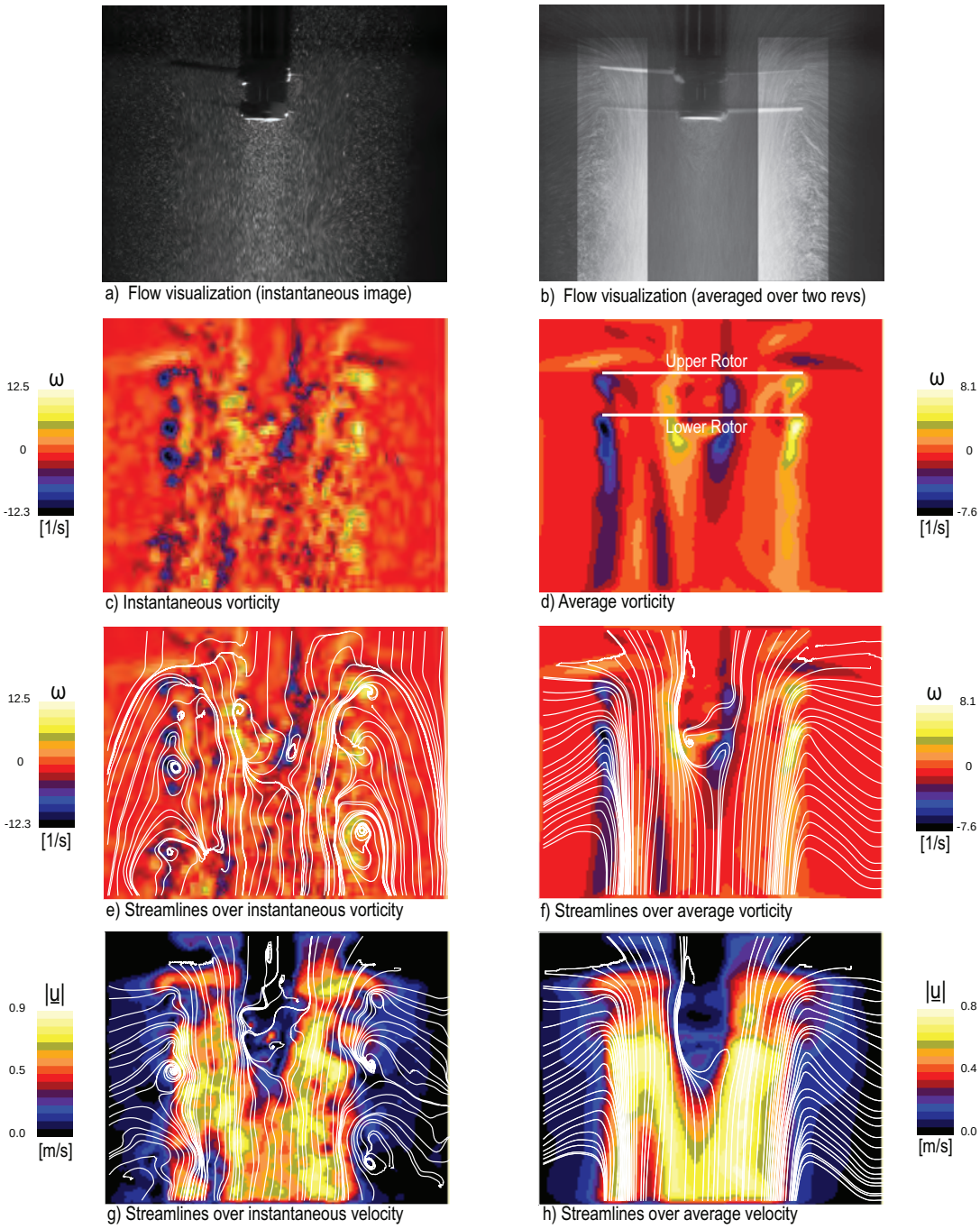

Figure 4.16: Flow field of a two-bladed coaxial rotor with rotor spacing of 37.5% of the rotor radius at $N = 8$ rps. First row (a,b): particle flow visualization. Average field in frame (b) is locally brightness- and contrast-enhanced to highlight the wake contraction of both rotors. In rows 2-4 are shown PIV measurements. Second row (c,d): vorticity fields. Third row (e,f): streamlines over vorticity. Fourth row (g,h): streamlines over speed. Streamlines in frame (e) are drawn from a moving reference frame and streamlines in frames (f-h) are drawn from a stationary reference frame.

4.6 Coaxial rotor with axial spacing of H/R=0.41

4.6.1 Flow images

Figures 4.17 shows the intricate wake characteristics of coaxial rotors and interactions between the helical filaments trailed from the blades of both rotors. The rotor speed in these experiments, which are indicated in Table 2.3 with the test numbers 9-12, ranged from 2 to 8 rps as before. Data representation is similar to those presented in Figure 4.7. The axial rotor spacing was adjusted to 41% of the rotor radius by fitting the coaxial rotors with spacer 3, resulting in a 10% and 65%-increase in axial spacing between the rotors compared to spacer 2 ($H/R = 0.375$) and spacer 1 ($H/R = 0.25$) cases, respectively. The rotor drive system and the disk spacers are designed in a way that when changing the axial distance between the rotors by using removable disk spacers, the position of the upper rotor is fixed and only that of the lower rotor is changed in each different rotor spacing tested. The lower rotor filament is seen to be contorted out of its orderly helical shape at 6 & 8 rps instantaneous images. Note the extreme strain the lower rotor filament is experiencing. Double tube structure formed by the coaxial wakes is clear in the time-averaged views. As the interrotor space is increased, the cross-sectional area of the impinging wake of the leading disk (upper rotor) on the inner part of the trailing disk (lower rotor) is decreased. However, the axial separation distance between the rotors is not sufficiently long for the upper rotor wake to be still considered fully-developed before it is ingested by the lower rotor similar to the aforementioned two cases (spacer 1 & 2). Upper rotor wake can be considered to be fully-developed when the streamlines of the rotor wake assume a straight profile rather than curvature and the contracted wake area reaches to a constant value as discussed in PIV results of previous two cases. The phase-averaged images reveals the persistence of the flow field throughout the duration of the test. The tip vortex circulation-based Reynolds numbers at this rotor spacing are provided on the fourth column of Table 4.1 along with their standard deviation and estimated to be about 10600 for 2 rps, 19100 for 4 rps, 34000 for 6 rps, and 31400 for 8 rps cases.

Figure 4.18 shows the evolution of the coaxial rotor wakes during one complete rotor revolution at 8 rps at this rotor spacing. Data representation is similar to those of Figure 4.8 and 4.13. The successive vortices from each of the rotors are labeled in a similar manner to the previous cases. As it is evident in the images, the individual filaments, especially those from the lower rotor, undergo strong deformation within a rotor revolution beneath the lower rotor similar to what is observed in previous cases, where rotor spacing is in between $0.25 \leq H/R \leq 0375$, although they appear to differ in to the extent of the deformations they experience. Consecutive images 11-15 of the figure clearly show that the lower rotor vortices is undergoing extreme strain, resulting in the streamwise elongation of the vortices up to a length of about a rotor radius. This feature is also seen in images at other rotor speeds given in Figure 4.17, albeit vaguely at 2 and 4 rps.

4.6.2 Vortex Instabilities and wake geometry

Long-wave instability mode

The interaction between the helical filaments occurs following a mechanism similar to that observed and discussed in previous cases. The helical tip vortices develop long-wave pairing instabilities where the adjacent filaments and successive portions of the turns of each filament travel at different downward speeds which, in turn, results in entanglement and coalescence of the vortices into bigger diffuse ones up to a rotor radius in the wake beneath the lower rotor. The merging of the vortices l1 & l2 is seen in image 18 in Figure 4.18. The interaction appears to start as a classical leapfrogging process but in a very short time period it leads to unusual deformations that is unprecedented in single rotor runs as observed above. As before, the interaction of the upper filaments with the lower rotor blades (interrotor BVIs) results in disintegration

of upper filaments into three different pieces as they are cut through twice as they go through the lower rotor after which they diffuse quickly. The leapfrogging process between the vortices l1 & l2 is preceded by the interaction, which is another long-wave instability, between the adjacent turns of the vortex l1 where the backward portion of the vortex l1 spirals around the forward portion followed by leapfrogging of the vortex l2 through the former. What is interesting in the images is that the forward portion of the vortex l2 and backward portion of vortex l1 acquire much more speed than their backward and forward portions, respectively, which result in extreme strain in the lower rotor filaments and destruction of their orderly helical shapes. Frames 9 and 10 in Figure 4.18 reveal this complex behavior of the vortices l1 and l2. In Appendix A, rest of the evolution images of vortex wake at the same rotor spacing during one complete rotor revolution at 6, 4 & 2 rps are provided in Figures A.37, A.39, and A.41, respectively.

Short-wave instabilities

Figure 4.19 shows the development of short-wave instabilities along the vortex filaments where each frame from (a) to (d) is from a corresponding rotor speed 2-8 rps. Similar short-wave instability characteristics as seen in previous cases are visible in these images. Increased rotor spacing appears not to alter the development of short-wave instabilities, at least in an obvious way. Note again the more stable forms of upper rotor filaments as opposed to lower rotor vortices in each particular rotor speed.

Wake contraction and xt diagram

Figure 4.20 shows the contraction and axial convection rates of the tip vortices from both rotors at 8 rps at the same rotor spacing. Data representation is similar to that shown in Figure 4.10. The similar observations apply in this case, too. From the average images in Figure 4.17, the wake contraction ratio for the upper wake at the plane of the lower rotor is about 0.74, a much smaller value expected as a result of increased rotor spacing. As before, the lower rotor wake does not contract as much as that of upper rotor when operated either in isolation or in tandem with the lower rotor.

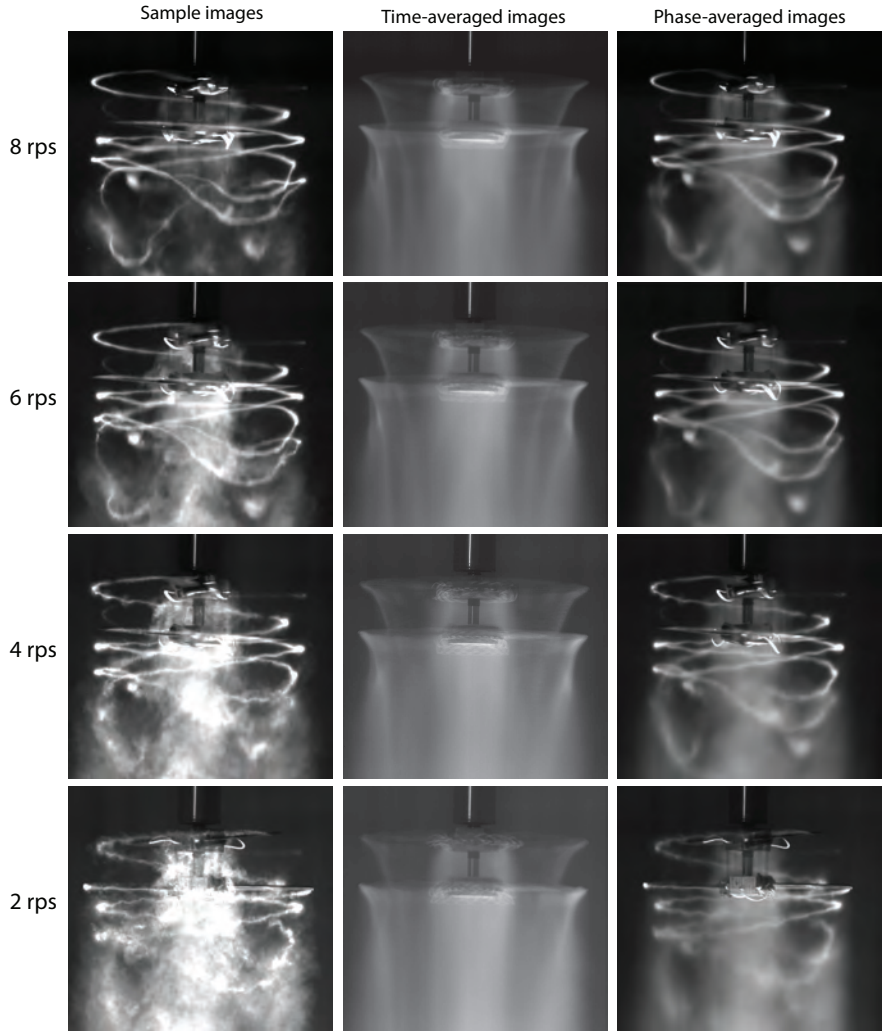

Figure 4.17: Two-bladed coaxial rotor (spacer3), $H/R = 0.41$: Flow visualization images at 8 rps (first row), 6 rps (second row), 4 rps (third row) & 2 rps (fourth row). Left column shows instantaneous flow images, the middle column shows the averaged flow fields, and the right column shows the phased-averaged images.

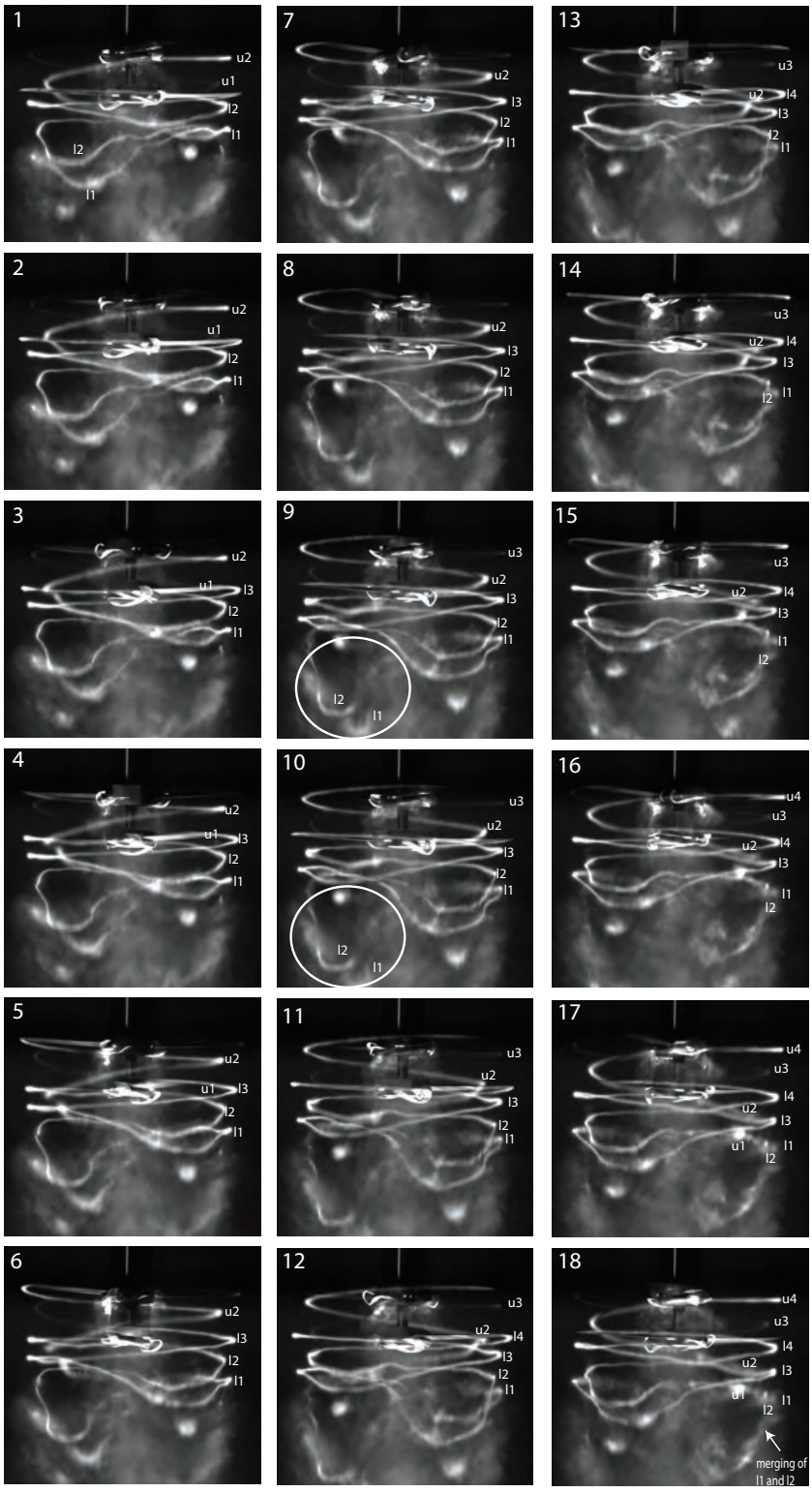

Figure 4.18: Vortex wake evolution of the coaxial rotors with axial spacing of H/R=0.41 during one complete rotor revolution at 8 rps. Images are 20° ($\pi/9$ rad) apart. Time separation between successive images is 6.94 ms. Adjacent vortices are labeled with odd and even numbers. The odd numbers are used to refer to successive vortices from one of the two blades while the even numbers are used to identify the successive vortices from the other blade.

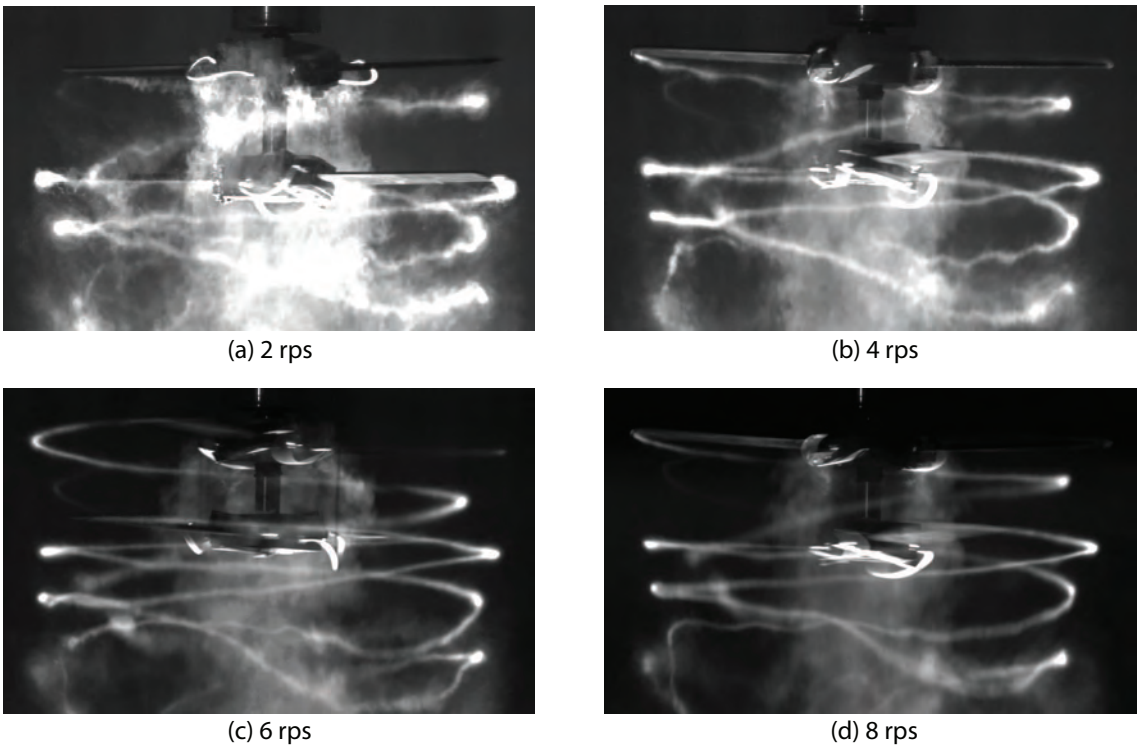

Figure 4.19: Sample flow images showing short-wave instabilities along the vortex filaments for all rotor speeds. Coaxial rotors are spaced at a 41% of the rotor radius (Spacer 3).

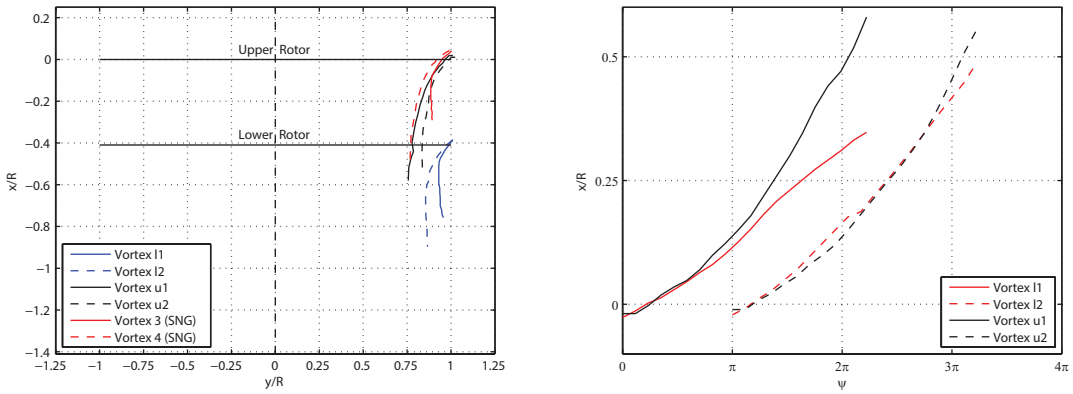

Figure 4.20: Trajectories of helical filaments trailed from coaxial rotor spaced at 41% of the rotor radius as well as those from the single rotor are shown. Right: spatial positions of tip vortices showing wake contraction. Left: xt diagram of the vortex filaments at 8 rps ($\psi = \Omega t$). Vortex labeling is similar to those in Figure 4.18

PIV

Figure 4.21 shows the corresponding PIV measurements at 8 rps where data representation is similar to those in Figure 4.11. The positions of the upper and lower rotors are marked in frame (d) in second row. Average streamline pattern is similar to previous cases where rotor separation is smaller. The instantaneous vorticity plot in frame (c) reveals the merging of the tip vortices. The average views does not show noticeable

deviations from the axisymmetry. Orbiting of lower vortices around one another is visible from the video sequence. In Appendix A, rest of the PIV results at this rotor spacing at 6, 4 & 2 rps are provided in Figures A.38, A.40, and A.42, respectively.

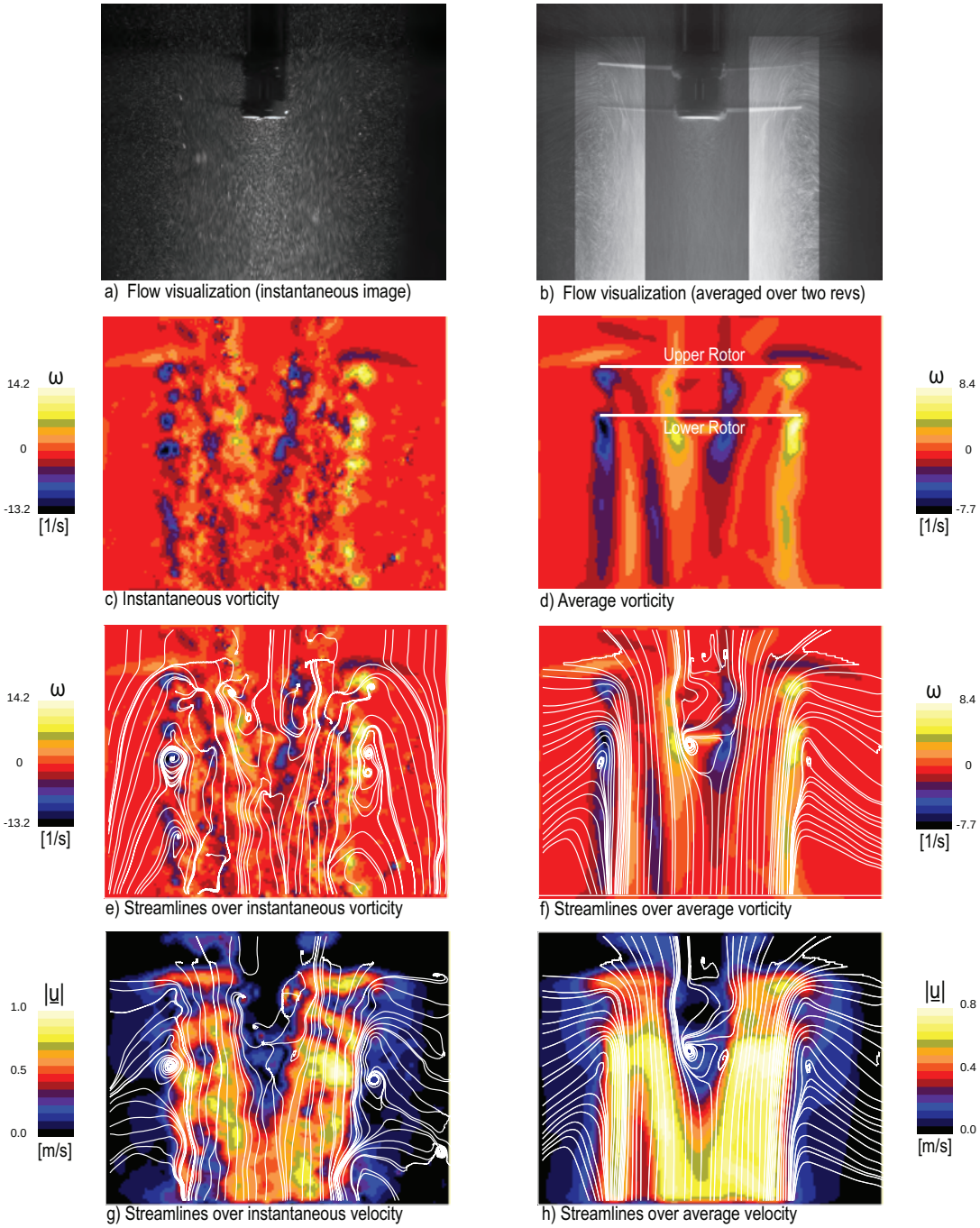

Figure 4.21: Flow field of a two-bladed coaxial rotor with rotor spacing of 41% of the rotor radius at $N = 8$ rps. First row (a,b): particle flow visualization. Average field in frame (b) is locally brightness- and contrast-enhanced to highlight the wake contraction of both rotors. In rows 2-4 are shown PIV measurements. Second row (c,d): vorticity fields. Third row (e,f): streamlines over vorticity. Fourth row (g,h): streamlines over speed. Streamlines in frame (e) are drawn from a moving reference frame and streamlines in frames (f-h) are drawn from a stationary reference frame.

4.7 Coaxial rotor with axial spacing of H/R=0.5

4.7.1 Flow images

Figure 4.22 shows the flow visualization images from the sets of experiments conducted at the rotor speeds of 2-8 rps which are indicated in Table 2.3 with the test numbers 13-16. The rotor-on-rotor distance was set to $H/R = 0.5$ (spacer 4). Data representation is similar to those in Figure 4.7. The rotor spacing is about twice as long as that of the spacer-1 case, in which the rotor spacing is the smallest. Sample images on the left show the intricate nature of the flow field as the upper rotor wake convects through and below the lower disk, leading to further complications there such as the formation of hairpin-shaped vortex structures which is recognizable at 8 rps flow images and underway at 2-6 rps frames. Time-averaged data show the contracted upper rotor wake and its splitting path as it is ingested by the lower rotor. Larger and smaller contraction rates of the upper and lower rotor wakes are clearly visible in these average images, respectively. The phase-averaged images are clear indication of the repeatable flow pattern during the entire length of the particular tests. The tip vortex circulation-based Reynolds numbers at this rotor spacing are provided on the fifth column of Table 4.1 along with their standard deviation and estimated to be about 10000 for 2 rps, 18600 for 4 rps, 34600 for 6 rps, and 31200 for 8 rps cases.

Figure 4.23 shows the temporal evolution of the coaxial vortex wake during two consecutive rotor revolutions at 8 rps at this rotor spacing of $H/R = 0.5$. Image representation is similar to those in Figures 4.8, 4.13, and 4.18. Successive vortices of the upper and lower rotors are marked u1-u6, and l0-l6, respectively. The vortex l0 in image 1 of the figure is marked to show the exceptional clarity of the hairpin-shaped vortex (see images 1-11 for downstream evolution of this vortex structure). Formation of hairpin vortices is a result of the extreme deformation of lower vortex filaments from their orderly helical shapes within a rotor revolution, which is apparent in the figure.

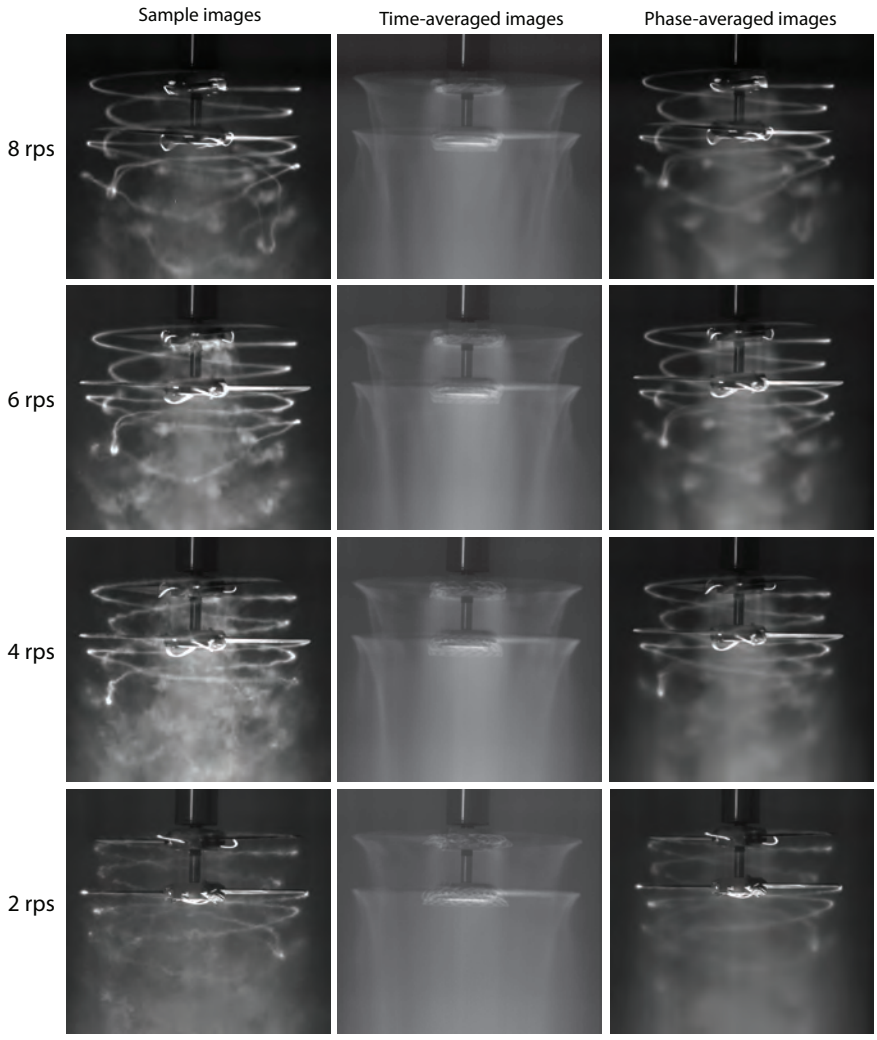

Figure 4.22: Two-bladed coaxial rotor (spacer4), $H/R = 0.5$: Flow visualization images at 8 rps (first row), 6 rps (second row), 4 rps (third row) & 2 rps (fourth row). Left column shows instantaneous flow images, the middle column shows the averaged flow fields, and the right column shows the phase-averaged images.

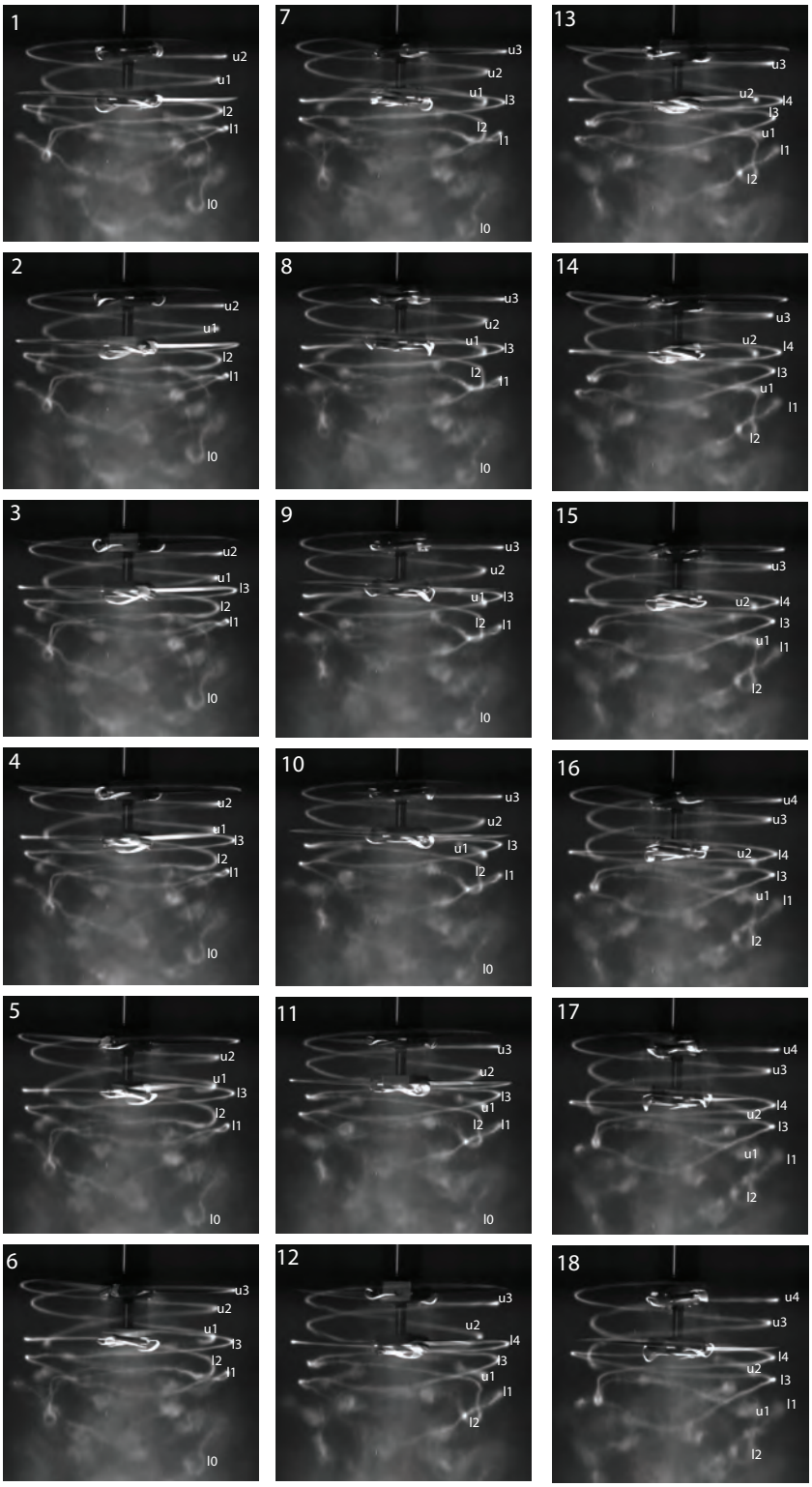

Figure 4.23: The first of two revolutions where the wake vortex evolution of the coaxial rotors with axial spacing of H/R=0.5 during two complete rotor revolutions at 8 rps. Images are 20° ($\pi/9$ rad) apart. Time separation between successive images is 6.94 ms. Adjacent vortices are labeled with odd and even numbers. The odd numbers are used to refer to successive vortices from one of the two blades while the even numbers are used to identify the successive vortices from the other blade.

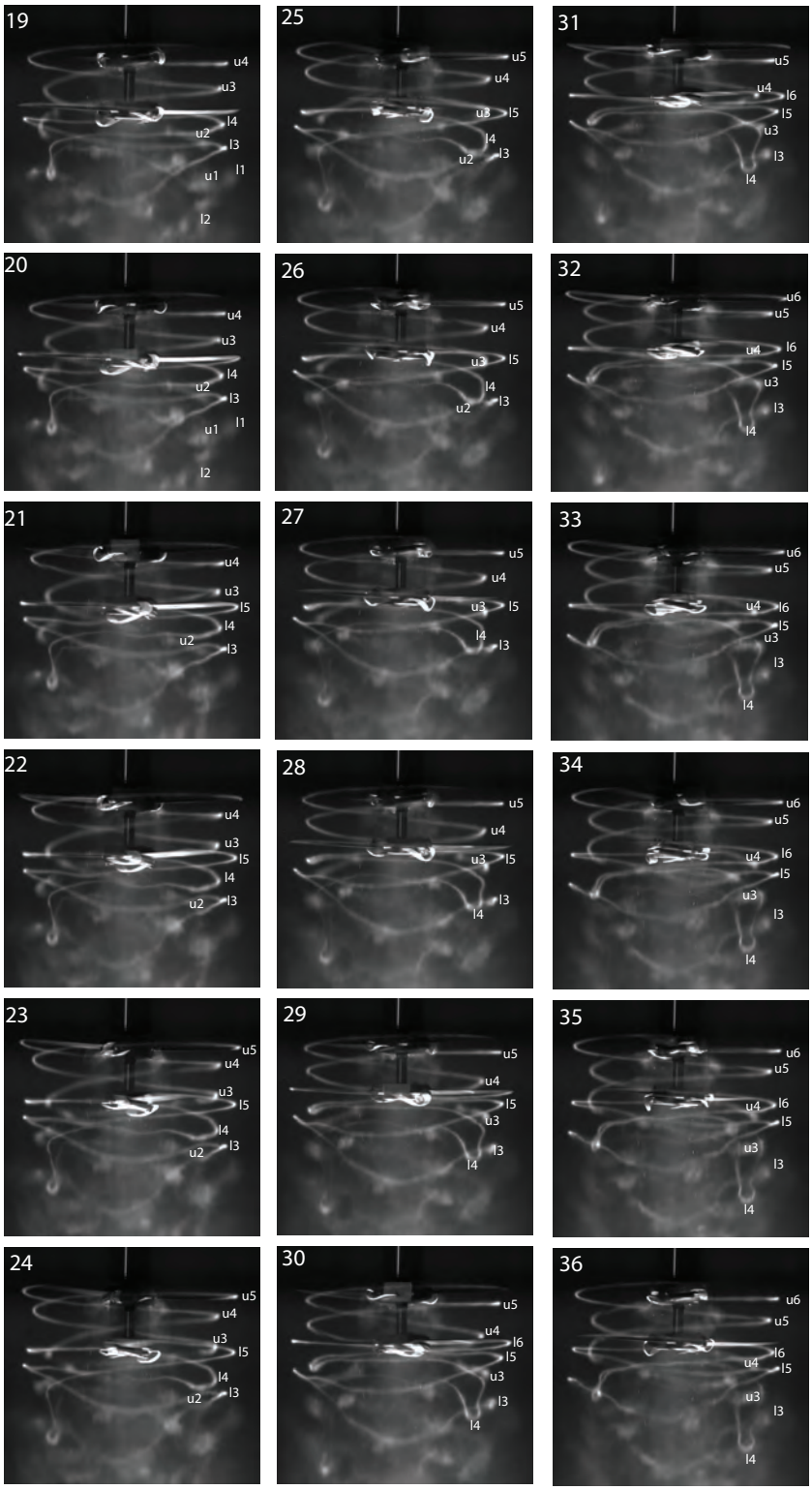

Figure 4.23: The second of two revolutions where the wake vortex evolution of the coaxial rotors with axial spacing of H/R=0.5 during two complete rotor revolutions at 8 rps. Images are 20° ($\pi/9$ rad) apart. Time separation between successive images is 6.94 ms. Adjacent vortices are labeled with odd and even numbers. The odd numbers are used to refer to successive vortices from one of the two blades while the even numbers are used to identify the successive vortices from the other blade.

4.7.2 Vortex instabilities and wake geometry

Long-wave instability mode

From an assessment of the flow visualization images, the following observations regarding the coaxial rotor wake and vortex instabilities are made: The interaction mechanism that takes place between the vortex filaments appear to be similar to those mentioned in the previous cases. The passing of the upper rotor filaments through the lower ones leads to strong mutual interactions between the lower rotor filaments and the adjacent portions of the each of them. The lower rotor filaments develop a leapfrogging process between each other as observed in all of the previously mentioned cases. This interaction process, in general, differs to the extent the filaments undergo deformations and the shapes they deform to during the interactions where they eventually become interweaved and diffuse. Also, the each lower rotor filament undergoes long-wave pairing instabilities between the adjacent portions of the helix turns where they spiral around each other. As can be seen from the sequential images in the first part of the Figure 4.23, frames 1-18, the trailing vortex l2 attempts to leapfrog through the leading vortex l1 where the former speeds up and shrinks in size, contracting more inward, while the latter expands outward as it slows down. This leapfrogging effect is further followed by streamwise stretching of the vortex l2, successive to l0, near the slipstream boundaries and vortex l1, successive to l3, in the central part of the wake beneath the lower rotor. Such features are depicted clearly in images 1 (vortices l0 & l1) and 18 (vortices l2 & l3) in Figure 4.23. This deformation and stretching of the perturbed vortices, which are trailed from lower rotor blades, result in the eventual formation of the hairpin-shaped vortices in the far wake region. The vortex l2 attains the shape of hairpin-shaped vortices near the wake boundaries. The forward (or tip) portion of a hairpin vortex is termed as 'vortex head' and the backward portions that are primarily aligned with the streamwise flow direction or the rotor axis are termed as 'vortex legs' (see Figure 1 of Haidari & Smith [61] for a schematic view and more details about hairpin vortices)). This formation of new vortex structure is clearly discernible in Figure 4.23 from image 10 to image 18. Also what is shown in images 1-5 in the same figure is two hairpin vortices formed following the deformation of filament l0. In Fig. 4.24 is shown the enlarged view of image 4 from Fig. 4.23. What is given in this figure is the clear visualization of two hairpin vortices formed. The head parts and legs of the vortices are marked in the figure. In the right half of the figure, the accelerated vortex head and two elongated vortex legs of the hairpin vortex, which is marked in the figure as hairpin vortex 1, is shown. On the left half of the figure, another vortex, marked as hairpin vortex 2, is seen. Also, vortices l0 & l1 are marked in the figure. Hairpin vortices are observed to be formed out of the even-numbered vortices (l0, l2, l4...), i.e. which trail from the same rotor blade, throughout the entire duration of the video sequence. To put it differently, as discussed in the previous rotor spacing cases, in the initiation of leapfrogging process which is followed by strong deformation of the vortices, two vortex filaments do not reverse their roles, even-numbered vortices always assumes the role of the trailing vortex while the odd-numbered ones has the role of leading vortex in the context of leapfrogging effect. An interesting feature observed from the careful investigation of the video sequence comprised of 450 successive images (a total of 25 rotor revolutions) reveals that although the flow pattern appears almost to be the same in every revolution, which can be seen from the phase-averaged images in Fig/ 4.22, the interaction between the adjacent portions of the lower filament 1 occurs exactly in the same way in every two rotor revolutions. As can be seen from the images 1-10 of Fig. 4.23, in first of this two-revolution flow pattern, the adjacent portions of the vortex l0 undergo a type of vortex-pairing instability between each other in which they spiral around each other during the formation of the hairpin vortices. This is also what is happening in Fig. 4.24 where hairpin vortices are shown where the backward (trailed later in time) and forward (trailed earlier in time) portions of the vortex l0 are marked. In the second rotor revolution, the hairpin vortices also form. This time, however, the adjacent portions of the vortex l4, which will comprise the legs of the hairpin vortex shortly, does not spiral around each other as in the preceding revolution. Near the vortex head of the hairpin vortex, the adjacent portions of the vortex l4 come very close to each other before they are elongated as the vortex head accelerates downstream of the flow. This process is underway in images 18-30 of Fig. 4.23. Formation of these hairpin vortices near the wake boundaries was not observed during flow visualization studies of the single rotor tests which is

given in Figure 4.3 as well as in the previous studies. As before, the upper rotor vortices appear to be very stable at the interrotor space and do not exhibit any noticeable interactions between one another. Their fate is also similar to those in the previous case when they encounter the lower rotor blades and interact with them, during which they break off into separate portions. Subsequently, they coalesce with the portions of the lower rotor vortices into bigger diffuse vortices as seen in image 18 where u1 and portions of l2 seem to merge. Similar vortex interactions and eventual formations of vortex structures are at play at other rotor speeds, too. However, due to diffuse nature of the flows at 2 & 4 rps, these patterns are not as clear as those at 6 & 8 rps images. In Appendix A, rest of the evolution images of vortex wake at the same rotor spacing during one complete rotor revolution at 6, 4 & 2 rps are provided in Figures A.43, A.45, and A.47, respectively.

Short-wave instabilities

Figure 4.25 shows the development of short-wave instabilities along the vortex filaments at rotor speed of 2-8 rps. At 2 & 4 rps images, the short waves along the filament are clearly visible before the commencement of deformation of the vortex filament. In frame (c) of 6 rps, the short waves are visible on the elongated leg of the hairpin vortex, which are marked with white arrow. As before, at 6 & 8 rps, in general short-wave instabilities develop long after the formation of the filaments, especially those from the lower rotor, and hard to separate them from the long-wave instability characteristics the vortex filaments are observed to exhibit. As before, further increase in rotor spacing seems to have little effect, if any, on short-wave instability characteristics. Note again the more stable forms of upper rotor filaments as opposed to lower rotor vortices in each particular rotor speed.

Wake contraction and xt diagram

Figure 4.26 shows the contraction and axial convection rates of the tip vortices from both rotors at 8 rps at this rotor spacing. Data representation is similar to that shown in Figure 4.10. Vortex trajectories of vortex u1 and u2 reveals that the latter travels at a faster rate than the former, an indication of possible long-wave instability characteristics between them. However, this rotor spacing of 50% of the radius does not allow this interactions to develop further. Also, trajectories of vortex l1 and l2 is the result of their aforementioned leapfrogging effect between each other. Difference in the wake contractions of upper and lower rotors are manifest on the left part of the figure. From the average images in Figure 4.22, the wake contraction ratio for the upper wake at the plane of the lower rotor is about 0.78. Lower rotor wake contracts to about 90% of the rotor radius, which is markedly higher than that of the upper rotor. Also, the higher axial convection rates of the upper rotor filaments compared to those when operated in isolation is clear in the left plot. The higher convection rate of the lower rotor vortex l2 is a result of the streamwise deformation, which results in hairpin vortex with elongated legs.

PIV

Figure 4.27 shows the corresponding PIV measurements at 8 rps where data representation is similar to those in Figure 4.11. The positions of the upper and lower rotors are marked in frame (d) in second row.In the average views, the development of streamline patterns toward a more straight profile in the vicinity of the lower rotor is seen compared to before, a consequence of increased rotor spacing and approaching of the upper rotor wake toward a fully-developed state at the plane of the lower disk. Individual tip vortices are identifiable in the instantaneous vorticity plots in frames (c) and (e). 2-D PIV measurements does not reveal the formation of hairpin vortex structures which are observed in dye visualization runs. In Appendix

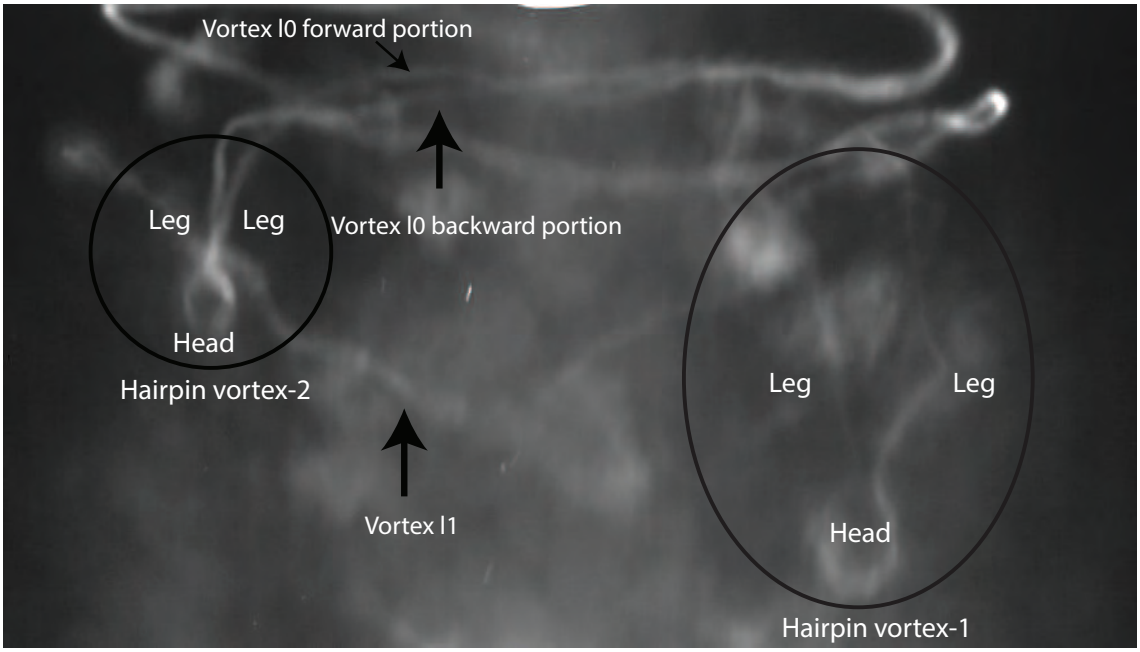

Figure 4.24: Enlarged view of image 4 from Figure 4.23 that clearly shows the hairpin-like vortices near the wake boundaries

A, rest of the PIV results at this rotor spacing at 6, 4 & 2 rps are provided in Figures A.44, A.46, and A.48, respectively.

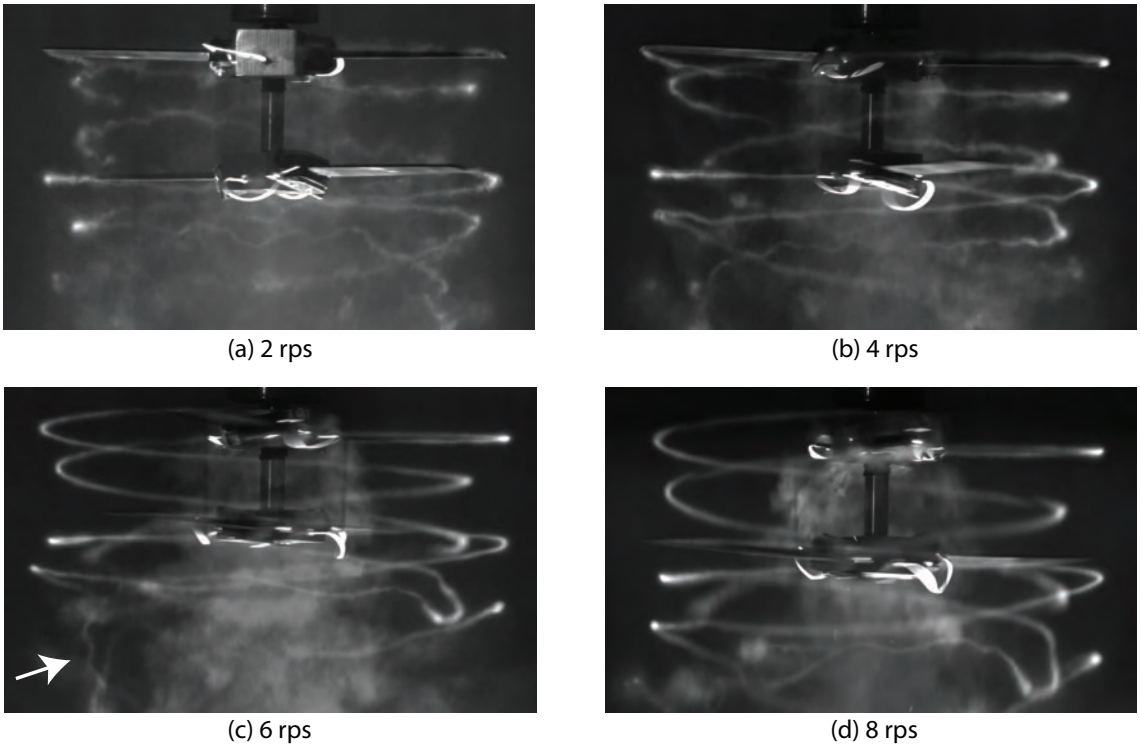

Figure 4.25: Sample flow images showing short-wave instabilities along the vortex filaments for all rotor speeds. Coaxial rotors are spaced at 50% of the rotor radius (Spacer 4).

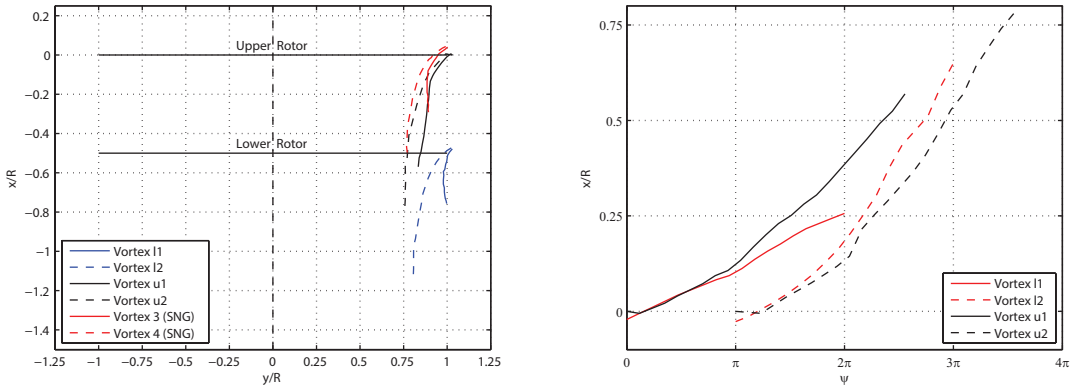

Figure 4.26: Trajectories of helical filaments trailed from coaxial rotor spaced at half the rotor radius as well as those from the single rotor are shown. Right: spatial positions of tip vortices showing wake contraction. Left: xt diagram of the vortex filaments at 8 rps ($\psi = \Omega t$). Vortex labeling is similar to those in Figure 4.23

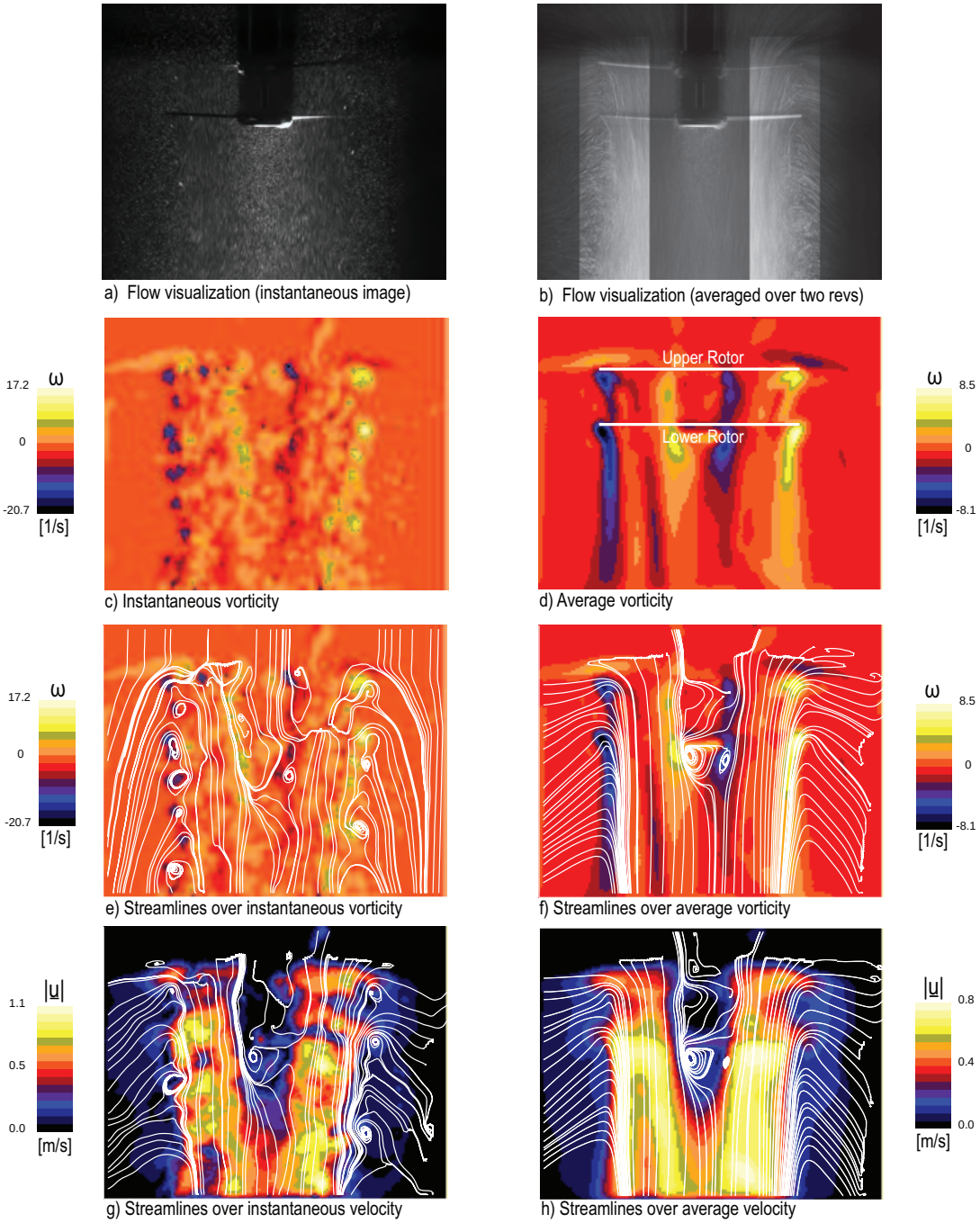

Figure 4.27: Flow field of a two-bladed coaxial rotor with rotor spacing of 50% of the rotor radius at $N = 8$ rps. First row (a,b): particle flow visualization. Average field in frame (b) is locally brightness- and contrast-enhanced to highlight the wake contraction of both rotors. In rows 2-4 are shown PIV measurements. Second row (c,d): vorticity fields. Third row (e,f): streamlines over vorticity. Fourth row (g,h): streamlines over speed. Streamlines in frame (e) are drawn from a moving reference frame and streamlines in frames (f-h) are drawn from a stationary reference frame.

4.8 Coaxial rotor with axial spacing of H/R=0.625

4.8.1 Flow images

Figure 4.28 shows the flow visualization images from the series of experiments conducted at the rotor speeds of 2-8 rps which are indicated in Table 2.3 with the test numbers 17-20. Rotors are spaced approximately 62.5% of the rotor radius (spacer 5). Data representation in the figure is similar to those in Figure 4.11. Individual helical filaments trailed from the upper rotor is easily identifiable in the space between the rotors and can be tracked up to a duration of one and half rotor revolutions before they go through the lower rotor. 6 & 8 rps images suggest that the a long-wave pairing instability mode between the upper vortices is underway, which will be discussed in due course. As before, the flow fields reveal the strong interactions and subsequent deformations of the tip vortices in the near wake region beneath the lower rotor. Time-averaged images in the middle part of the figure displays the different wake contractions of the upper rotor vortices which confirm the developing long-wave instability mode as seen in images on the left. The tip vortex circulation-based Reynolds numbers at this rotor spacing are provided on the sixth column of Table 4.1 along with their standard deviation and estimated to be about 9850 for 2 rps, 17900 for 4 rps, 40000 for 6 rps, and 38200 for 8 rps cases.

Figure 4.29 shows the temporal evolution of the coaxial vortex wake during two complete rotor revolutions. Image representation and vortex labeling are similar to those in previous cases. These sequential images further reveal the developing long-wave instability mode between the vortices of the upper rotor. Of all the rotor spacings tested up to here where $H/R \leq 0.5$, this particular rotor separation of $H/R = 0.625$ appears to be the first one where the upper rotor filaments exhibit noticeable long-wave instability characteristics albeit not in a complete manner since they are intercepted by the lower rotor at downstream distances. It is also clear in the images that the upper rotor filaments retain their orderly helical shapes in the space between the rotors before they interact with lower rotor blades. Although the vortex stretching is seen to occur in a similar way to the previous case of 50% rotor spacing where hairpin-shaped vortex structures are formed, no such clear structures are seen to form inside the wake here. Also note the deformation of the lower rotor filaments within the first rotor revolution as before.

4.8.2 Vortex instabilities and wake geometry

Long-wave instability mode

As can be observed from the sequential images provided in Fig. 4.29 (images 1-12), the upper vortex filaments, which are labeled as u1 and u2, exhibit a long-wave instability mode before they encounter the lower rotor. Vortex u2 increases its speed and contracts inward but there is not sufficient interrotor space for it to pass through the vortex u1 in order to complete the leapfrogging process. The interaction between the upper rotor filaments lead to another interaction between the lower rotor filaments. Although the interaction mechanism between the lower rotor filaments is similar to the previous cases, it, too, differs in the way that the adjacent portions of each lower rotor filament interact with each other and the ultimate shape they attain before they become entangled and diffuse in the far wake region. Following the formation of lower vortex l1, its adjacent portions of first helix turn travel at different downward speeds, the forward portion having a higher transfer rate than that of the backward portion. What is more, adjacent portions of the lower vortex l2 orbits around each other manifesting a vortex-pairing instability. This self-interaction of the vortex l2 is preceded by the passing of the upper vortex u1 and upper vortex u2 through the lower rotor, which apparently triggered this interaction between the neighboring portions of the lower rotor filaments. In addition to these interactions between the filaments, the lower rotor filaments develop leapfrogging process

similar to previous tests carried out with smaller rotor spacings. Vortex l2, already having been orbiting around its own neighboring portions, accelerates by contracting radially inward more and then passes through the vortex l1, a process which can be easily tracked in successive images 1-10 in Fig. 4.29. That the vortex l2 develops this instability between the contiguous portions of one helix turn is accentuated by the passing of the upper filaments through the lower rotor in quick succession as compared to the previous cases, which does not yield enough time for vortex l2 to develop without the stronger induced effect of vortex u2. Flow pattern beneath the lower rotor shows small variations during consecutive rotor revolutions, which is manifest in image sequences of 1-5 and 19-23 in Figure 4.29. Upper filaments at the interrotor space does not exhibit such an aperiodicity between consecutive revolutions compared to those of lower filaments. The flow patterns at 2-6 rps show similarities to 8 rps case, a general feature observed in all of previous rotor spacing cases. In Appendix A, rest of the evolution images of vortex wake at the same rotor spacing during one complete rotor revolution at 6, 4 & 2 rps are provided in Figures A.49, A.51, and A.53, respectively.

Short-wave instabilities

Figure 4.30 presents sample frames at each rotor speed that reveal short-wave instability characteristics along the vortex filaments. Similar observations are made as in previous cases. Upper rotor filaments does not develop short-wave instabilities even long after their formation at 6 & 8 rps compared to lower rotor filaments here and in previous spacings. At 2 & 4 rps images, the short waves are clearly visible just from the inception of the filaments. In frame (c) of 6 rps, the short wave is marked with white arrow. More stable nature of the upper rotor vortex filaments is noted at the interrotor area, after which they become diffuse and hard to track individually.

Wake contraction and xt diagram

Figure 4.31 shows the contraction and axial convection rates of the tip vortices from both rotors at 8 rps. Data representation is similar to that shown in Figure 4.10. Vortex trajectories of vortex u1 and u2 reveals the aforementioned long-wave instability mode between the upper rotor vortices, a feature that is not apparent in previous cases discussed. Note the difference in wake contraction and axial convection rates of upper and lower rotor vortices. From the average images in Figure 4.28, the wake contraction ratio for the upper wake at the plane of the lower rotor is about 0.78 as in the previous case where axial spacing is 50% of the rotor radius with an eventual wake contraction of about 0.66 in the far wake region beneath the lower rotor. As clear in the figure, vortex u2 contracts much more inward than vortex u1, a result of leapfrogging effect between these two vortices. Lower rotor wake contracts to about 92% of the rotor radius, which is markedly higher than that of the upper rotor both at the lower disk and in the far wake region. Also, note the the higher axial convection rates of the upper rotor filaments compared to those both when operated in isolation and lower rotor filaments. The extreme deformation experienced by the lower rotor filaments makes it difficult to track their positions in the wake due to nonuniform deformation of adjacent portions of helix turns.

PIV

Figure 4.32 shows the corresponding PIV measurements at 8 rps where data representation is similar to those in Figure 4.11. The positions of the upper and lower rotors are marked in frame (d) in second row. Similar features can be extracted from the PIV results as in the previous case. In Appendix A, rest of the PIV results at this rotor spacing at 6, 4 & 2 rps are provided in Figures A.50, A.52, and A.54, respectively.

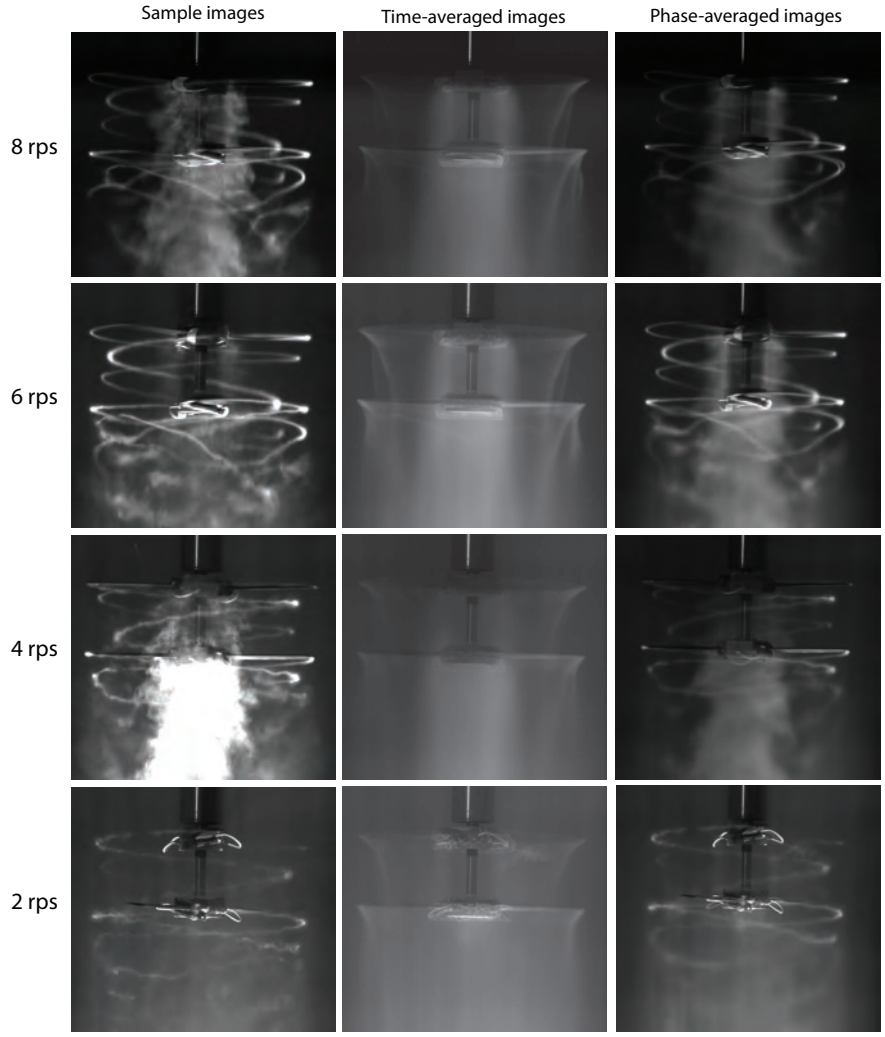

Figure 4.28: Two-bladed coaxial rotor (spacer5), $H/R = 0.625$: Flow visualization images at 8 rps (first row), 6 rps (second row), 4 rps (third row) & 2 rps (fourth row). Left column shows instantaneous flow images, the middle column shows the averaged flow fields, and the right column shows the phase-averaged images.

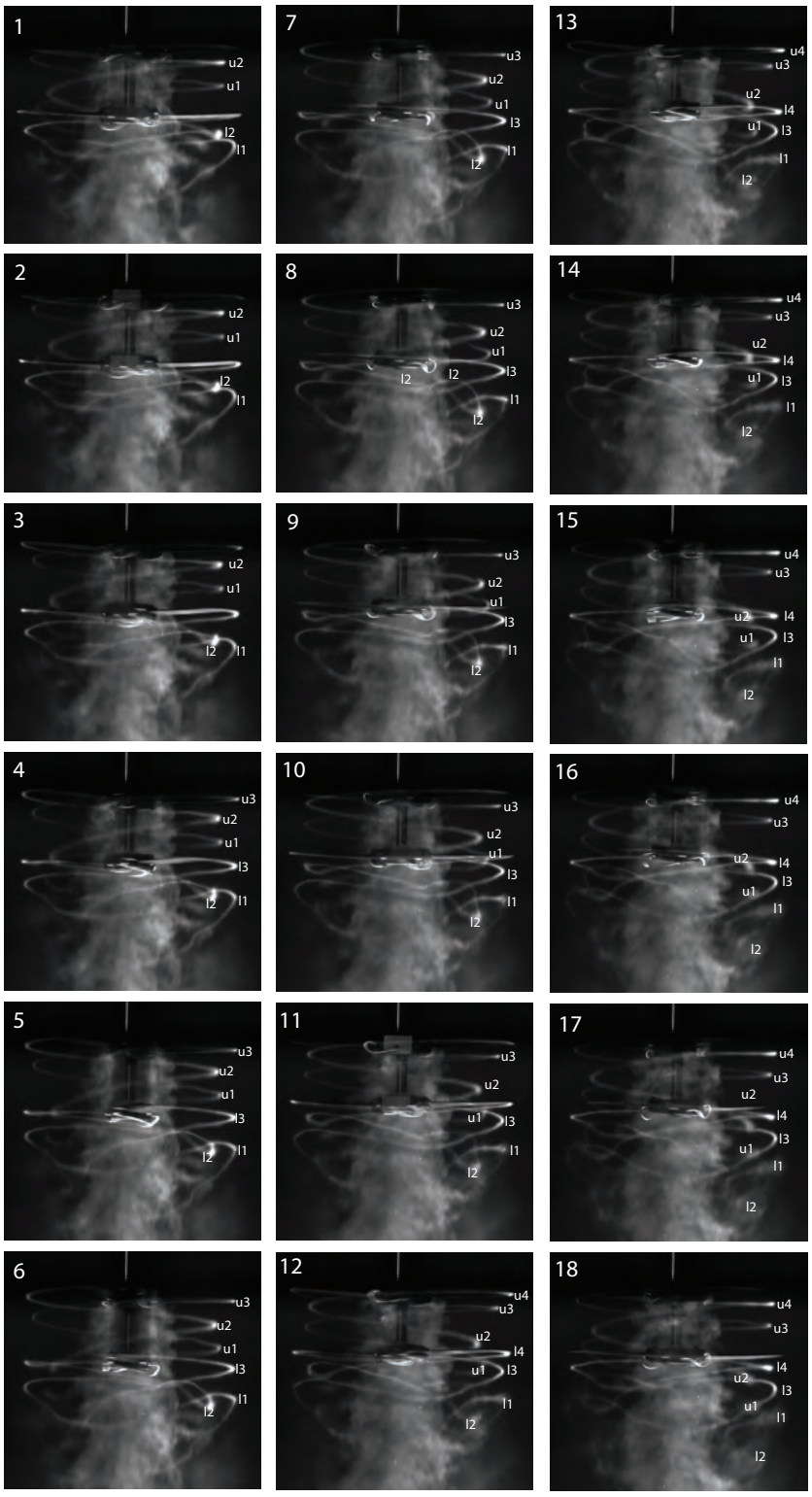

Figure 4.29: The first of two revolutions where the wake vortex evolution of the coaxial rotors with axial spacing of H/R=0.625 during two complete rotor revolution at 8 rps. Images are 20° ($\pi/9$ rad) apart. Time separation between successive images is 6.94 ms. Adjacent vortices are labeled with odd and even numbers. The odd numbers are used to refer to successive vortices from one of the two blades while the even numbers are used to identify the successive vortices from the other blade.

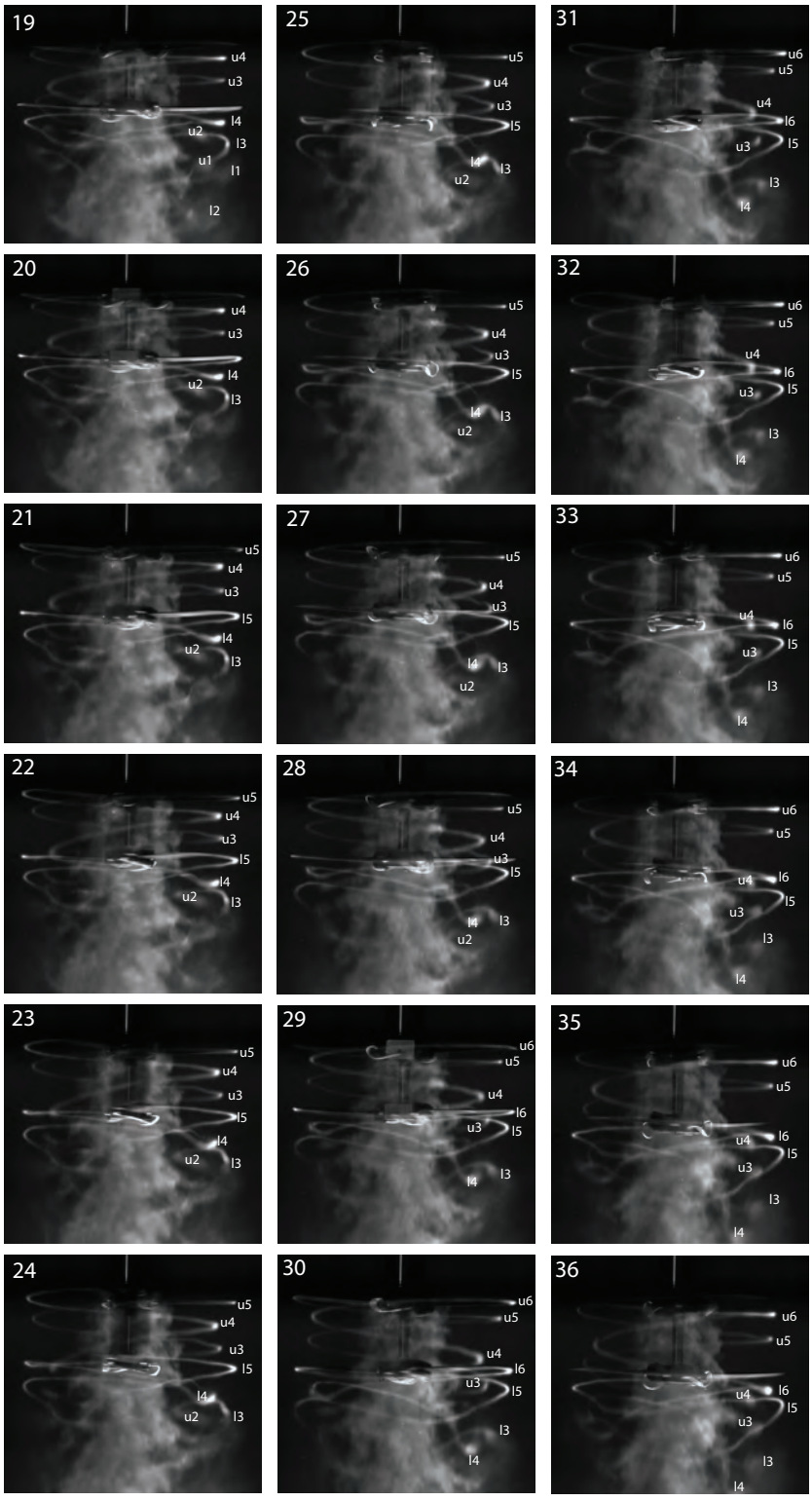

Figure 4.29: The second of two revolutions where the wake vortex evolution of the coaxial rotors with axial spacing of H/R=0.625 during two complete rotor revolution at 8 rps. Images are 20° ($\pi/9$ rad) apart. Time separation between successive images is 6.94 ms. Adjacent vortices are labeled with odd and even numbers. The odd numbers are used to refer to successive vortices from one of the two blades while the even numbers are used to identify the successive vortices from the other blade.

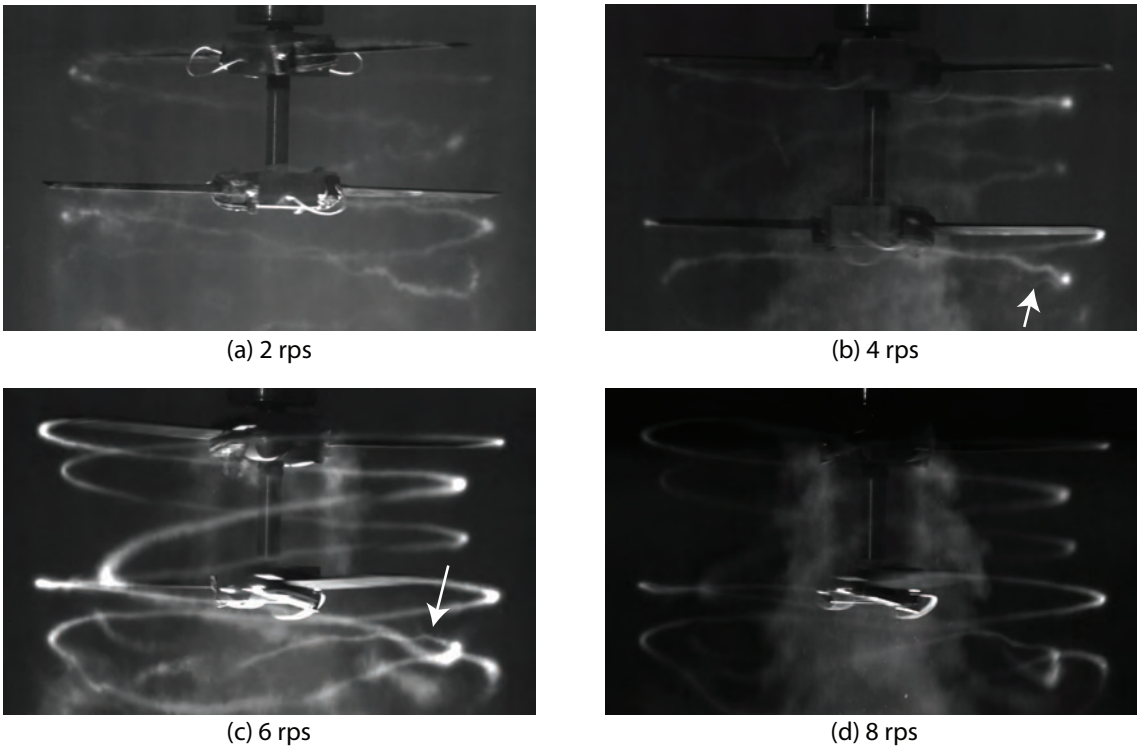

Figure 4.30: Sample flow images showing short-wave instabilities along the vortex filaments for all rotor speeds. Coaxial rotors are spaced at 62.5% of the rotor radius (Spacer 5).

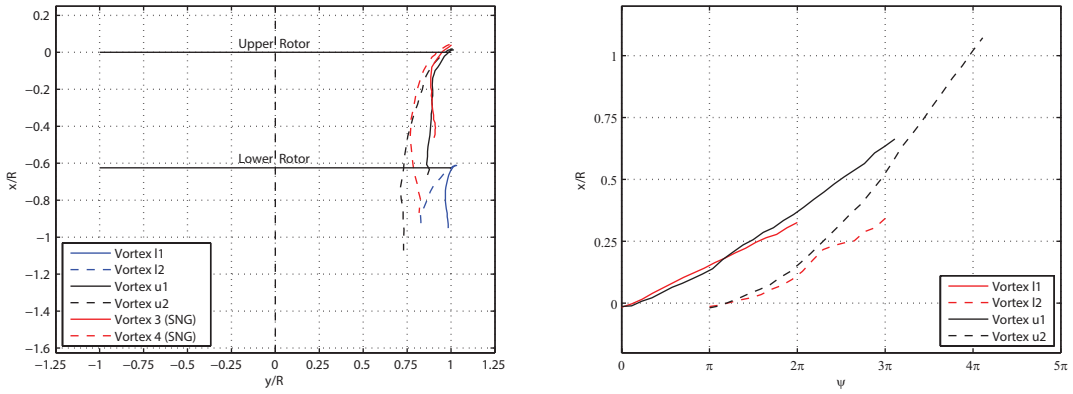

Figure 4.31: Trajectories of helical filaments trailed from coaxial rotor spaced at 62.5% of the rotor radius as well as those from the single rotor are shown. Right: spatial positions of tip vortices showing wake contraction. Left: xt diagram of the vortex filaments at 8 rps ($\psi = \Omega t$). Vortex labeling is similar to those in Figure 4.29

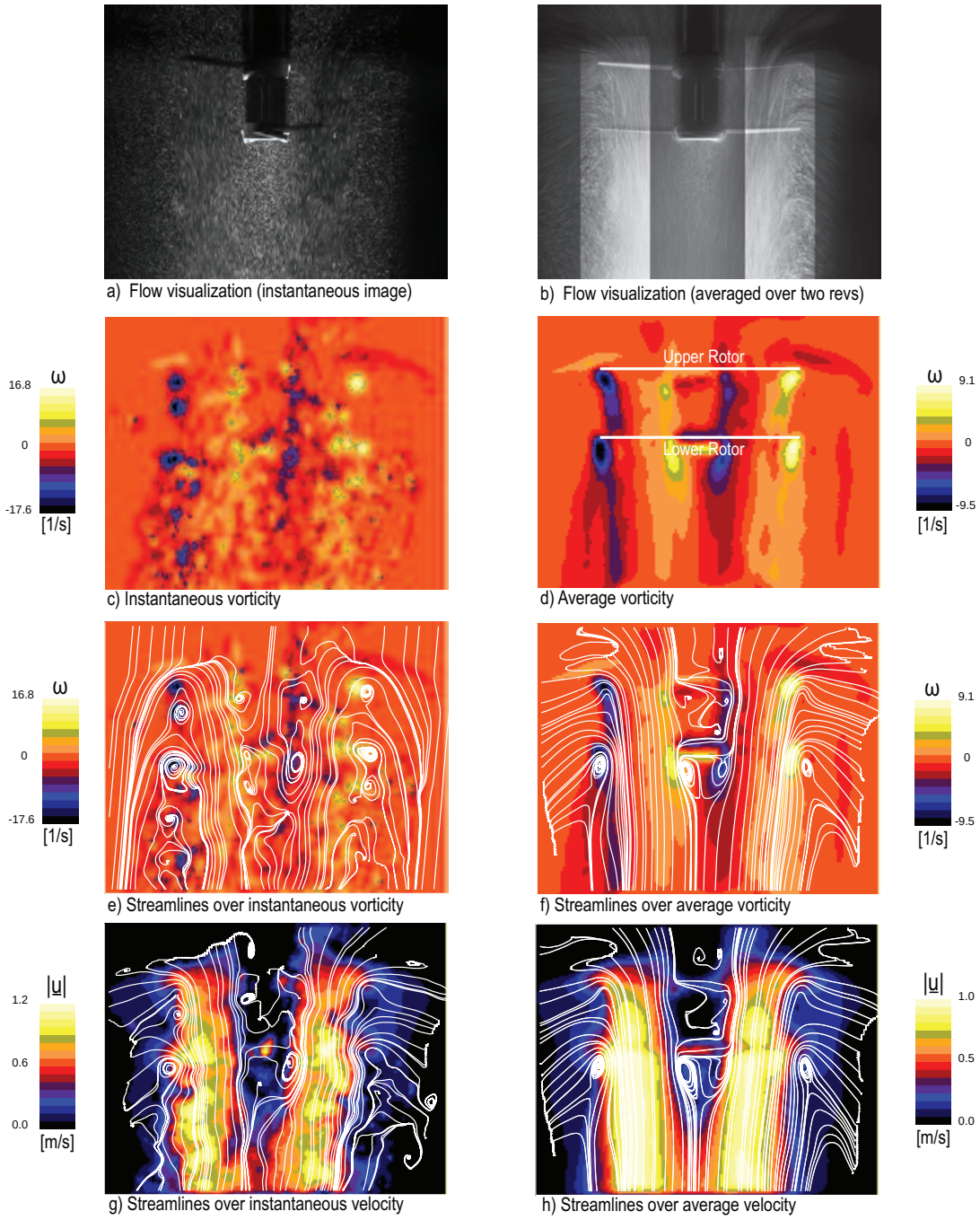

Figure 4.32: Flow field of a two-bladed coaxial rotor with rotor spacing of 62.5% of the rotor radius at $N = 8$ rps. First row (a,b): particle flow visualization. Average field in frame (b) is locally brightness- and contrast-enhanced to highlight the wake contraction of both rotors. In rows 2-4 are shown PIV measurements. Second row (c,d): vorticity fields. Third row (e,f): streamlines over vorticity. Fourth row (g,h): streamlines over speed. Streamlines in frame (e) are drawn from a moving reference frame and streamlines in frames (f-h) are drawn from a stationary reference frame.

4.9 Coaxial rotor with axial spacing of H/R=0.75

4.9.1 Flow images

Figure 4.33 shows the flow visualization images from the sets of experiments conducted at the rotor rotation rates of 2-8 rps which are indicated in Table 2.3 with the test numbers 21-24. The axial separation distance between the coaxial rotors was set to three quarters of a rotor radius, $H/R = 0.75$ (spacer 6). Data representation is similar to what is presented in Figure 4.11. As the interrotor spacing is increased more and more closer to a rotor radius, the tip vortices trailed from the blade tips of the upper rotor has sufficient space to develop mutual interactions between each other similar to what is observed in single rotor tests presented earlier in the chapter. Also, the rotor spacing provides a measure of the effect of the lower rotor on the upper, which diminish as the rotors become more and more separated from each other. Since the slipstream of the upper rotor is ingested by the lower rotor, the former always affects the latter profoundly albeit at varying cross sectional areas at the plane of the latter. However, it cannot be fully ascertained yet even at this rotor spacing that the upper rotor wake is fully developed and independent of the effects induced by the lower rotor. Time-averaged images reveal the mutual interaction between the upper rotor filaments which are seen to contract at different rates. The tip vortex circulation-based Reynolds numbers at this rotor spacing are provided on the seventh column of Table 4.1 along with their standard deviation and estimated to be about 8900 for 2 rps, 16400 for 4 rps, 34200 for 6 rps, and 33000 for 8 rps cases.

Figure 4.34 shows the the vortex wake evolution of the coaxial rotors at this rotor spacing during a complete rotor revolution at 8 rps. Data representation and vortex labeling are as before. Evolution of the long-wave pairing instabilities between the upper rotor filaments is visible in sequential images. Also, the complex interactions taking place between the filaments is clear beneath the lower rotor where lower filaments also develop similar vortex pairing instability characteristics and undergo strong deformations as before.

4.9.2 Vortex instabilities and wake geometry

Long-wave instability mode

The first obvious feature to notice when investigating the flow visualization videos of this particular case is that the upper rotor filaments develop a complete leapfrogging process between each other which is clear throughout the evolution images given in Fig. 4.34. This leapfrogging process is initiated by the trailing vortex u2, which contracts more inward, shrinks in diameter and accelerates downstream. Then, this accelerated vortex u2 passes through the vortex u1 which ceases the contraction and expands outward, however small and hard to notice. Leapfrogging of vortices u1 and u2 can be tracked from the frames 1-10 in the figure. Also, in image 18 of the same figure, the vortices u3 and u4 which are preceded by the vortices u1 an u3, respectively, is seen to repeat the same process. Subsequent to passing of vortex u2 through vortex u1, the filaments appear to reverse their roles and attempt to repeat the leapfrogging process one more time. This time, vortex u1 starts to contract and accelerates while vortex u2 ceases to contract and then starts to expand. Additionally, this acceleration may also be further increased by the sucking action of the lower rotor when the upper vortices reach the vicinity of it. The time-averaged images in the middle part of Figure 4.37 clearly shows the acceleration of vortex u1 just above the lower rotor. However, before the filaments complete this second leapfrogging, they encounter and interact with the lower rotor blades. Following their ingestion by the lower rotor they become extremely diffuse, and their subsequent locations become hard to trace.This particular rotor spacing of 75% of the rotor disk radius is the first case in which the helical filaments trailed from the upper rotor complete a leapfrogging process between each other at the interrotor

space. This is mainly attributed to the increased rotor separation which further reduces the induced effect of the lower rotor on the upper rotor and, hence, allow the upper rotor filaments to develop more stronger mutual interactions between each other until they reach the vicinity of the lower rotor. In the previous case where $H/R = 0.625$, a process akin to what is seen here seems to be underway but there is not sufficient space for the filaments to render this process complete.

Subsequent to leapfrogging of upper rotor filaments through lower filament l3, the adjacent portions of the first turn of the lower vortex l3 exhibit long-wave pairing instability characteristics in which they start to orbit around each other. This process is accelerated by the passing of the turns of the upper rotor filaments u1 and u2 in quick intervals through the lower vortex 3 following its formation. As this is process underway, the lower vortex l4 attempts to leapfrog through the vortex l3 in a similar mechanism as observed in the previous cases discussed above. These two processes, orbiting and leapfrogging, are manifest in the sequential images provided in Fig. 4.34. During the leapfrogging of vortex l2 through vortex l1, the former starts to deform and lose its orderly helical shape. The portions of the helix l2 in the outer wake region gather much more speed than its portions that lay in the central wake region and experience a decrease in it radius as it goes through the vortex l1 which already has started to expand radially outward and orbit around its adjacent portions at the same time. During this process, vortex l1 and l2 contact each other, which result in sooner diffusion and destruction of vortices, in particular of vortex l1 as seen in images 1-5 in the figure. The lower vortex l2 evolves to a shape that is different from an orderly helix, resembling a hairpin vortex with a fatter head and largely separated elongated vortex legs unlike what is observed in spacer 4 case when the rotor spacing is half the rotor radius as given in Figure 4.24. Unlike vortex l1, the adjacent portions of a turn of the vortex l2 do not exhibit this orbiting behavior. During the leapfrogging of lower filaments, vortex l1 becomes diffuse following the passage of vortex l2. One interesting feature to note is that the upper and lower filaments are observed to develop different characteristics during the long-wave pairing instabilities. While the upper rotor filaments exhibit leapfrogging characteristics similar to what is observed in single rotor tests, and retain their orderly helical shapes during this process, the lower rotor filaments undergo strong deformations and subsequently lose their orderly helical shapes within first rotor revolution just from their inception, a clear indication of the strong stability of upper rotor filaments as opposed to those of lower rotor filaments. In Appendix A, rest of the evolution images of vortex wake at the same rotor spacing during one complete rotor revolution at 6, 4 & 2 rps are provided in Figures A.55, A.57, and A.59, respectively.

Short-wave instabilities

Figure 4.35 presents sample frames at each rotor speed where similar observations regarding the development of short-wave instabilities can be made as in previous cases. There is not clear patterns of short wave formations along the filaments at 6 & 8 rps whereas at 2 & 4 rps, the formation of the short-waves is clear just from the inception.

Wake contraction and xt diagram

Figure 4.36 shows the contraction and axial convection rates of the tip vortices from both rotors at 8 rps. Data representation is similar to that shown in Figure 4.10.Vortex trajectories given in the right plot of the figure are clear indications of long-wave instability modes between the vortices of each rotor where the adjacent vortices orbit around each other. Position data of vortex u1 shows the contraction-expansion-contraction behavior of the vortex at the interrotor space. As before, the upper rotor filaments travel downstream at higher rates than those from single and lower rotors.As in the case of spacer 5 and 6, the wake contraction ratio for the upper wake at the plane of the lower rotor is about 0.78 with an eventual wake contraction of about 0.66 in the far wake region beneath the lower rotor while lower rotor wake contracts to

about 90% of the rotor radius.

PIV

Figure 4.37 shows the corresponding PIV measurements at 8 rps where data representation is similar to those in Figure 4.11. The positions of the upper and lower rotors are marked in frame (d) in second row. As before, the orbiting of lower rotor vortices around one another is visible in PIV videos, too. Also, adjacent upper vortices shows signs of leapfrogging effect, albeit incomplete, before they interact with the lower rotor blades as discussed while talking about flow visualization images. In Appendix A, rest of the PIV results at this rotor spacing at 6, 4 & 2 rps are provided in Figures A.56, A.58, and A.60, respectively.

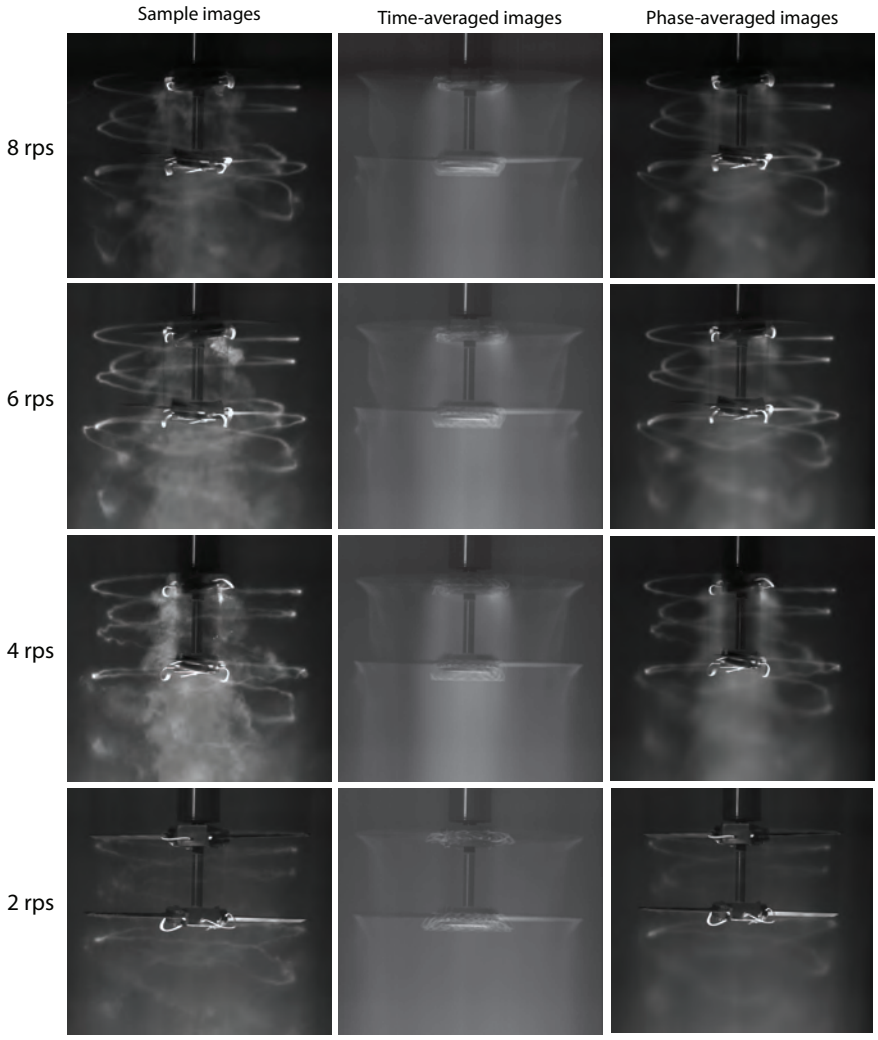

Figure 4.33: Two-bladed coaxial rotor (spacer6), $H/R = 0.75$: Flow visualization images at 8 rps (first row), 6 rps (second row), 4 rps (third row) & 2 rps (fourth row). Left column shows instantaneous flow images, the middle column shows the averaged flow fields, and the right column shows the phase-averaged images.

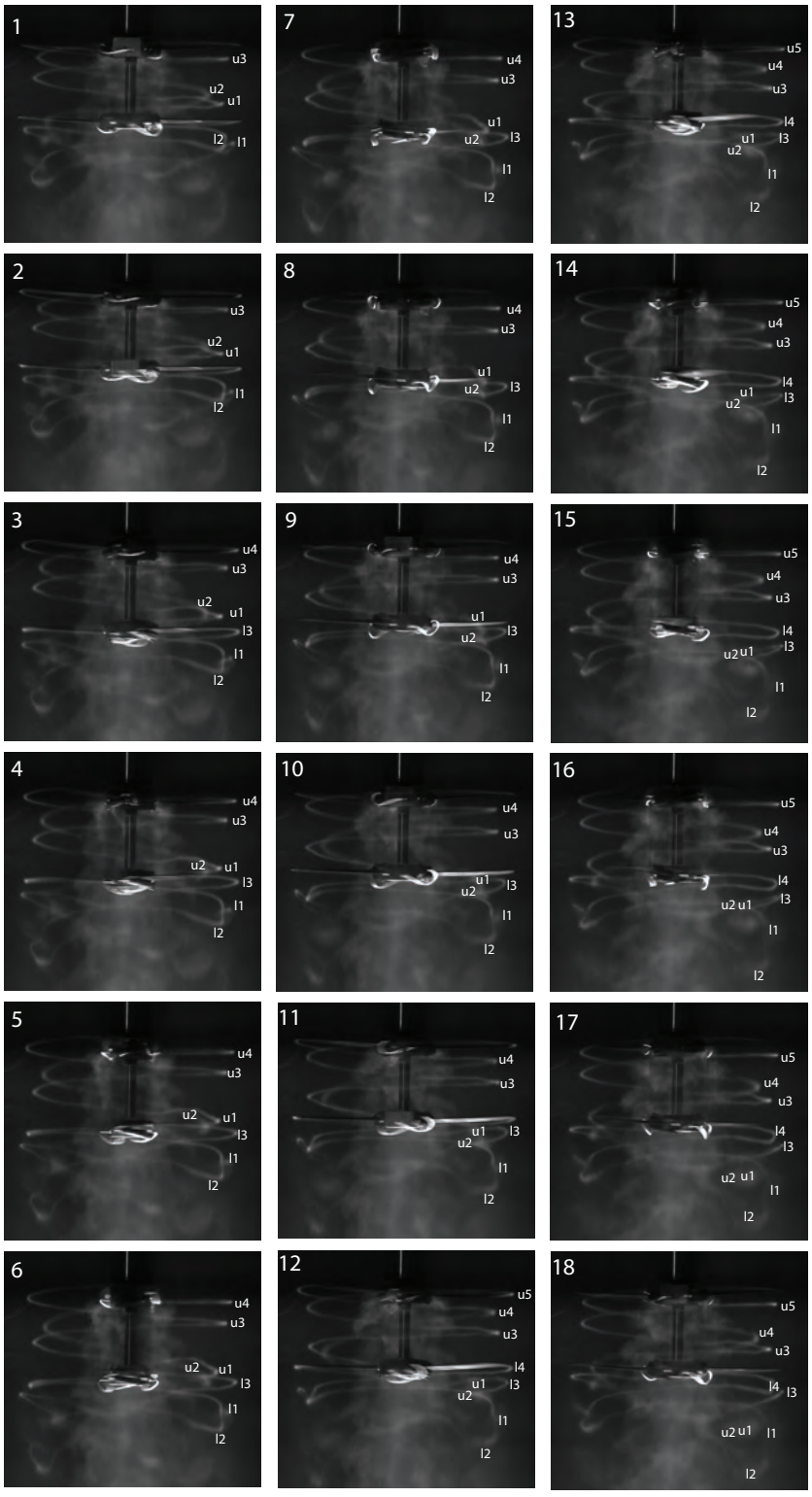

Figure 4.34: Vortex wake evolution of the coaxial rotors with axial spacing of H/R=0.75 during one complete rotor revolution at 8 rps. Images are 20° ($\pi/9$ rad) apart. Time separation between successive images is 6.94 ms. Adjacent vortices are labeled with odd and even numbers. The odd numbers are used to refer to successive vortices from one of the two blades while the even numbers are used to identify the successive vortices from the other blade.

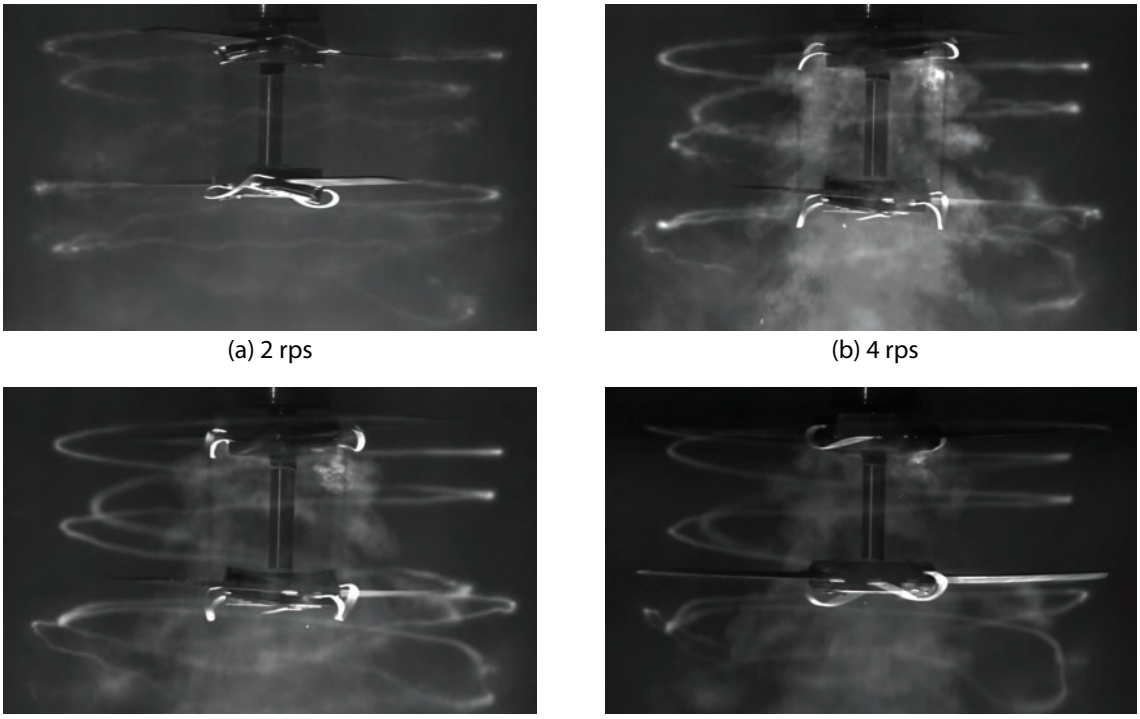

Figure 4.35: Sample flow images showing short-wave instabilities along the vortex filaments for all rotor speeds. Coaxial rotors are spaced at 75% of the rotor radius (Spacer 6).

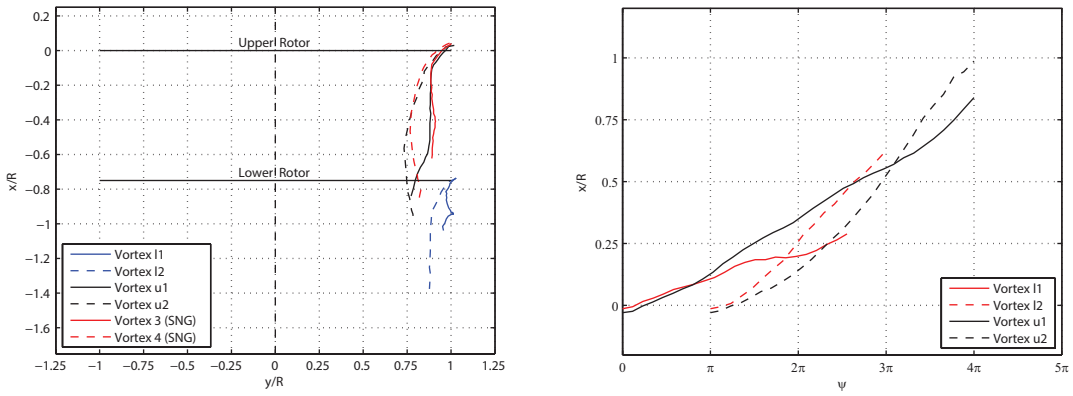

Figure 4.36: Trajectories of helical filaments trailed from coaxial rotor spaced at 75% of the rotor radius as well as those from the single rotor are shown. Right: spatial positions of tip vortices showing wake contraction. Left: xt diagram of the vortex filaments at 8 rps ($\psi = \Omega t$). Vortex labeling is similar to those in Figure 4.34

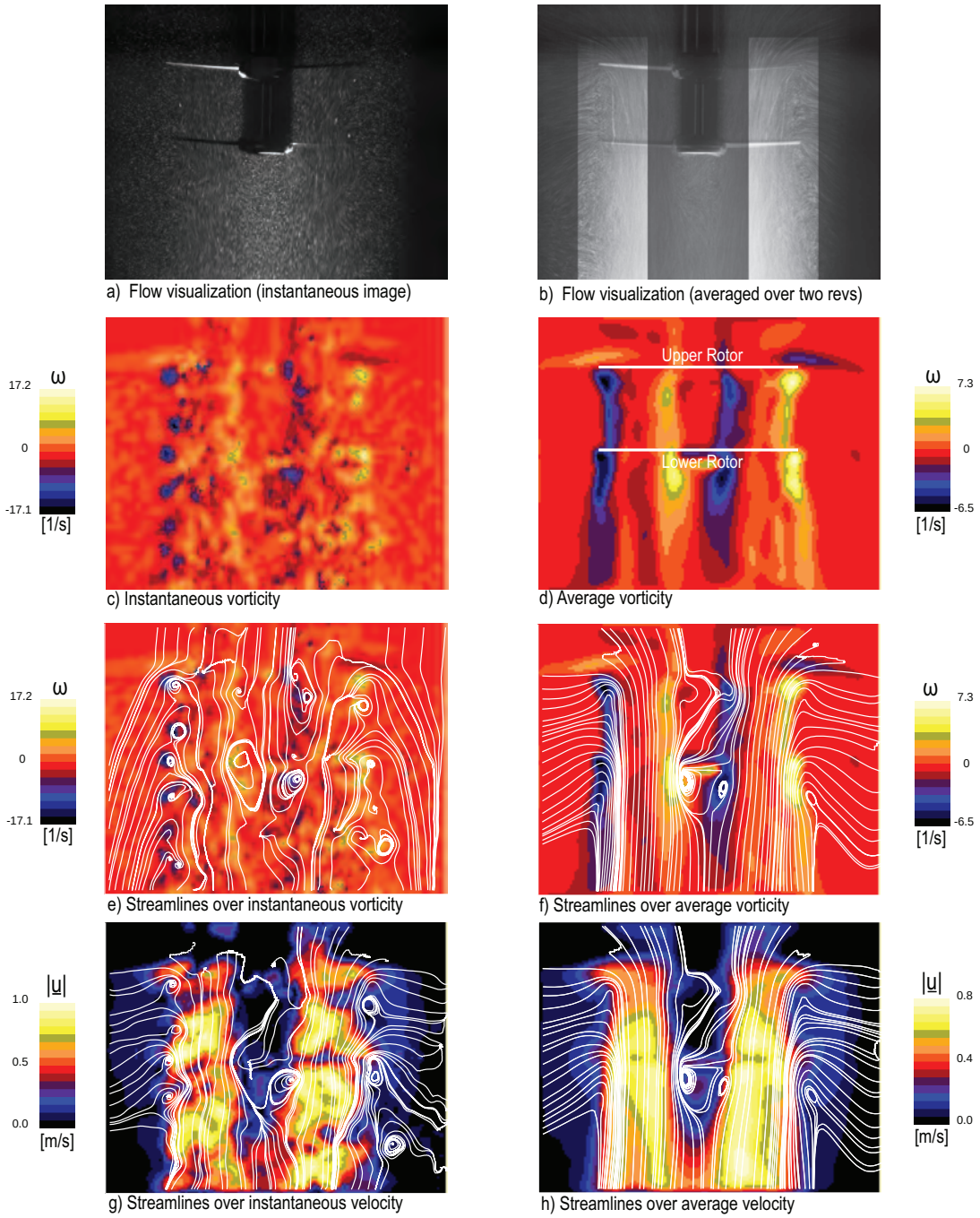

Figure 4.37: Flow field of a two-bladed coaxial rotor with rotor spacing of 75% of the rotor radius at $N = 8$ rps. First row (a,b): particle flow visualization. Average field in frame (b) is locally brightness- and contrast-enhanced to highlight the wake contraction of both rotors. In rows 2-4 are shown PIV measurements. Second row (c,d): vorticity fields. Third row (e,f): streamlines over vorticity. Fourth row (g,h): streamlines over speed. Streamlines in frame (e) are drawn from a moving reference frame and streamlines in frames (f-h) are drawn from a stationary reference frame.

4.10 Coaxial rotor with axial spacing of H/R=0.8

4.10.1 Flow images

Figure 4.38 shows the flow visualization images from the sets of experiments conducted at the rotor speeds of 2-8 rps which are indicated in Table 2.3 with the test numbers 25-28. The rotor spacing is set to 80% of the rotor radius (spacer 7), a 5%-increase from the preceding case where $H/R = 0.75$ (spacer 6). Data representation is similar to those in the previous cases. Time-averaged images show the contraction-expansion behavior of the upper rotor vortices as they orbit around each other during leapfrogging and while moving downstream. Subsequent expansion of the wake just above the lower disk is due to reversing of the roles between the vortices just before they are ingested by the lower rotor. Note also the difference in difference contraction rates of upper and lower rotor wakes. Instantaneous and phase-averaged flow images reveal that the wake beneath the lower rotor comprises of highly-deformed and interweaved vortex filaments, a pattern observed in all previous cases, albeit in different strength and extents, while the very stable helical filaments off upper rotor blades lay in the wake at the interrotor space. The tip vortex circulation-based Reynolds numbers at this rotor spacing are provided on the eight column of Table 4.1 along with their standard deviation and estimated to be about 8300 for 2 rps, 14400 for 4 rps, 33500 for 6 rps, and 33400 for 8 rps cases.

Figure 4.39 shows the coaxial rotor wake evolution during a complete rotor revolution at 8 rps. Data presentation and vortex labeling is done in a similar way as before. Sequential images in the figure reveal the similarity of the characteristics of the upper rotor vortices exhibit as in the preceding case where the rotor spacing is three quarter of rotor radius. Formation of hairpin-like vortex structures are underway as shown in image 18 (see vortex l2).

4.10.2 Vortex instabilities and wake geometry

Long-wave instability mode

As observed and reported in the preceding case, the interrotor spacings of about 75% of rotor radius and higher allows the upper rotor filaments to develop long-wave pairing instabilities between each other. The characteristics upper rotor filaments manifest during this long-wave pairing instability appears to very much akin to that observed in the preceding case where $H/R = 0.75$. This process can be tracked from the successive images 1-10 as shown in Figure 4.39 between the vortices u1 and u2. In both cases of spacer 6 and 7, first leapfrogging between the upper filaments at the inter-rotor space is completed in the vicinity of the lower rotor, after which the filaments are seen to attempt to reverse their roles. The turns of the lower vortex l2 develops long-wave pairing instability mode between its neighboring portions of its each turn just from its inception in which the adjacent portions start to spiral around one another as clearly seen in all the instantaneous flow images (2-8 rps) in Fig.4.39 as well as in images of Figure 4.39. This is followed by leapfrogging of this lower vortex l2 through lower vortex l1 in a similar mechanism to previous cases. During the course of this process, lower vortex l2 undergoes deformation from its orderly helical shape near the tip regions. It becomes elongated near the end of its cross sectional area, forming a hairpin-like vortex structure, the evolution of which can be tracked from the successive images 1-18 in Fig. 4.39. Formation of this hairpin-like vortex from the orderly helical filament of the lower rotor follows a similar process as seen before. Lateral separation between the legs of this newly elongated vortex is larger on the left half of the images in the figure than that on the right half of the images, which is best seen in image 10 of the same figure. By the time lower filament l2 passes the backward portion of the turn of the lower filament l1, the latter has already deformed and become very diffuse (see image 13-14). As before, upper rotor filaments

maintain a very stable nature until they reach the plane of the lower rotor whereas those from the lower rotor tend to become extremely unstable after a very short time elapsed following their generation. In Appendix A, rest of the evolution images of vortex wake at the same rotor spacing during one complete rotor revolution at 6, 4 & 2 rps are provided in Figures A.61, A.63, and A.65, respectively.

Short-wave instabilities

Phase-averaged images of 2 & 4 rps cases in Figure 4.38 is clear manifestation of the short-wave instability pattern developed by the vortex filaments at these speeds, particular those from the upper rotor. Also, Figure 4.40 presents sample frames at each rotor speed where similar characteristics are seen regarding the development of short-wave instabilities as seen in all the previous cases discussed. At 2 & 4 rps, vortices beneath the lower rotor cannot be tracked after the first revolution, which further makes it difficult to track the development of these short-waves. Throughout the runs at 6 & 8 rps, the short waves form along the filaments which are elongated in the streamwise direction as marked with white arrows in Figure 4.40.

Wake contraction and xt diagram

Figure 4.41 shows the contraction and axial convection rates of the tip vortices from both rotors at 8 rps. Data representation is similar to that shown in Figure 4.10. Similar characteristics seem to be at play regarding the axial convection rates of the vortices as in the case of spacer 6 where the rotor separation is three quarter of the radius. Position data of vortex u2 reveals its contraction-expansion behavior clearly. It starts to expand at the same time when the vortex u1 starts to contract in an attempt to reverse their roles following their completion of first leapfrogging. From the average images in Figure 4.38, the wake contraction ratio for the upper wake at the plane of the lower rotor is estimated to be about 0.70, a markedly smaller value than those at smaller rotor spacings. Adjacent vortices of the lower rotor contracts to about 75% and 95% of the rotor radius. This difference in the contraction of the lower rotor vortices is obvious in flow images (see vortices l1 and l2 in Figure 4.39).

PIV

Figure 4.42 shows the corresponding PIV measurements at 8 rps where data representation is similar to those in Figure 4.11. The positions of the upper and lower rotors are marked in frame (d) in second row. Similar characteristics are at play regarding the behavior of vortices as in the previous case of spacer 6. Intricate nature of the wake beneath the lower rotor is seen in frame (c). Streamlines are assuming a more straight profile as shown in frames (f) & (h). In Appendix A, rest of the PIV results at this rotor spacing at 6, 4 & 2 rps are provided in Figures A.62, A.64, and A.66, respectively.

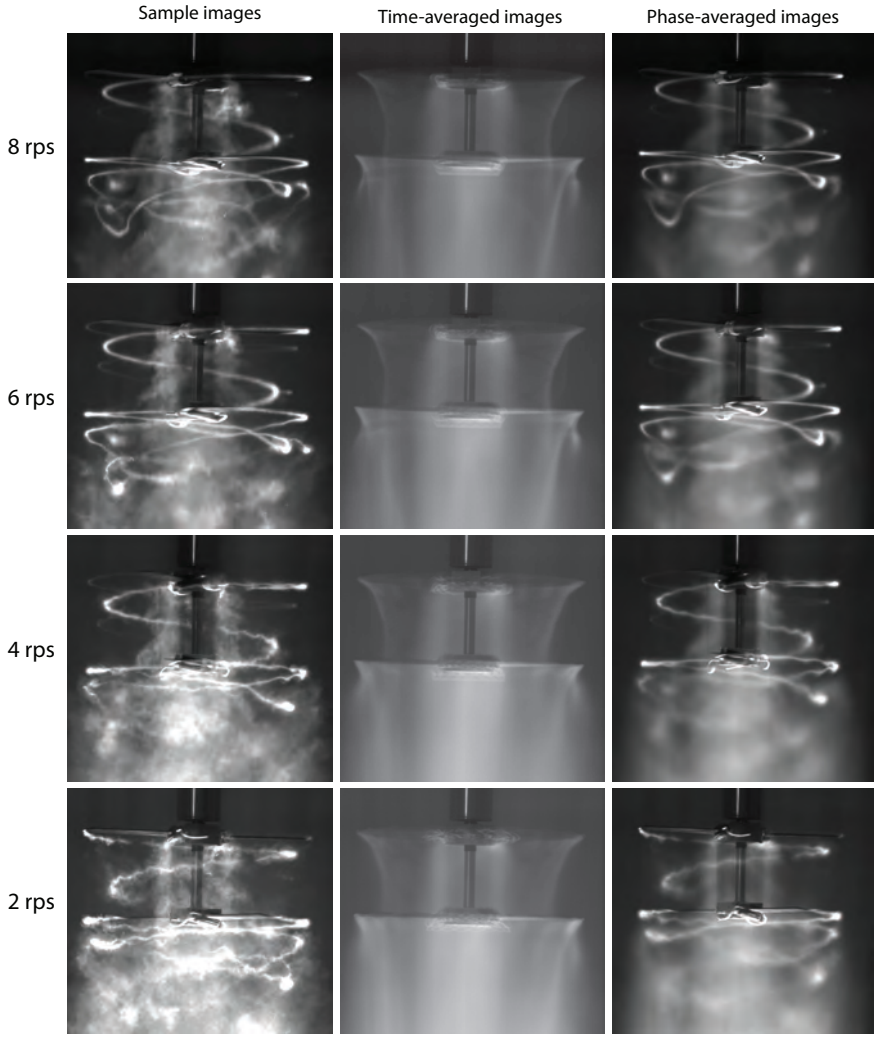

Figure 4.38: Two-bladed coaxial rotor (spacer7), $H/R = 0.8$: Flow visualization images at 8 rps (first row), 6 rps (second row), 4 rps (third row) & 2 rps (fourth row). Left column shows instantaneous flow images, the middle column shows the averaged flow fields, and the right column shows the phase-averaged images.

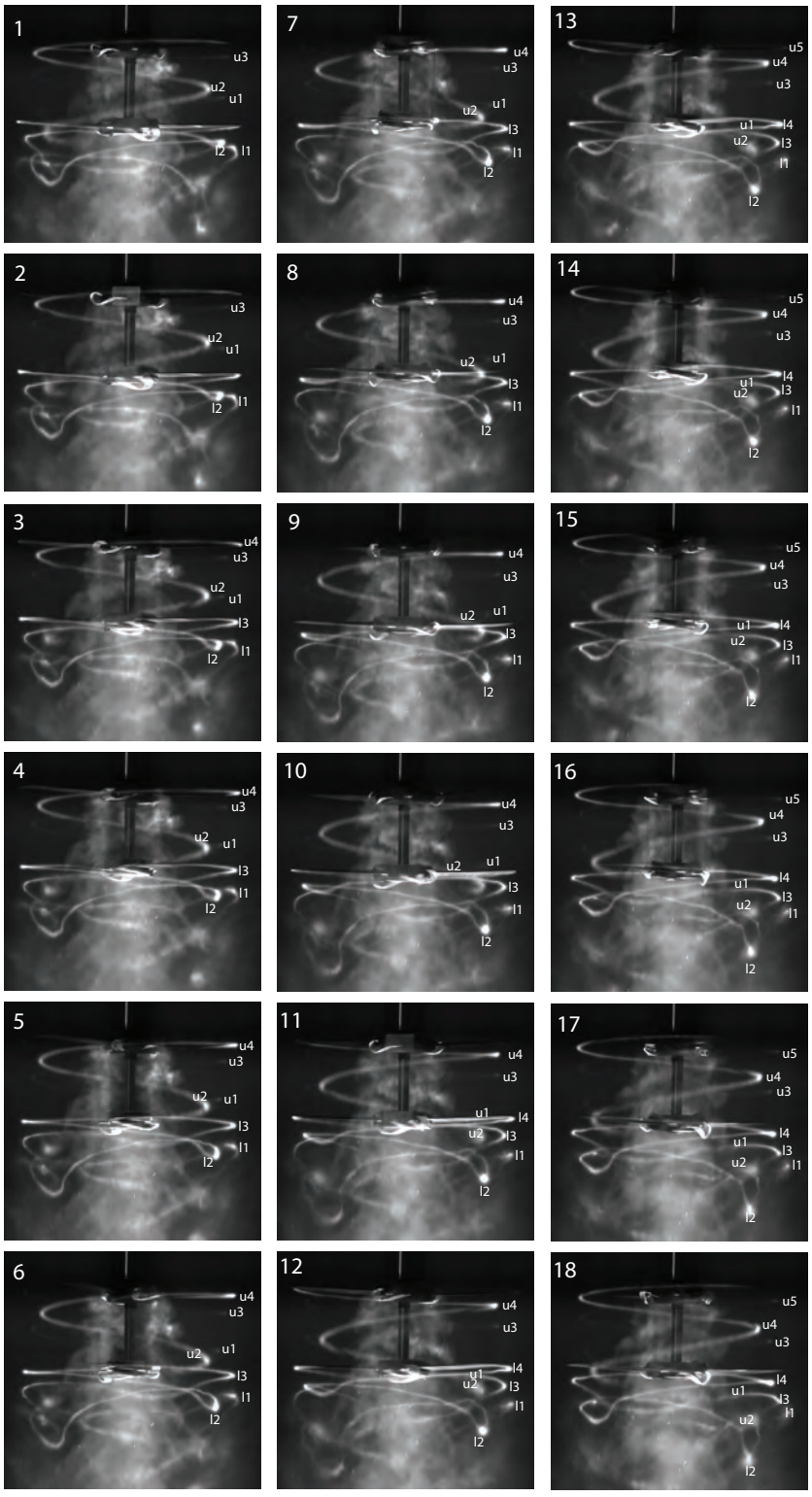

Figure 4.39: Vortex wake evolution of the coaxial rotors with axial spacing of H/R=0.8 during one complete rotor revolution at 8 rps. Images are 20° ($\pi/9$ rad) apart. Time separation between successive images is 6.94 ms. Adjacent vortices are labeled with odd and even numbers. The odd numbers are used to refer to successive vortices from one of the two blades while the even numbers are used to identify the successive vortices from the other blade.

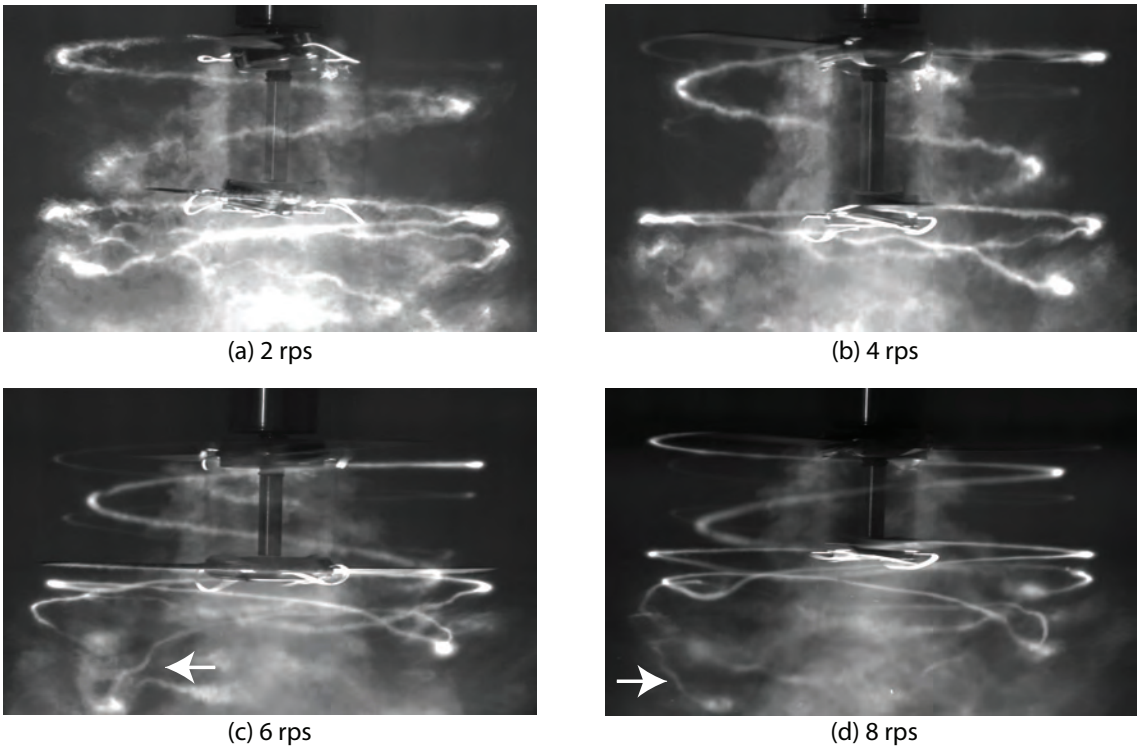

Figure 4.40: Sample flow images showing short-wave instabilities along the vortex filaments for all rotor speeds. Coaxial rotors are spaced at 80% of the rotor radius (Spacer 7).

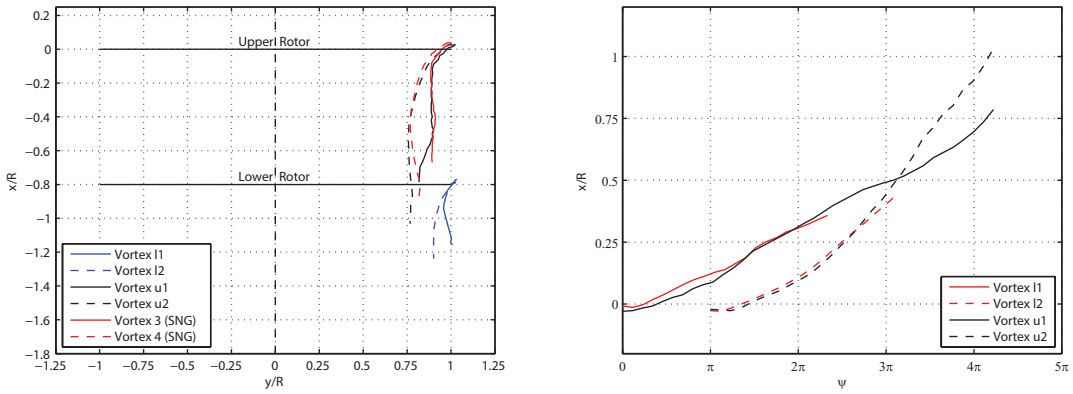

Figure 4.41: Trajectories of helical filaments trailed from coaxial rotor spaced at 80% of the rotor radius as well as those from the single rotor are shown. Right: spatial positions of tip vortices showing wake contraction. Left: xt diagram of the vortex filaments at 8 rps ($\psi = \Omega t$). Vortex labeling is similar to those in Figure 4.39

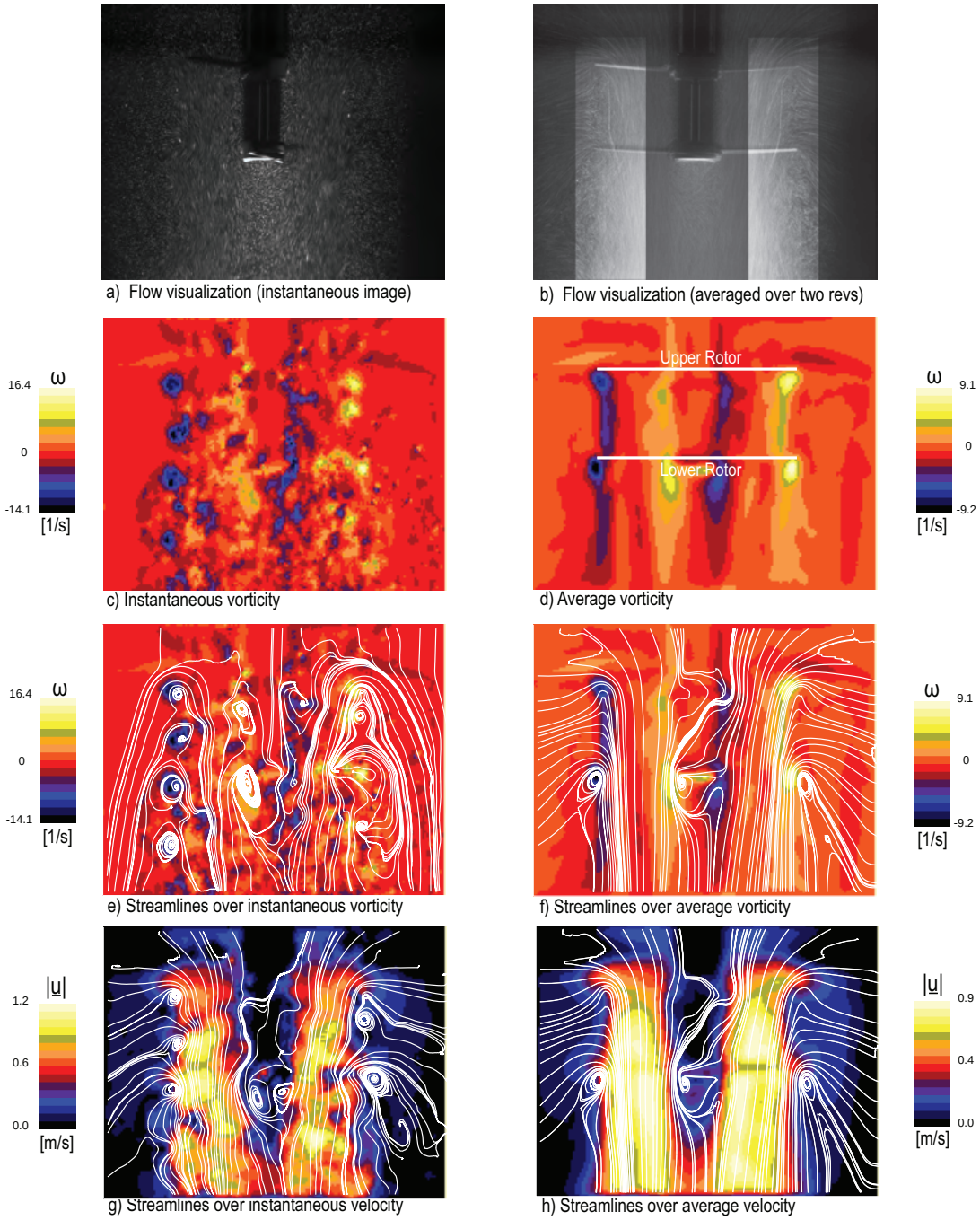

Figure 4.42: Flow field of a two-bladed coaxial rotor with rotor spacing of 80% of the rotor radius at $N = 8$ rps. First row (a,b): particle flow visualization. Average field in frame (b) is locally brightness- and contrast-enhanced to highlight the wake contraction of both rotors. In rows 2-4 are shown PIV measurements. Second row (c,d): vorticity fields. Third row (e,f): streamlines over vorticity. Fourth row (g,h): streamlines over speed. Streamlines in frame (e) are drawn from a moving reference frame and streamlines in frames (f-h) are drawn from a stationary reference frame.

4.11 Coaxial rotor with axial spacing of H/R=0.875

4.11.1 Flow images

Figure 4.43 shows, with a similar data representation as before, the flow visualization images from the sets of experiments conducted at the rotor speeds of 2-8 rps which are indicated in Table 2.3 with the test numbers 29-32. The coaxial rotors are spaced at 87.5% of the rotor radius (spacer 8). The rotors are widely separated from each other. The sample images of 6 and 8 rps cases reveal the extreme strain experienced by the lower filament which is evident on the bottom left parts of the images. The filament appears to continue to deform downstream even after it is out of the camera angle. The tip vortex circulation-based Reynolds numbers at this rotor spacing are provided on the ninth column of Table 4.1 along with their standard deviation and estimated to be about 8400 for 2 rps, 15300 for 4 rps, 33600 for 6 rps, and 27500 for 8 rps cases. Time-averaged images suggest similar behaviors of the rotor wakes as in spacer 7 case where the axial separation is 80% percent.

Figure 4.44 shows the wake vortex evolution of the coaxial rotor of the same axial separation during two complete rotor revolutions, in which the vortices are marked as before. At the bottom left corners of images 1-10 can be tracked the evolution of extreme deformation the lower filament is experiencing just as shown in Figure 4.43.

4.11.2 Vortex instabilities and wake geometry

Long-wave instability mode

The helical tip vortex filaments trailed from the upper rotor exhibit long-wave pairing instability characteristics where trailing upper filament leapfrogs through the leading upper filament similar to before in the cases where the rotor separation is at least 75% of the rotor radius. This leapfrogging effect is only repeated once although the role of the filaments appears to be reversed there is not enough space between the rotors for the leading upper filament to leapfrog through the trailing upper filament. This is evident in images in Figure 4.44. Image 1 of the figure shows when upper vortex u1 passed through the upper vortex u2. Image 19 also shows the same process where the vortex u4 is seen to have leapfrogged through the vortex u3, trailed successive to vortex u2 and u1, respectively. Finally, image 36 of the same figure shows the passing of vortex u6 through u5, which clearly indicates the persistent behavior of upper rotor filaments in every rotor revolution. As observed and reported in all the previous cases, subsequent to passing through the lower rotor and interaction with its blades, the upper rotor filaments become extremely diffuse and their subsequent locations become difficult to track. However, they can be individually tracked easily at the interrotor space until they reach the vicinity of the lower disk. Basically, for this widely-spaced coaxial rotor, the effects of the lower rotor on the upper rotor can be considered to be diminished, albeit not completely, since there is ample space between the rotors to develop mutual interactions similar to what is seen in single rotor experiments.

Unlike upper rotor filaments, which maintain their orderly helical shapes and appear to be very stable before they are ingested by the lower rotors, each filament that comes off the each blade of the lower rotor becomes unstable quickly by undergoing strong deformations and losing their orderly helical shapes within the first rotor revolution. The lower rotor filaments exhibit long-wave pairing instability characteristics both between the adjacent portions of one complete helix turn of the either filaments (intrafilaments), which is not observed on upper rotor filaments of this particular spacing as well as the previous ones, and between different filaments (interfilaments). Adjacent portions of the lower helix l4 start to orbit around each other

within first rotor revolution, the development of which can be tracked in Fig. 4.44 starting from image 6. Subsequent to orbiting, the backward portion of first turn of this vortex l4 travels downstream at a faster rate than that of the forward portion as clearly seen in these images. The lower rotor filaments appear to exhibit leapfrogging effect although it significantly differs from that of the upper filaments in the way that the adjacent portions of both lower filaments travel at different speeds which results in extreme straining and subsequent unusual shapes attained by them in the far wake region. The lower filament l3 experiences extreme strain during these strong interactions with the lower filament l2 such that the forward portion of second (or succeeding) helix turn, one revolution later, passes the backward portion of the first (or preceding) helix turn, one revolution earlier, as seen in image 12 (on lower left side) in the evolution figure. In Appendix A, rest of the evolution images of vortex wake at the same rotor spacing during one complete rotor revolution at 6, 4 & 2 rps are provided in Figures A.67, A.69, and A.71, respectively.

Short-wave instabilities

Figure 4.45 presents sample frames at each rotor speed where the development of short-wave instabilities is clear. At 4 rps in frame (b), development of short-wave instabilities is seen just from the beginning, which grow in amplitude as the filaments approach the plane of the lower rotor. At 6 & 8 rps, the short waves form along the filaments which undergo deformation and are marked with white arrows in Figure 4.40. Short-wave instabilities at these speeds become superimposed with the long-wave instability mode shortly.

Wake contraction and xt diagram

Figure 4.41 shows the contraction and axial convection rates of the tip vortices from both rotors at 8 rps. Data representation is similar to that shown in Figure 4.10. Vortices from the upper rotor exhibit very similar characteristics regarding long-wave instability mode, axial convection and radial contraction rates as observed when the rotors are spaced at 80% of the rotor radius. As before, the lower rotor wake contraction is markedly higher than those when upper rotor is operated both in tandem and in isolation.

PIV

Figure 4.47 shows the corresponding PIV measurements at 8 rps where data representation is similar to those in Figure 4.11. The positions of the upper and lower rotors are marked in frame (d) in second row. As seen in frame (c) lower rotor vortices can only be tracked in a small distance beneath the rotor as well as upper rotor vortices after their interaction with the blades. Also, note the obvious expansion in the lower rotor wake as sen in frame (d) of the figure along with in the streamline patterns in frame (h). In Appendix A, rest of the PIV results at this rotor spacing at 6, 4 & 2 rps are provided in Figures A.68, A.70, and A.72, respectively.

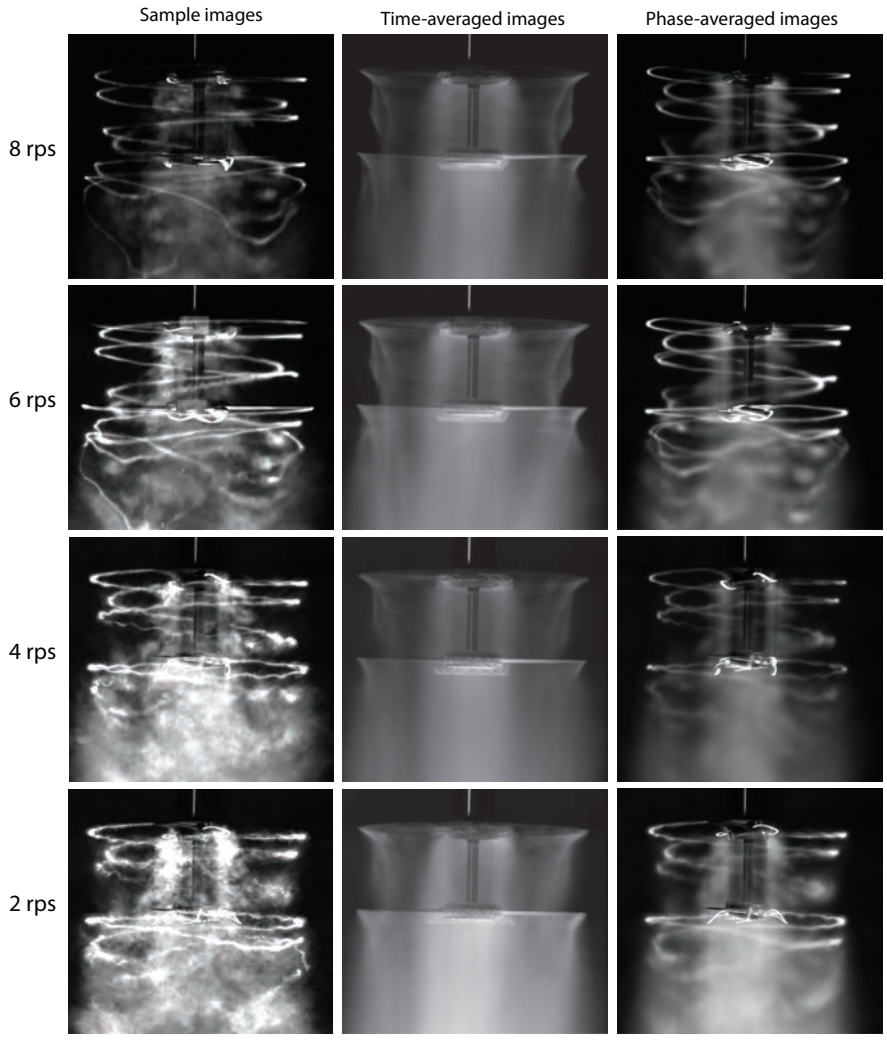

Figure 4.43: Two-bladed coaxial rotor (spacer8), $H/R = 0.875$: Flow visualization images at 8 rps (first row), 6 rps (second row), 4 rps (third row) & 2 rps (fourth row). Left column shows instantaneous flow images, the middle column shows the averaged flow fields, and the right column shows the phase-averaged images.

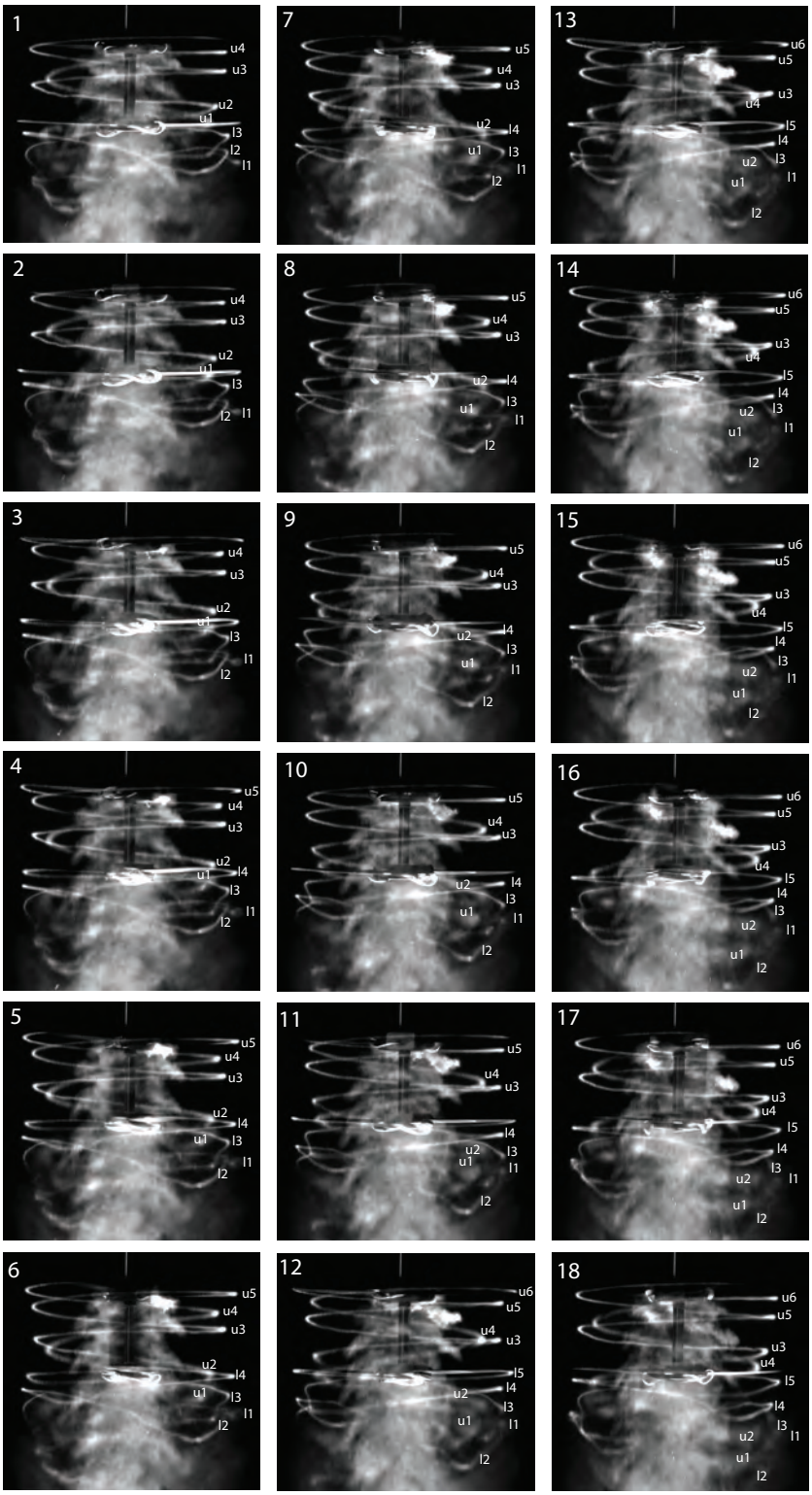

Figure 4.44: The first of two revolutions where the vortex wake evolution of the coaxial rotors with axial spacing of H/R=0.875 during two complete rotor revolutions at 8 rps. Images are 20° ($\pi/9$ rad) apart. Time separation between successive images is 6.94 ms. Adjacent vortices are labeled with odd and even numbers. The odd numbers are used to refer to successive vortices from one of the two blades while the even numbers are used to identify the successive vortices from the other blade.

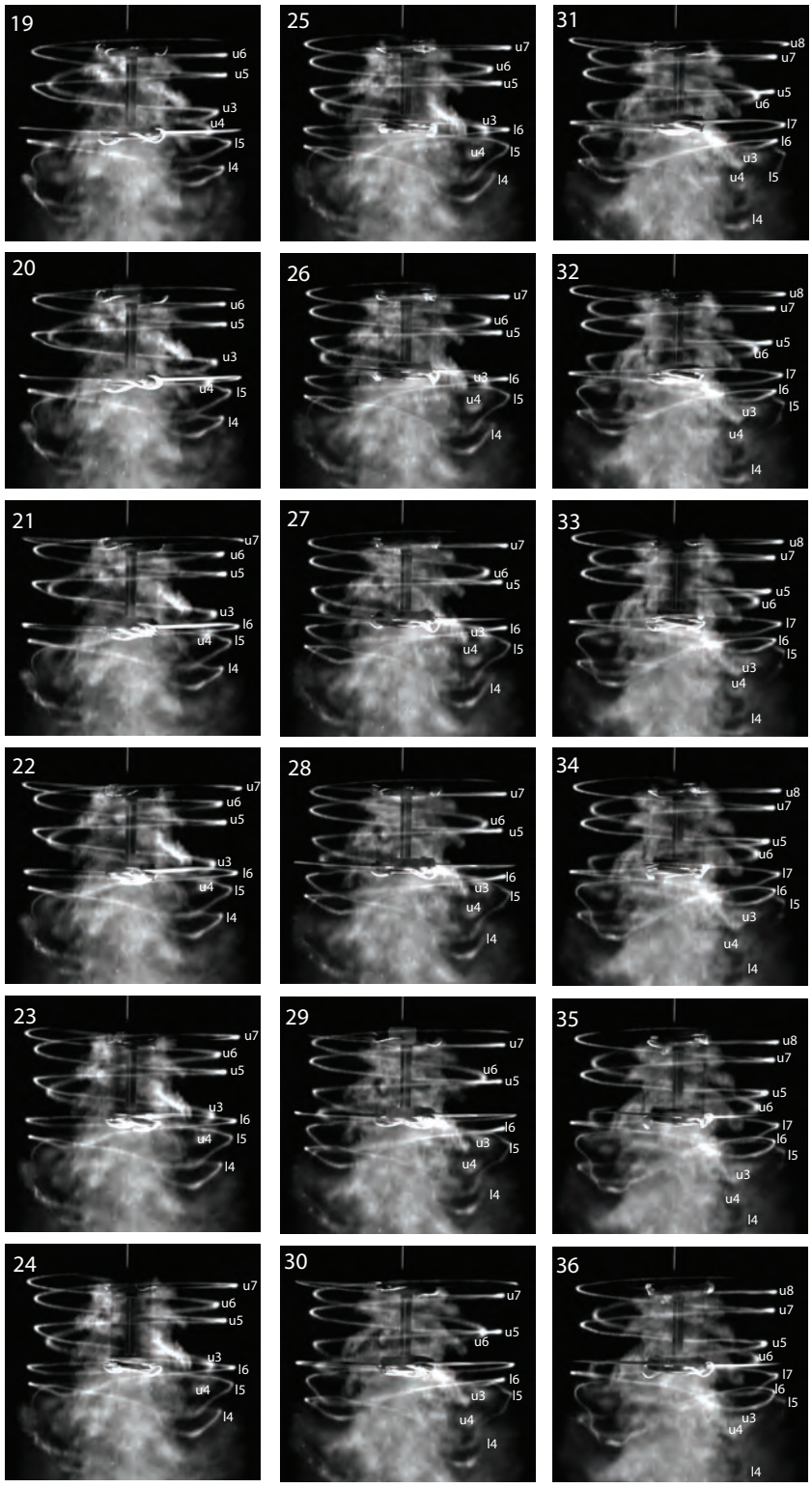

Figure 4.44: The second of two revolutions where the vortex wake evolution of the coaxial rotors with axial spacing of H/R=0.875 during two complete rotor revolutions at 8 rps. Images are 20° ($\pi/9$ rad) apart. Time separation between successive images is 6.94 ms. Adjacent vortices are labeled with odd and even numbers. The odd numbers are used to refer to successive vortices from one of the two blades while the even numbers are used to identify the successive vortices from the other blade.

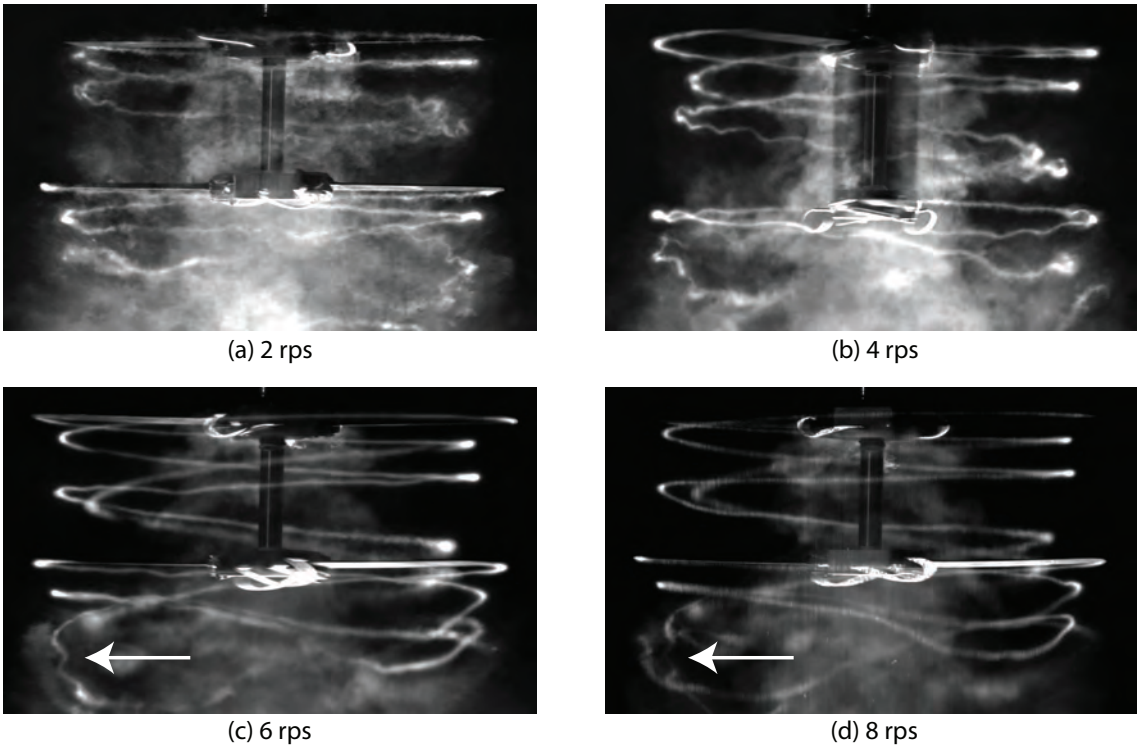

Figure 4.45: Sample flow images showing short-wave instabilities along the vortex filaments for all rotor speeds. Coaxial rotors are spaced at 87.5% of the rotor radius (Spacer 8).

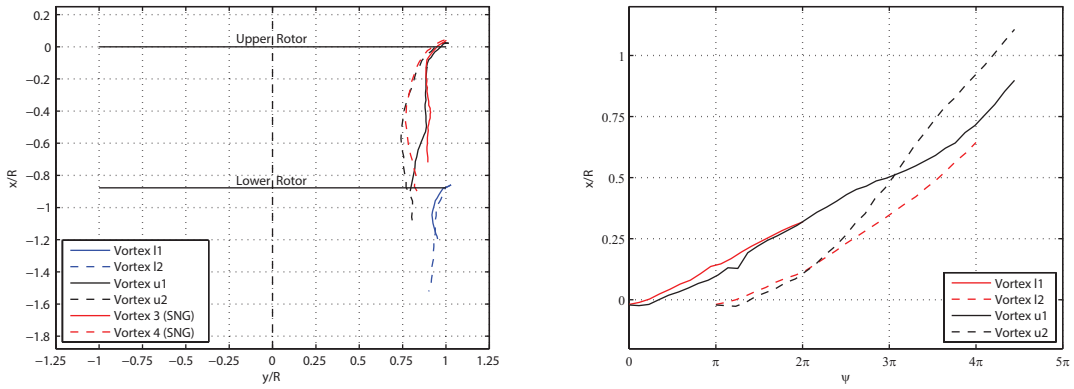

Figure 4.46: Trajectories of helical filaments trailed from coaxial rotor spaced at 87.5% of the rotor radius as well as those from the single rotor are shown. Right: spatial positions of tip vortices showing wake contraction. Left: xt diagram of the vortex filaments at 8 rps ($\psi = \Omega t$). Vortex labeling is similar to those in Figure 4.44

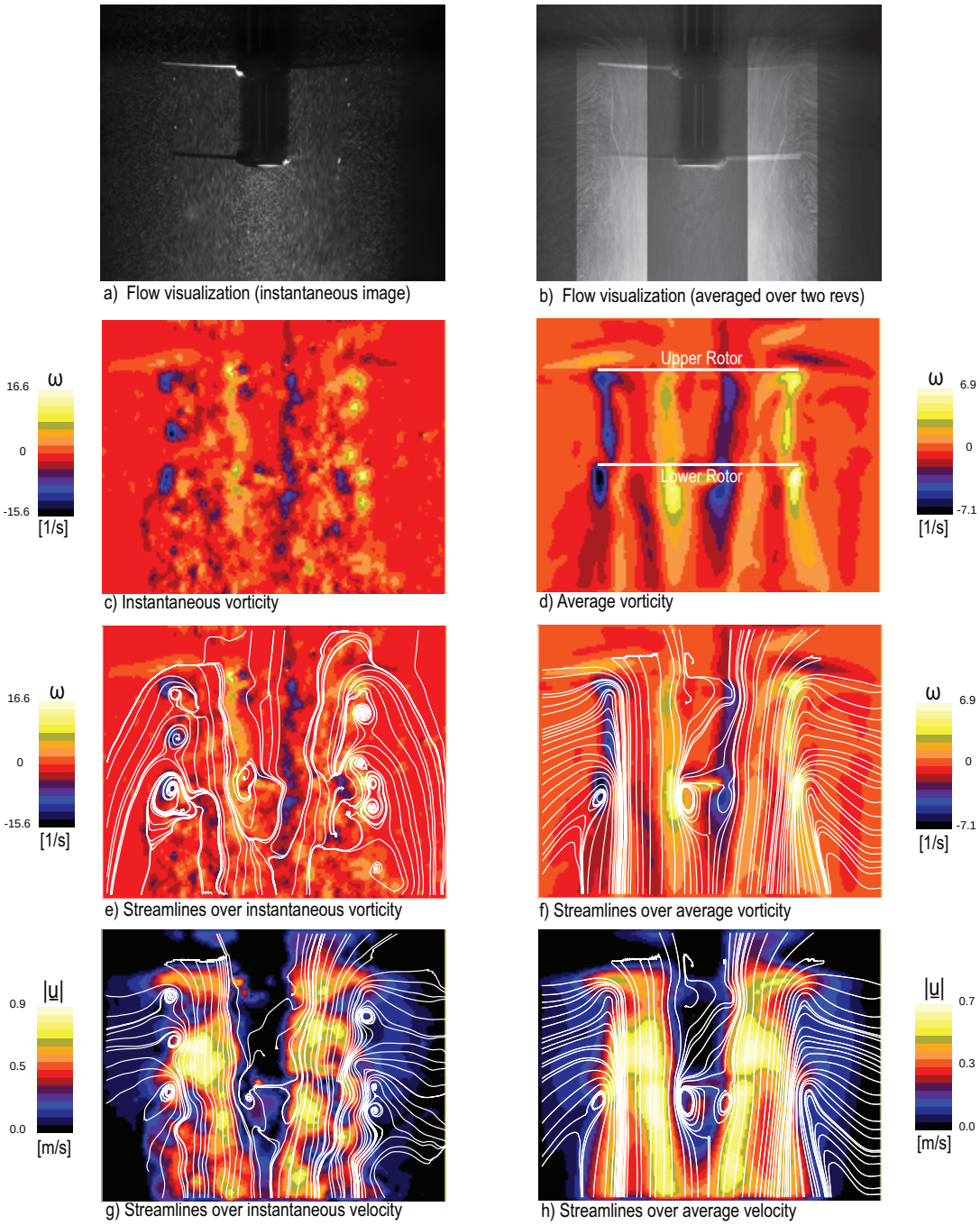

Figure 4.47: Flow field of a two-bladed coaxial rotor with rotor spacing of 87.5% of the rotor radius at $N = 8$ rps. First row (a,b): particle flow visualization. Average field in frame (b) is locally brightness- and contrast-enhanced to highlight the wake contraction of both rotors. In rows 2-4 are shown PIV measurements. Second row (c,d): vorticity fields. Third row (e,f): streamlines over vorticity. Fourth row (g,h): streamlines over speed. Streamlines in frame (e) are drawn from a moving reference frame and streamlines in frames (f-h) are drawn from a stationary reference frame.

4.12 Coaxial rotor with axial spacing of H/R=1.0

4.12.1 Flow images

Figure 4.48 shows the flow visualization images from the sets of experiments conducted at the rotor speeds of 2-8 rps which are indicated in Table 2.3 with the test numbers 33-36. The axial separation distance between the coaxial rotors was set to a rotor radius (spacer 9). Comparison of the characteristics of the upper rotor wake at this separation distance with the previously discussed cases where rotor spacings are $H/R \leq 0.875$ reveals that the flow pattern at the interrotor space repeats itself in every two revolutions. This feature is manifest in the phase-averaged flow images as seen in Figure 4.48 for rotor rotational speeds of 6 and 8 rps. However, the flow pattern at 2 and 4 rps cases appear to repeat itself in every rotor revolution. These characteristics are very akin to those observed during single rotor tests, which is discussed at the beginning of this chapter. The lower rotor filaments exhibit significantly distinct characteristics during each revolution of the two-revolution period while the upper rotor filaments behave in slightly different ways during the same time period, which will be discussed in due course. The tip vortex circulation-based Reynolds numbers at this rotor spacing are provided on the tenth column of Table 4.1 along with their standard deviation and estimated to be about 8500 for 2 rps, 15800 for 4 rps, 27500 for 6 rps, and 29200 for 8 rps cases.

Figure 4.49 provides the vortex wake evolution of coaxial rotors spaced at one rotor radius during two complete rotor revolutions. Vortex labeling and image representation are similar to previous cases. The comparison of the evolution images at the same rotor azimuth (e.g. compare image 1 and 19, 2 and 20 etc. in Figure 4.49) also reveals two-rev periodicity of the flow pattern both beneath and above the lower rotor. Image 10 in the figure reveals the intricate nature of the wake beneath the lower rotor where the vortex filaments have become interweaved. No clear formation of new vortex structures are observed as opposed to some of the previous rotor spacings (see spacer 5 case, $H/R = 0.5$, for example).

4.12.2 Vortex instabilities and wake geometry

Long-wave instability mode

Similar to spacer 6, 7 & 8 cases where the rotor spacing is $0.75 \leq H/R \leq 0.875$, the upper rotor filaments develop long-wave pairing instabilities. Although the instability mechanism occurs in a similar way to previously discussed cases, it differs in its period, the time it takes the pattern to repeat itself, and the interaction between the adjacent portions of the upper filaments. The period is two rotor revolutions for the coaxial rotors spaced at a rotor radius. During first rotor revolution the images of which are shown in the first part of the Figure 4.49 (images 1-18), the upper filament u2 leapfrogs through upper filament u1 just as observed in the previous three cases. The vortex u2 gathers more speed, shrinks in size and passes through the vortex u1 which in turn slows down and expands in size, during which the neighboring portions of the turn of the helices do not develop any noticeable interactions between each other. During the second rotor revolution the images of which are shown in the second part of the Figure 4.49 (images 19-36), the successive vortex u4 still leapfrogs through the successive vortex u3, albeit at farther downstream location compared to one revolution earlier. Note the locations of the vortices u1 & u2 and u3 & u4 in image 1 and 19, respectively, which is indicative of these different flow patterns in successive rotor revolutions. In image 1, the vortex u2 is seen to have passed through the vortex u1 while image 19 shows as the vortex u4 is about go through the vortex u3. Another difference in flow pattern in successive rotor revolutions is that the adjacent portions of the turn of the upper vortex u3 start to orbit around each other as upper vortex u4 passes through the former during the second rotor revolution, which is in progress in image 36. This image 36 also shows the vortex u6 after it has passed through the vortex u5 similar to vortices u2 & u1 in image

1. Also, during this second revolution of two-rev period, the upper vortex u4 experiences deformation and becomes elongated just above the lower disk after it has passed through the upper vortex u3. This occurred following to the orbiting of the adjacent portions of the upper filament 3 around each other.

Lower rotor filaments exhibit two-revolution periodicity as the upper rotor filaments do. Although the lower filaments from the previous case where $H/R = 0.875$ appear to have two-rev periodicity for the flow pattern to repeat itself, in each revolution either filament behaves in similar ways as explained in detail in discussion therein but the flow pattern differs to the extent the lower filaments deform during first and second revolutions. For this case, however, the lower rotor filaments exhibit the same exact pattern in every two revolutions and they significantly have different characteristics between two consecutive rotor revolutions. This is manifest in the phase-averaged images given in Figure 4.48 however only for 6 and 8 rps cases. The flow pattern repeats itself in every revolution for the rotor speeds of 2 and 4 rps similar to that of upper rotor filaments. The lower filaments develop long-wave pairing instabilities shortly after their formation within first rotor revolution. Also, the lower filament l1 develops mutual interactions by orbiting of its adjacent portions of the helix turn around each other, which is readily seen in images 1-5 in the figure. While the lower filament l1 undergoes this process, the lower filament l2 attempt to leapfrog through the former in a very short time following its formation and its neighboring portions start to spiral around each other. During this process two vortices contact each other which result in immediate destruction and diffusion of the vortices. This process takes less than a rotor revolution to complete from the inception of the lower filament l2 and can be seen in images 1-10 in its entirety. During the second revolution of this two-rev period. the lower filament l3 exhibits a characteristic that resembles the role of the trailing vortex during a leapfrogging process, where it quickly contracts radially inward more than the other three filaments during two-rev period and its speed increases at the same time. However, the two filaments from the previous revolution has already developed long-wave instability mode and contacted each other, resulting in their immediate destruction and diffusion. This lower filament l3 then starts to orbit around itself and becomes elongated near the wake boundaries. Lower filament l4 experiences strong deformation and becomes elongated in the same way as seen in image 36 in Figure 4.49. In Appendix A, rest of the evolution images of vortex wake at the same rotor spacing during one complete rotor revolution at 6, 4 & 2 rps are provided in Figures A.73, A.75, and A.77, respectively.

Short-wave instabilities

Figure 4.50 presents sample frames at each rotor to reflect short-wave instability characteristics. In frame (b) of 4 rps, the short-waves are clearly visible. At both 6 & 8 rps, the vortex filaments appear to develop a short-wave shortly after their formation as opposed to previous cases. From an assessment of all flow images, rotor spacing can be considered to be of little importance in terms of short-wave instability characteristics. Instead,

Wake contraction and xt diagram

Figure 4.51 shows the contraction and axial convection rates of the tip vortices from both rotors at 8 rps. Trajectories of adjacent vortices from the upper rotor during two consecutive revolutions are plotted both when the upper rotor is operated in isolation (single rotor) and in tandem (coaxial rotor). xt diagram given in the right part of the figure clearly shows that the vortex pair u3 and u4 starts to orbit around each other earlier than the vortex pair u1 and u2 similar to what is observed during the rotor is operated in isolation, which is shown in Figure 4.5. Note also the similarity of wake contractions at these two cases. Upper rotor wake contraction ratio is about 0.9 (vortex u3) at the plane of the lower rotor, which is markedly higher than those found in previous cases. Vortex u1 and u2 appear to contract to 75% of the rotor radius at the same location. Lower rotor wake contraction ratios are 0.88 and 0.95 during two consecutive revolutions, which can be seen in time-averaged images in Figure 4.48.

PIV

Figure 4.52 shows the corresponding PIV measurements at 8 rps where data representation is similar to those in Figure 4.11. The positions of the upper and lower rotors are marked in frame (d) in second row. Average particle flow visualization data given in frame (b) shows the interaction between the adjacent vortices that come off the upper rotor. The average vorticity plot shows numerous vorticity ridges. The average velocity marks the wake and its growth. The average streamline pattern of the fluid ingested into the rotors show that the slipstream of the upper rotor has vanishing curvature as it is intercepted by the lower rotor. In Appendix A, rest of the PIV results at this rotor spacing at 6, 4 & 2 rps are provided in Figures A.74, A.76, and A.78, respectively.

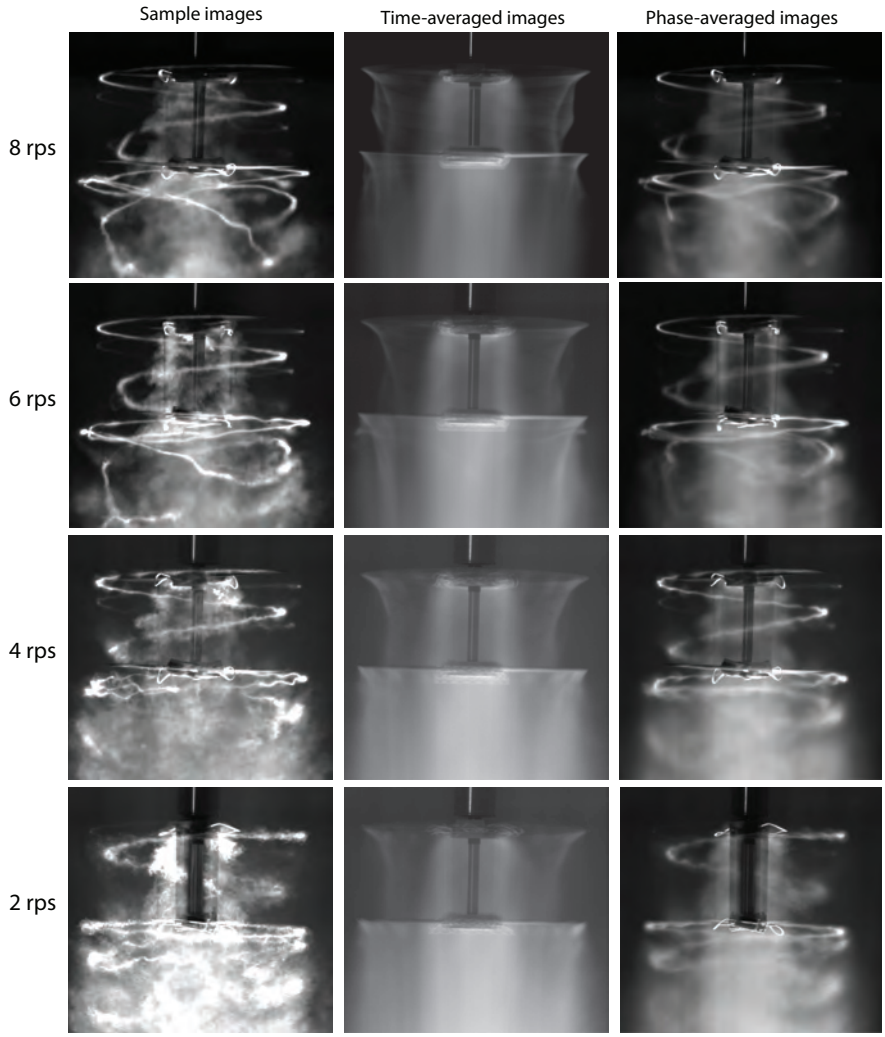

Figure 4.48: Two-bladed coaxial rotor (spacer9), $H/R = 1.0$: Flow visualization images at 8 rps (first row), 6 rps (second row), 4 rps (third row) & 2 rps (fourth row). Left column shows instantaneous flow images, the middle column shows the averaged flow fields, and the right column shows the phase-averaged images.

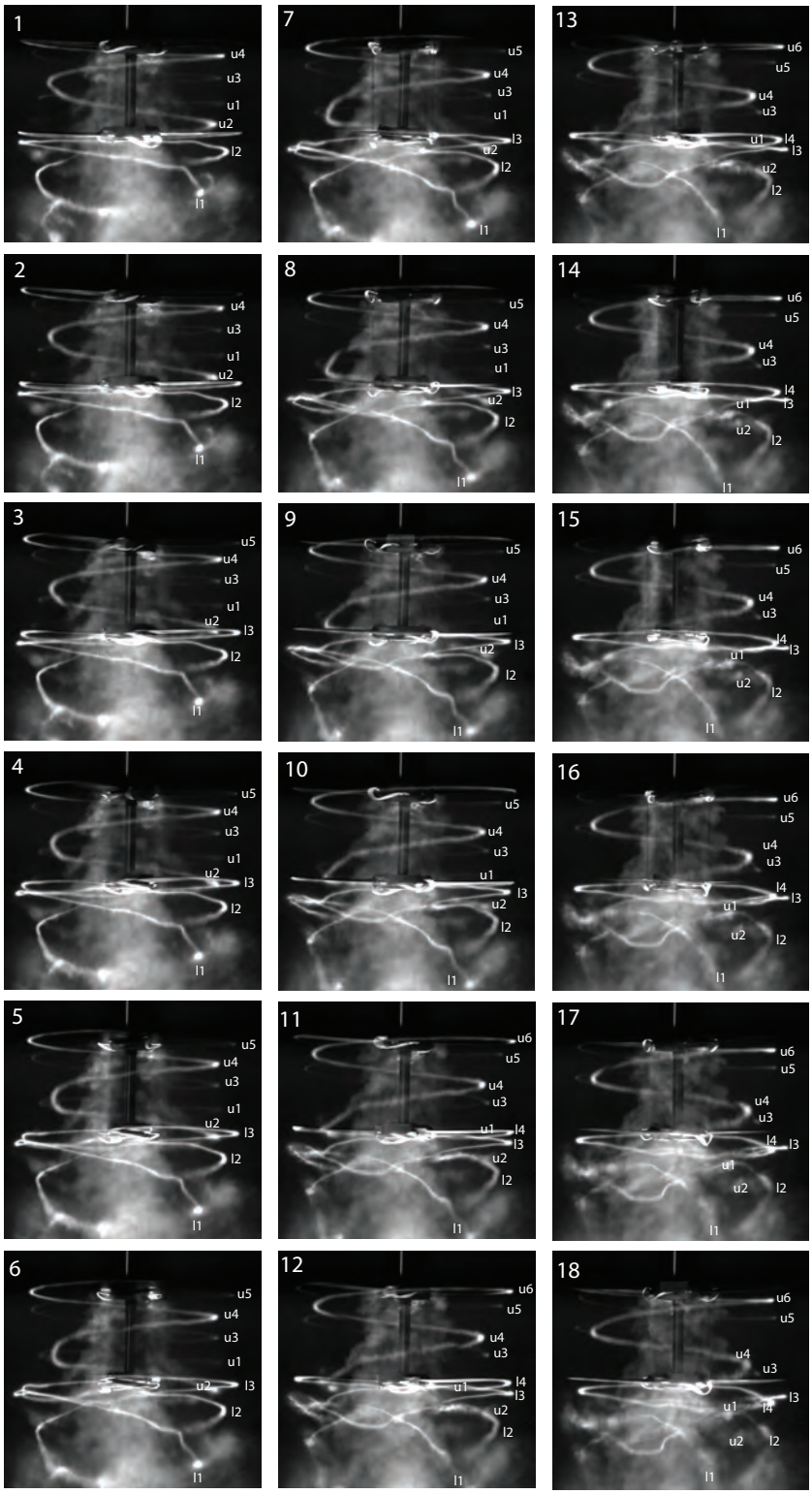

Figure 4.49: The first of two revolutions where the wake vortex evolution of the coaxial rotors with axial spacing of H/R=1 during two complete rotor revolution at 8 rps. Images are 20° ($\pi/9$ rad) apart. Time separation between successive images is 6.94 ms. Adjacent vortices are labeled with odd and even numbers. The odd numbers are used to refer to successive vortices from one of the two blades while the even numbers are used to identify the successive vortices from the other blade.

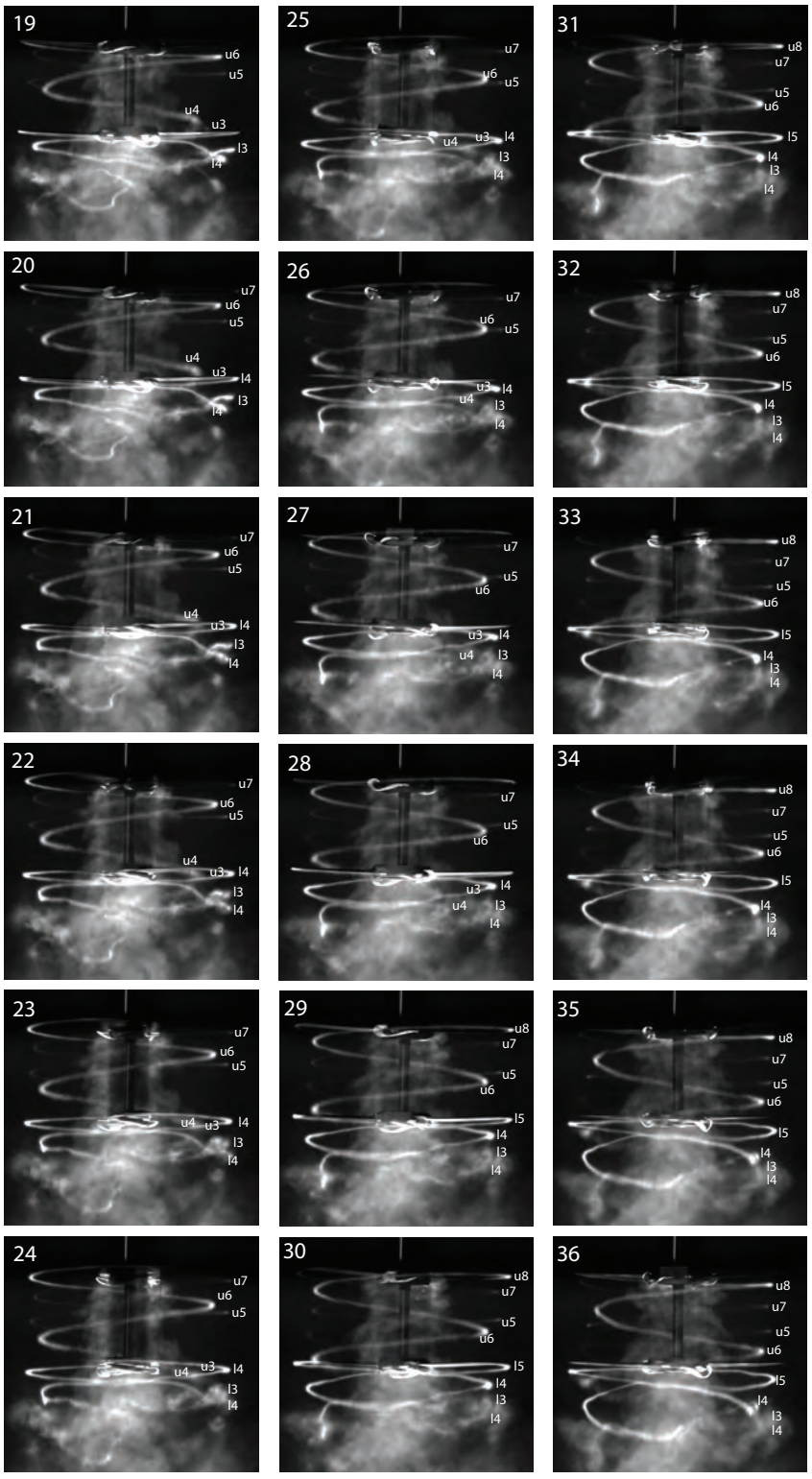

Figure 4.49: The second of two revolutions where the wake vortex evolution of the coaxial rotors with axial spacing of H/R=1 during two complete rotor revolution at 8 rps. Images are 20° ($\pi/9$ rad) apart. Time separation between successive images is 6.94 ms. Adjacent vortices are labeled with odd and even numbers. The odd numbers are used to refer to successive vortices from one of the two blades while the even numbers are used to identify the successive vortices from the other blade.

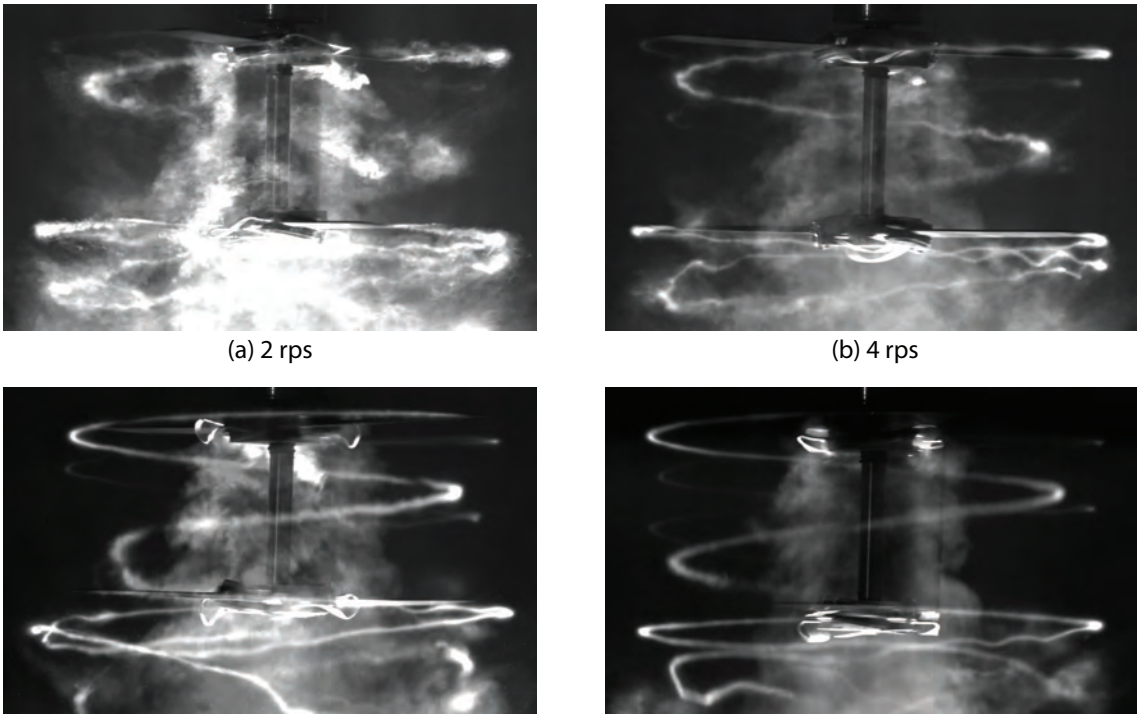

Figure 4.50: Sample flow images showing short-wave instabilities along the vortex filaments for all rotor speeds. Coaxial rotors are spaced at one rotor radius (Spacer 9).

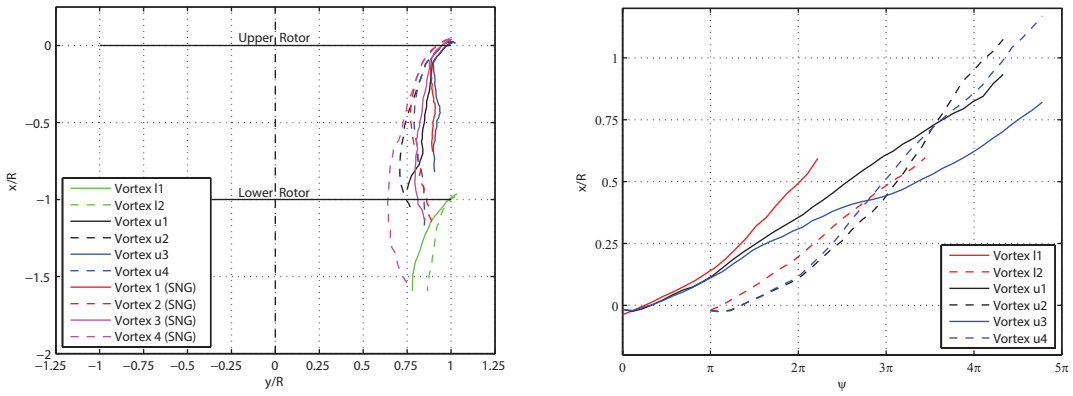

Figure 4.51: Trajectories of helical filaments trailed from coaxial rotor spaced at one rotor radius as well as those from the single rotor are shown. Right: spatial positions of tip vortices showing wake contraction. Left: xt diagram of the vortex filaments at 8 rps ($\psi = \Omega t$). Vortex labeling is similar to those in Figure 4.49.

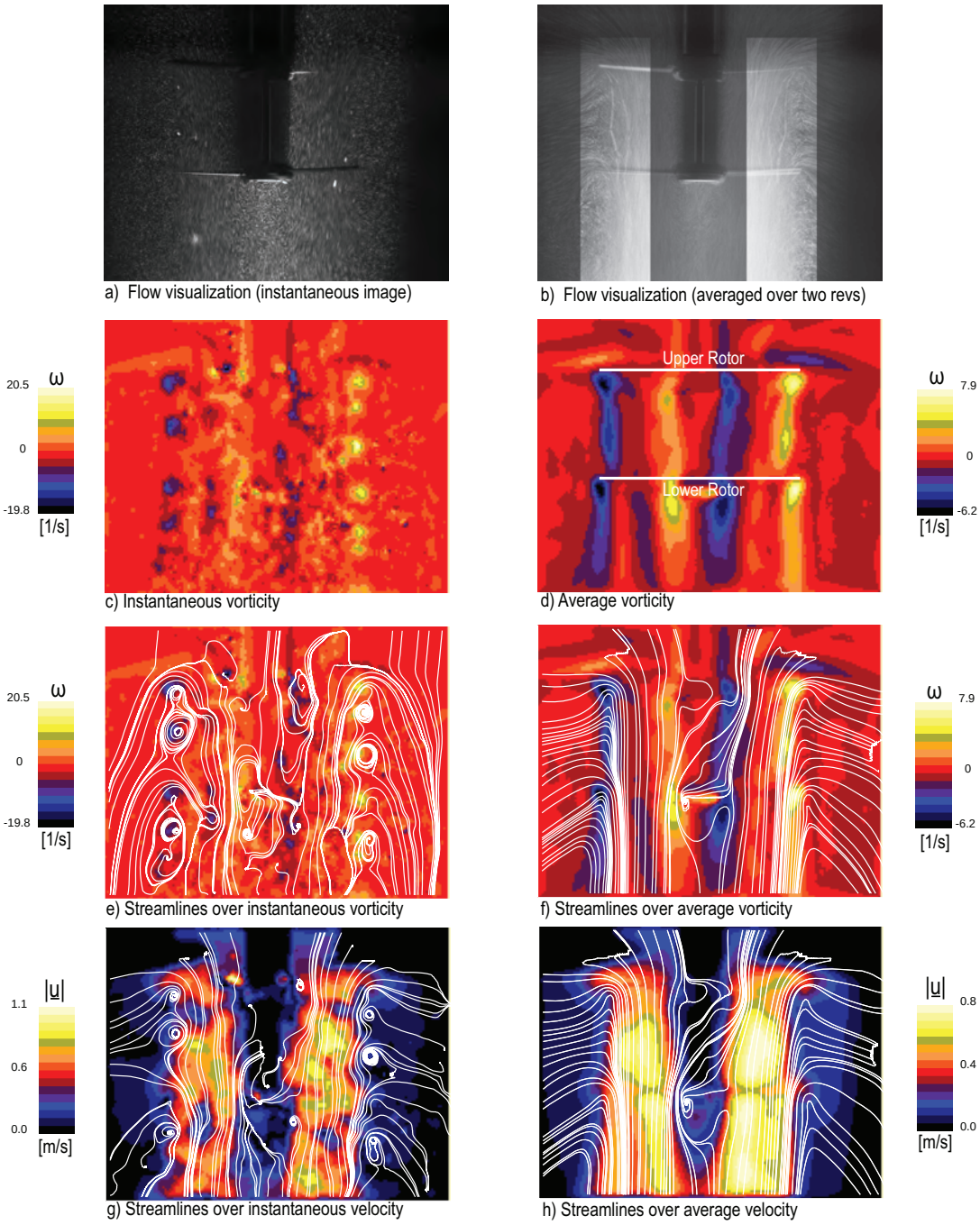

Figure 4.52: Flow field of a two-bladed coaxial rotor with rotor spacing of one rotor radius at $N = 8$ rps. First row (a,b): particle flow visualization. Average field in frame (b) is locally brightness- and contrast-enhanced to highlight the wake contraction of both rotors. In rows 2-4 are shown PIV measurements. Second row (c,d): vorticity fields. Third row (e,f): streamlines over vorticity. Fourth row (g,h): streamlines over speed. Streamlines in frame (e) are drawn from a moving reference frame and streamlines in frames (f-h) are drawn from a stationary reference frame.

Chapter 5

Discussion

In this chapter, a discussion on the results of experiments conducted at all rotor speeds and rotor spacings, both in one and two-bladed configurations, will be presented. As given in previous chapters in detail, comprehensive sets of experiments have been conducted in order to investigate vortex instabilities of coaxial rotors spaced at varying rotor separations ranging from a quarter to one rotor radius with a total of nine different axial separations. In addition to coaxial experiments, single rotor experiments have been also carried out for comparison purposes by removing the lower rotor from the coaxial set and operating the upper rotor in isolation.

5.1 Effect of Reynolds number

Figure 5.1 shows the sample flow images from the experiments conducted at 4 rps (right) & 8 rps (left) for rotors with one blade. First row gives the flow images of the single-bladed rotor and the remaining two rows show the flow images of coaxial rotor having one blade per rotor at two different rotor spacings. Figures 5.2 and 5.3 show a sample flow image from each of the sets of experiments at 8 and 4 rps for two-bladed rotor configurations, respectively. Description of each image (rotor spacing) is given on the left side of the first-column images and on the right of the second-column images in all figures. Single rotor flow image is provided on the top left frame of the figures at each speed. Images are presented in the increasing order of the rotor spacings from top to bottom and left to right.

All of the images from coaxial rotor experiments given in Figure 5.2 reveal the complexities in the rotor wake brought about by the operation of two rotors in tandem, the most apparent of which is the extreme deformation experienced by the lower rotor tip vortex filaments soon after their inception, which is unusual in the wakes of single rotor configurations as readily seen from the top left image of the figure. Viscosity-dominated nature of the flow field at 4 rps as shown in Figure 5.3, however, renders it difficult to trace these similar deformation trends of the vortices farther in the downstream direction in the wake at this rotor speed. Flow field at 6 rps resembles more to what is observed at 8 rps and flow field at 2 rps looks more like that at 4 rps, as previously shown in the preceding chapters as well as given in Appendix A. This is further confirmed by the tip vortex circulation-based Reynolds numbers, Re_Γ (see Table 4.1), where lower values of Re_Γ signals more viscous nature of the flow fields at 2 & 4 rps compared to relatively higher values at 6 & 8 rps.

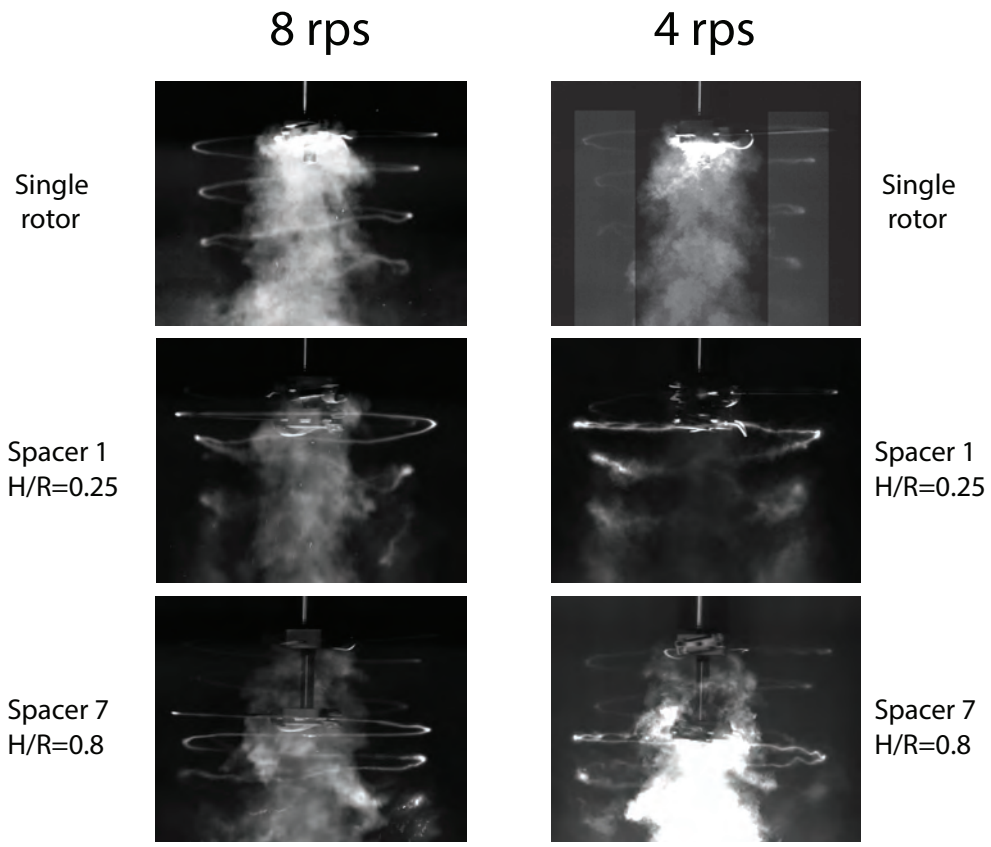

Figure 5.1: Sample flow images from one-bladed rotor experiments, both in single and coaxial configurations. Left column shows 8 rps images and right column shows 4 rps images. Image description (rotor spacing) is given on the left of the first-column images and on the right of the second-column images. Flow images from single rotor tests at each speed are shown on top row of the figure.

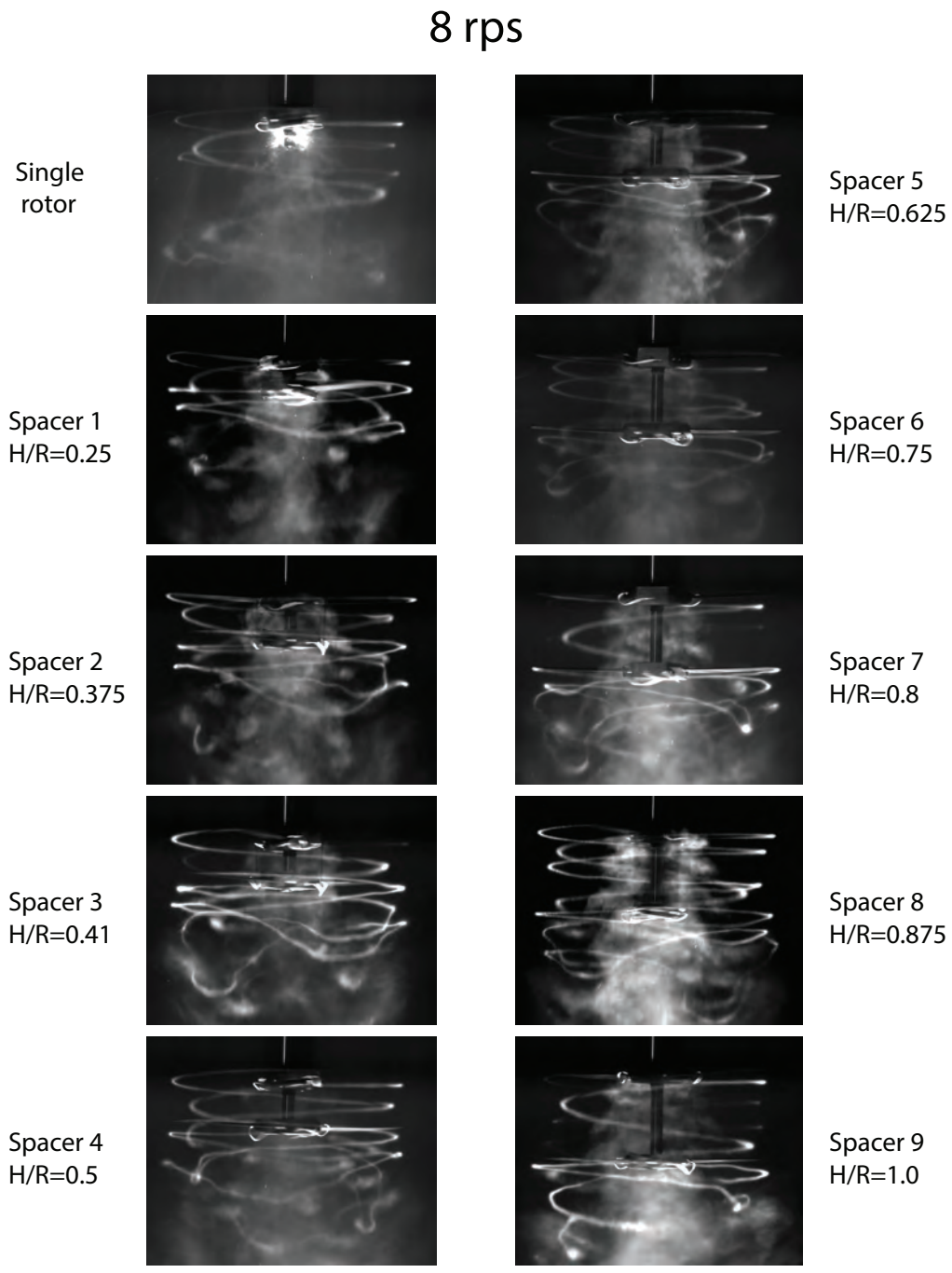

Figure 5.2: Sample flow images at 8 rps from two-bladed rotor experiments, both in single and coaxial configurations. Image description (rotor spacing) is given on the left of the first-column images and on the right of the second-column images. Flow image from single rotor tests is shown on top left frame of the figure.

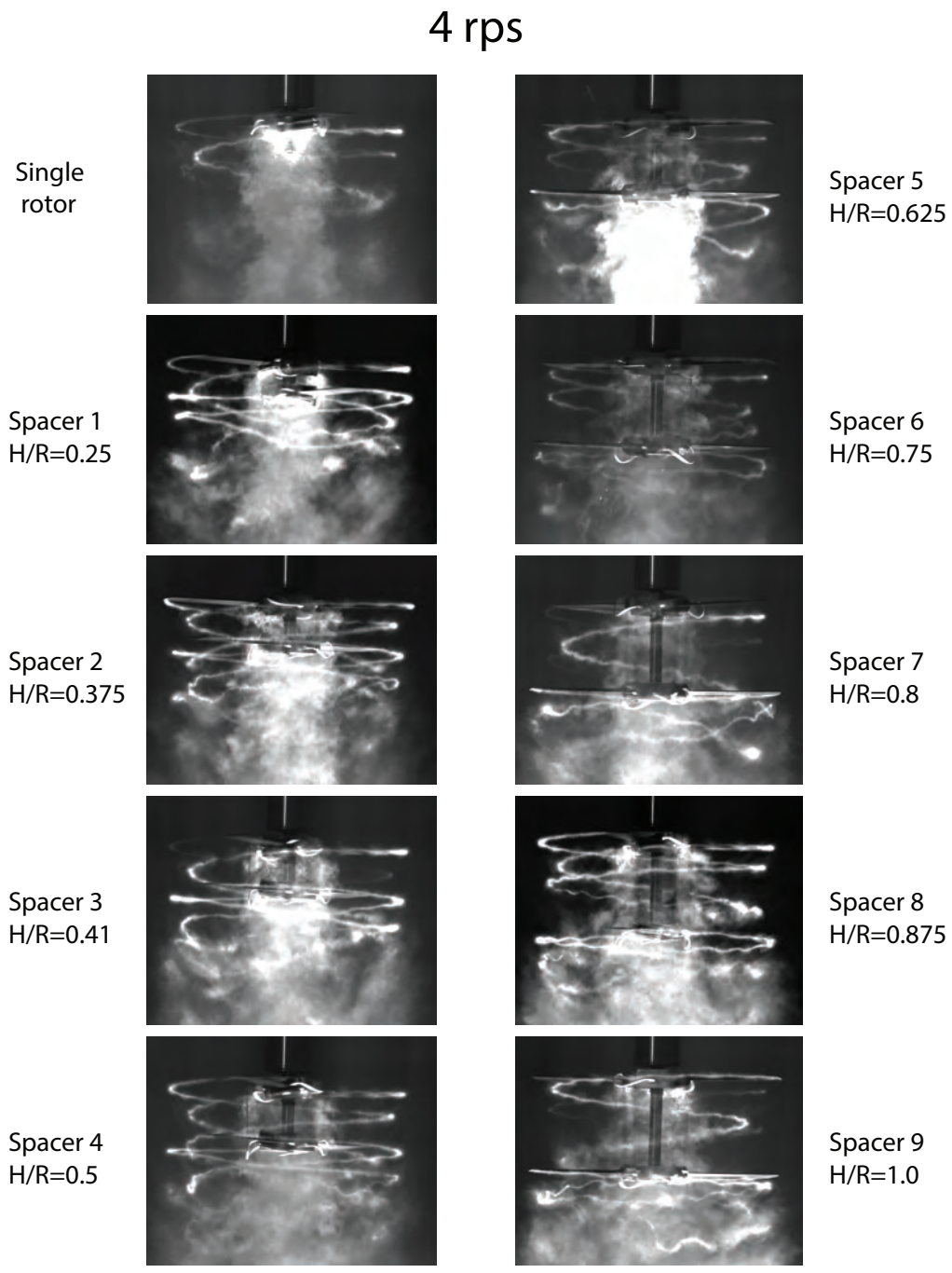

Figure 5.3: Sample flow images at 4 rps from two-bladed rotor experiments, both in single and coaxial configurations. Image description (rotor spacing) is given on the left of the first-column images and on the right of the second-column images. Flow image from single rotor tests is shown on top left frame of the figure.

5.2 Long-wave instabilities

Although the deformation trends exhibited by the lower rotor filaments appear similar at different rotor spacings, they differ in the shapes or structures attained by the vortices at downstream distances of the rotor wake at each particular rotor separation tested. What is meant by similar is the mechanism of the development of these deformations, which is initiated by the long-wave vortex instability characteristics exhibited by the tip vortices. In this type of instability mode, which is also referred as leapfrogging process, two adjacent vortices trailed from the blade tips of the lower rotor start to orbit around each other as they travel together in the streamwise direction. This is when these vortices start to develop these kinds of unusual deformations as the turns of the trailing vortex leapfrog through the turns of the leading vortex. Although this type of instability mode is also observed in single rotor tests, the contribution from the vortices trailed from the upper rotor affect the behavior of the lower vortices significantly, resulting in extreme deformation of the latter. These lower vortices become elongated in the streamwise direction and at some rotor spacings they deform to vortex structures resembling hairpin vortices, losing their orderly helical shapes. The most notable example of this kind of vortex structure formation is observed at rotor spacing of 50% of the rotor radius, which is shown at the bottom left frame of Figure 5.2. Regardless of the rotor separation, the lower rotor continually operates in the wake of the upper rotor, resulting in mutual interactions between the vortices trailed from both rotor. Also, as the upper rotor filaments pass through the plane of the lower rotor, they interact with the lower rotor blades (interrotor BVIs), which, in turn, cause them to become diffuse and make their subsequent locations hard to follow in the wake. The wakes from both rotors become coalesced beneath the lower rotor in the far wake region.

In all rotor separations tested, one obvious feature is that the upper rotor vortices possess a more stable nature as opposed to those from the lower rotor, which become unstable within first rotor revolution and undergo extreme strain at some instances. See Spacer 9 case, for example, where upper rotor vortices behave as if they come off single rotor blade tips and lower rotor vortices get destructed easily and quickly. It can be inferred that the lower rotor has a stabilizing effect (in terms of vortex stability) on the upper rotor filaments whereas the upper rotor has a destabilizing effect on the lower rotor filaments. In all cases, it is observed that the pitch of the helices from the lower rotor is smaller than that from the upper rotor, which is another cause for stronger interactions and deformations of lower rotor vortices.

5.3 Short-wave instabilities

In all cases, at rotor speeds of 2 & 4 rps, short-wave instabilities develop along all filaments. At 6 & 8 rps, however, filaments exhibit short-wave instability characteristics long after their generation and only locally, which become superimposed with the stronger long-wave instability mode in the downstream locations of the wake. Figures 5.4-5.8 show the short-wave instability wavelength data which are extracted from the flow visualization images from all cases. In each figure, on the left is plotted the raw wavelength data in image pixels against the vortex age (ψ), which is measured in radians. These raw data, which is first converted from pixel to cm ($1px \approx 0.0348cm$), is then rendered dimensionless by the rotor radius and plotted on the right sides of each figure against the vortex age one more time. Since the wake radius shows variations at different rotor spacings, rotor radius is used instead to make the short-wave instability wavelengths non-dimensional. The legend for these five figures is shown on top of Figure 5.4. In all of these five figures, blue symbols show the wavelength data from one-bladed coaxial rotor experiments at 2 & 4 rps. Symbols in red and black colors mark the short-wave instability wavelengths along the lower and upper rotor filaments at 4 rps at all rotor separations, respectively. Similarly, symbols in magenta and cyan colors mark the short-wave instability wavelengths along the lower and upper rotor filaments at 2 rps at all rotor separations, respectively. In Table 5.1, average short-wave instability wavelengths are presented where each of the columns correspond to data shown in Figures 5.4-5.7, respectively. These wavelength data, both in

the figures and table, suggests that there is not a particular pattern for short-wave instability wavelengths at a particular rotor (upper and lower rotors), rotor separation and speed shown although average wavelengths along the upper rotor filaments is slightly lower than those along the lower rotor filaments as given in Table 5.1. In general, it can be inferred from the flow visualization images and the figure that the short-wave instabilities are mostly affected by the rotor speed instead of rotor separation and rotor configuration (from a comparison of images at 6-8 rps to 2-4 rps). Non-dimensional short-wave instability wavelengths (λ/R) are mostly concentrated between 0.15 to 0.3 as can be seen on the right plot of the figure, which is further confirmed by the consolidated average wavelength value of 0.23 (from Figure 5.8). Wavelength data is extracted wherever the flow field is clear so the number of wavelengths shown in the figure may show irregular variations depending on rotor separation, configuration, and the rotor speed. Although the wavelength data does not suggest a clear distinction between the upper and the lower rotor filaments, it is clear from the flow visualization images that the amplitude of the short waves along the lower rotor filaments grow in magnitude rapidly as opposed to those along the upper rotor filaments. This is also another confirmation of the observation that the upper rotor filaments appear to possess a more stable nature than those from the lower rotor.

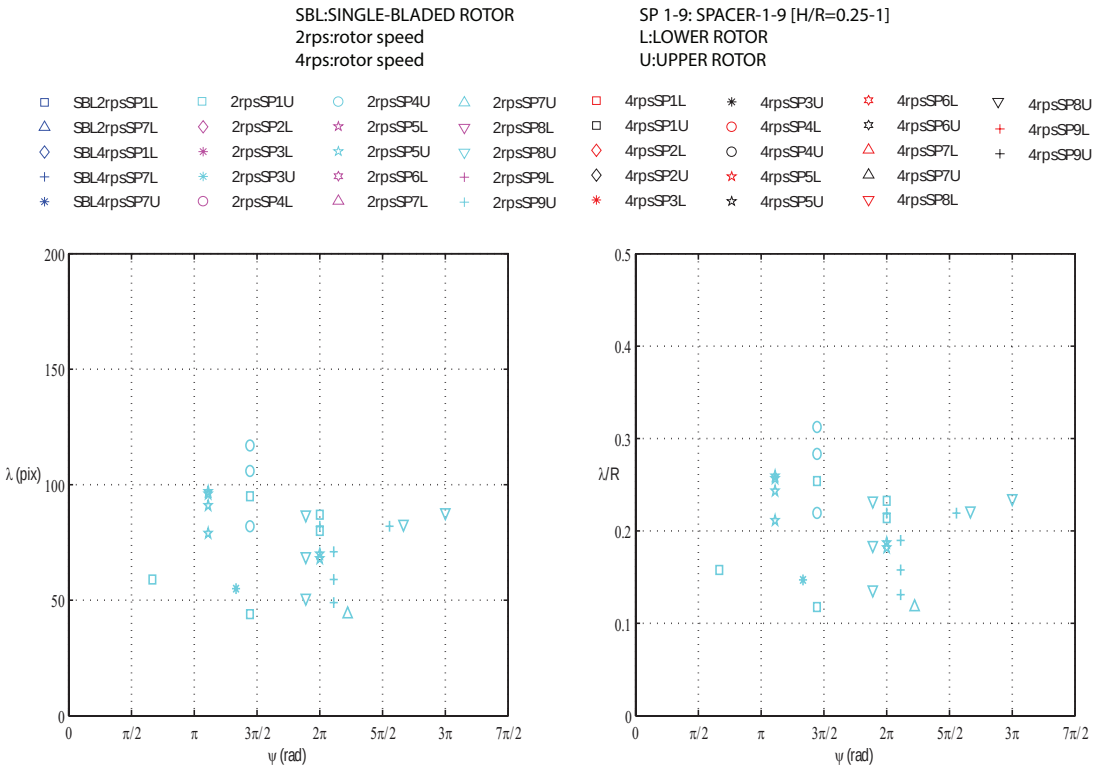

Figure 5.4: Short-wave instability wavelengths along upper rotor filaments at 2 rps are shown. Wavelength data is extracted from flow visualization images of all coaxial rotor experiments. Left: raw wavelength data in image pixels plotted against the vortex age. Right: wavelengths are rendered dimensionless by the rotor radius and plotted against the vortex age one more time. Legend is provided on top of the figure.

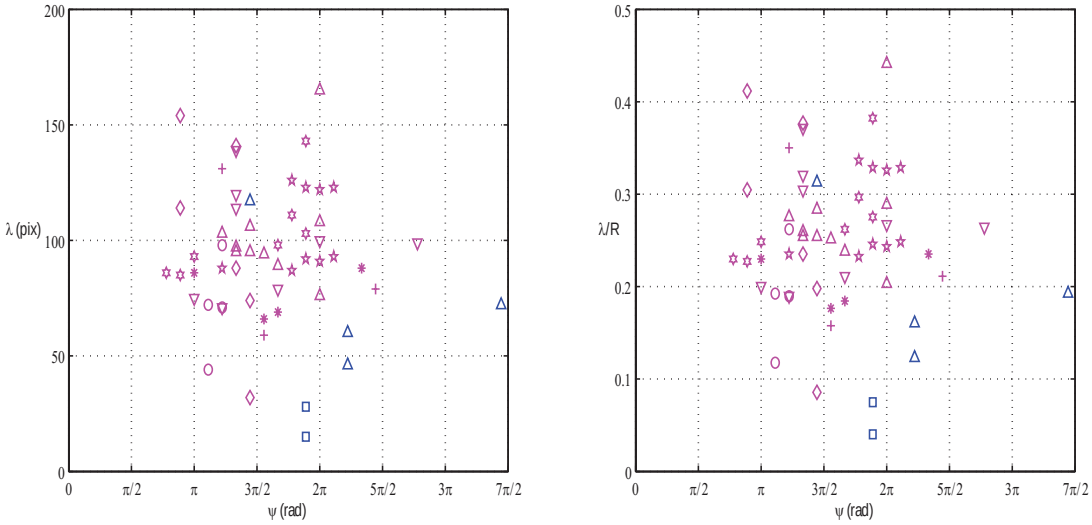

Figure 5.5: Short-wave instability wavelengths along lower rotor filaments at 2 rps are shown. Wavelength data is extracted from flow visualization images of all coaxial rotor experiments. Left: raw wavelength data in image pixels plotted against the vortex age. Right: wavelengths are rendered dimensionless by the rotor radius and plotted against the vortex age one more time. See Figure 5.4 for legend.

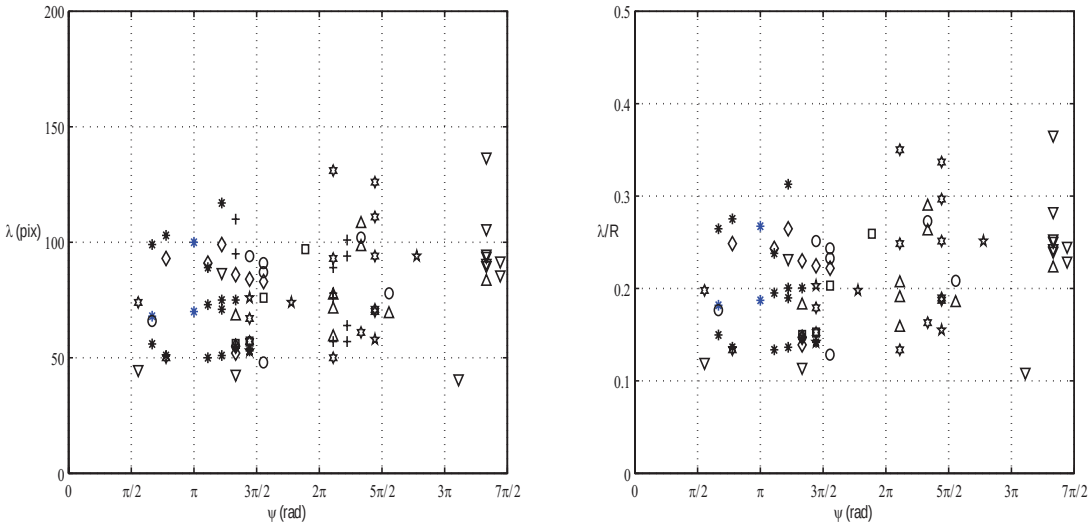

Figure 5.6: Short-wave instability wavelengths along upper rotor filaments at 4 rps are shown. Wavelength data is extracted from flow visualization images of all coaxial rotor experiments. Left: raw wavelength data in image pixels plotted against the vortex age. Right: wavelengths are rendered dimensionless by the rotor radius and plotted against the vortex age one more time. See Figure 5.4 for legend.

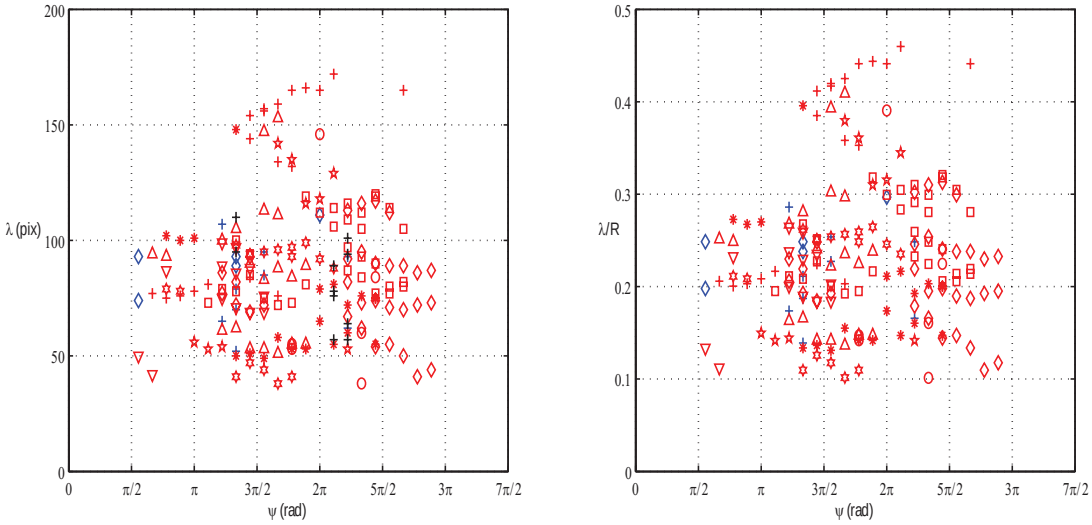

Figure 5.7: Short-wave instability wavelengths along lower rotor filaments at 4 rps are shown. Wavelength data is extracted from flow visualization images of all coaxial rotor experiments. Left: raw wavelength data in image pixels plotted against the vortex age. Right: wavelengths are rendered dimensionless by the rotor radius and plotted against the vortex age one more time. See Figure 5.4 for legend.

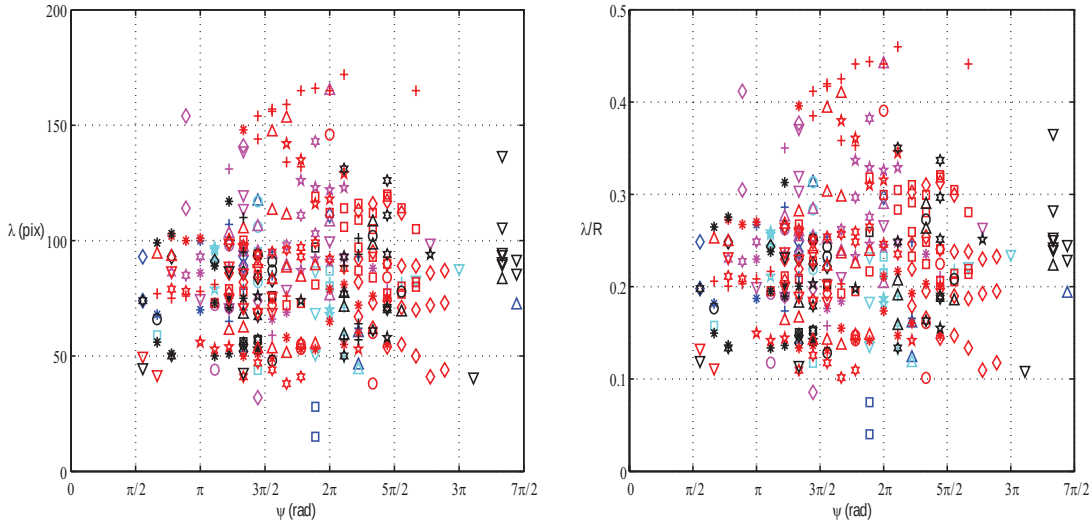

Figure 5.8: Consolidated short-wave instability wavelengths at 2 & 4 rps are shown. Wavelength data is extracted from flow visualization images of all coaxial rotor experiments. Left: raw wavelength data in image pixels plotted against the vortex age. Right: wavelengths are rendered dimensionless by the rotor radius and plotted against the vortex age one more time. See Figure 5.4 for legend.

Average short-wave instability wavelengths		
Average wavelengths (pixels-λ/R)	2 rps	4 rps
Upper Rotor	77±19 (pixels) 0.206±0.051(λ/R)	79±21 (pixels) 0.211±0.056 (λ/R)
Lower Rotor	97±26 (pixels) 0.259±0.07 (λ/R)	88±30 (pixels) 0.235±0.08 (λ/R)

Table 5.1: Average values of short-wave instability wavelengths (dimensional & non-dimensional). These values correspond to those wavelengths plotted in Figures 5.4-5.7. Average values are provided separately for the data at 2 rps, 4 rps, upper rotor, and lower rotor along with consolidated averages of all short-wave instability wavelengths. Also what is shown is the standard deviations in each case.

5.4 Single blade versus two blades per rotor

Experiments have been conducted at two different rotor separations ($H/R = 0.25$ and $H/R = 0.8$) for one-bladed coaxial rotors, the results of which are shown in Figure 5.1. Although one-bladed rotors are not in existence in real-life applications, these experiments are intended to provide insight into the flow features of such rotor models. Two distinct flow features are observed at two different rotor separations. When the coaxial rotors are spaced at a quarter radius, the upper rotor vortex and lower rotor vortex develop long-wave instability in which they orbit around each other followed by the deformation of the subsequent lower rotor vortices within a rotor revolution. When the rotor spacing is increased to 80% of the radius, the lower rotor vortices retain their orderly helical shapes as opposed to Spacer 1 case. Similar observations are valid regarding the stability of upper and lower rotor vortices as in the two-bladed runs. Figure 5.1 clearly shows these flow features at 4 & 8 rps. Increasing the number of blades amounts to a corresponding decrease in the pitch of the helices, which, in turn, results in stronger mutual interactions between the subsequent helical filaments for two-bladed rotors operated both in isolation and in tandem.

5.5 Independence of the upper wake for large separations

The axial separation between the rotors affect the behavior of the upper rotor tip vortices. In the limiting case when the rotors are deemed to be sufficiently far apart form each other such that the effect of lower rotor on the upper rotor can be considered negligible, the upper rotor behaves like a single rotor, i.e. the tip vortex filaments exhibit classical long-wave instability mode characteristics, which is basically the flow field of the single rotor tests given in top left frame of Figure 5.2. A close investigation of the flow fields generated by the upper rotor at all rotor spacings reveal that when the rotors are spaced at least one rotor radius, which is given by the bottom right frame of the same figure, they exhibit very similar characteristics to the single rotor tests. This can be observed from a comparison of single rotor and spacer-9 test results. Up to rotor spacing of 62.5% radius (Spacer 1-4 tests), the upper rotor filaments do not have sufficient interrotor space to develop long-wave instability characteristics before they are intercepted by the lower rotor. When rotors are fitted with Spacer 5, where $H/R = 0.625$, the adjacent upper rotor vortices attempt to leapfrog through each other as shown in top right frame of Figure 5.2. However, this process is not fully completed since the vortices reach the plane of the lower rotor and interact with the blades there, resulting in their disintegration and subsequent diffusion. As the rotor spacing is increased further, the vortices develop long-wave instability in a complete manner. When the rotor separation becomes one rotor radius, the flow field between the rotors shows two-revolution periodicity, i.e. the exact flow pattern repeats itself in every two rotor revolutions. From these observations, it can be inferred that when the coaxial rotors are spaced at least at one rotor radius, the tip vortices from the upper rotor start to behave as if they trail

from a single rotor configuration. In other words, when axial separation between the rotors is one rotor radius, the upper rotor wake can be considered to be unaffected by the lower rotor although the opposite is not true.

5.6 Hairpin vortices

As the lower rotor vortices exhibit long-wave instability characteristics between each other, the subsequent tip vortices from a particular blade of the lower rotor deform out of their orderly helical shapes. As stated earlier, the vortex structures resembling hairpin-like vortices are formed following these deformations, the most clear of which is observed at rotor spacing of 50% of the rotor radius, which is given at the bottom left frame of Figure 5.2. At some other rotor spacings (Spacer 3 and 8 cases, for example), hairpin-like vortices have a fatter vortex head with largely-separated vortex legs compared to others (such as Spacer 4) where two hairpin vortices are formed in the streamwise direction as previously confirmed by flow images. At one radius separation, however, formation of such vortex structures is not observed, instead vortices are disrupted enormously beneath the lower rotor within a short interval of time, which is seen at bottom right frame of Figure 5.2. Spacer 9 case of one radius separation of the rotors is noticeably different from the rest of the coaxial experiments in terms of the behaviors of the vortices from both rotors of the coaxial set. Flow images from the single rotor experiments, both from the current and previous studies, does not possess characteristics such as the formation of hairpin-like vortex structures out of initially helix-shaped vortex filaments as observed in some of the coaxial rotor experiments. This is one of the main differences between the flow fields of single and coaxial rotors.

5.7 Wake width

Figure 5.9 shows the vortex trajectories at all rotor spacings and configurations. The left plot shows the trajectories of the vortices trailed from one of the two blades of each rotor and the right plot shows the trajectories of the vortices trailed from the other blade. Singe rotor vortex trajectories are marked with '*' for comparison purposes. Rotor separation of $H/R = 1$ is not a consideration into the discussion, instead it is intended to sufficiently separate upper and lower vortex trajectories for clarity. As observed in previous studies, which are discussed in Chapter 1, the upper rotor vortices contract more inward and at a higher downward speed than both those from single rotor (i.e. isolation) and lower rotor. Also, single rotor wake contraction is larger than that of the lower rotor. Upper rotor wake contraction does not show large deviations at different rotor spacings. Different contraction and speed characteristics exhibited by different rotors (upper, lower, and single) is due to the induced effects caused by vortex filaments from one rotor on those of the other. Different contraction and convection rates of adjacent vortices from the same rotor is brought about by the interaction between those vortices as in the case of the long-wave instability developed by these vortices. It is also possible that uncontrollable variations in blade geometry and collective angles affect these characteristics to a certain degree, however small. In general, upper rotor wake contracts to about 70% of the rotor radius while the lower rotor contracts to about 90% of the radius, which is markedly higher than the former. Long-wave instabilities developed by the vortices cause an expansion in the wake following an initial rapid contraction as observed from the average images given in the previous chapter. This expansion further changes the cross section on the inner part of the lower rotor that is impinged upon by the upper rotor wake. This is an important parameter that largely affect the rotor performance. The scatter in the lower rotor vortex trajectories (left plot) is a result of extreme deformation experienced by these vortices. Forward and backward portions of a particular vortex experiences extreme strain and this further makes it challenging to extract position data as accurately as possible.

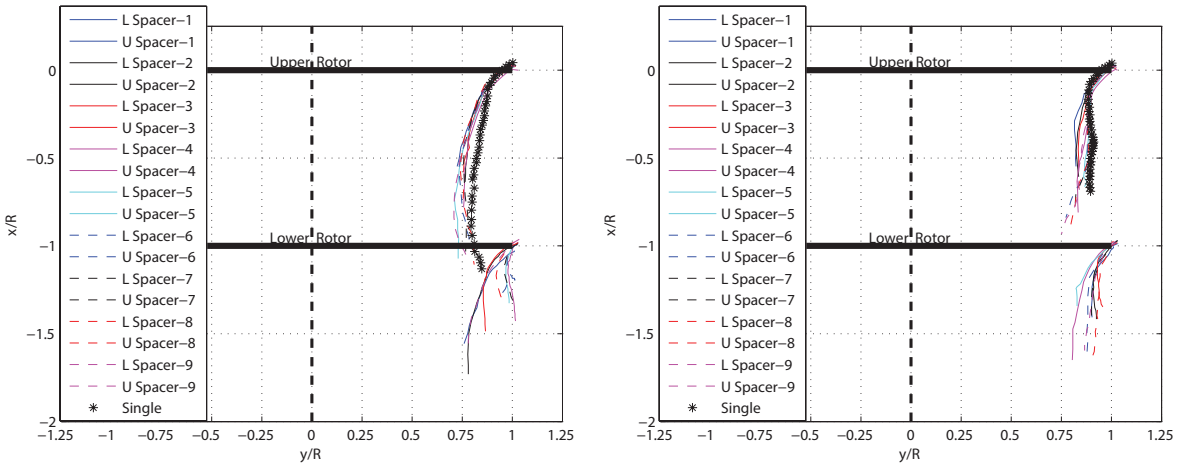

Figure 5.9: Vortex trajectories at all rotor separations including single rotor vortices for two-bladed rotor experiments. Left plot shows all vortex trajectories from one of the two blades and the right plot shows trajectories of the vortices trailed from the other blade. Single rotor vortex trajectories are marked with '*' for comparison purposes. Letters 'L' and 'U' denote lower and upper rotors, respectively. Rotor separations corresponding to Spacer 1-9 are provided in Table 2.2.

,

Chapter 6

Conclusion

In the present work the problem of the stability of helical filaments shed from a coaxial rotor configuration was addressed experimentally using flow visualization and particle image velocimetry techniques. Specifically, effect of rotor rotational speed and axial rotor spacing on the wake and stability characteristics of the coaxial rotors have been investigated. For the purposes of this study, a drive system for coaxial rotors which can also be reduced to operate in single rotor configuration by removing one of the rotors was designed and built. A convenient way of changing rotor separation was achieved through the design of independent and easily removable disk spacers. These disk spacers were used to vary the rotor separation from a quarter to one radius, giving a total of nine different rotor separations. A number of flow visualization images at each specific rotor separation and speed are captured and presented along with the results of processed PIV image pairs and particle visualization photos, both in instantaneous and average fields. Following conclusions are drawn based on these experimental data:

For the one-bladed coaxial rotor experiments, of which only two different rotor spacings are tested, helical tip vortex filament trailed from the lower rotor blade is observed to develop strong deformations soon after its formation when the rotors are spaced at a quarter rotor radius as opposed to that of the upper rotor. This deformation is markedly higher at the rotor spacing of $0.25R$ compared to that at $H/R = 0.8$. The upper and lower rotor vortices are seen to develop long-wave vortex pairing instabilities where they orbit around each other as they travel downstream, particularly at smaller rotor spacing, which is also confirmed in PIV results. Successive turns of the upper rotor helices appear to be stable as opposed to unstable nature of the lower rotor helix in both rotor separations. At $H/R = 0.8$, the upper rotor wake contraction (70% of the rotor radius) is markedly higher than that of the lower rotor (90% of the rotor radius). Vortex filaments develop short-wave instabilities at 2 & 4 rps just immediately after their inceptions in both rotor separations.

In the two-bladed configurations, in all cases tip vortices trailed from the lower rotor experience extreme distortions, resulting in the loss of their orderly helical shapes, which is a clear manifestation of the effect of the upper rotor on the lower one. At smaller rotor spacings up to 50% radius, lower rotor filaments develop long-wave vortex pairing instabilities in similar ways to what is found in single rotor wakes although they differ to the extent lower vortex filaments undergo deformations. At this rotor spacing range, upper rotor filaments does not have sufficient space between the rotors to develop mutual interactions before they reach the plane of the lower rotor and interact with lower rotor blades, i.e. interrotor blade-vortex interactions (BVIs). As the rotor spacing is further increased up to a rotor radius, upper rotor filaments are seen to develop long-wave pairing instabilities similar to what is observed in the wakes of single rotor runs. A comparison of single rotor and coaxial rotor videos reveal that when the coaxial rotors are spaced at least at one rotor radius, the tip vortices from the upper rotor start to behave as if they trail from a single rotor configuration. As in the one-bladed configurations, upper rotor filaments possess a more stable nature

whereas those from lower rotor becomes unstable within first rotor revolution beneath the lower rotor.

At rotor spacing of 50% radius, hairpin vortices are observed to form beneath the lower rotor during the long-wave instability mode developed by the lower rotor filaments where streamwise elongation of the vortex filament from a particular blade of the lower rotor in each rotor revolution is observed. At other rotor spacings, similar deformation of the vortex filaments in the streamwise direction is seen to occur however distinct hairpin vortex structures are only seen at the rotor spacing of $0.5R$. Flow images from the single rotor experiments, both from the current and previous studies, does not possess characteristics such as the formation of hairpin-like vortex structures out of initially helix-shaped vortex filaments as observed in some of the coaxial rotor experiments. This is one of the main differences between the flow fields of single and coaxial rotors.

The upper rotor wakes contract to more inward than those of the lower rotor wakes for all the rotor separation distances tested, which is also confirmed from the PIV measurements and particle visualization results. Increasing rotor spacing changes the wake contraction of the upper rotor at the plane of the lower rotor where it reaches a more fully-developed state towards the rotor spacing of one radius. This is further confirmed from the streamline patterns from the PIV results.

Regardless of the rotor spacing, short-wave instabilities formed along the helical filaments at 2 & 4 rps cases from their generation whereas at 6 & 8 rps filaments are only observed to develop these types of instabilities long after their formation and not in an explicit manner since they become superimposed with long-wave instability mode where filaments develop strong distortions beneath the lower rotor. Short-wave instability wavelengths at 2 & 4 rps (λ/R) are found to be concentrated about 0.15-0.3 at all rotor separations.

Bibliography

[1] Tokaty, G. A., *A history and philosophy of fluid mechanics*, Dover Publications, 1994.

[2] McGowen, S. S., *Helicopters: an illustrated history of their impact*, ABC-CLIO, 2005.

[3] Coleman, C. P., "A survey of theoretical and experimental coaxial rotor aerodynamic research," *National Aeronautics and Space Administration, Ames Research Center*, Vol. 3675., 1997.

[4] Kasjanikov, V. A., "Coaxial helicopters-current status and future developments," *Vertiflite*, Sept.–Oct, 1990.

[5] Tischenko, M.N., "Soviet Helicopter Technology," *Vertiflite*, Vol. 35, (5), 1989, pp. 76–86.

[6] Cheney, M. C., "The ABC helicopter," *Journal of the American Helicopter Society*, Vol. 14, (4), 1969, pp. 10–19.

[7] Hirschberg, M., "Sikorsky Pushes Forward with X2 Technology Demonstrator," *Vertiflite*, Vol. 51, (3), 2005, pp. 12.

[8] Yoon, S. and Chan, W. M and Pulliam, T. H., "Computations of Torque-Balanced Coaxial Rotor Flows," 55th AIAA Aerospace Sciences Meeting, 2017, pp. 0052.

[9] Colucci, F., "Tern Over and Fly," *Vertiflite*, Vol. 63, (3), 2017, pp. 56–57.

[10] "Kamov Ka-50," Wikipedia. Retrieved from *https://en.wikipedia.org/wiki/Kamov-Ka-50* (Last accessed August 24, 2017).

[11] "Sikorsky S-69," Wikipedia. Retrieved from *https://en.wikipedia.org/wiki/Sikorsky-S-69* (Last accessed August 24, 2017).

[12] "EHANG 184," EHANG. Retrieved from *http://www.ehang.com/ehang184/gallery/* (Last accessed August 24, 2017).

[13] "Sikorsky S-97 Raider," Lockheed Martin. Retrieved from *http://www.lockheedmartin.com/content/dam/lockheed/data/ms2/photo/rotary-wing/s-97-high-res.jpg* (Last accessed August 24, 2017).

[14] Conlisk, A. T., "Modern helicopter aerodynamics," *Annual review of fluid mechanics*, Vol. 29, (1), 1997, pp. 515–567.

[15] Leishman, J. G., *Principles of Helicopter Aerodynamics*, Cambridge University Press, New York, NY, 2006, pp. 257-260.

[16] Widnall, S. E., "The stability of a helical vortex filament," *Journal of Fluid Mechanics*, Vol. 54, (4), 1972, pp. 641–663.

[17] Sullivan, J. P., "An experimental investigation of vortex rings and helicopter rotor wakes using a laser Doppler velocimeter," DTIC Document, 1973.

[18] Tsai, C. and Widnall, S. E., "The stability of short waves on a straight vortex filament in a weak externally imposed strain field," *Journal of Fluid Mechanics*, Vol. 73, (4), 1976, pp. 721–733.

[19] Widnall, S. E. and Bliss, D. B. and Tsai, C., "The instability of short waves on a vortex ring," *Journal of Fluid Mechanics*, Vol. 66, (1), 1974, pp. 35–47.

[20] Wang, H., "Short wave instability on vortex filaments," *Physical review letters*, Vol. 80, (21), 1998, pp. 4665.

[21] Ohanian, C. V., McCauley, G. J., and Savaş, Ö., "A Visual Study of Vortex Instabilities in the Wake of a Rotor in Hover, "*Journal of the American Helicopter Society*, Vol. 57, (4), 2012, pp. 1-8.

[22] Leishman, J. G. and Bagai, A., "Challenges in understanding the vortex dynamics of helicopter rotor wakes," *AIAA journal*, Vol. 36, (7), 1998, pp. 1130-1140.

[23] Leweke, T. and Le Dizès, S. and Williamson, C. H. K., "Dynamics and instabilities of vortex pairs," *Annual Review of Fluid Mechanics*, Vol. 48, 2016, pp. 507-541.

[24] Kerswell, R. R., "Elliptical instability," *Annual Review of Fluid Mechanics*, Vol. 34, (1), 2002, pp. 83–113.

[25] Crow, S. C., "Stability theory for a pair of trailing vortices," *AIAA journal*, Vol. 8, (12), 1970, pp. 2172–2179.

[26] Felli, M. and Camussi, R. and Di Felice, F., "Mechanisms of evolution of the propeller wake in the transition and far fields," *Journal of Fluid Mechanics*, Vol. 682, (1), 2011, pp. 5–53.

[27] Lim, T. T., "A note on the leapfrogging between two coaxial vortex rings at low Reynolds numbers," *Physics of Fluids*, Vol. 9, (1), 1997, pp. 239–241.

[28] Landgrebe, A. J., "The wake geometry of a hovering helicopter rotor and its influence on rotor performance," *Journal of the American Helicopter Society*, Vol. 17, (4), 1972, pp. 3–15.

[29] Okulov, V. L., "On the stability of multiple helical vortices," *Journal of Fluid Mechanics*, Vol. 521, 2004, pp. 319–342.

[30] Okulov, V. L. and Sorensen, J. N., "Stability of helical tip vortices in a rotor far wake," *Journal of Fluid Mechanics*, Vol. 576, 2007, pp. 1.

[31] Gupta, B. P. and Loewy, R. G., "Analytical Investigation of the Aerodynamic Stability of Helical Vortices Shed from a Hovering Rotor," DTIC Document, 1973.

[32] Gupta, B. P. and Loewy, R. G., "Theoretical analysis of the aerodynamic stability of multiple, interdigitated helical vortices," *AIAA journal*, Vol. 12, (10), 1974, pp. 1381–1387.

[33] Tangler, J. L. and Wohlfeld, R. M. and Miley, S. J., "An experimental investigation of vortex stability, tip shapes, compressibility, and noise for hovering model rotors," NASA Technical Report, 1973.

[34] Caradonna, F. and Henley, E. and Silva, M. and Huang, S. and Komerath, N. M. and Reddy, U. and Mahalingam, R. and Funk, R. and Wong, O. and Ames, R. and Darden, L. and Villareal, L. and Gregory, J., "Performance measurement and wake characteristics of a model rotor in axial flight," *Journal of the American Helicopter Society*, Vol. 44, (2), 1999, pp. 101–108.

[35] Mueller, R. H. G., "Special vortices at a helicopter rotor blade," *Journal of the American Helicopter Society*, Vol. 35, (4), 1990, pp. 16–22.

[36] Tangler, J. L., "Experimental investigation of the subwing tip and its vortex structure," NASA Technical Report, 1978.

[37] Martin, P. B. and Bhagwat, M. J. and Leishman, J. G., "Visualization of a helicopter rotor wake in hover," 17th Applied Aerodynamics Conference, 1999, pp. 3225.

[38] Jain, R.t and Conlisk, A. T., "Interaction of Tip-Vortices in the Wake of a Two-Bladed Rotor in Axial Flight," *Journal of the American Helicopter Society*, Vol. 45, (3), 2000, pp. 157–164.

[39] Chen, A. L. and Jacob, J. D. and Savas, Ö., "Dynamics of corotating vortex pairs in the wakes of flapped airfoils," *Journal of Fluid Mechanics*, Vol. 382, 1999, pp. 155–193.

[40] Bristol, R. L. and Ortega, J. M. and Marcus, P. S. and Savas, Ö., "On cooperative instabilities of parallel vortex pairs," *Journal of Fluid Mechanics*, Vol. 517, 2004, pp. 331–358.

[41] Taylor, M. K., "A balsa-dust technique for air-flow visualization and its application to flow through model helicopter rotors in static thrust," National Advisory Committee for Aeronautics (NACA) Technical Note 2220, 1950.

[42] Taylor, M. K., "Air-Flow Visualization for Several Rotor Configuration," National Advisory Committee for Aeronautics (NACA) Technical Note 2220, 1950. Retrieved from *https://www.youtube.com/watch?v=rxO5DdkJhcc* (Last accessed August 24, 2017).

[43] Andrew, M. J., "Coaxial rotor aerodynamics in hover," *Vertica*, Vol. 5, 1981, pp. 163–172.

[44] Nagashima, T and Nakanishi, K., "Optimum performance and wake geometry of co-axial rotor in hover," *Vertica*, Vol. 7, 1983, pp. 225–239.

[45] Akimov, A. I. and Butov, V. P. and Bourtsev, B. N. and Selemenev, S. V., "Flight investigation of coaxial rotor tip vortex structure," Annual Forum Proceedings-American Helicopter Society, Vol. 50, 1994, pp. 1431-1431.

[46] Kim, H. W. and Brown, R. E., "Coaxial rotor performance and wake dynamics in steady and manoeuvring flight," Annual Forum Proceedings-American Helicopter Society, Vol. 62, (1) 2006, pp. 20.

[47] Kim, H. W. and Brown, R. E., "A comparison of coaxial and conventional rotor performance," *Journal of the American Helicopter Society*, Vol. 55, (1), 2010, pp. 12004–12004.

[48] Harrington, R. D., "Full-scale-tunnel investigation of the static-thrust performance of a coaxial helicopter rotor," DTIC Document, 1951.

[49] McAlister, K. W. and Tung, C. and Rand, O. and Khromov, V. and Wilson, J. S., "Experimental and numerical study of a model coaxial rotor," American Helicopter Society 62nd Annual Forum, Phoenix, AZ, 2006.

[50] Leishman, J. G. and Syal, M., "Figure of merit definition for coaxial rotors," *Journal of the American Helicopter Society*, Vol. 53, (3), 2008, pp. 290–300.

[51] Leishman, J. G. and Ananthan, S., "An optimum coaxial rotor system for axial flight," *Journal of the American Helicopter Society*, Vol. 53, (4), 2008, pp. 366–381.

[52] Lei, Y. and Bai, Y. and Xu, Z. and Gao, Q. and Zhao, C., "An experimental investigation on aerodynamic performance of a coaxial rotor system with different rotor spacing and wind speed," *Experimental Thermal and Fluid Science*, Vol. 44, 2013, pp. 779–785.

[53] Ramasamy, M., "Hover performance measurements toward understanding aerodynamic interference in coaxial, tandem, and tilt rotors," *Journal of the American Helicopter Society*, Vol. 60, (3), 2015, pp. 1–17.

[54] Konuş, M. F. and Savaş, Ö., "Rotor vortex wake in close proximity of walls in hover," *Journal of the American Helicopter Society*, Vol. 61, (4), 2016, pp. 1–12.

[55] Green, R. B. and Caradonna, F. X. and others, "Coupled thrust and vorticity dynamics during vortex ring state," *Journal of the American Helicopter Society*, Vol. 54, (2), 2009, pp. 22001–22001.

[56] Stack, J. and Caradonna, F. X. and Savaş, Ö., "Flow visualizations and extended thrust time histories of rotor vortex wakes in descent," *Journal of the American Helicopter Society*, Vol. 50, (3), 2005, pp. 279–288.

[57] Sholl, M. and Savas, Ö., "A fast Lagrangian PIV method for study of general high-gradient flows," 35th Aerospace Sciences Meeting and Exhibit, 1997, pp. 493.

[58] Ortega, J. M. and Bristol, R. L. and Savas, Ö., "Experimental study of the instability of unequal-strength counter-rotating vortex pairs," *Journal of Fluid Mechanics*, Vol. 474, 2003, pp. 35–84.

[59] Batchelor, G. K., *An Introduction to Fluid Dynamics*, Cambridge University Press, 2000.

[60] Brand, A. and Dreier, M. and Kisor, R. and Wood, T., "The nature of vortex ring state," *Journal of the American Helicopter Society*, Vol. 56, (2), 2011, pp. 22001–22001.

[61] Haidari, A. H. and Smith, C. R., "The generation and regeneration of single hairpin vortices," *Journal of Fluid Mechanics*, Vol. 277, 1994, pp. 135–162.

Appendix A

Particle Image Velocimetry Measurements

A.1 Processing Parameters for WALPT

The following are the parameters used in WALPT processing of PIV image pairs:
lptmode, 0=singlepass, 1=small to large, 2=large to small, 3=LPT
3 2 0 1 0
file that contains the names of image files, prefix for outputfiles
ab.txt
image size nxc, nyc, pixr
1280 1024 8 1.00
flow size, nxf, nyf
1280 1024 flow offset, xf, yf
0 0
window size, nxw, nyw, 2**n
32 32
amod, min, max windows dimensions 2**n, correlaltion level corlvl
1 8 32 0.40
step size, nxs, nys
8 8
window type, wtype 1-7, see source listing
2
peak type, ptype 0=grid,1=parabolic,2=gaussian
2
laundary type, ltype 0=no laundering,1=rejection
0
extension parameter, 0= none, zero padding, 1= smooth (nth order)
0
filter widths (1/) fltrwx,fltrwy wavenlength in steps; exponent
9 9 2
wall parameters: nwalls, parex, motion, intflag, outmask 0 0 0 1 1
wall geometry file
plane1.raw

motion parameters: dxcg, dycg ,rot
0.00 0.00 0.00
0.00 0.00 0.00
9.00 0.00 0.00

A.2 Results of PIV Measurements

The results of PIV measurements at 2, 4 & 6 rps are presented from Figure 3.5 to Figure A.78. Data representation is similar to what is given in PIV results at 8 rps, which are shown in Chapters 3 & 4. Instantaneous fields are presented on the left columns and the average ones on the right. In frames (a) in the first rows, an instant of particle flow visualization is shown. In frames (b) are given averaged flow pictures. They are averaged over two rotor revolutions, i.e. 36 successive images. In row 2 is given instantaneous and average vorticity fields. Streamlines drawn over instantaneous and average vorticity fields are shown in third rows. Streamlines in frames (e) of row 3 are drawn in a moving reference frame to highlight the individual vortices. In fourth row of each figure is given instantaneous and average speeds, over which streamlines are drawn. Average images are constructed by superposing successive processed image pairs. There are a total of 2999 processed image pairs. The positions of the rotor disks are marked in frames (d) in second rows.

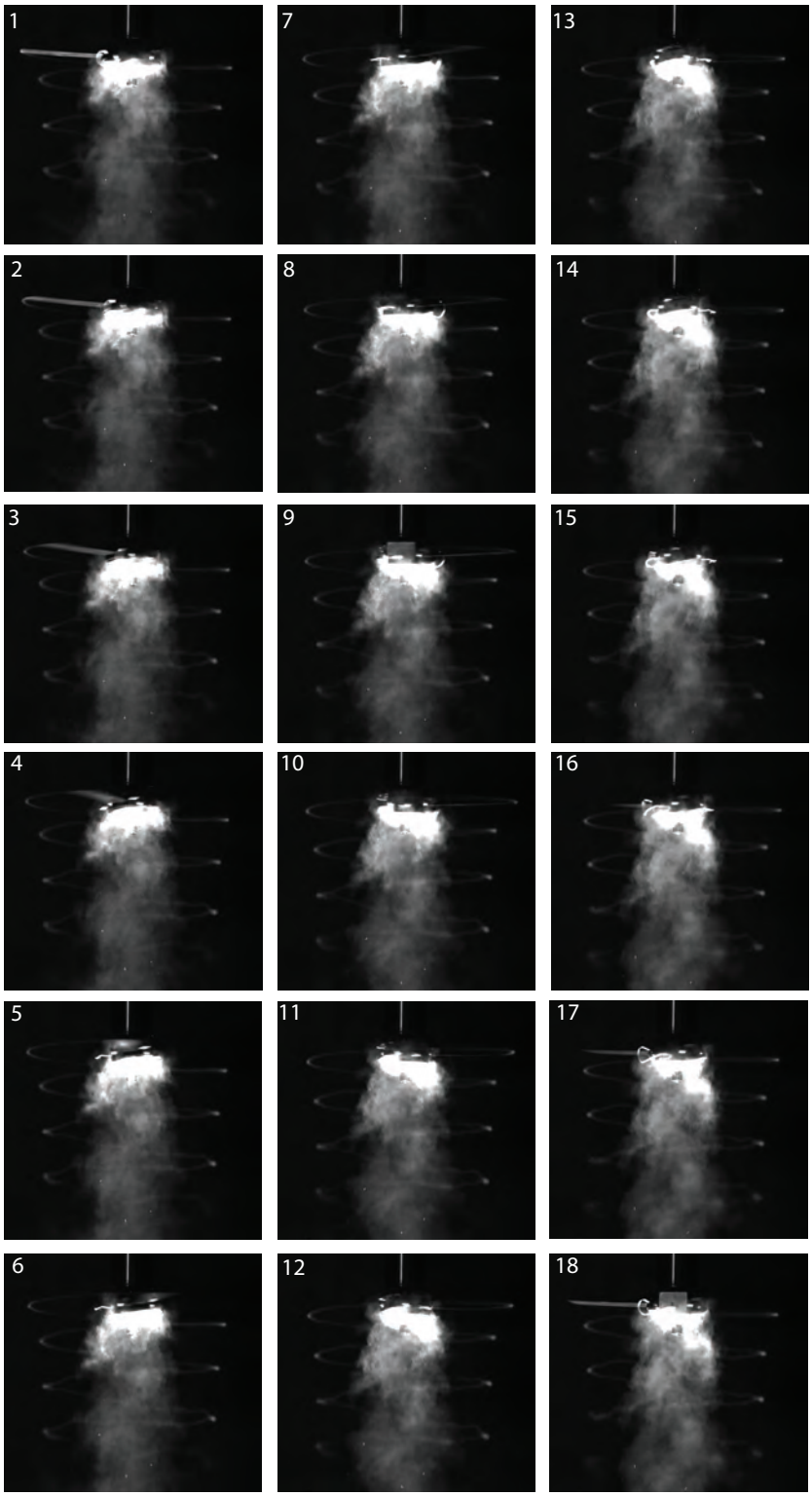

Figure A.1: Vortex wake evolution of the one-bladed single rotor during one complete rotor revolution at 6 rps. Images are 20° ($\pi/9$ rad) apart. Time separation between successive images is 9.26 ms.

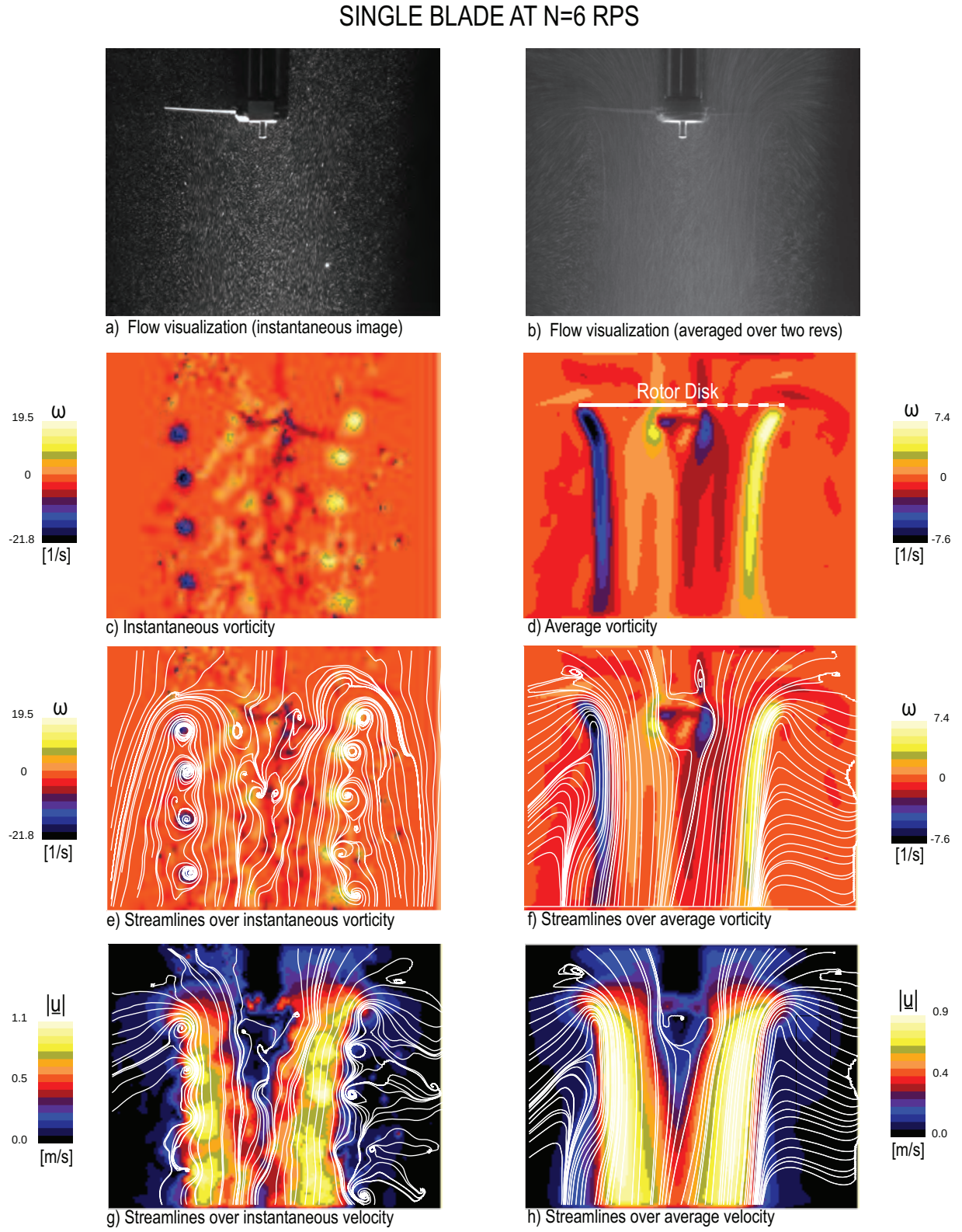

Figure A.2: Flow field of a single-bladed rotor at $N = 6$ rps. First row (a,b): particle flow visualization. In rows 2-4 are shown PIV measurements. Second row (c,d): vorticity fields. Third row (e,f): streamlines over vorticity. Fourth row (g,h): streamlines over speed. Streamlines in frame (e) are drawn from a moving reference frame and streamlines in frames (f-h) are drawn from a stationary reference frame.

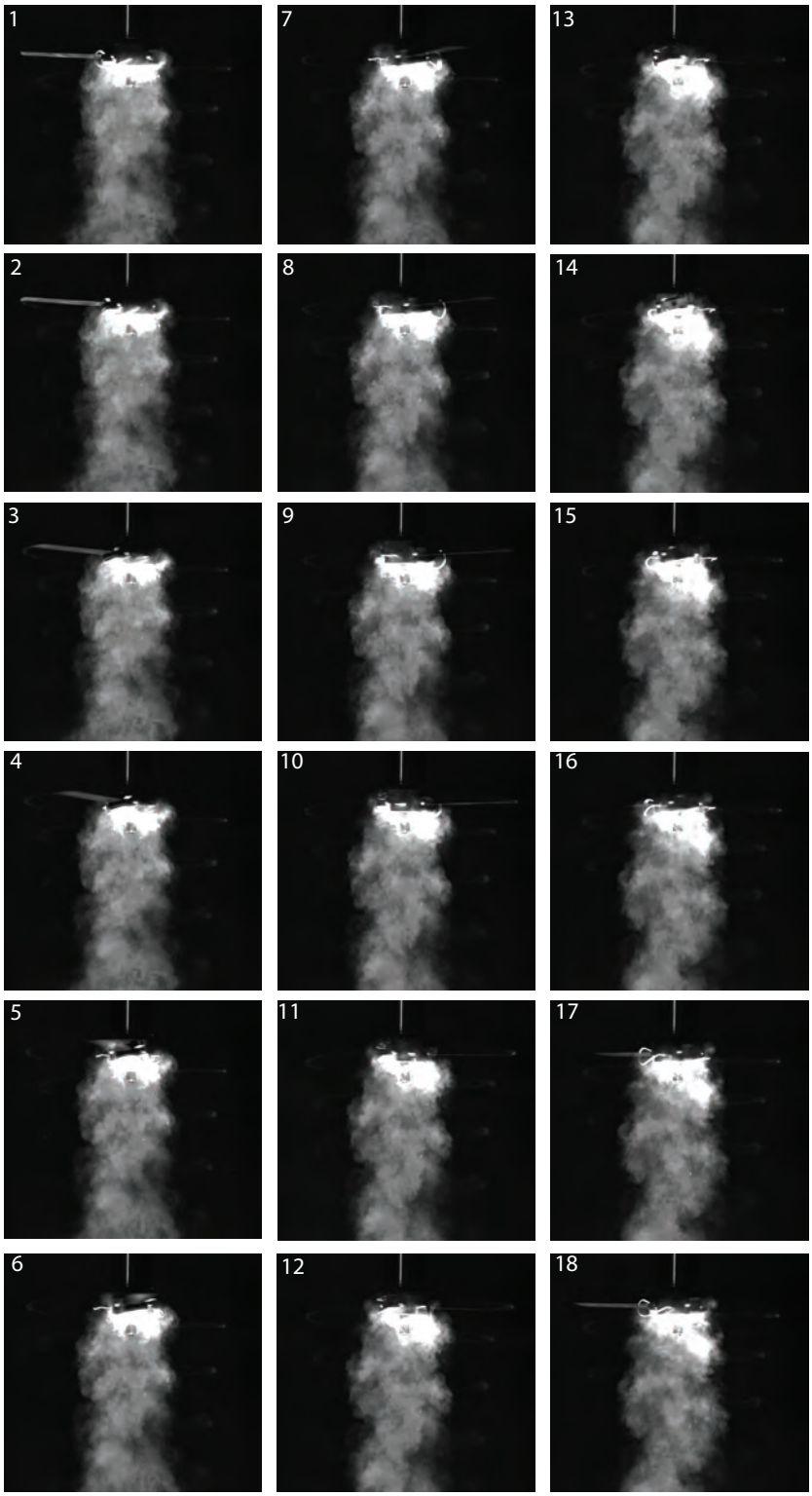

Figure A.3: Vortex wake evolution of the one-bladed single rotor during one complete rotor revolution at 4 rps. Images are 20° ($\pi/9$ rad) apart. Time separation between successive images is 13.89 ms.

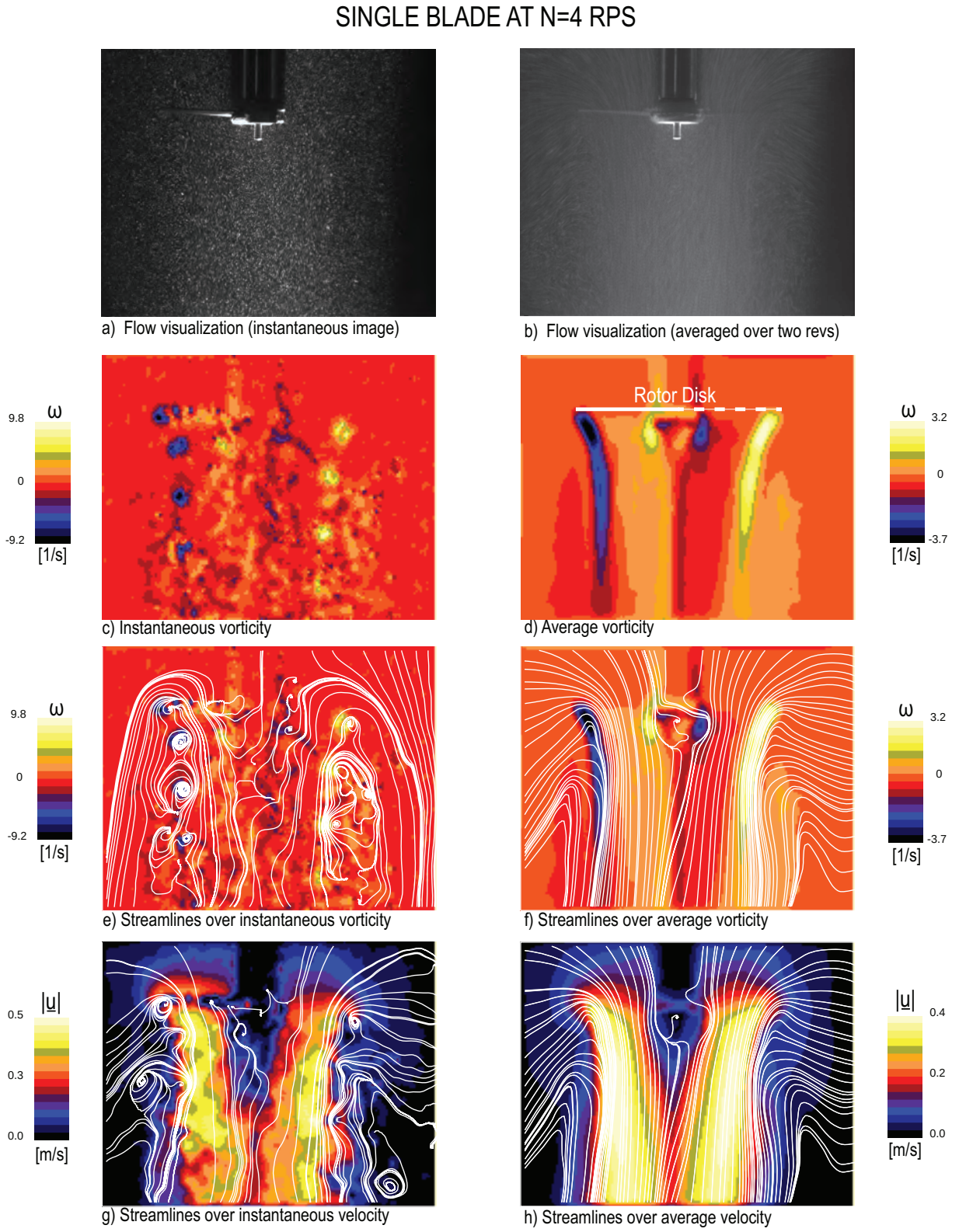

Figure A.4: Flow field of a single-bladed rotor at $N = 4$ rps. First row (a,b): particle flow visualization. In rows 2-4 are shown PIV measurements. Second row (c,d): vorticity fields. Third row (e,f): streamlines over vorticity. Fourth row (g,h): streamlines over speed. Streamlines in frame (e) are drawn from a moving reference frame and streamlines in frames (f-h) are drawn from a stationary reference frame.

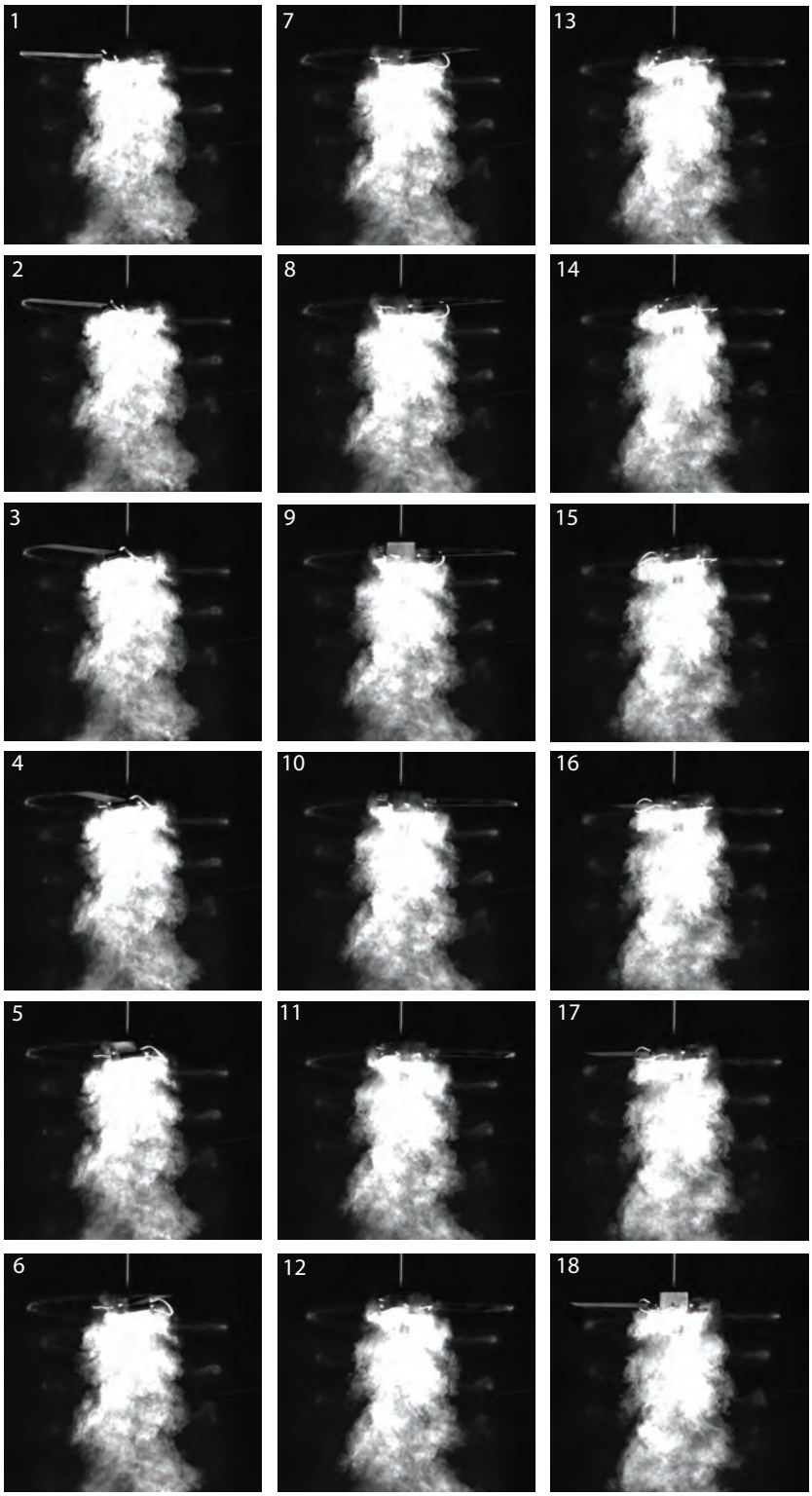

Figure A.5: Vortex wake evolution of the one-bladed single rotor during one complete rotor revolution at 2 rps. Images are 20° ($\pi/9$ rad) apart. Time separation between successive images is 27.78 ms.

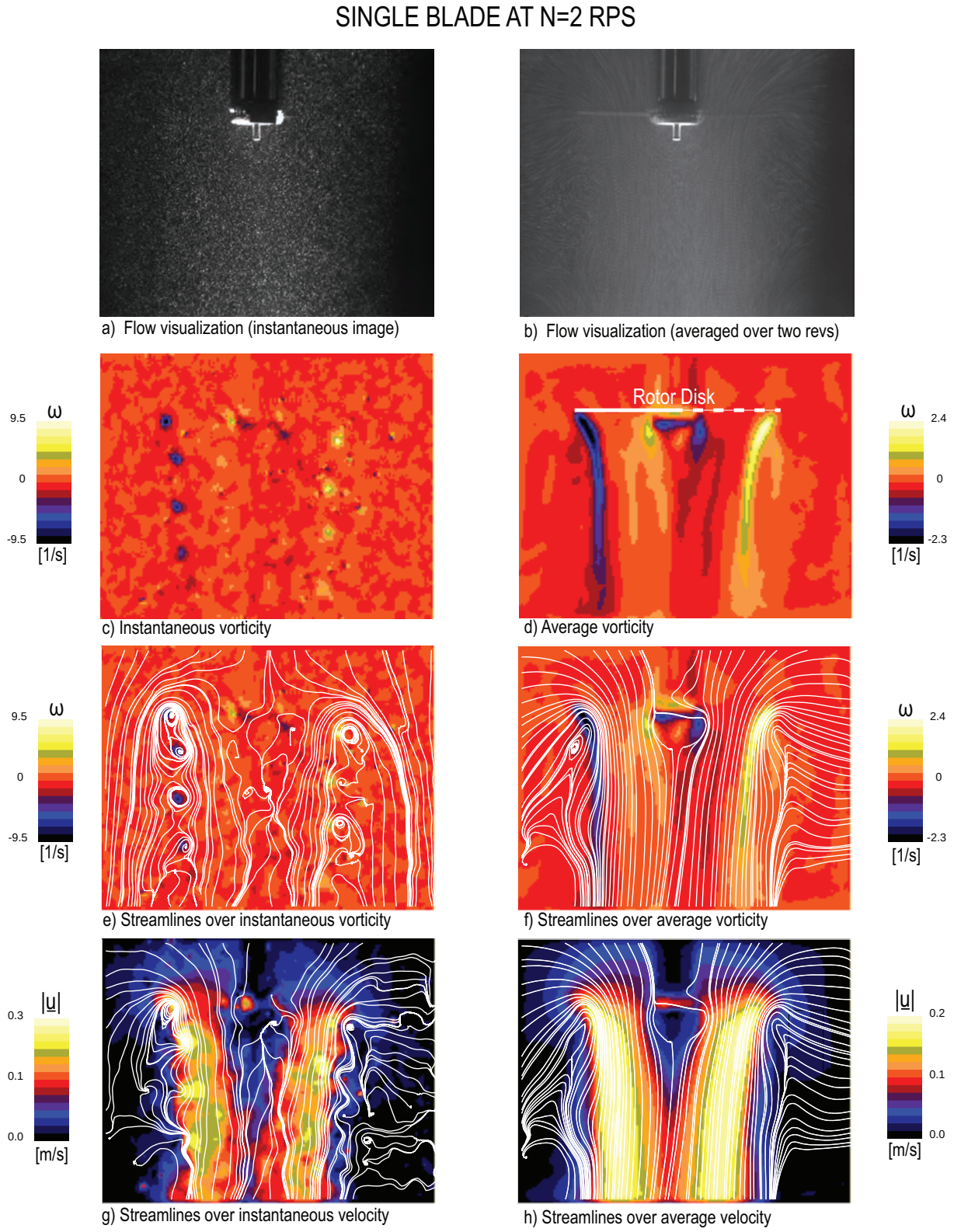

Figure A.6: Flow field of a single-bladed rotor at $N = 2$ rps. First row (a,b): particle flow visualization. In rows 2-4 are shown PIV measurements. Second row (c,d): vorticity fields. Third row (e,f): streamlines over vorticity. Fourth row (g,h): streamlines over speed. Streamlines in frame (e) are drawn from a moving reference frame and streamlines in frames (f-h) are drawn from a stationary reference frame.

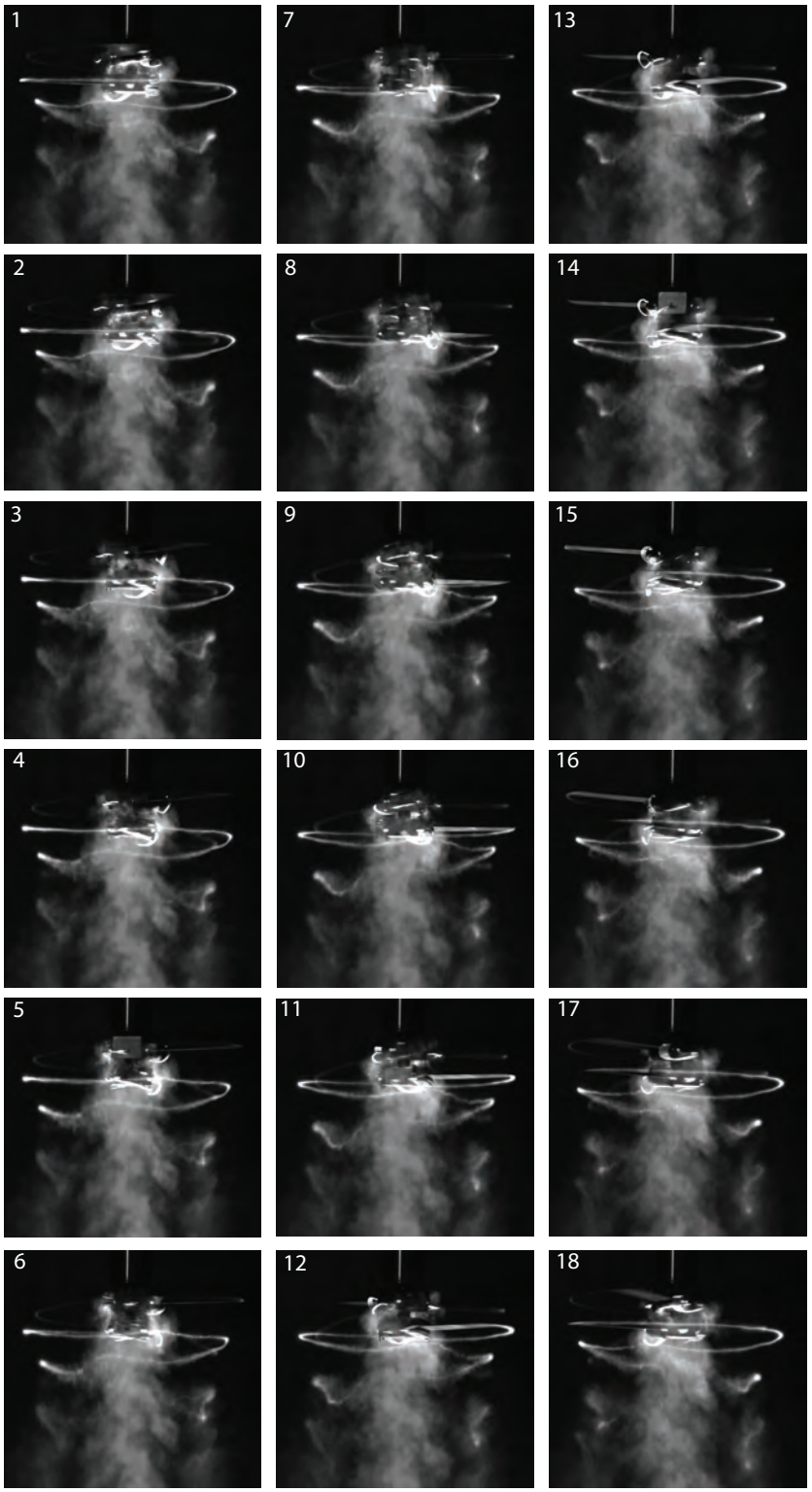

Figure A.7: Vortex wake evolution of the one-bladed coaxial rotors with axial spacing of H/R=0.25 during one complete rotor revolution at 6 rps. Images are 20° ($\pi/9$ rad) apart. Time separation between successive images is 9.26 ms.

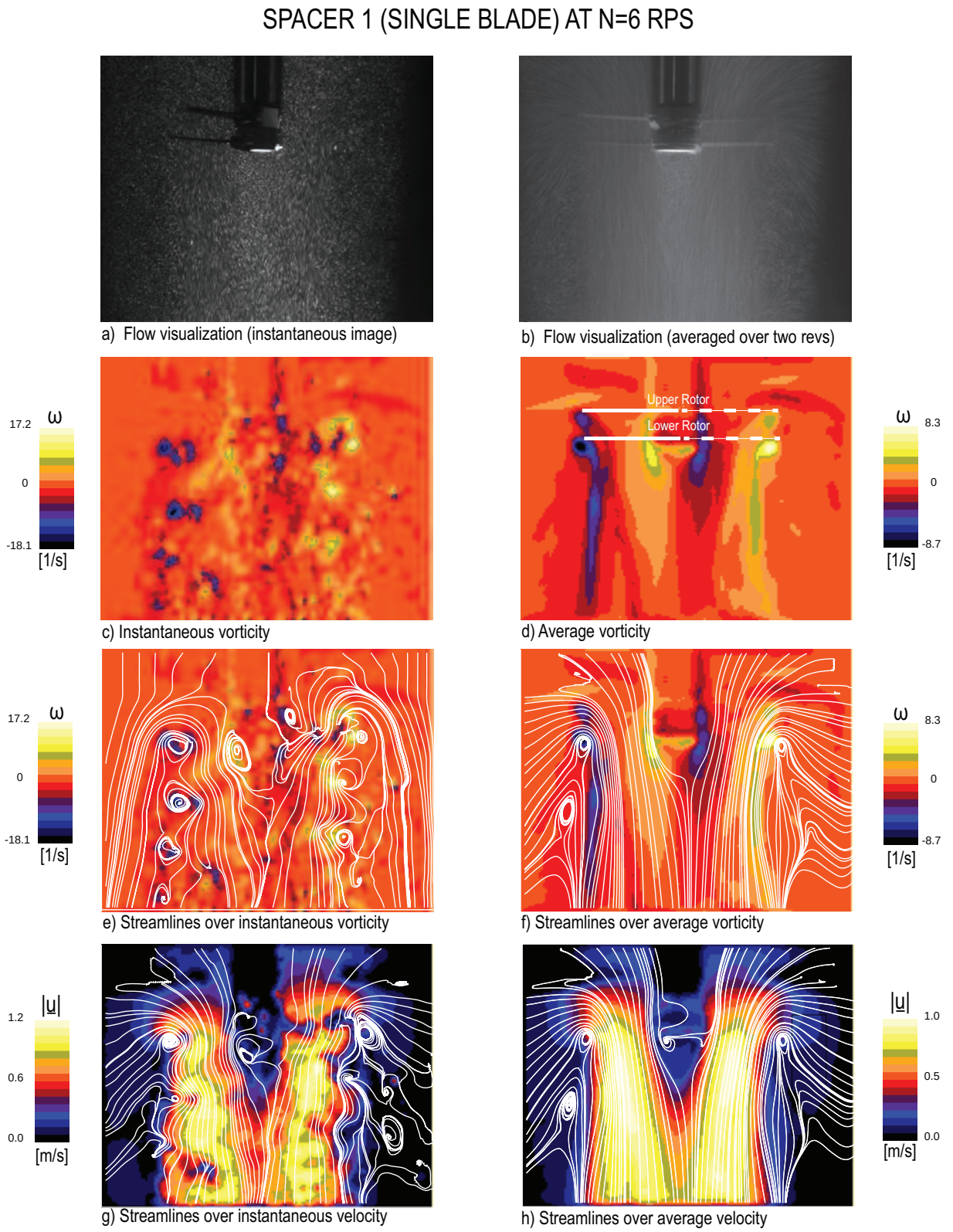

Figure A.8: Flow field of a single-bladed coaxial rotor (spacer1) at $N = 6$ rps. First row (a,b): particle flow visualization. In rows 2-4 are shown PIV measurements. Second row (c,d): vorticity fields. Third row (e,f): streamlines over vorticity. Fourth row (g,h): streamlines over speed. Streamlines in frame (e) are drawn from a moving reference frame and streamlines in frames (f-h) are drawn from a stationary reference frame.

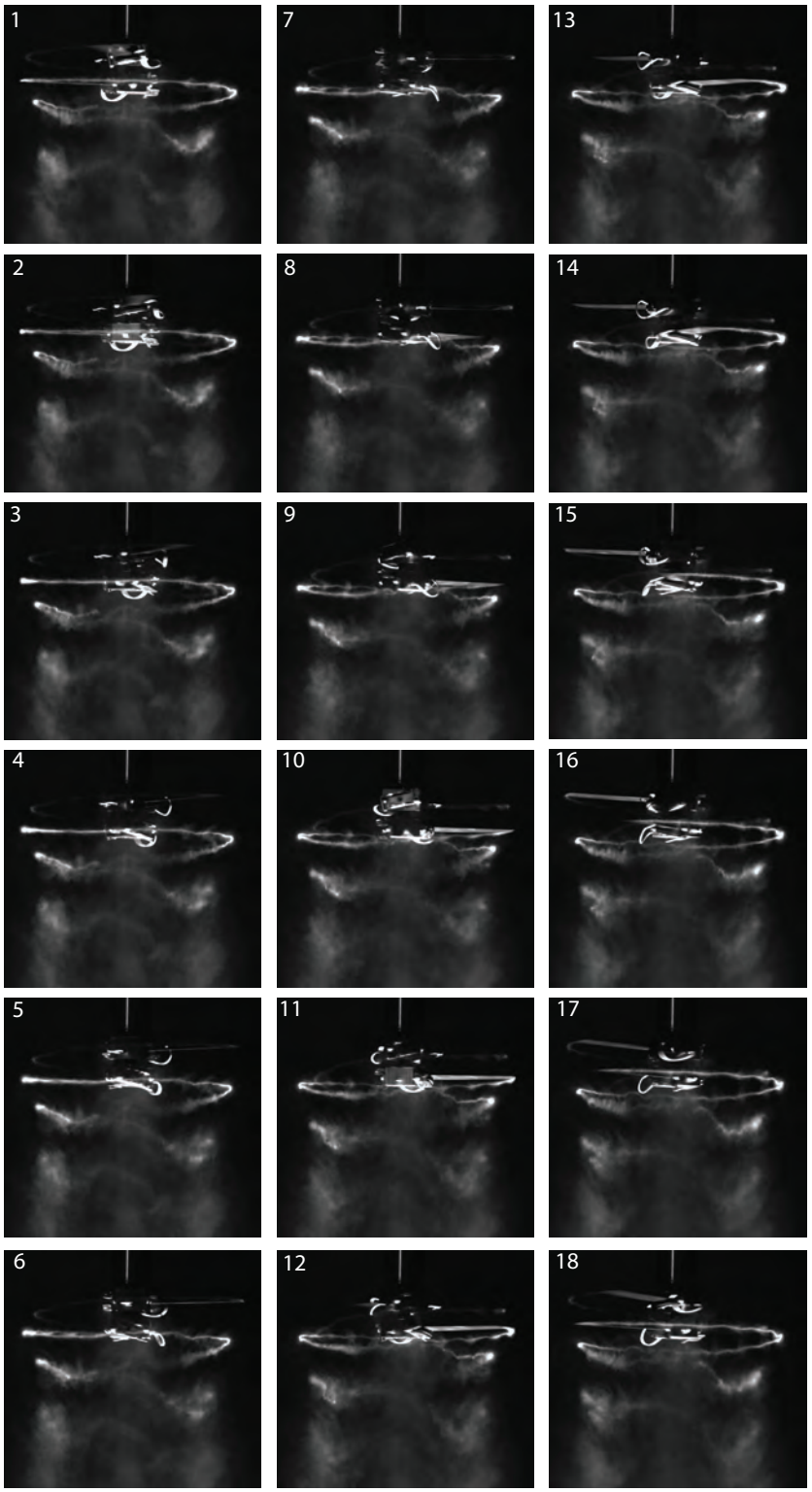

Figure A.9: Vortex wake evolution of the one-bladed coaxial rotors with axial spacing of H/R=0.25 during one complete rotor revolution at 4 rps. Images are 20° ($\pi/9$ rad) apart. Time separation between successive images is 13.89 ms.

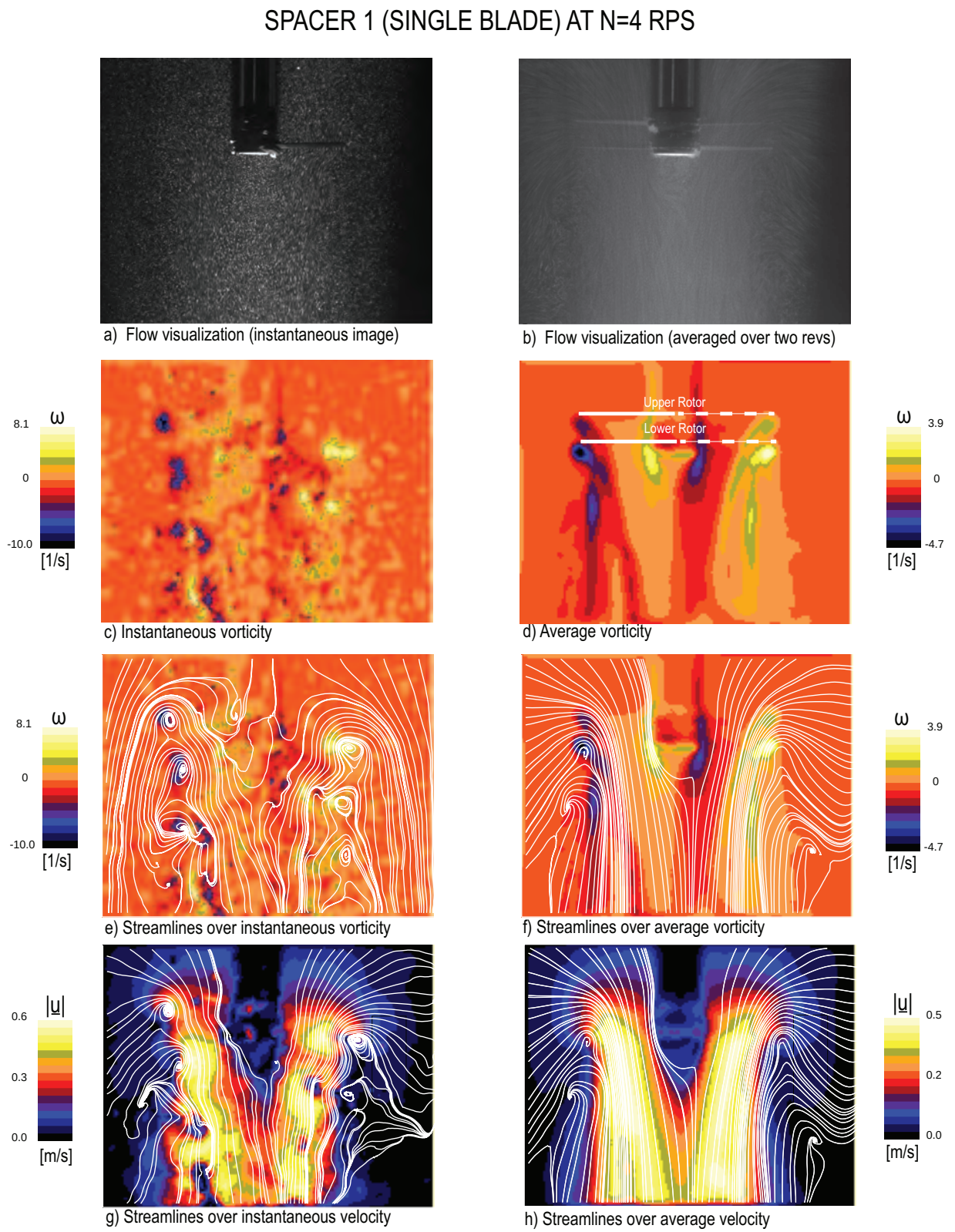

Figure A.10: Flow field of a single-bladed coaxial rotor (spacer1) at $N = 4$ rps. First row (a,b): particle flow visualization. In rows 2-4 are shown PIV measurements. Second row (c,d): vorticity fields. Third row (e,f): streamlines over vorticity. Fourth row (g,h): streamlines over speed. Streamlines in frame (e) are drawn from a moving reference frame and streamlines in frames (f-h) are drawn from a stationary reference frame.

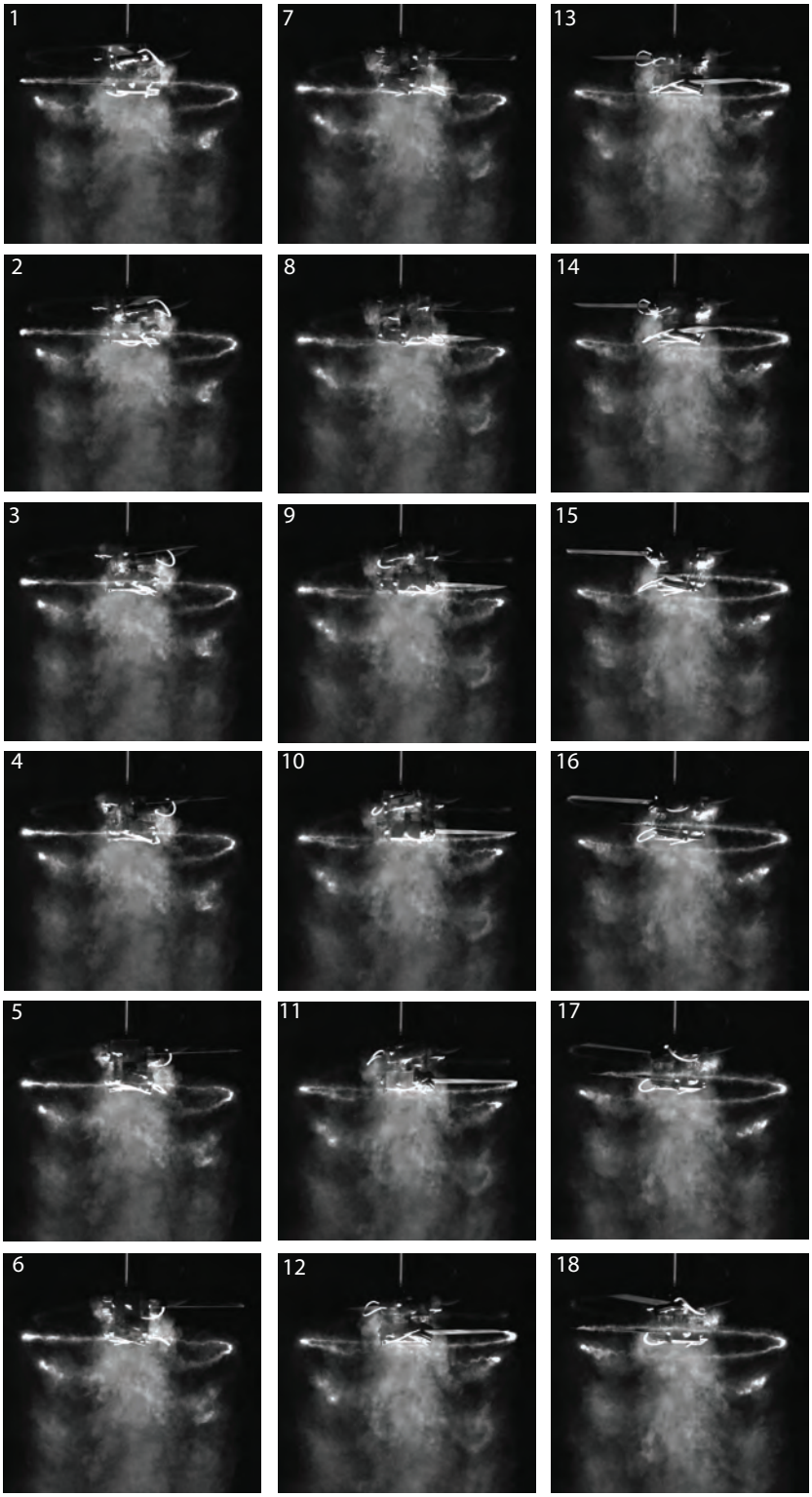

Figure A.11: Vortex wake evolution of the one-bladed coaxial rotors with axial spacing of H/R=0.25 during one complete rotor revolution at 2 rps. Images are 20° ($\pi/9$ rad) apart. Time separation between successive images is 27.78 ms.

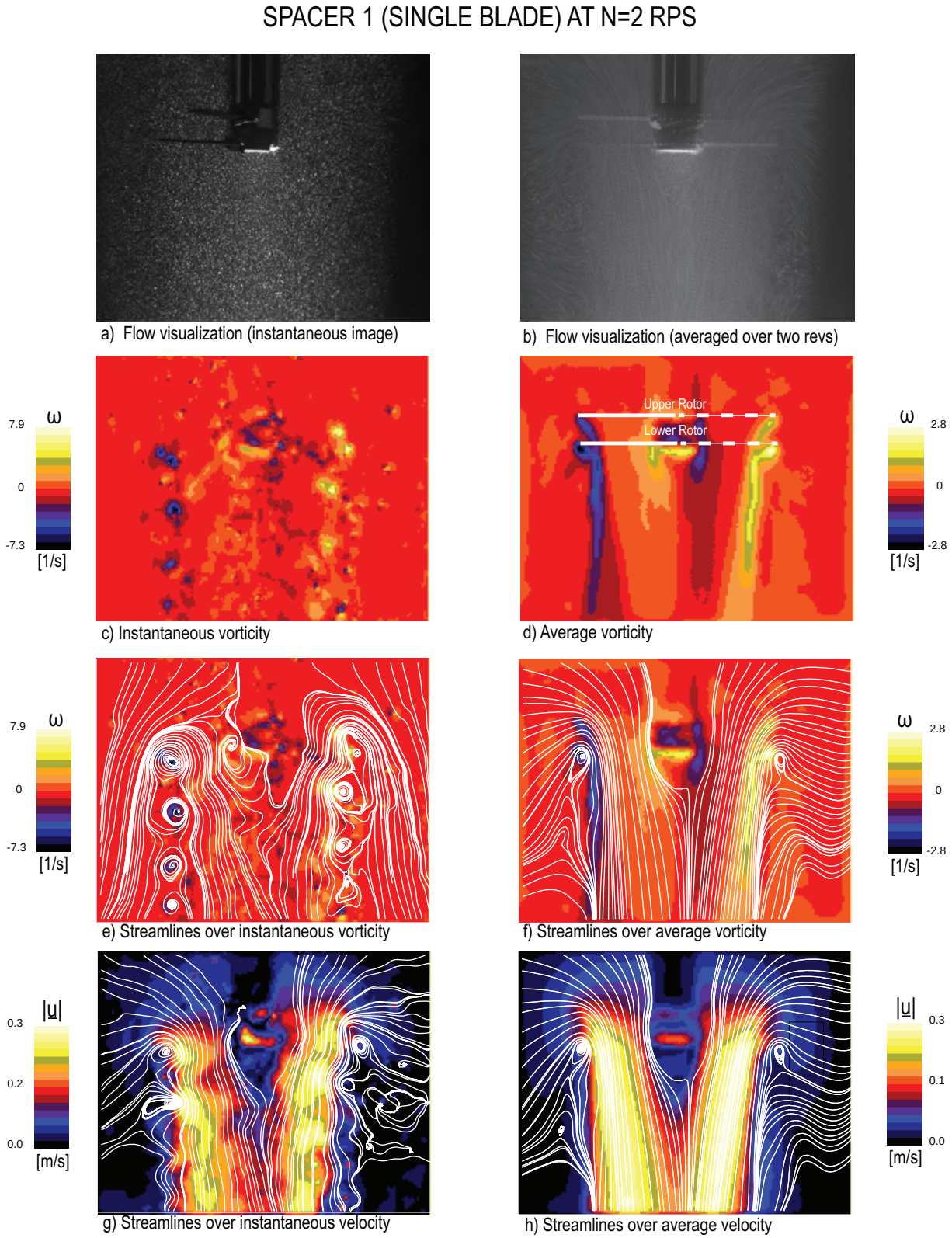

Figure A.12: Flow field of a single-bladed coaxial rotor (spacer1) at $N = 2$ rps. First row (a,b): particle flow visualization. In rows 2-4 are shown PIV measurements. Second row (c,d): vorticity fields. Third row (e,f): streamlines over vorticity. Fourth row (g,h): streamlines over speed. Streamlines in frame (e) are drawn from a moving reference frame and streamlines in frames (f-h) are drawn from a stationary reference frame.

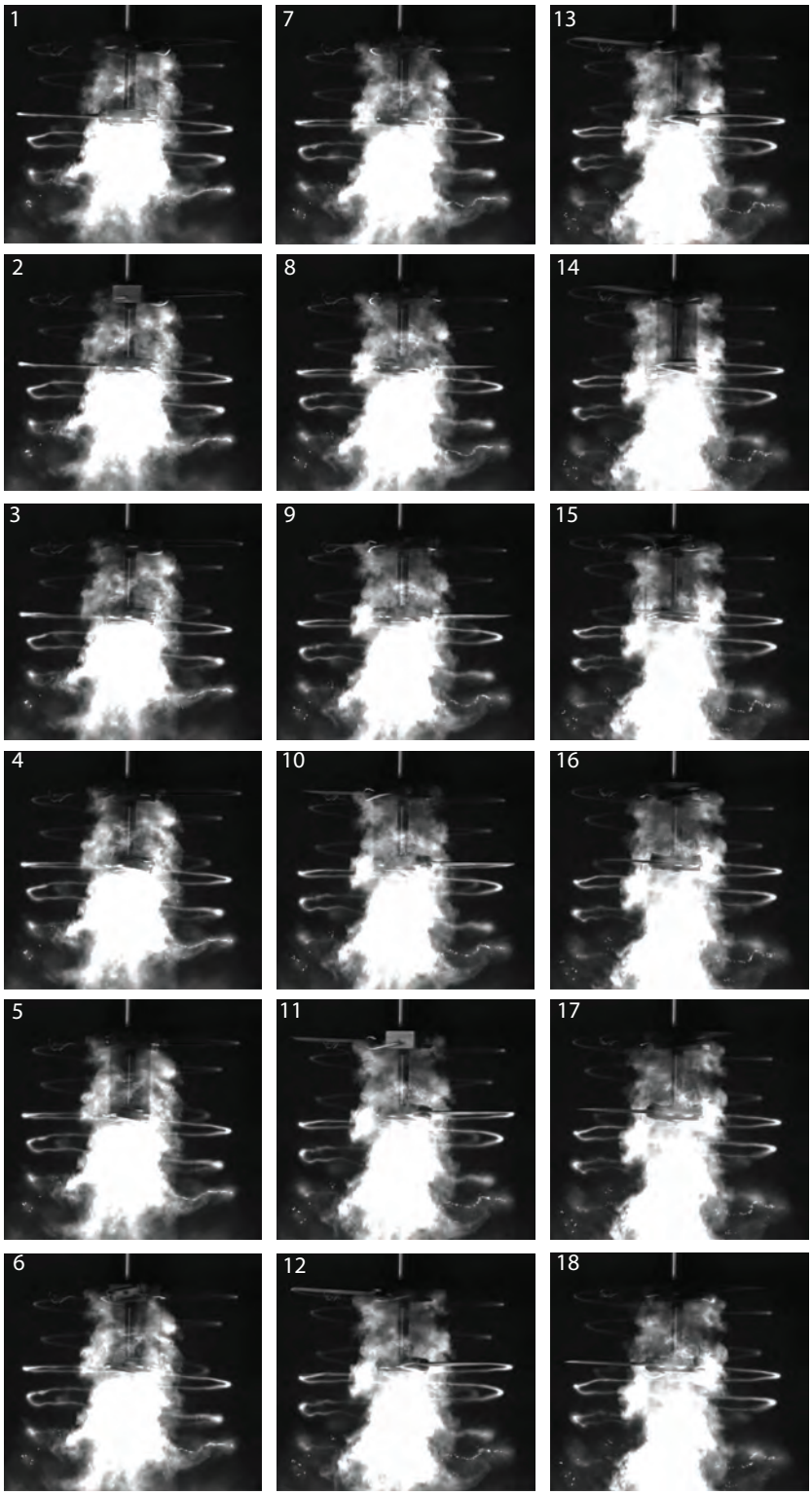

Figure A.13: Vortex wake evolution of the one-bladed coaxial rotors with axial spacing of H/R=0.8 during one complete rotor revolution at 6 rps. Images are 20° ($\pi/9$ rad) apart. Time separation between successive images is 9.26 ms.

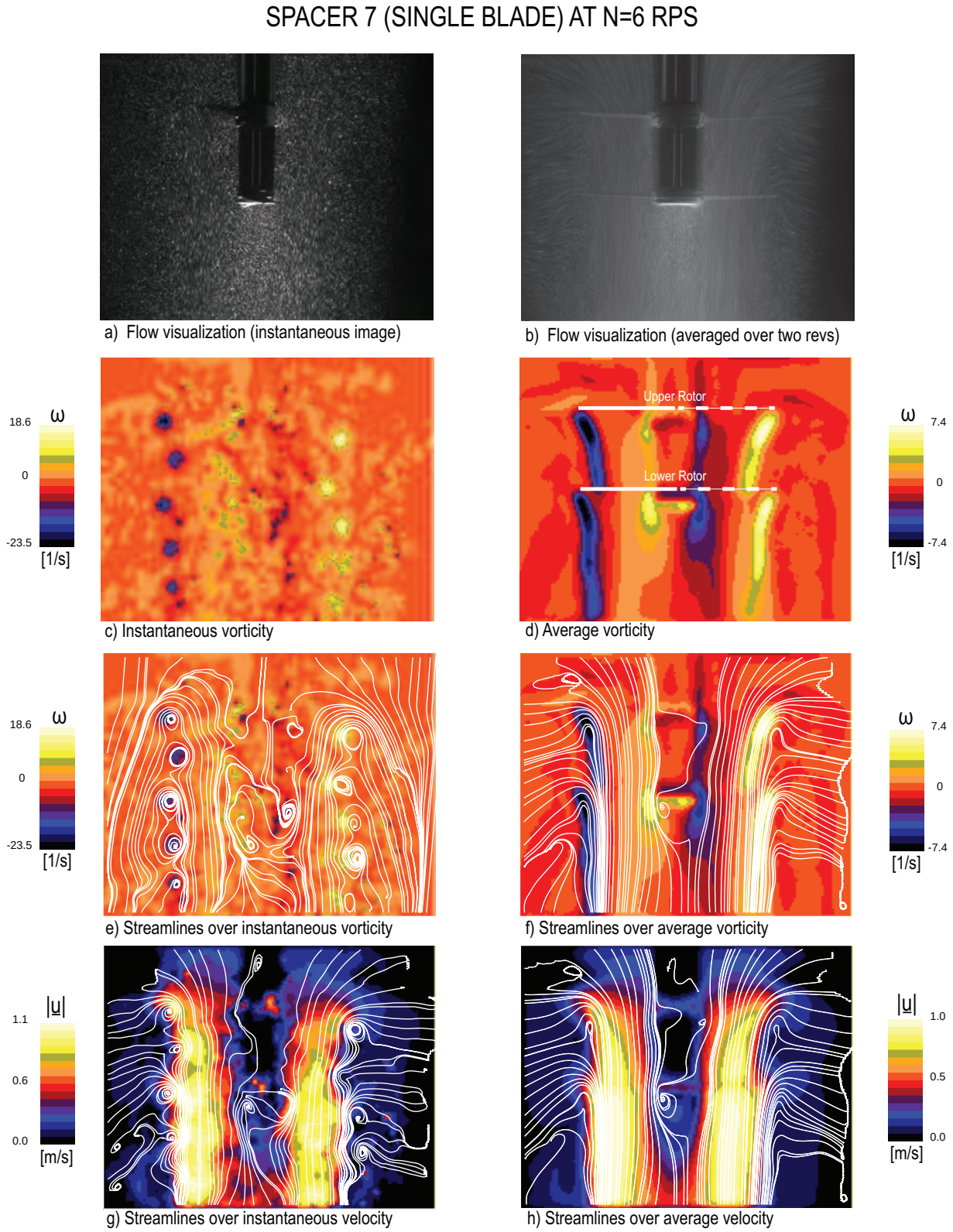

Figure A.14: Flow field of a single-bladed coaxial rotor (spacer7) at $N = 6$ rps. First row (a,b): particle flow visualization. In rows 2-4 are shown PIV measurements. Second row (c,d): vorticity fields. Third row (e,f): streamlines over vorticity. Fourth row (g,h): streamlines over speed. Streamlines in frame (e) are drawn from a moving reference frame and streamlines in frames (f-h) are drawn from a stationary reference frame.

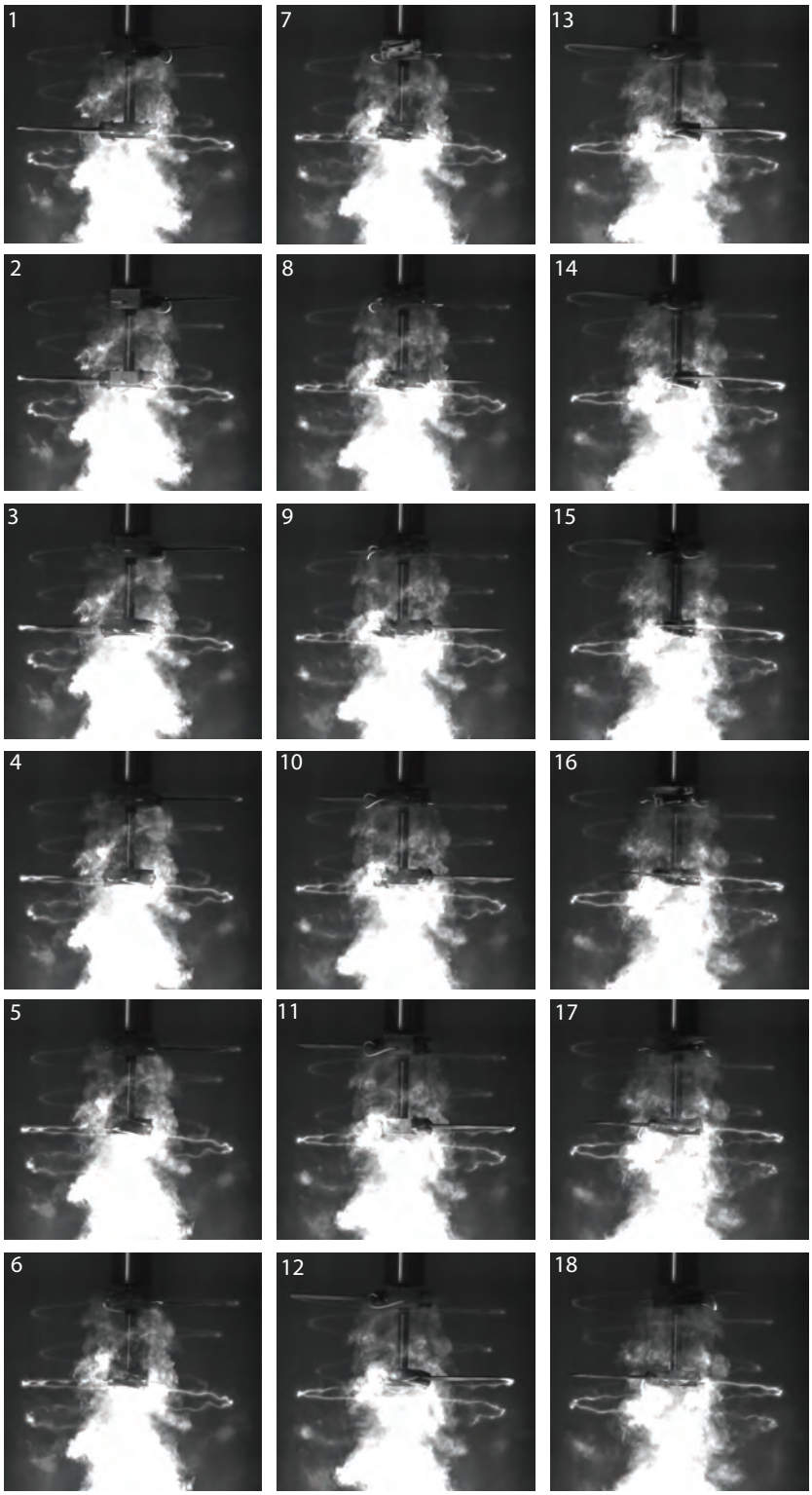

Figure A.15: Vortex wake evolution of the one-bladed coaxial rotors with axial spacing of H/R=0.8 during one complete rotor revolution at 4 rps. Images are 20° ($\pi/9$ rad) apart. Time separation between successive images is 13.89 ms.

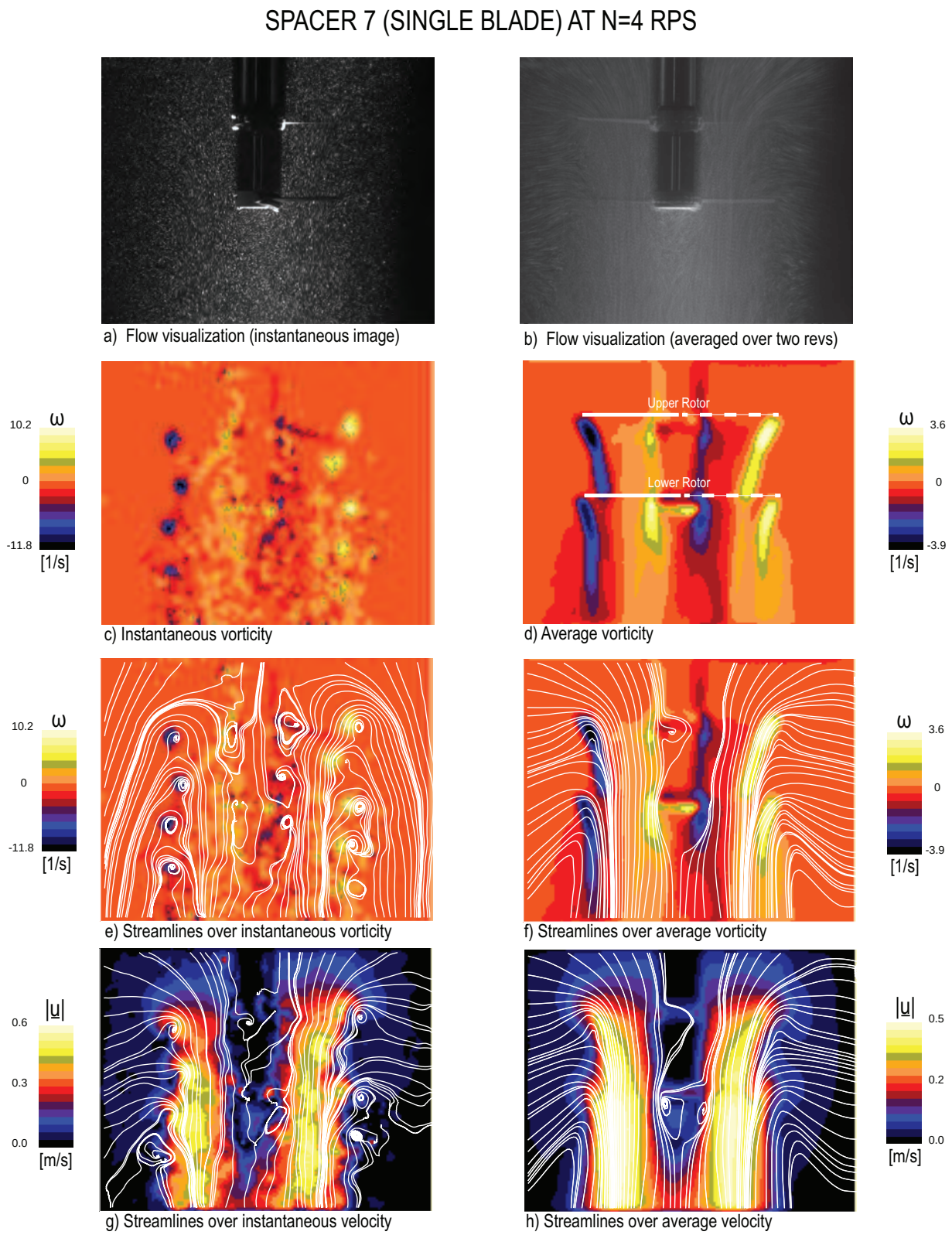

Figure A.16: Flow field of a single-bladed coaxial rotor (spacer7) at $N = 4$ rps. First row (a,b): particle flow visualization. In rows 2-4 are shown PIV measurements. Second row (c,d): vorticity fields. Third row (e,f): streamlines over vorticity. Fourth row (g,h): streamlines over speed. Streamlines in frame (e) are drawn from a moving reference frame and streamlines in frames (f-h) are drawn from a stationary reference frame.

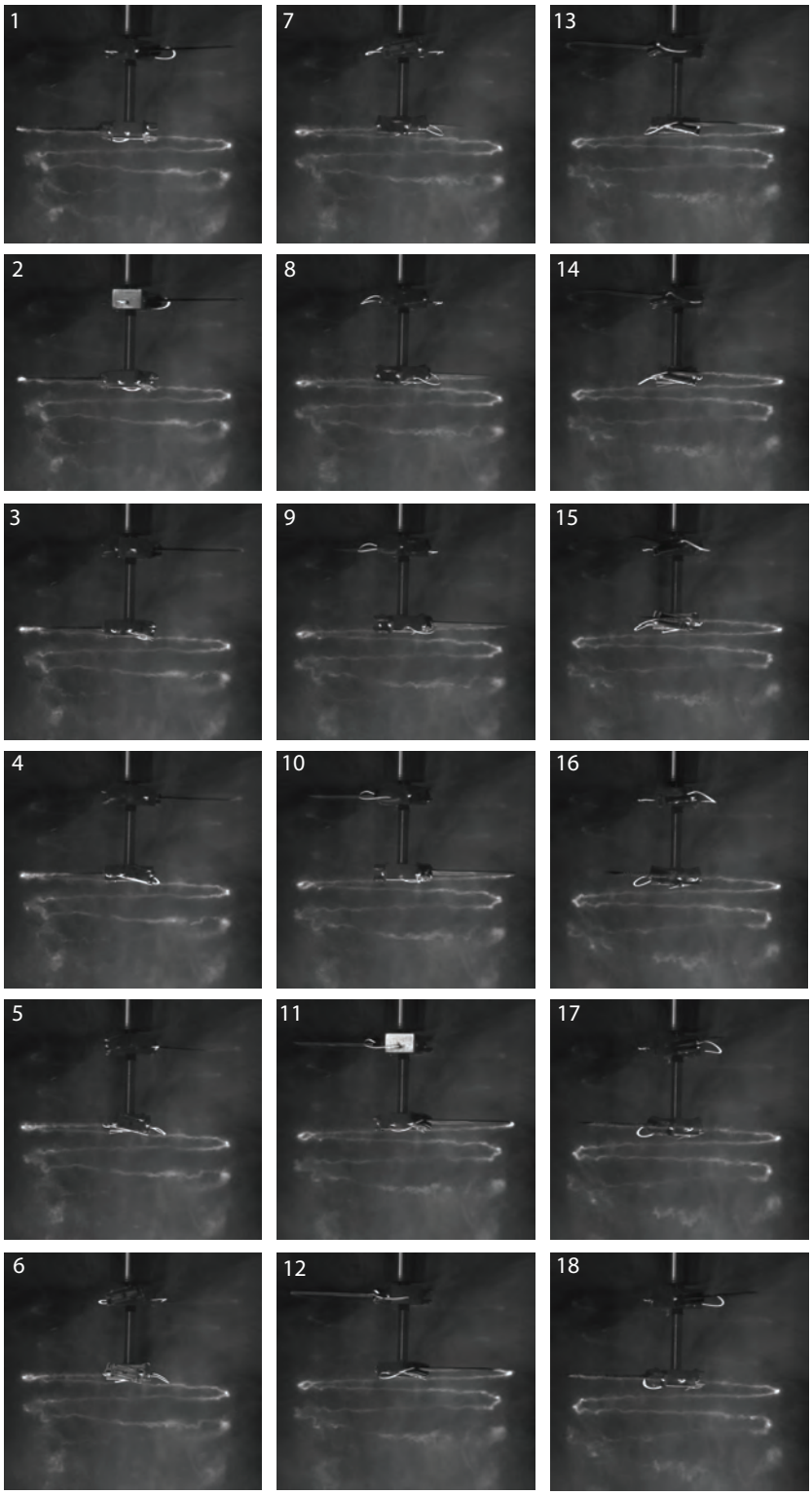

Figure A.17: Vortex wake evolution of the one-bladed coaxial rotors with axial spacing of H/R=0.8 during one complete rotor revolution at 6 rps. Images are 20° ($\pi/9$ rad) apart. Time separation between successive images is 27.78 ms.

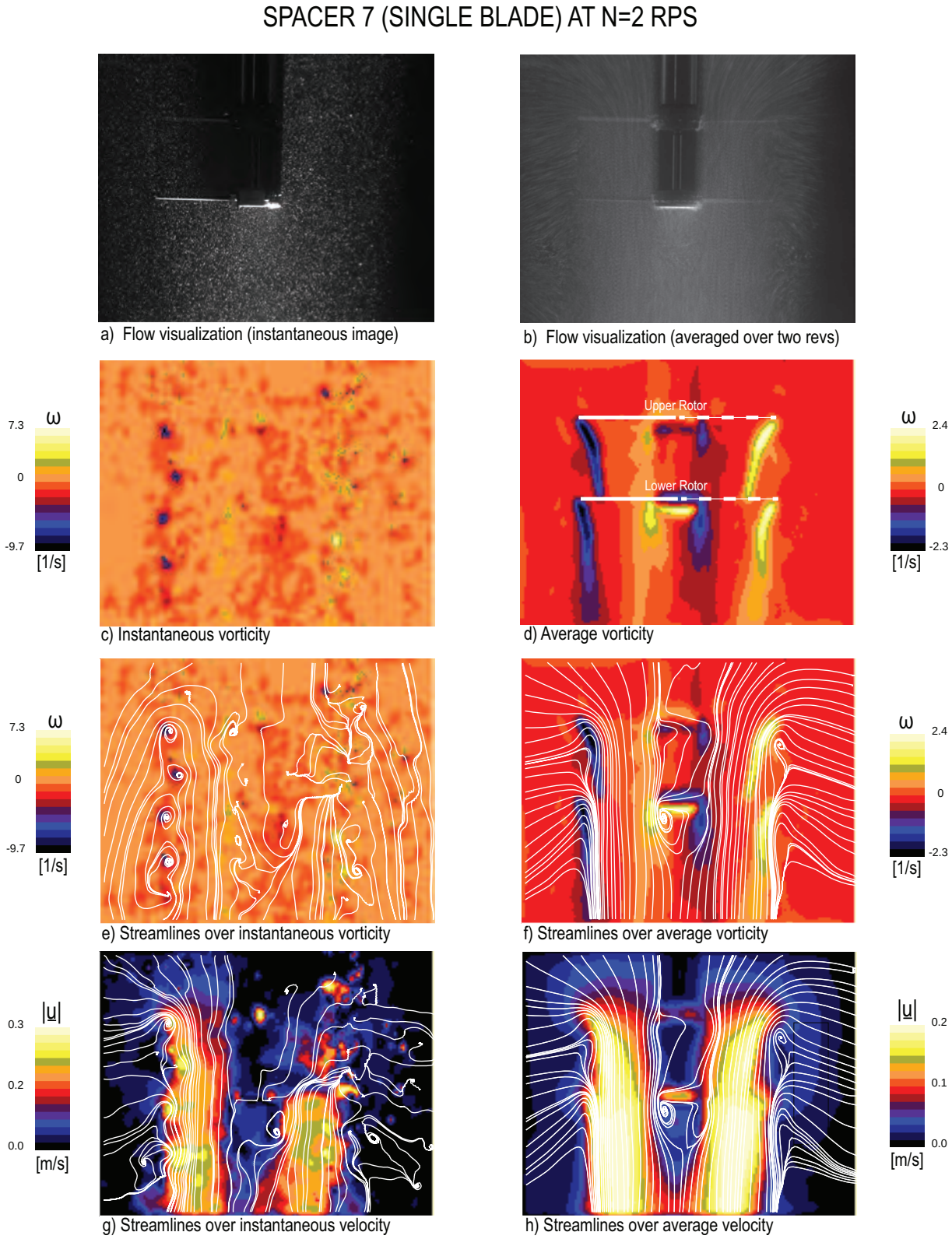

Figure A.18: Flow field of a single-bladed coaxial rotor (spacer7) at $N = 2$ rps. First row (a,b): particle flow visualization. In rows 2-4 are shown PIV measurements. Second row (c,d): vorticity fields. Third row (e,f): streamlines over vorticity. Fourth row (g,h): streamlines over speed. Streamlines in frame (e) are drawn from a moving reference frame and streamlines in frames (f-h) are drawn from a stationary reference frame.

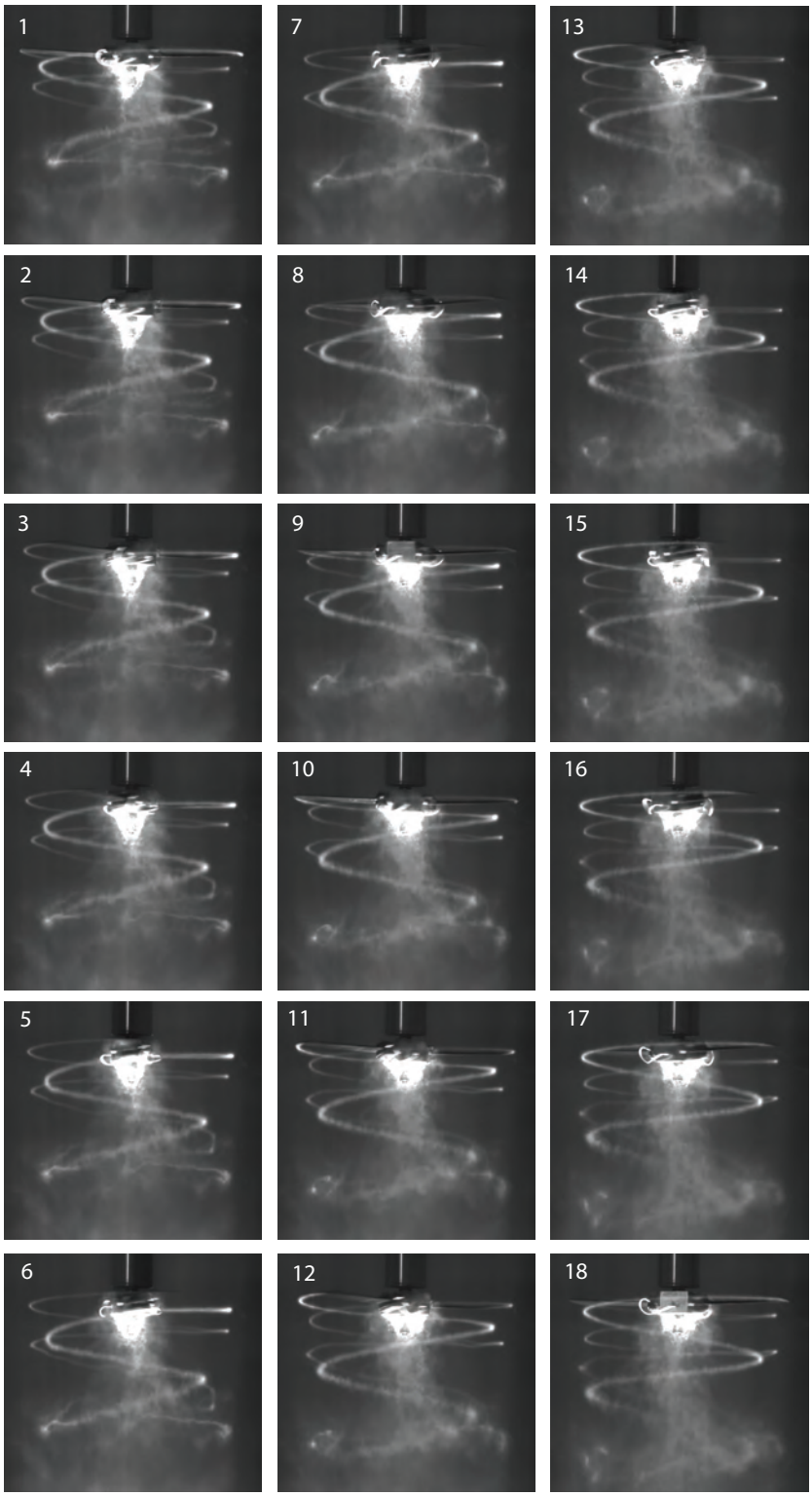

Figure A.19: Vortex wake evolution of the single rotor during one complete rotor revolution at 6 rps is shown. Images are 20° ($\pi/9$ rad) apart. Time separation between successive images is 9.26 ms.

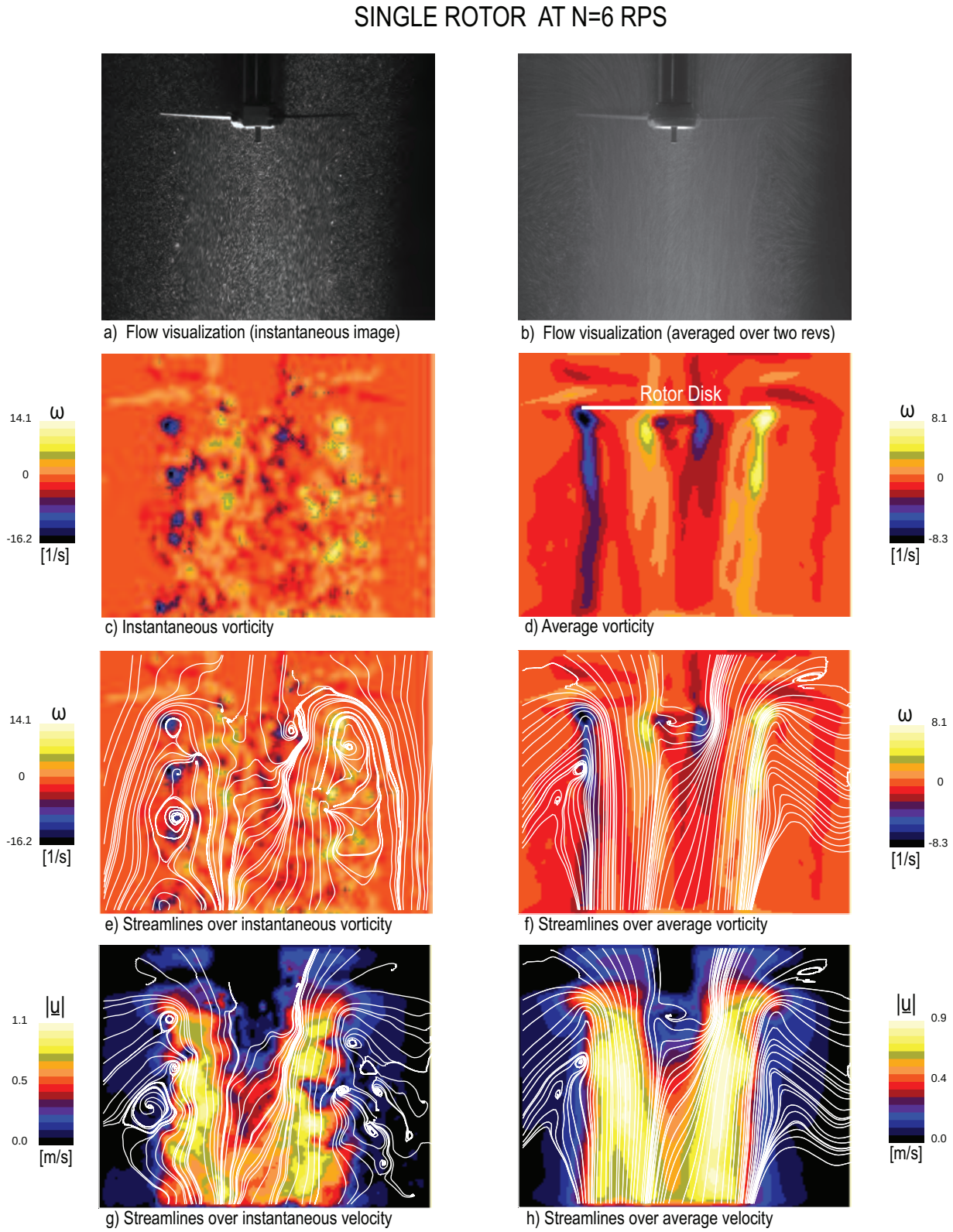

Figure A.20: Flow field of a two-bladed single rotor at $N = 6$ rps. First row (a,b): particle flow visualization. In rows 2-4 are shown PIV measurements. Second row (c,d): vorticity fields. Third row (e,f): streamlines over vorticity. Fourth row (g,h): streamlines over speed. Streamlines in frame (e) are drawn from a moving reference frame and streamlines in frames (f-h) are drawn from a stationary reference frame.

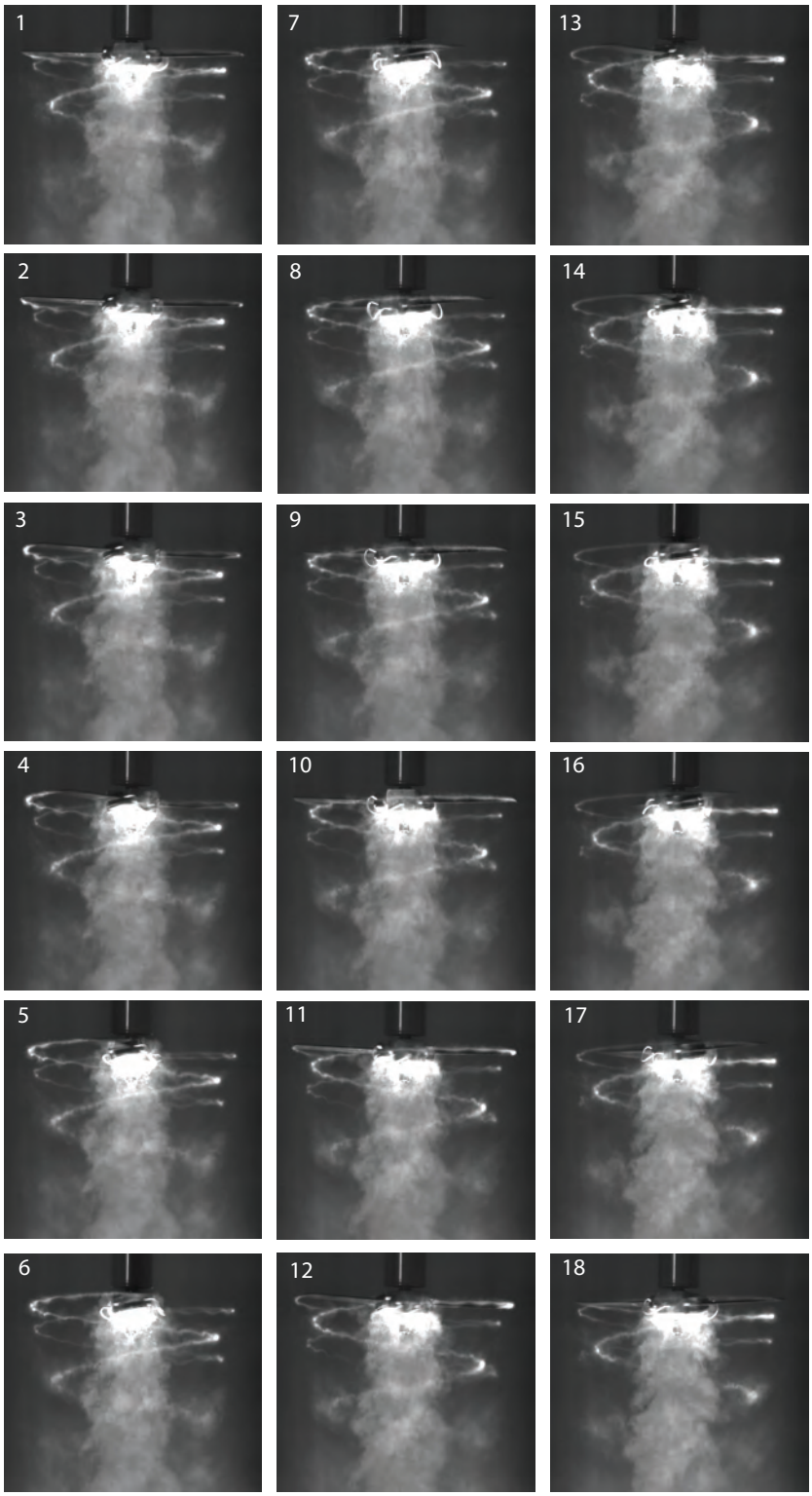

Figure A.21: Vortex wake evolution of the single rotor during one complete rotor revolution at 4 rps is shown. Images are 20° ($\pi/9$ rad) apart. Time separation between successive images is 13.89 ms.

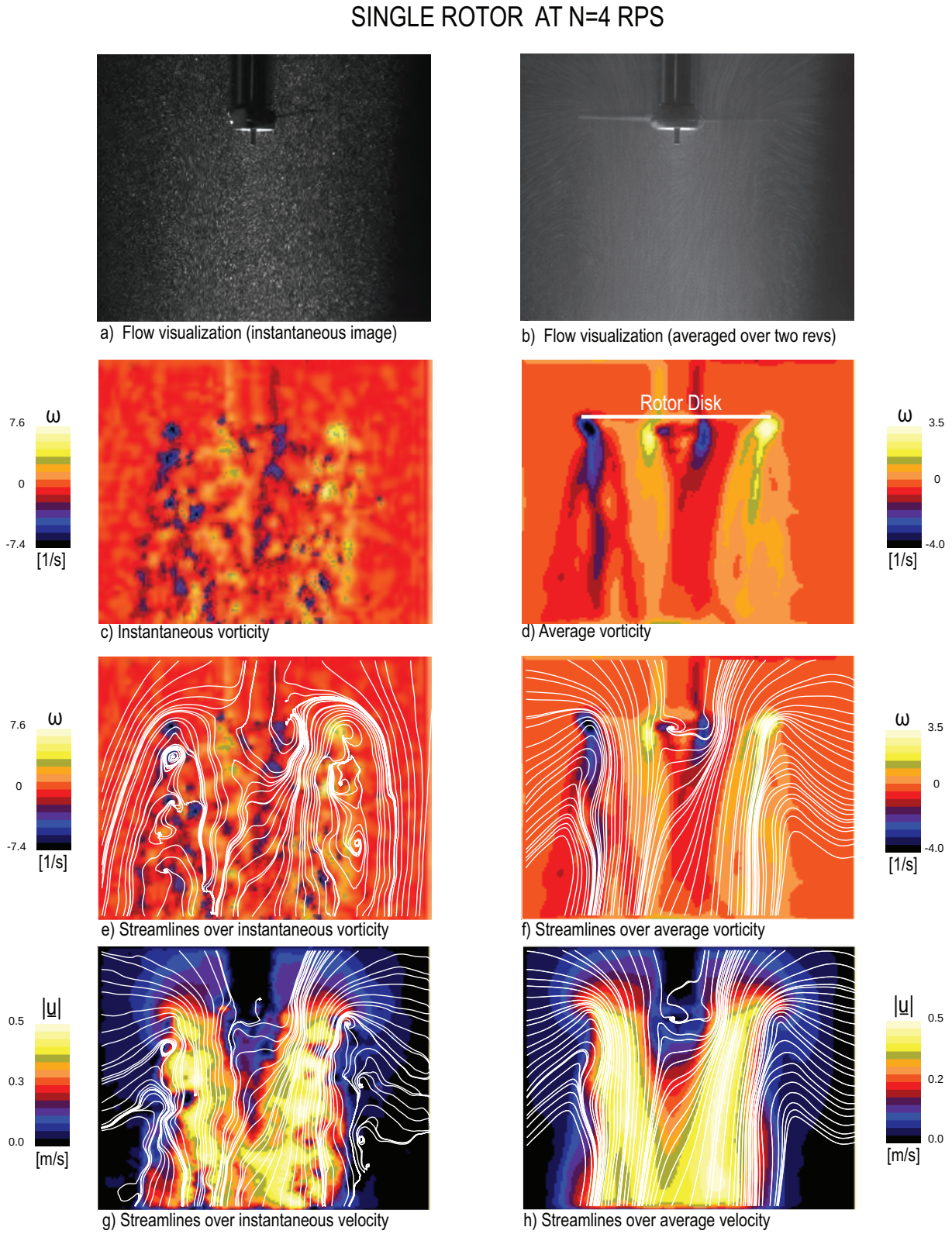

Figure A.22: Flow field of a two-bladed single rotor at $N = 4$ rps. First row (a,b): particle flow visualization. In rows 2-4 are shown PIV measurements. Second row (c,d): vorticity fields. Third row (e,f): streamlines over vorticity. Fourth row (g,h): streamlines over speed. Streamlines in frame (e) are drawn from a moving reference frame and streamlines in frames (f-h) are drawn from a stationary reference frame.

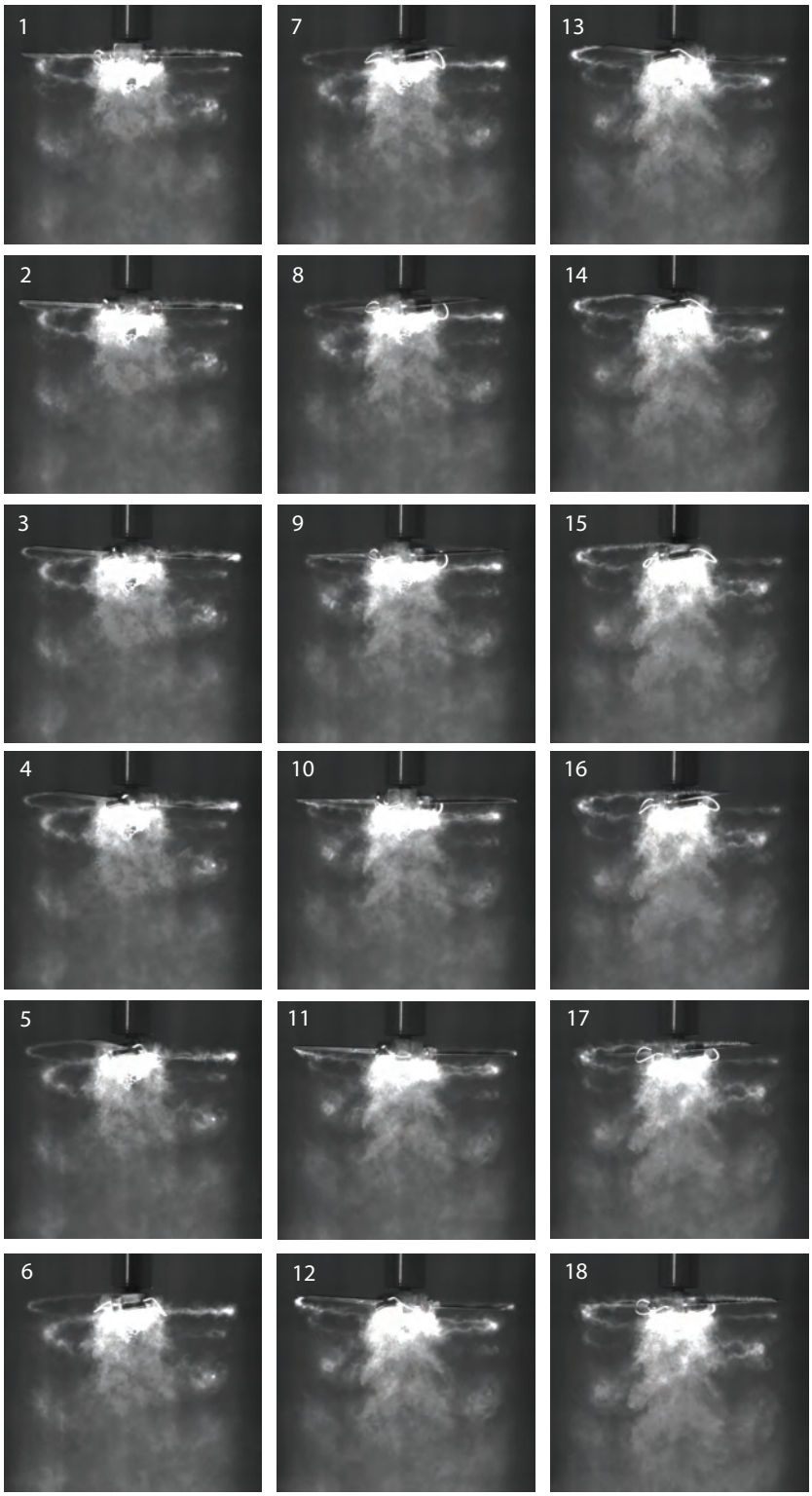

Figure A.23: Vortex wake evolution of the single rotor during one complete rotor revolution at 2 rps is shown. Images are 20° ($\pi/9$ rad) apart. Time separation between successive images is 27.78 ms.

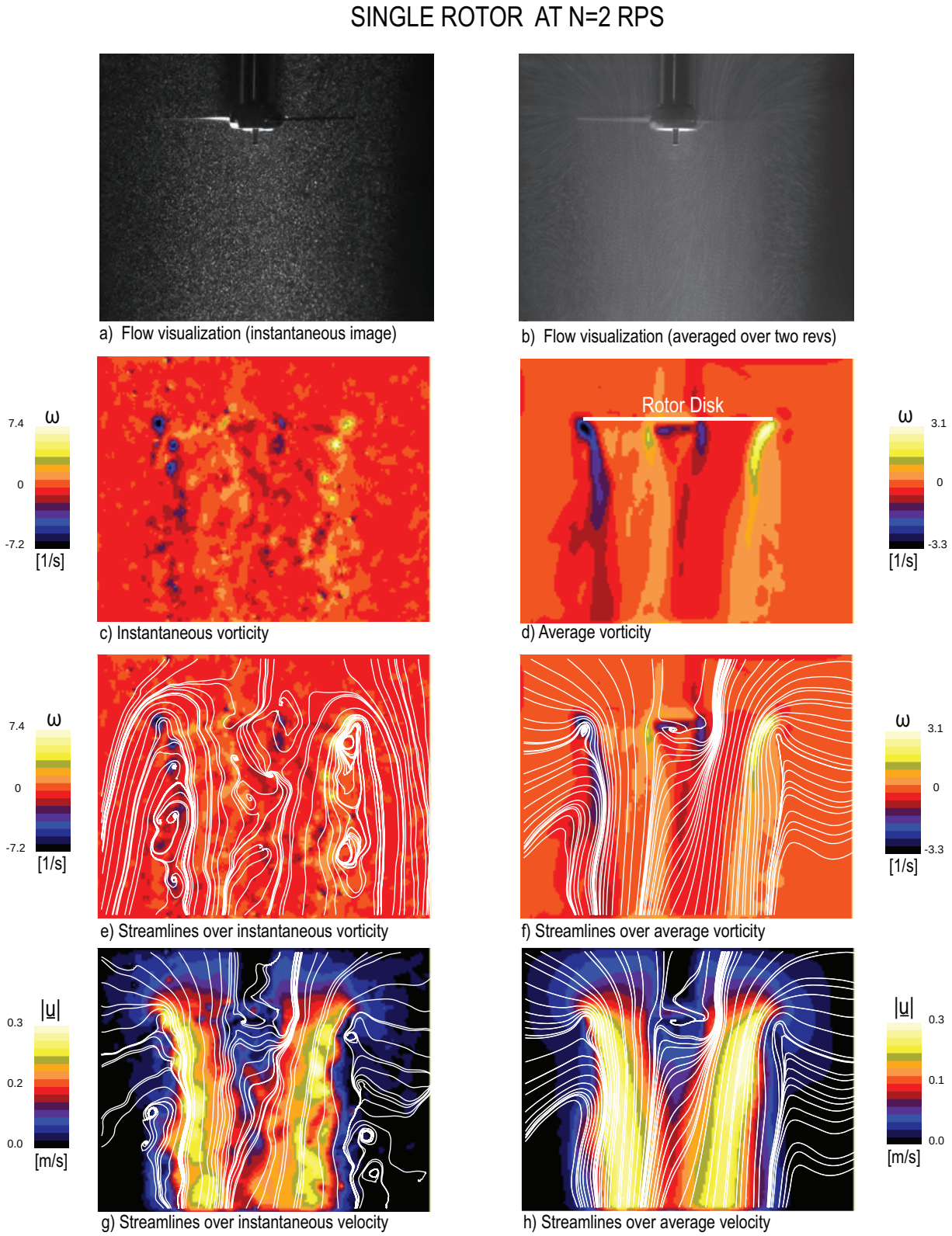

Figure A.24: Flow field of a two-bladed single rotor at $N = 2$ rps. First row (a,b): particle flow visualization. In rows 2-4 are shown PIV measurements. Second row (c,d): vorticity fields. Third row (e,f): streamlines over vorticity. Fourth row (g,h): streamlines over speed. Streamlines in frame (e) are drawn from a moving reference frame and streamlines in frames (f-h) are drawn from a stationary reference frame.

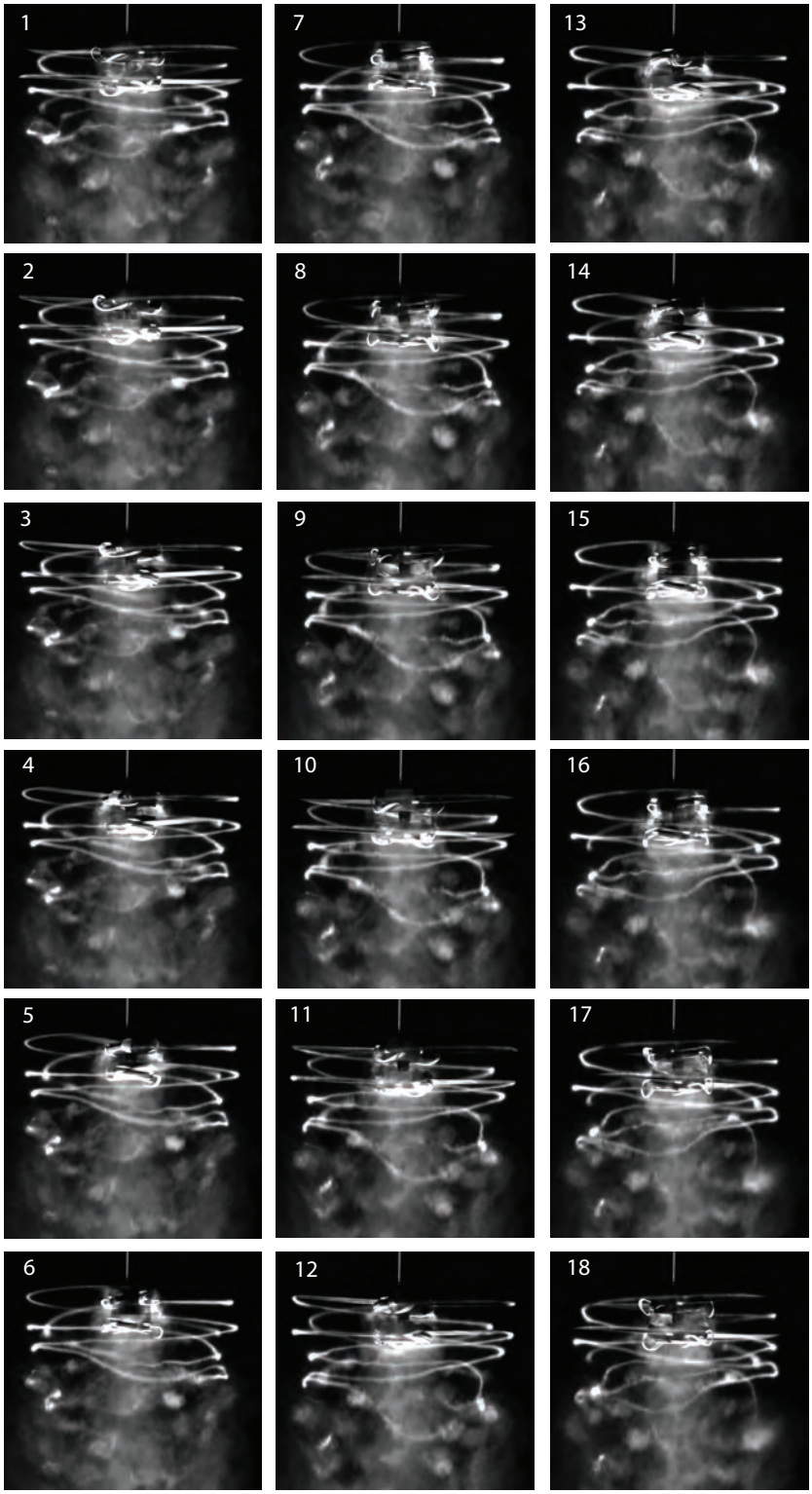

Figure A.25: Vortex wake evolution of the coaxial rotors with axial spacing of H/R=0.25 during one complete rotor revolutions at 6 rps. Images are 20° ($\pi/9$ rad) apart. Time separation between successive images is 9.26 ms.

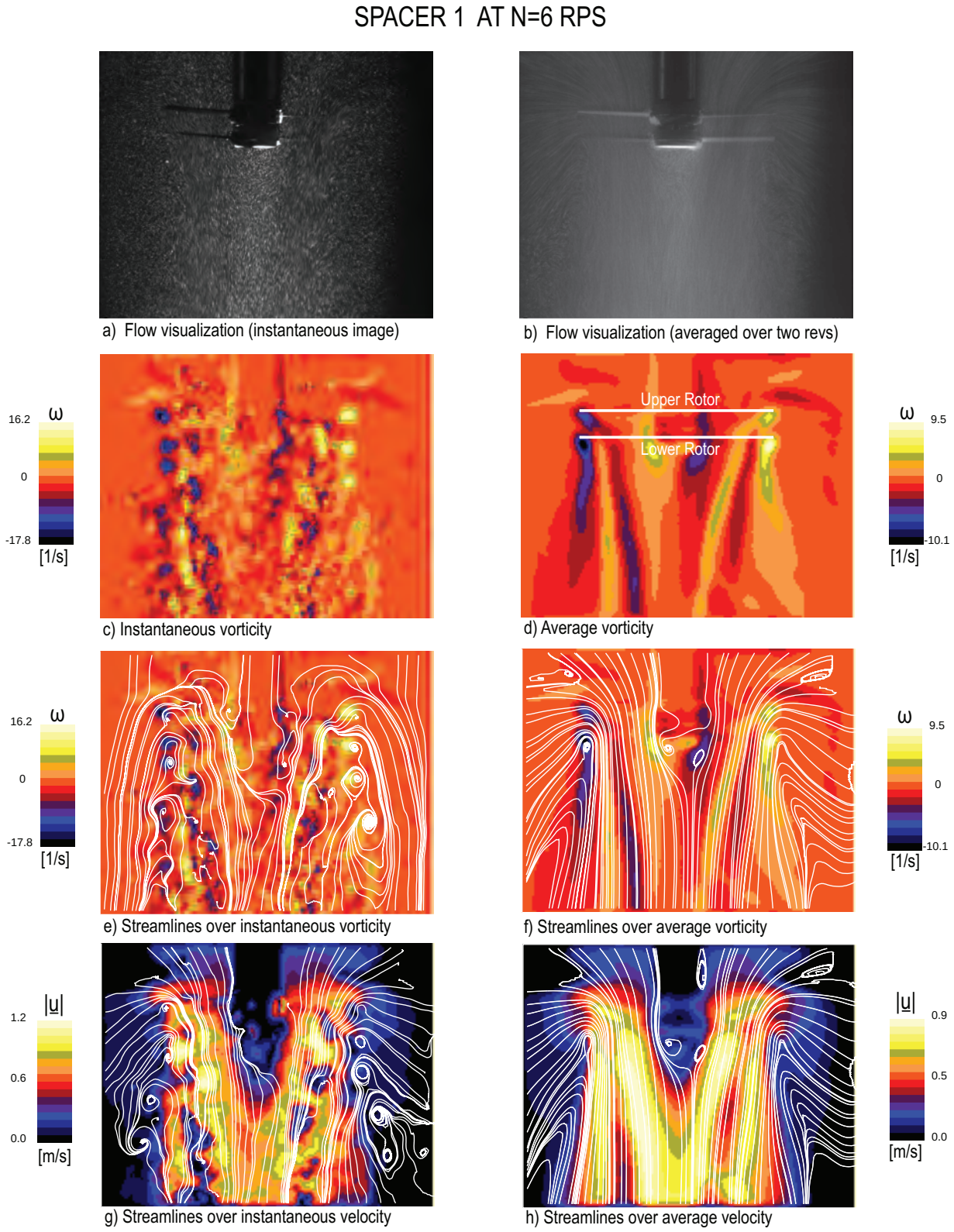

Figure A.26: Flow field of a two-bladed coaxial rotor (spacer1) at $N = 6$ rps. First row (a,b): particle flow visualization. In rows 2-4 are shown PIV measurements. Second row (c,d): vorticity fields. Third row (e,f): streamlines over vorticity. Fourth row (g,h): streamlines over speed. Streamlines in frame (e) are drawn from a moving reference frame and streamlines in frames (f-h) are drawn from a stationary reference frame.

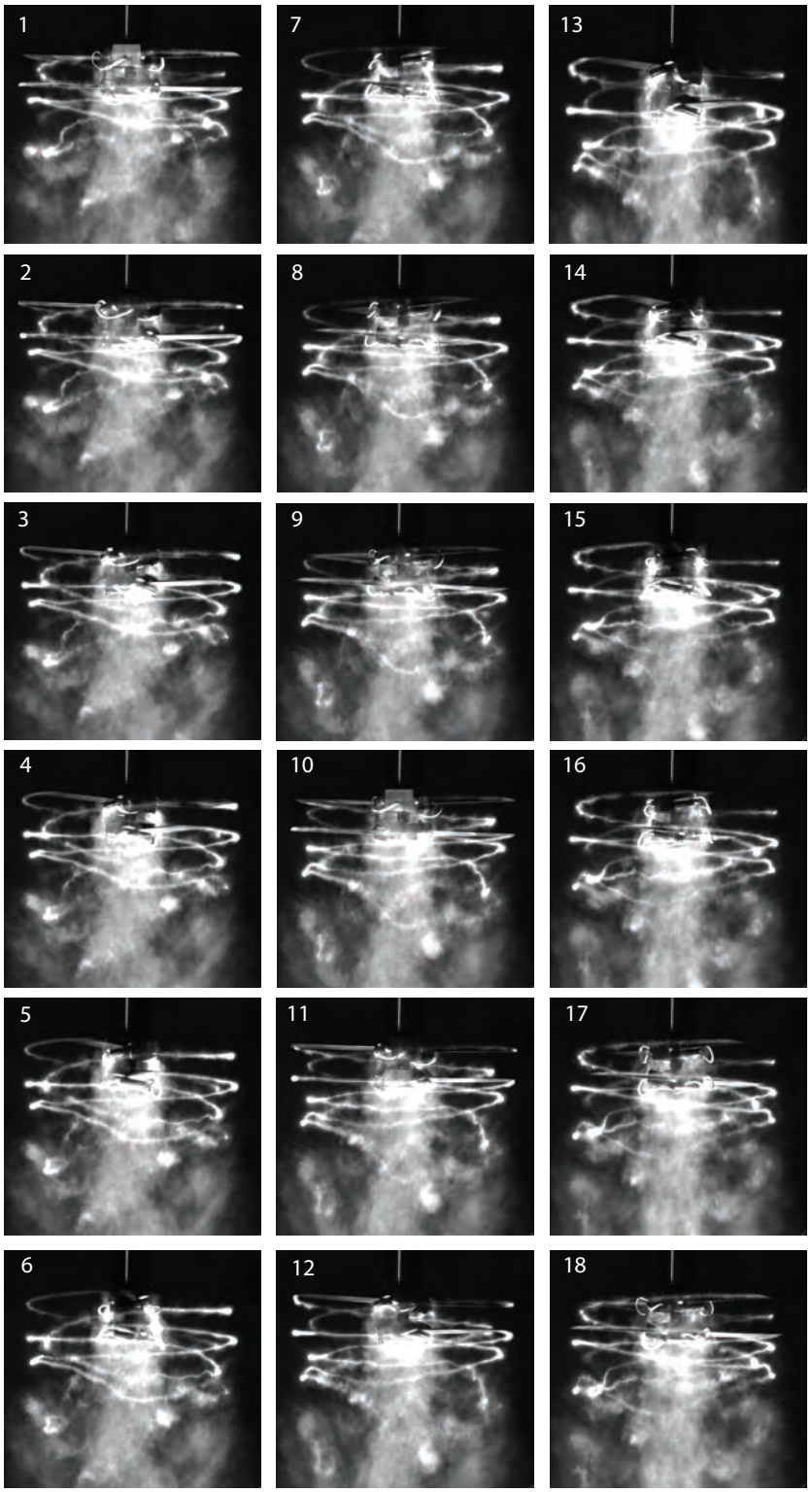

Figure A.27: Vortex wake evolution of the coaxial rotors with axial spacing of H/R=0.25 during one complete rotor revolutions at 4 rps. Images are 20° ($\pi/9$ rad) apart. Time separation between successive images is 13.89 ms.

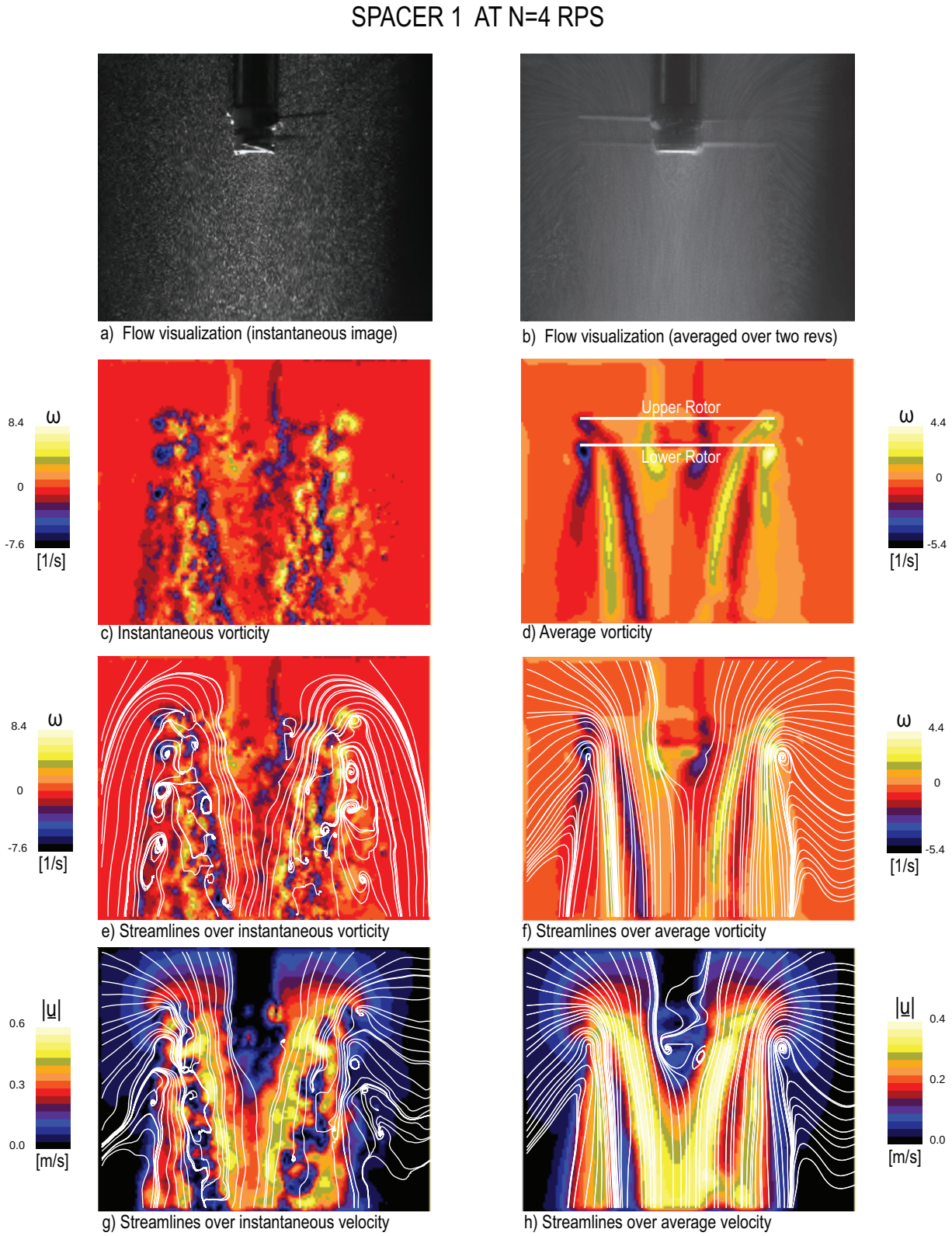

Figure A.28: Flow field of a two-bladed coaxial rotor (spacer1) at $N = 4$ rps. First row (a,b): particle flow visualization. In rows 2-4 are shown PIV measurements. Second row (c,d): vorticity fields. Third row (e,f): streamlines over vorticity. Fourth row (g,h): streamlines over speed. Streamlines in frame (e) are drawn from a moving reference frame and streamlines in frames (f-h) are drawn from a stationary reference frame.

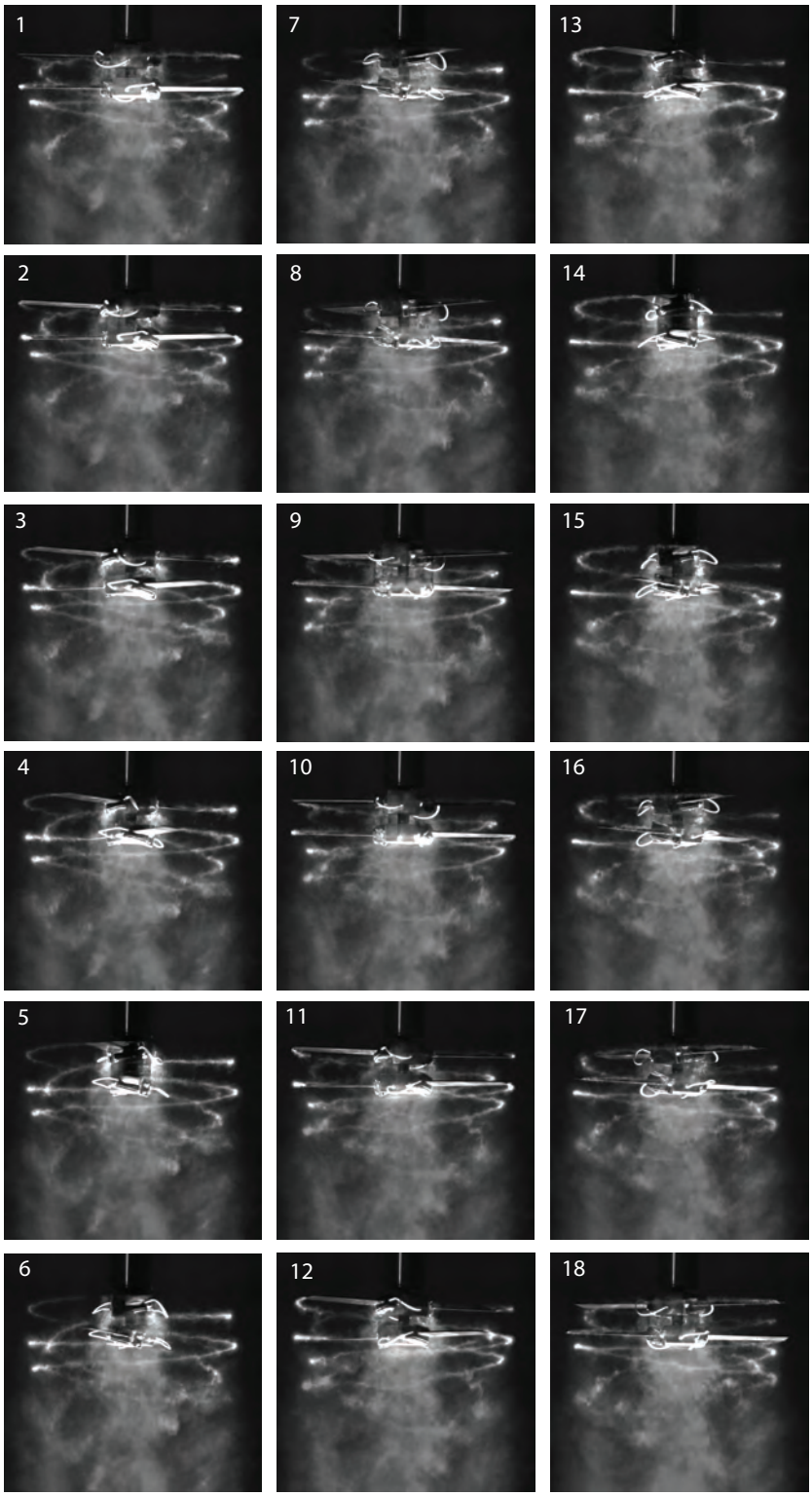

Figure A.29: Vortex wake evolution of the coaxial rotors with axial spacing of H/R=0.25 during one complete rotor revolutions at 2 rps. Images are 20° ($\pi/9$ rad) apart. Time separation between successive images is 27.78 ms.

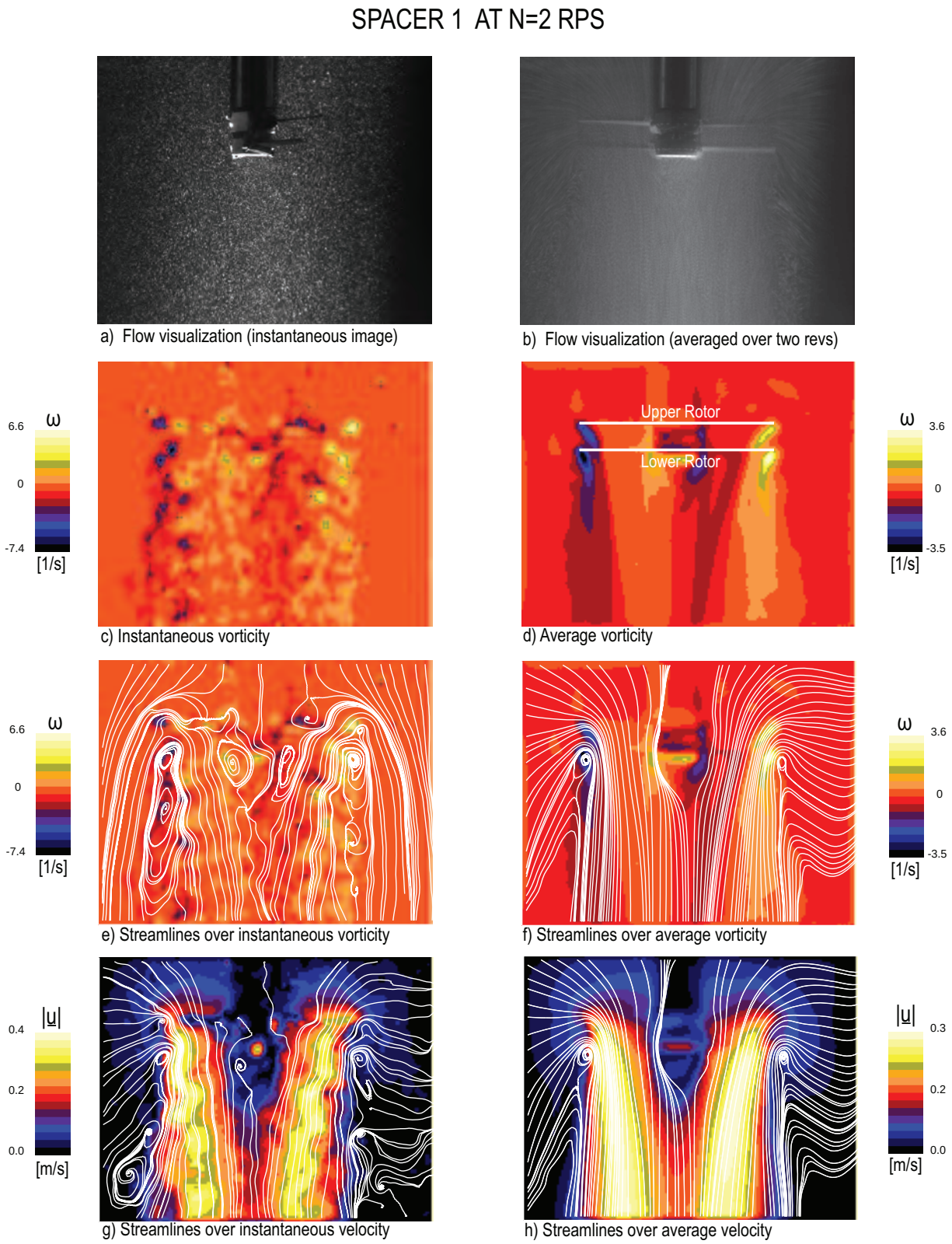

Figure A.30: Flow field of a two-bladed coaxial rotor (spacer1) at $N = 2$ rps. First row (a,b): particle flow visualization. In rows 2-4 are shown PIV measurements. Second row (c,d): vorticity fields. Third row (e,f): streamlines over vorticity. Fourth row (g,h): streamlines over speed. Streamlines in frame (e) are drawn from a moving reference frame and streamlines in frames (f-h) are drawn from a stationary reference frame.

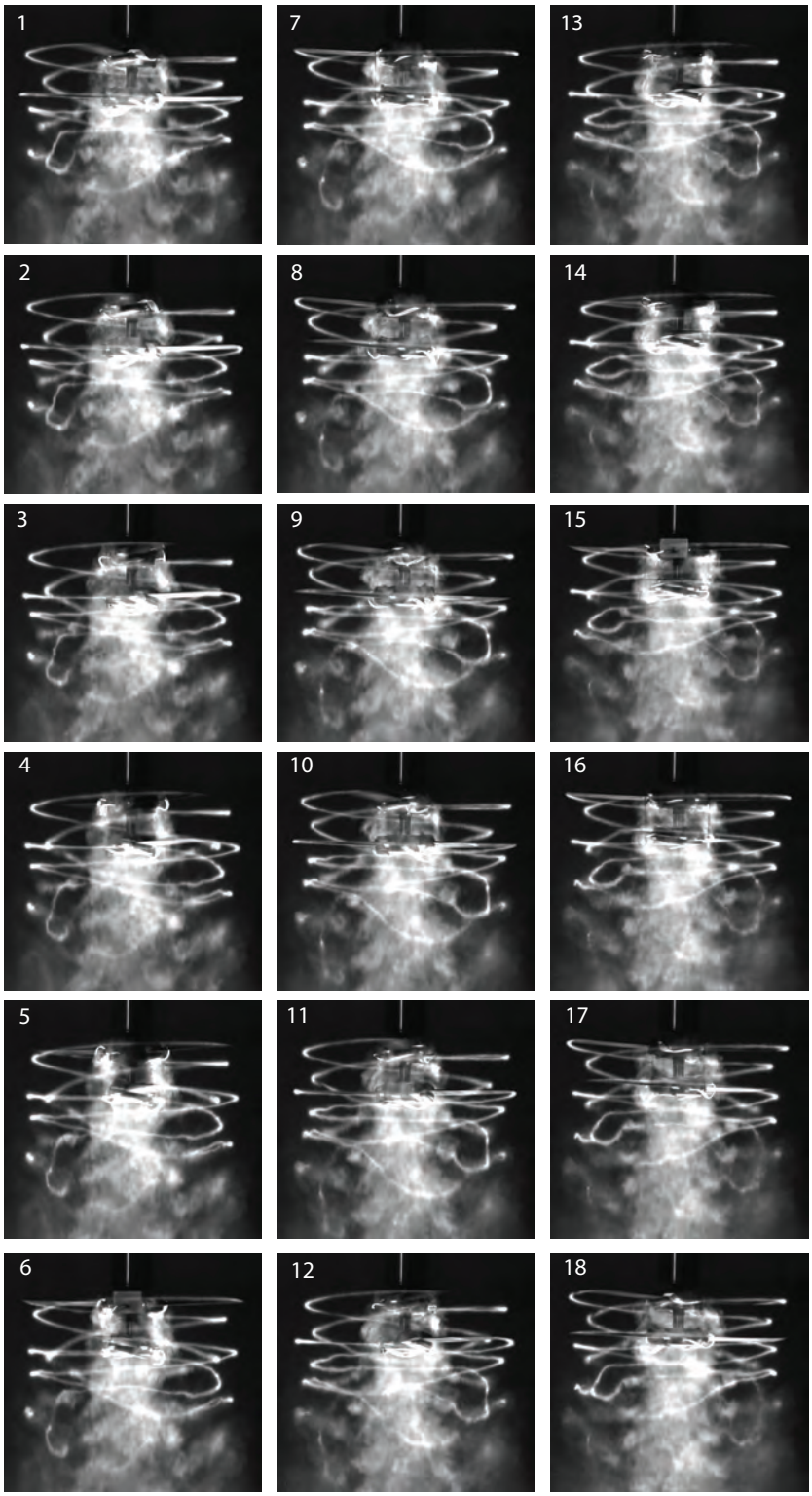

Figure A.31: Vortex wake evolution of the coaxial rotors with axial spacing of H/R=0.375 during one complete rotor revolutions at 6 rps. Images are 20° ($\pi/9$ rad) apart. Time separation between successive images is 9.26 ms.

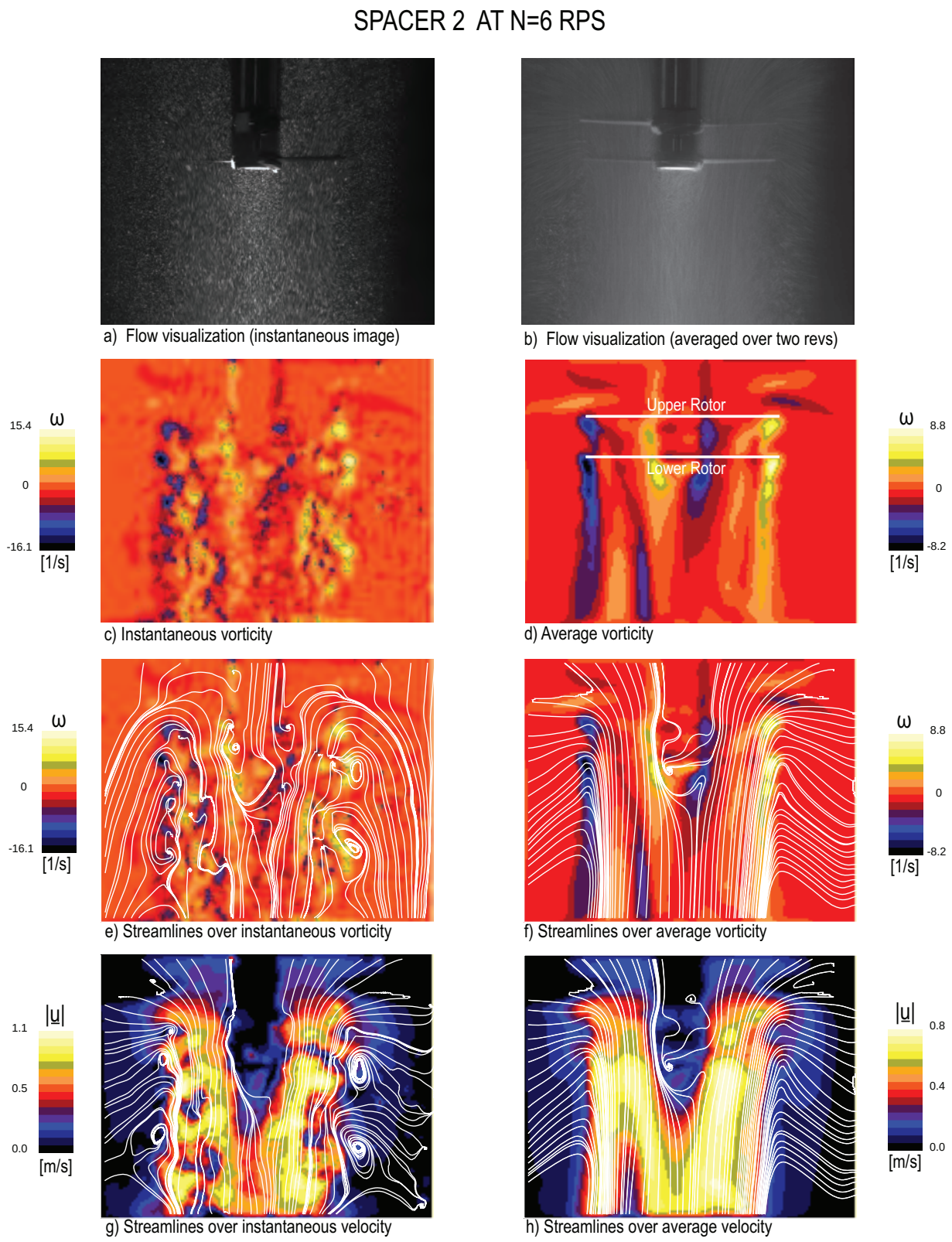

Figure A.32: Flow field of a two-bladed coaxial rotor (spacer2) at $N = 6$ rps. First row (a,b): particle flow visualization. In rows 2-4 are shown PIV measurements. Second row (c,d): vorticity fields. Third row (e,f): streamlines over vorticity. Fourth row (g,h): streamlines over speed. Streamlines in frame (e) are drawn from a moving reference frame and streamlines in frames (f-h) are drawn from a stationary reference frame.

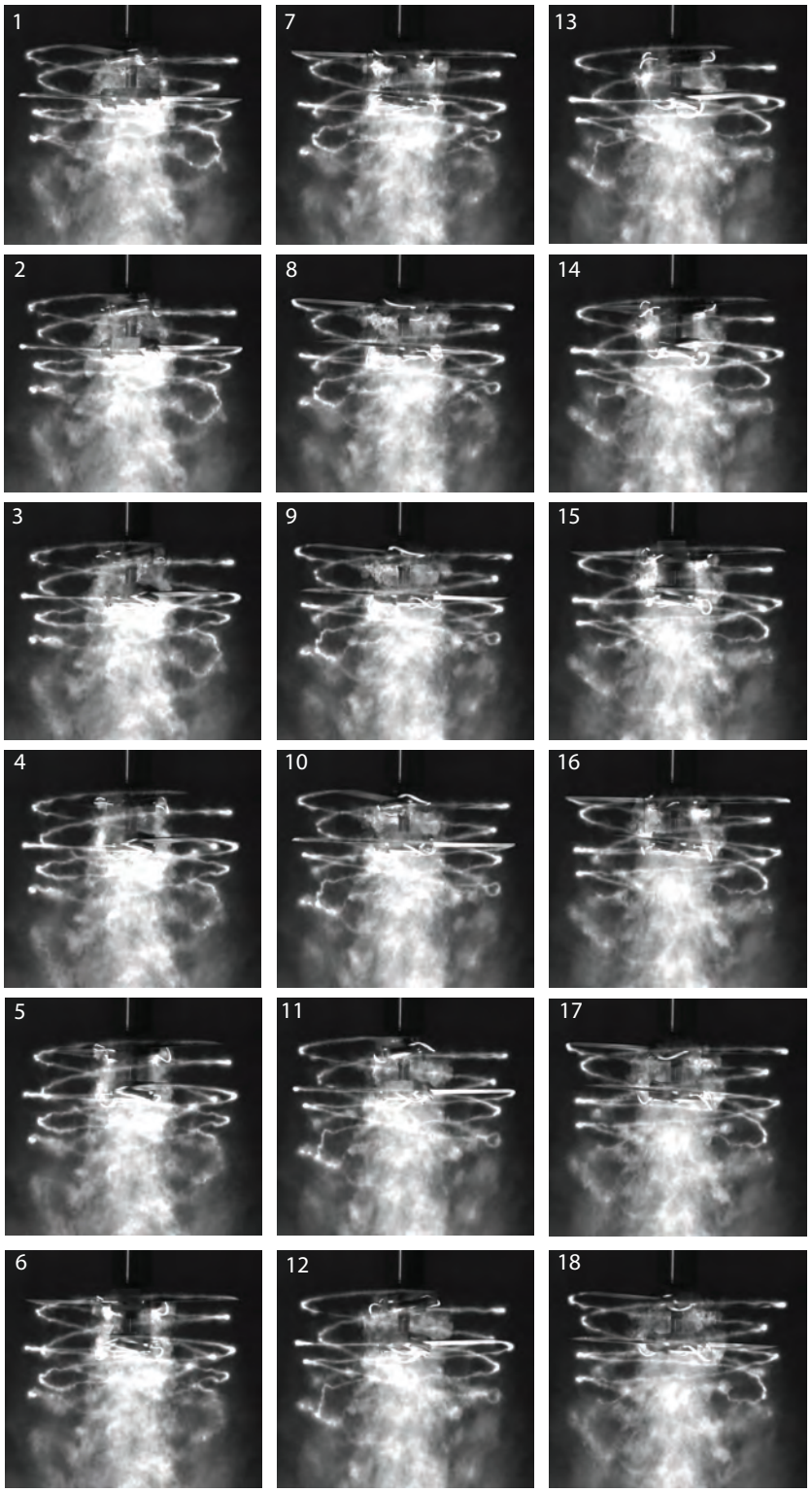

Figure A.33: Vortex wake evolution of the coaxial rotors with axial spacing of H/R=0.375 during one complete rotor revolutions at 4 rps. Images are 20° ($\pi/9$ rad) apart. Time separation between successive images is 13.89 ms.

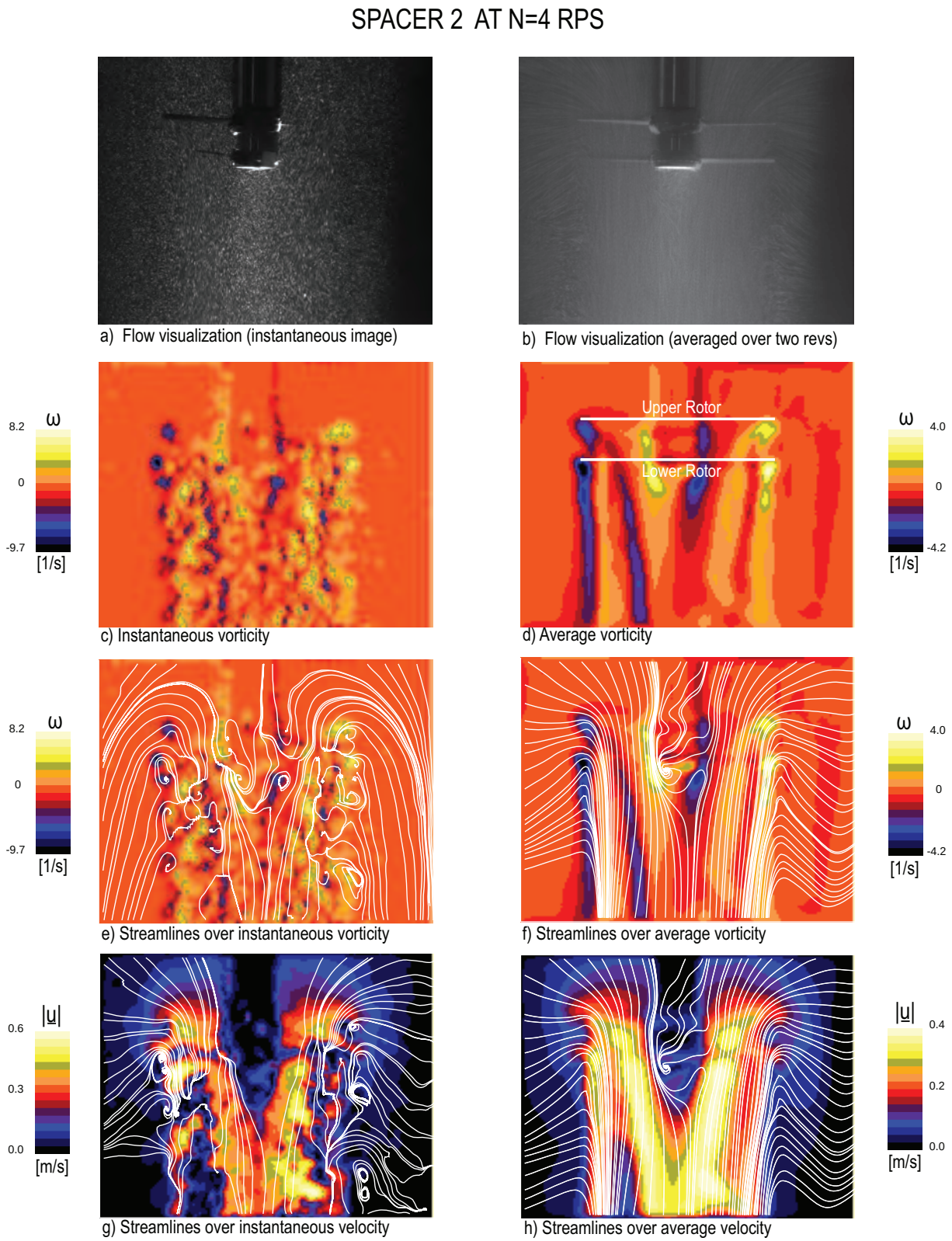

Figure A.34: Flow field of a two-bladed coaxial rotor (spacer2) at $N = 4$ rps. First row (a,b): particle flow visualization. In rows 2-4 are shown PIV measurements. Second row (c,d): vorticity fields. Third row (e,f): streamlines over vorticity. Fourth row (g,h): streamlines over speed. Streamlines in frame (e) are drawn from a moving reference frame and streamlines in frames (f-h) are drawn from a stationary reference frame.

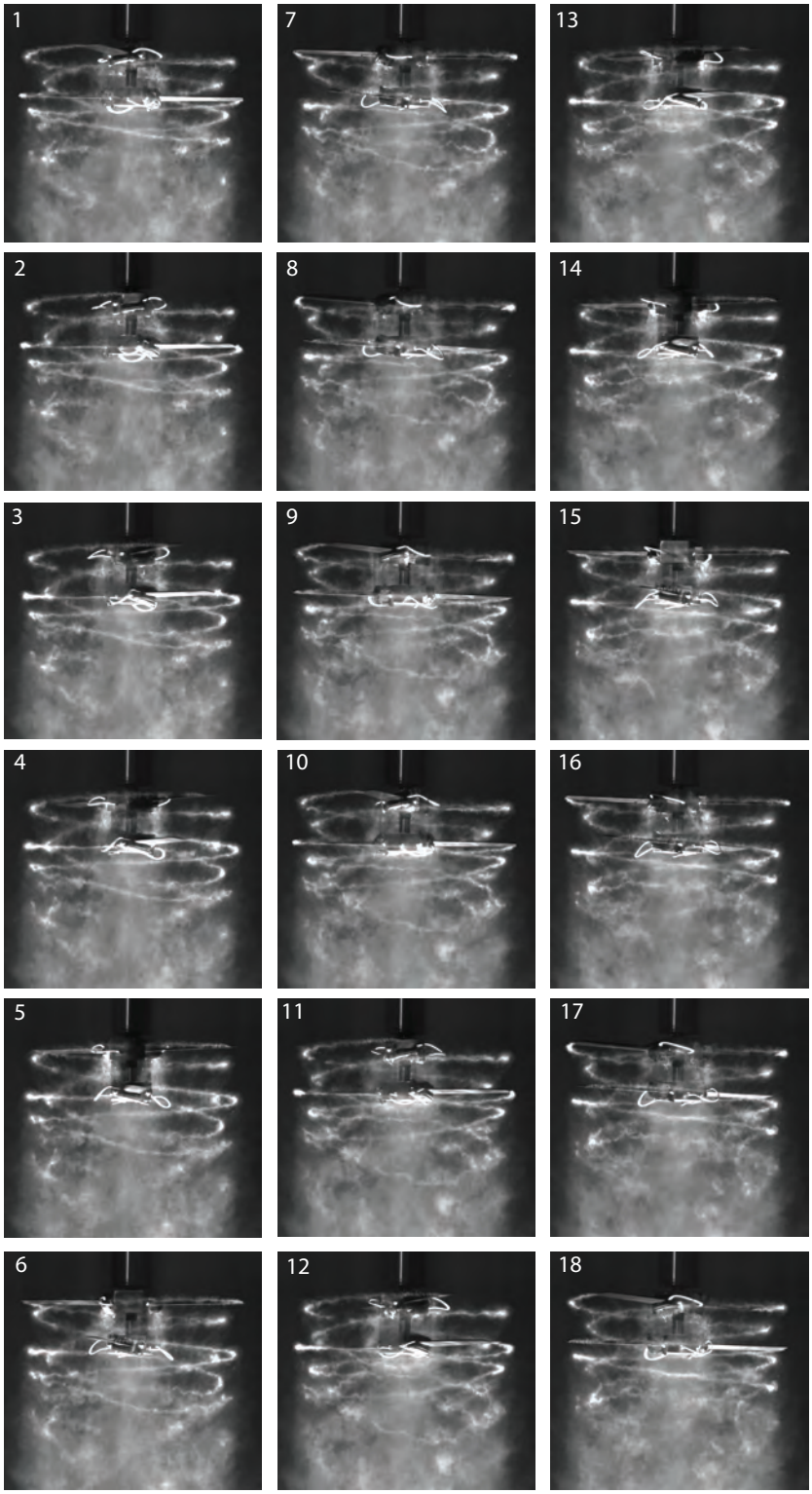

Figure A.35: Vortex wake evolution of the coaxial rotors with axial spacing of H/R=0.375 during one complete rotor revolutions at 2 rps. Images are 20° ($\pi/9$ rad) apart. Time separation between successive images is 27.78 ms.

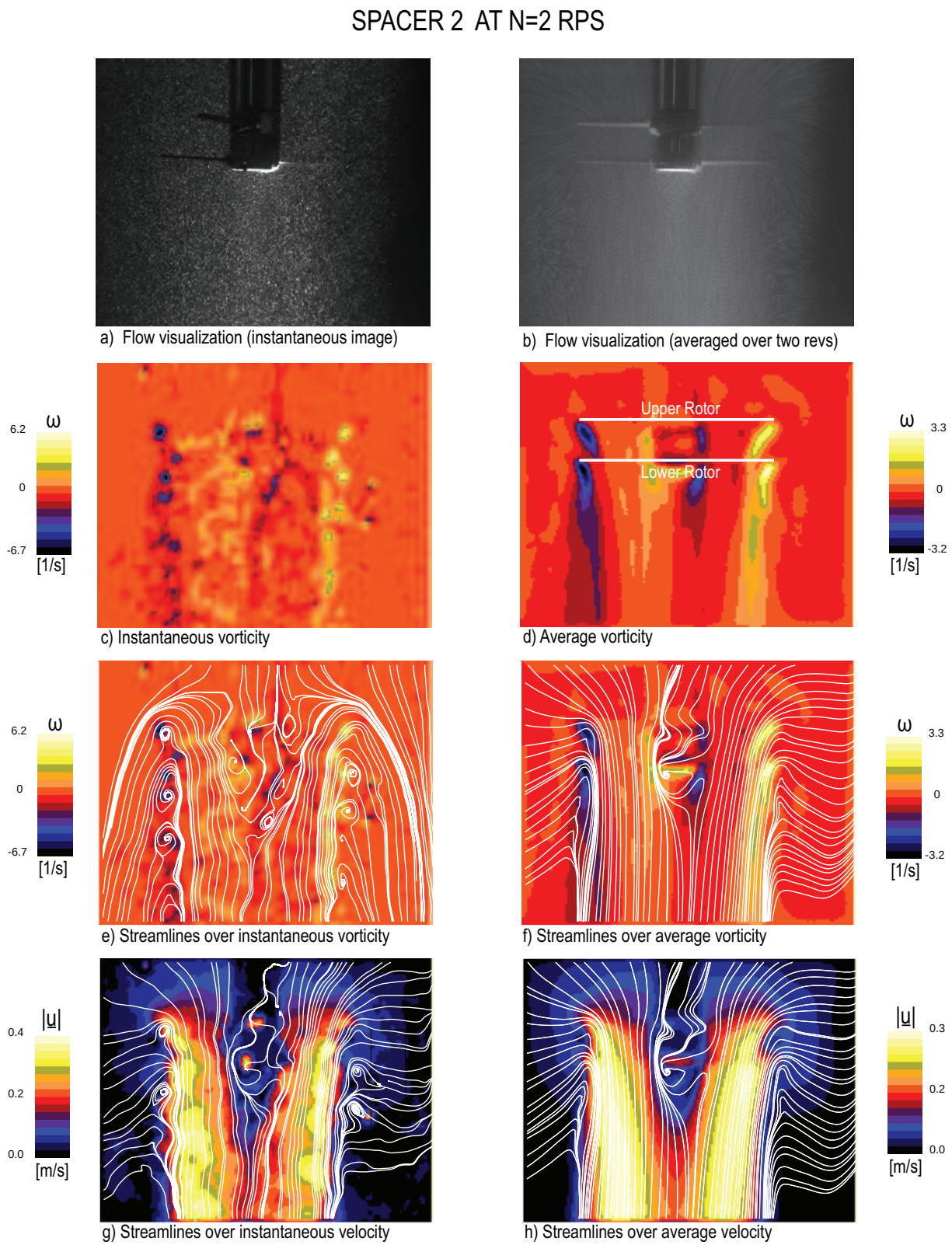

Figure A.36: Flow field of a two-bladed coaxial rotor (spacer2) at $N = 2$ rps. First row (a,b): particle flow visualization. In rows 2-4 are shown PIV measurements. Second row (c,d): vorticity fields. Third row (e,f): streamlines over vorticity. Fourth row (g,h): streamlines over speed. Streamlines in frame (e) are drawn from a moving reference frame and streamlines in frames (f-h) are drawn from a stationary reference frame.

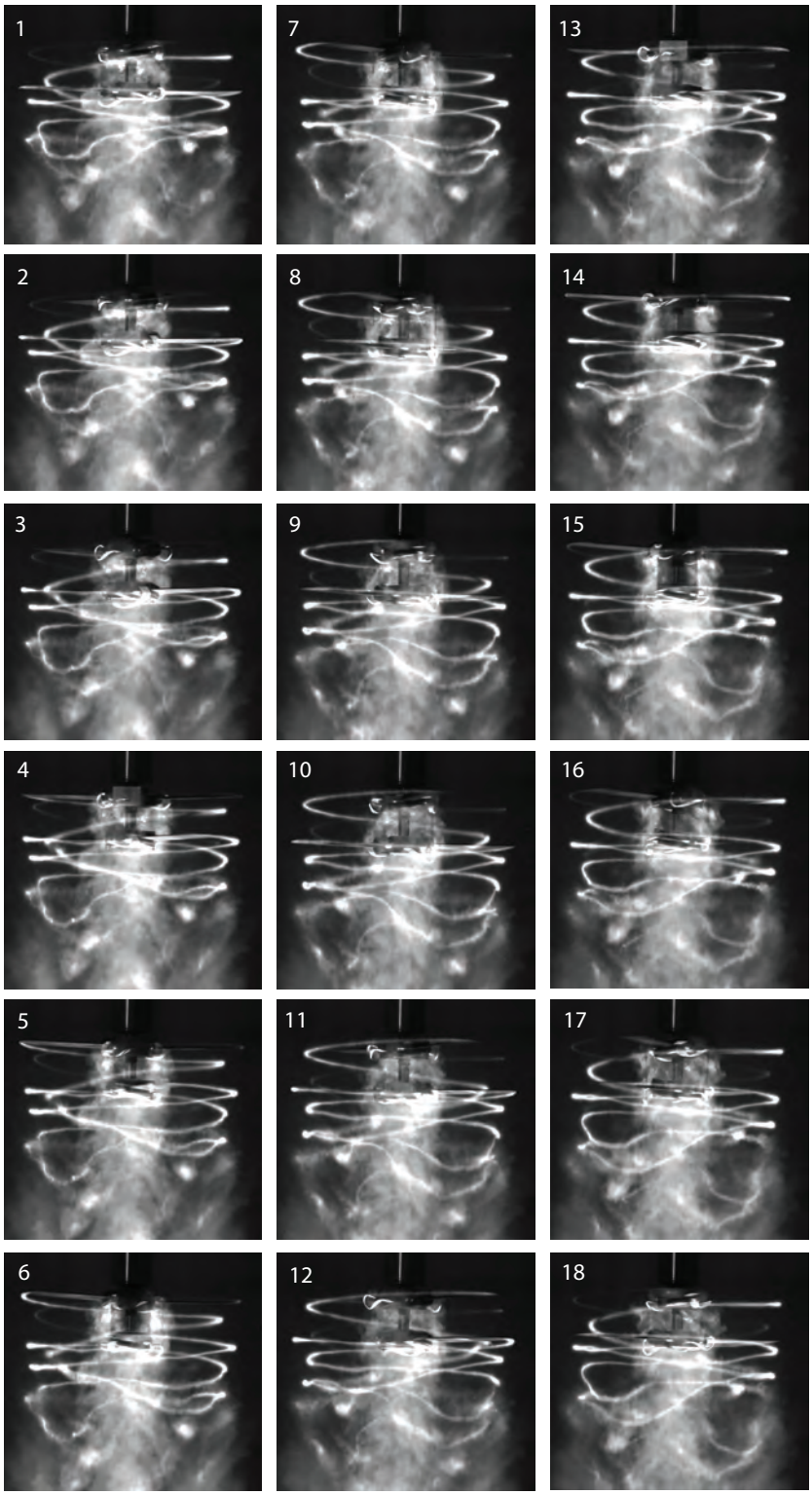

Figure A.37: Vortex wake evolution of the coaxial rotors with axial spacing of H/R=0.41 during one complete rotor revolutions at 6 rps. Images are 20° ($\pi/9$ rad) apart. Time separation between successive images is 9.26 ms.

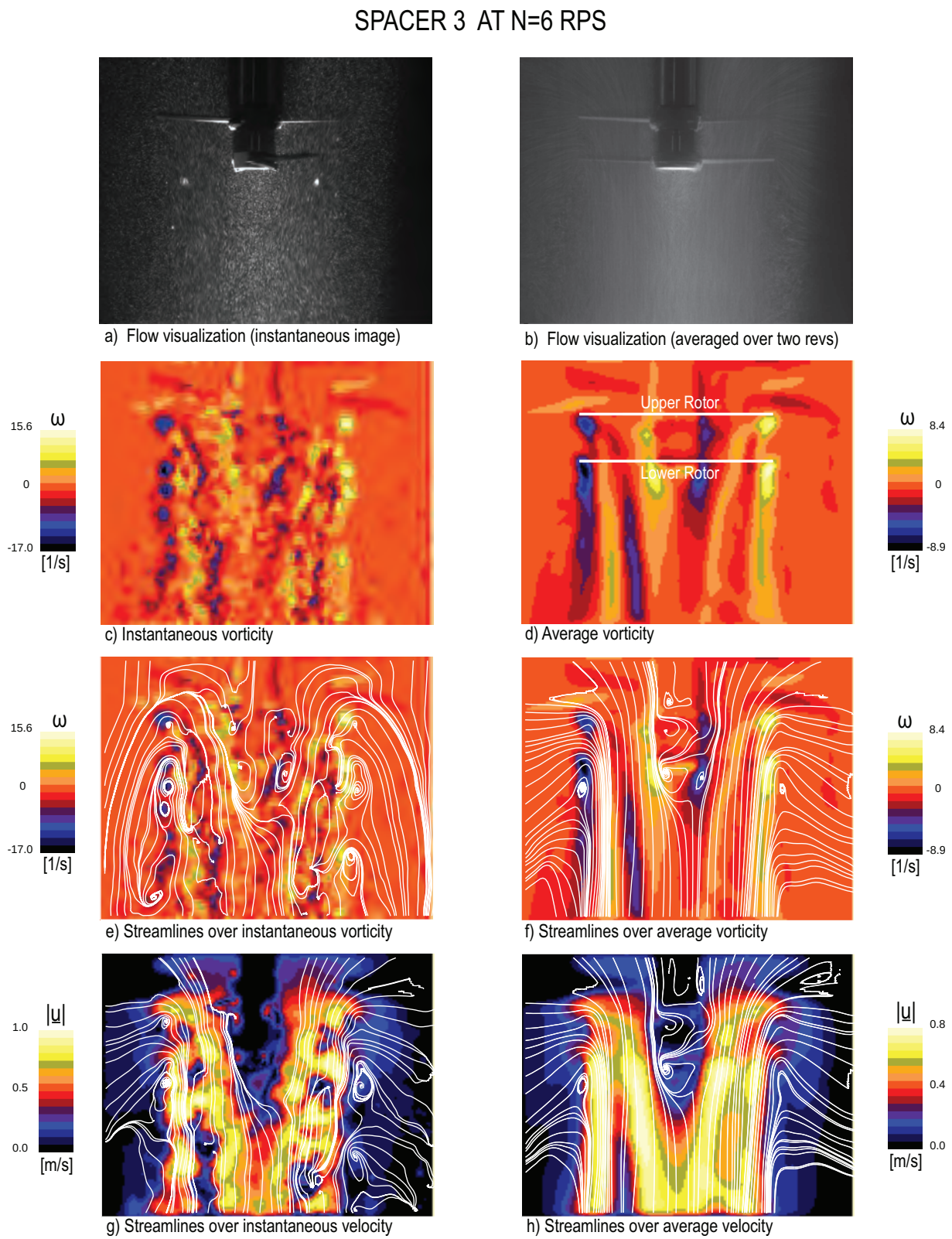

Figure A.38: Flow field of a two-bladed coaxial rotor (spacer3) at $N = 6$ rps. First row (a,b): particle flow visualization. In rows 2-4 are shown PIV measurements. Second row (c,d): vorticity fields. Third row (e,f): streamlines over vorticity. Fourth row (g,h): streamlines over speed. Streamlines in frame (e) are drawn from a moving reference frame and streamlines in frames (f-h) are drawn from a stationary reference frame.

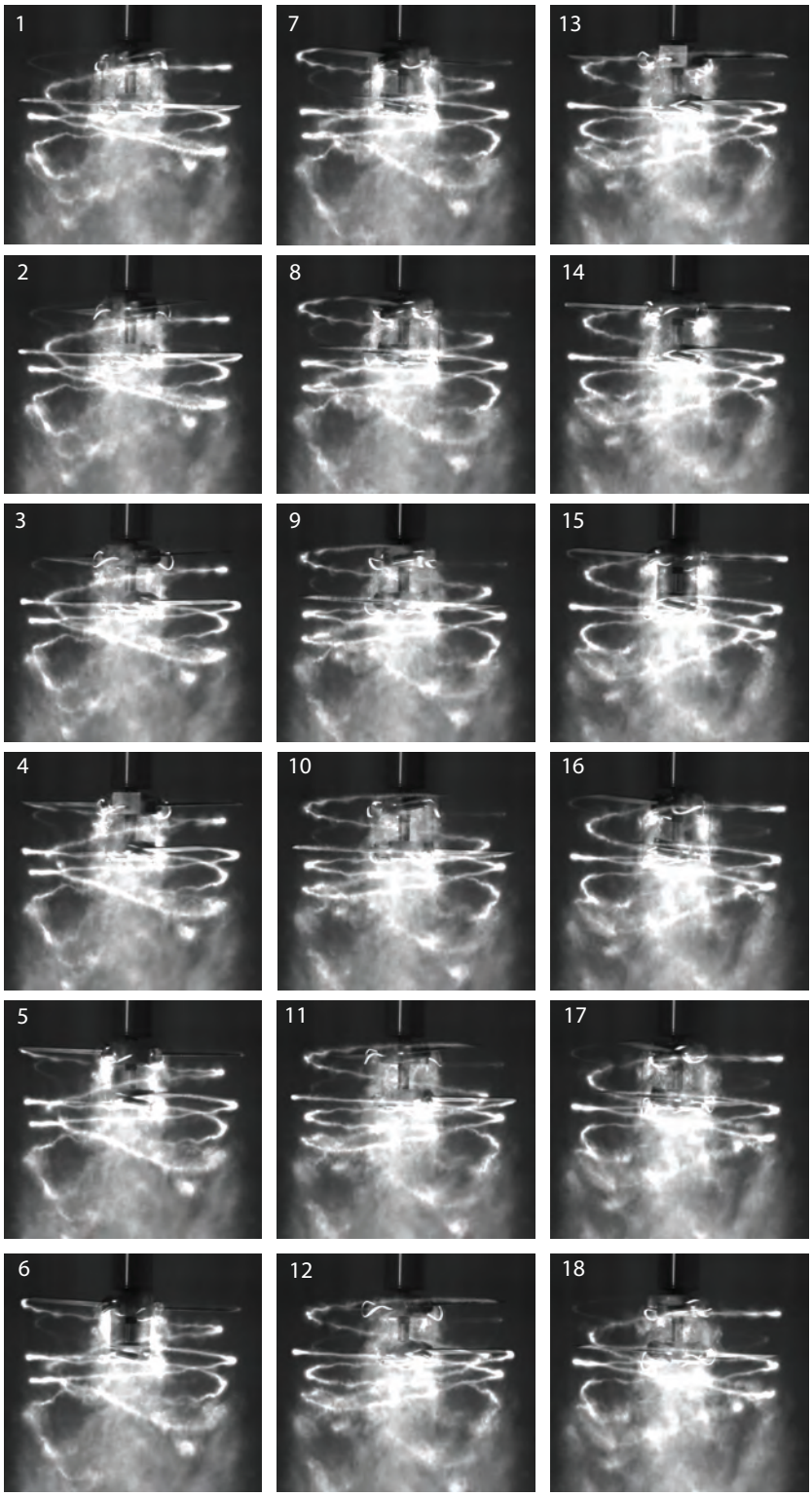

Figure A.39: Vortex wake evolution of the coaxial rotors with axial spacing of H/R=0.41 during one complete rotor revolutions at 4 rps. Images are 20° ($\pi/9$ rad) apart. Time separation between successive images is 13.89 ms.

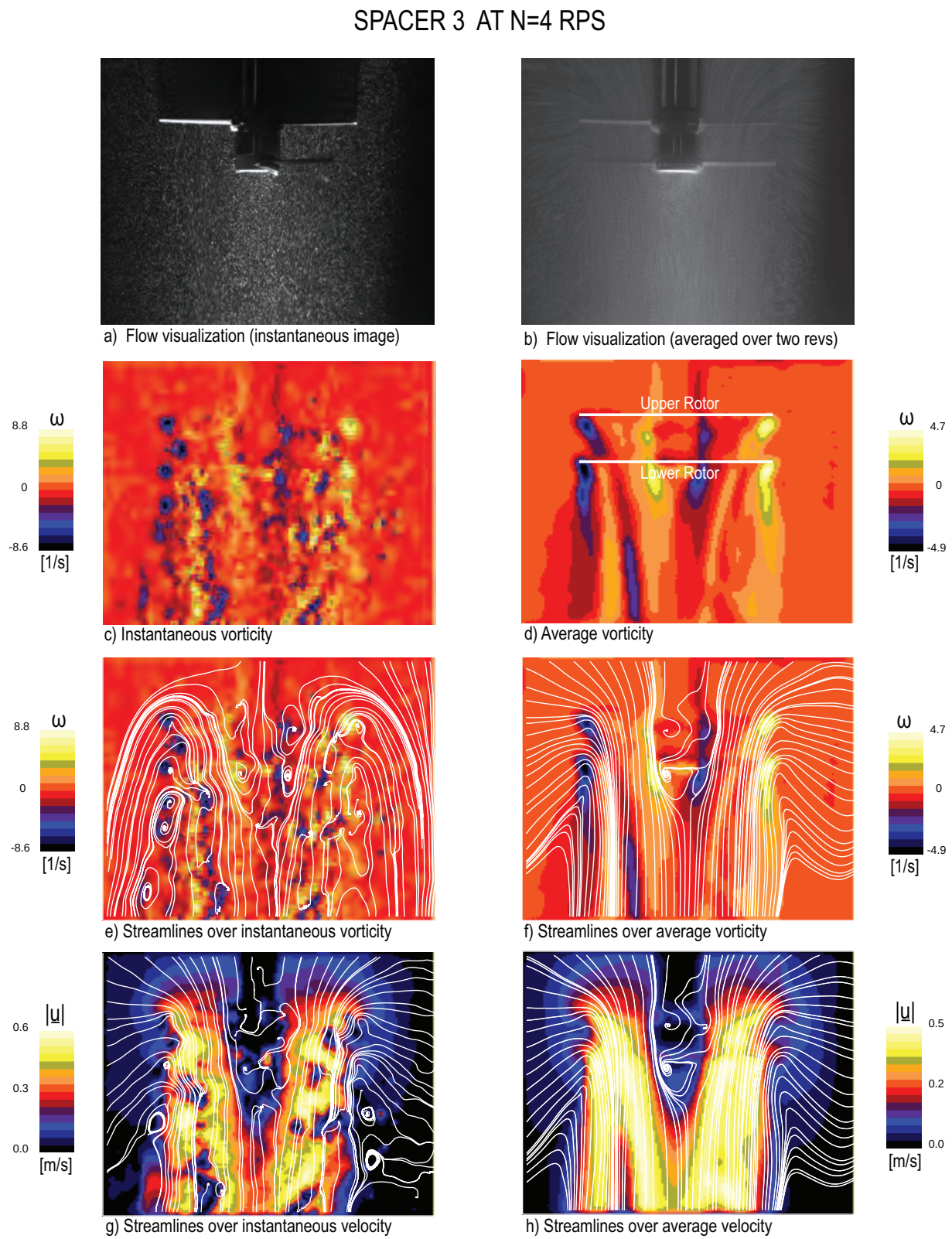

Figure A.40: Flow field of a two-bladed coaxial rotor (spacer3) at $N = 4$ rps. First row (a,b): particle flow visualization. In rows 2-4 are shown PIV measurements. Second row (c,d): vorticity fields. Third row (e,f): streamlines over vorticity. Fourth row (g,h): streamlines over speed. Streamlines in frame (e) are drawn from a moving reference frame and streamlines in frames (f-h) are drawn from a stationary reference frame.

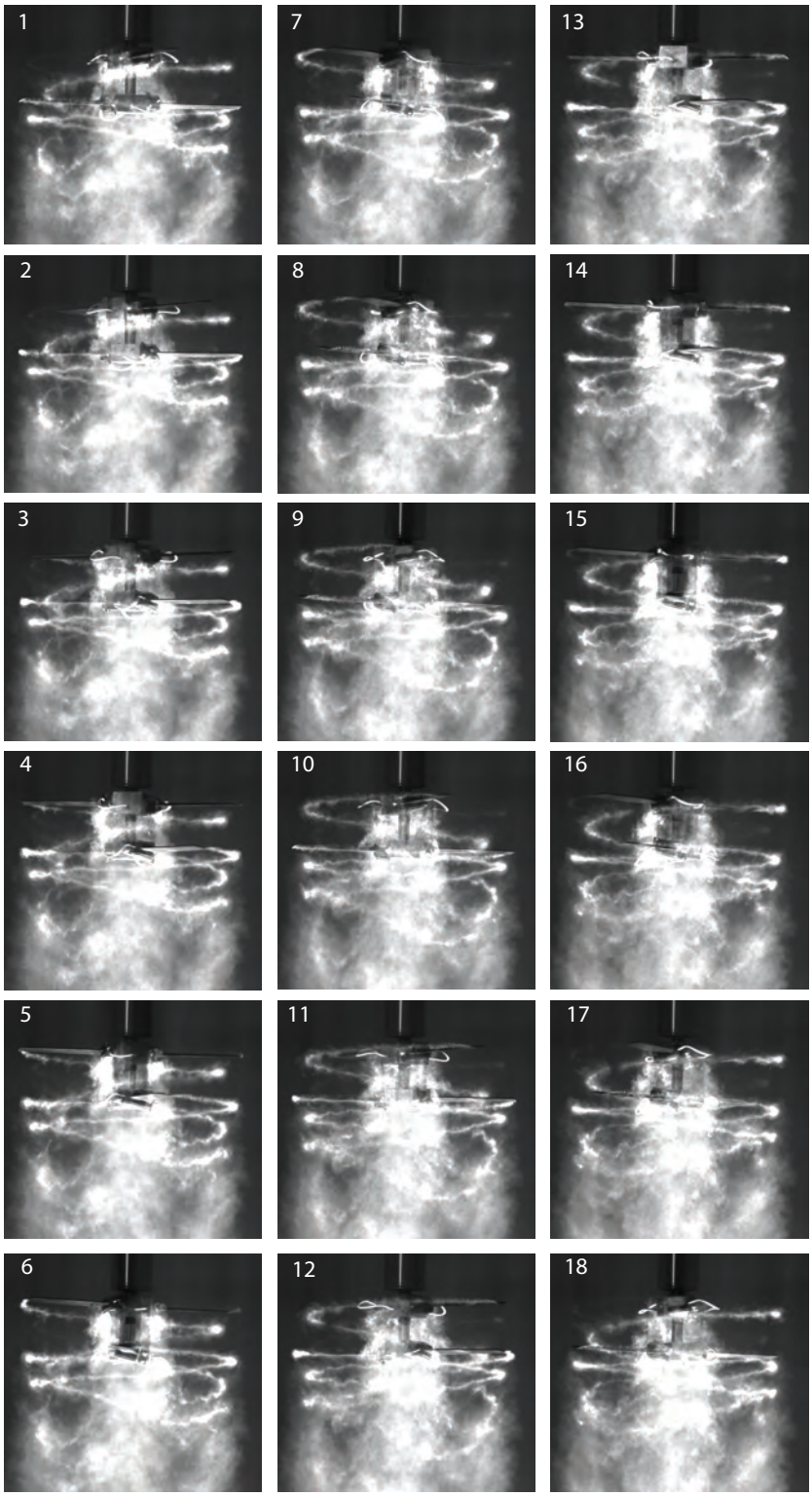

Figure A.41: Vortex wake evolution of the coaxial rotors with axial spacing of H/R=0.41 during one complete rotor revolutions at 2 rps. Images are 20° ($\pi/9$ rad) apart. Time separation between successive images is 27.78 ms.

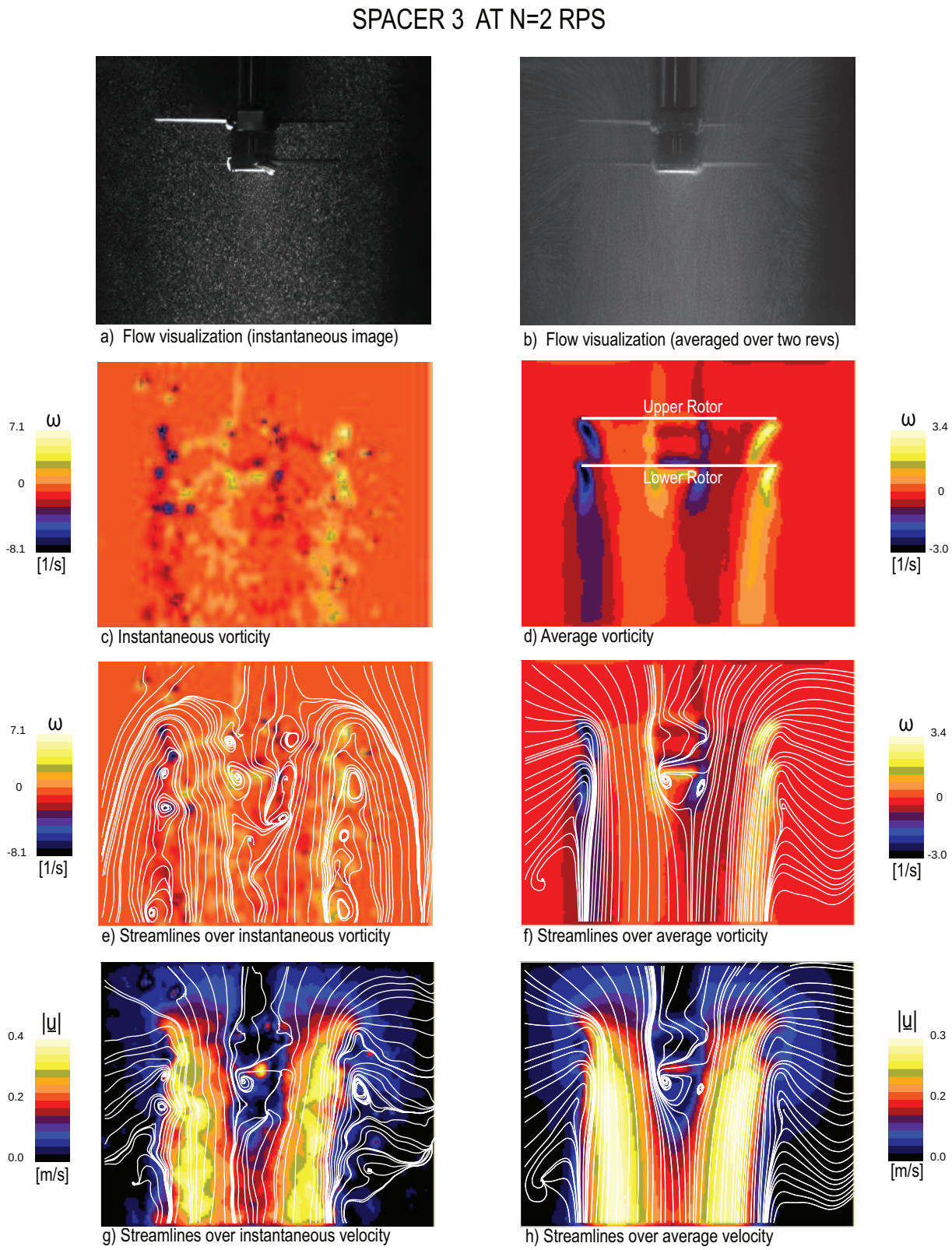

Figure A.42: Flow field of a two-bladed coaxial rotor (spacer3) at $N = 2$ rps. First row (a,b): particle flow visualization. In rows 2-4 are shown PIV measurements. Second row (c,d): vorticity fields. Third row (e,f): streamlines over vorticity. Fourth row (g,h): streamlines over speed. Streamlines in frame (e) are drawn from a moving reference frame and streamlines in frames (f-h) are drawn from a stationary reference frame.

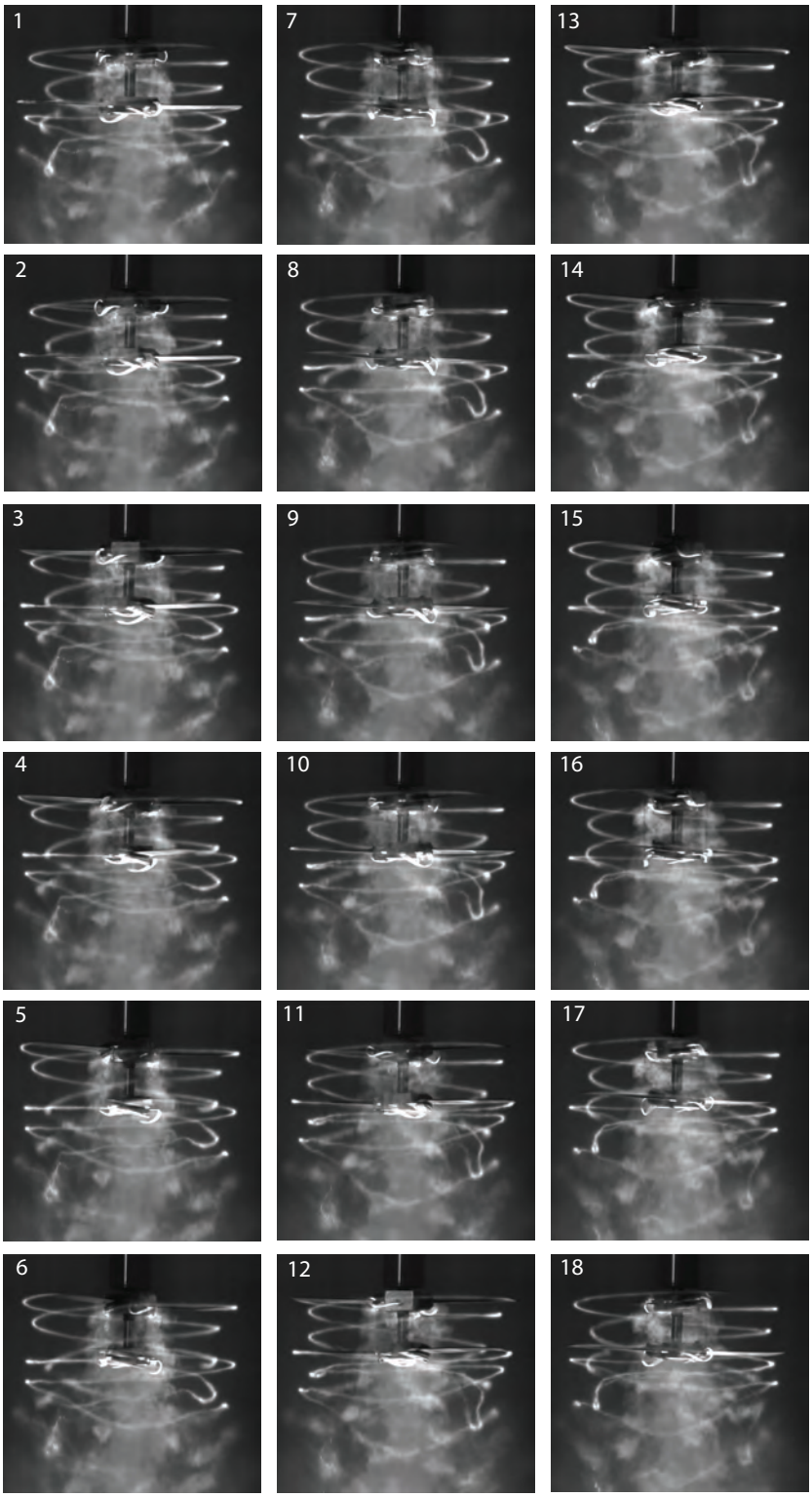

Figure A.43: Vortex wake evolution of the coaxial rotors with axial spacing of H/R=0.5 during one complete rotor revolutions at 6 rps. Images are 20° ($\pi/9$ rad) apart. Time separation between successive images is 9.26 ms.

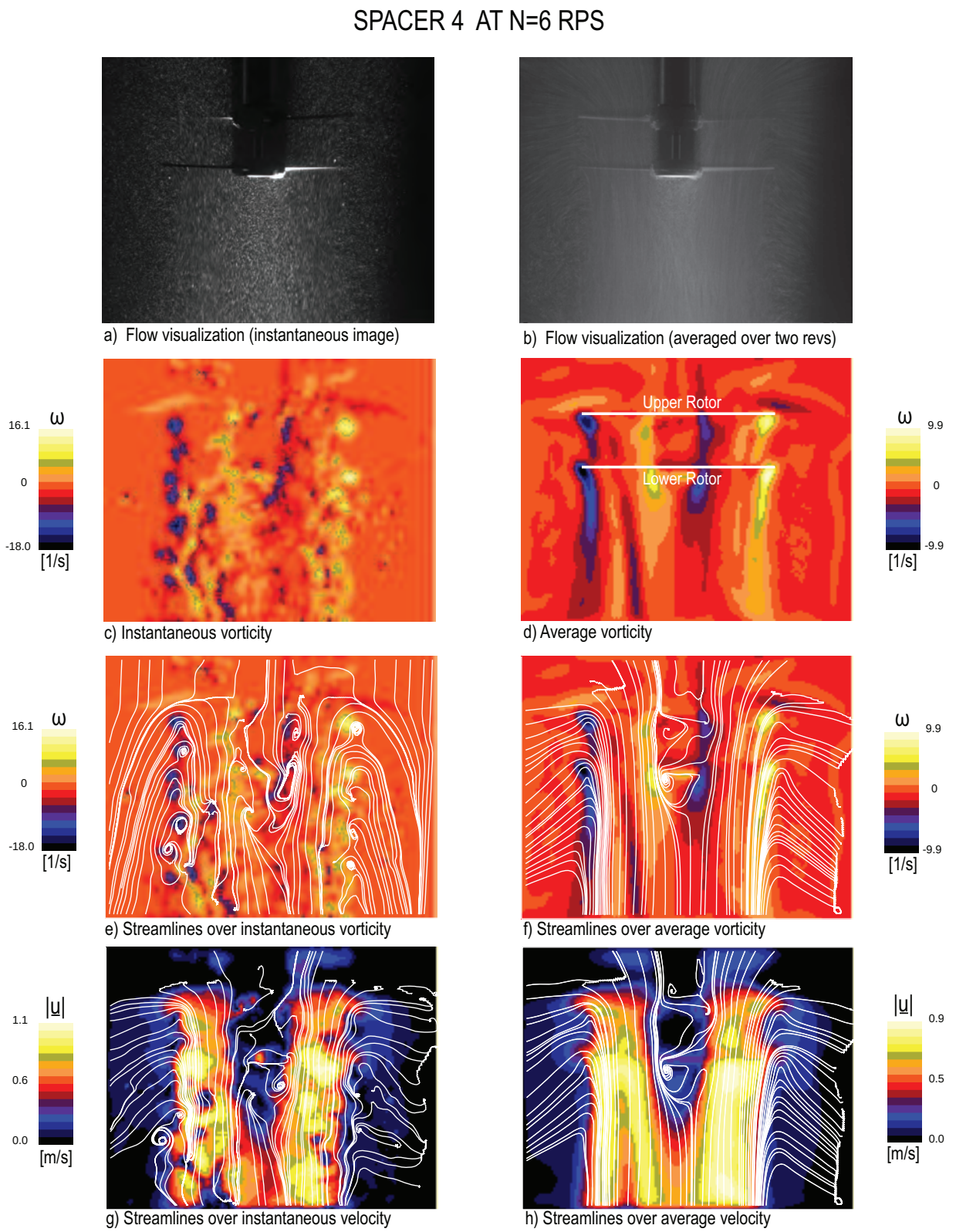

Figure A.44: Flow field of a two-bladed coaxial rotor (spacer4) at $N = 6$ rps. First row (a,b): particle flow visualization. In rows 2-4 are shown PIV measurements. Second row (c,d): vorticity fields. Third row (e,f): streamlines over vorticity. Fourth row (g,h): streamlines over speed. Streamlines in frame (e) are drawn from a moving reference frame and streamlines in frames (f-h) are drawn from a stationary reference frame.

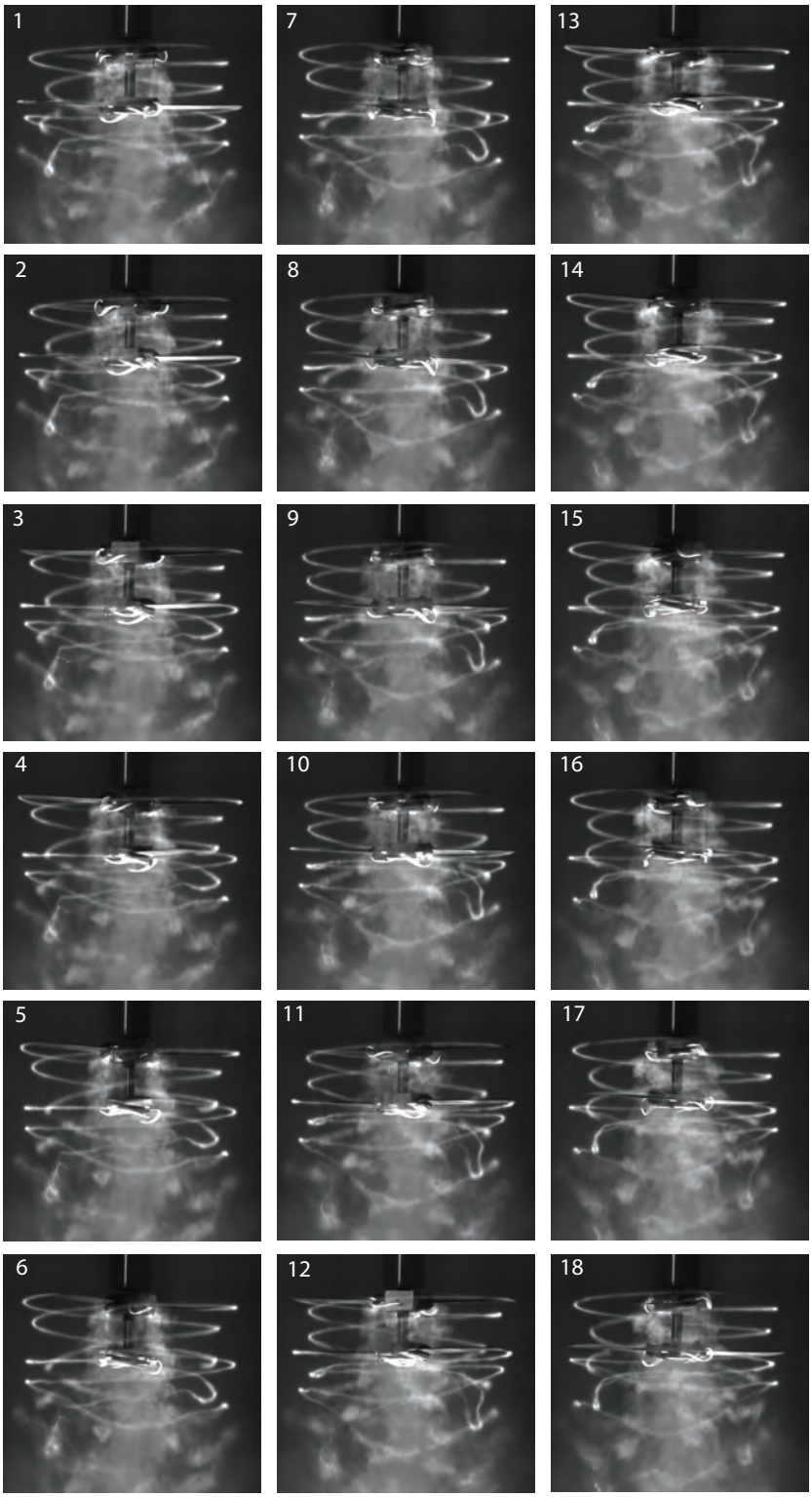

Figure A.45: Vortex wake evolution of the coaxial rotors with axial spacing of H/R=0.5 during one complete rotor revolutions at 4 rps. Images are 20° ($\pi/9$ rad) apart. Time separation between successive images is 13.89 ms.

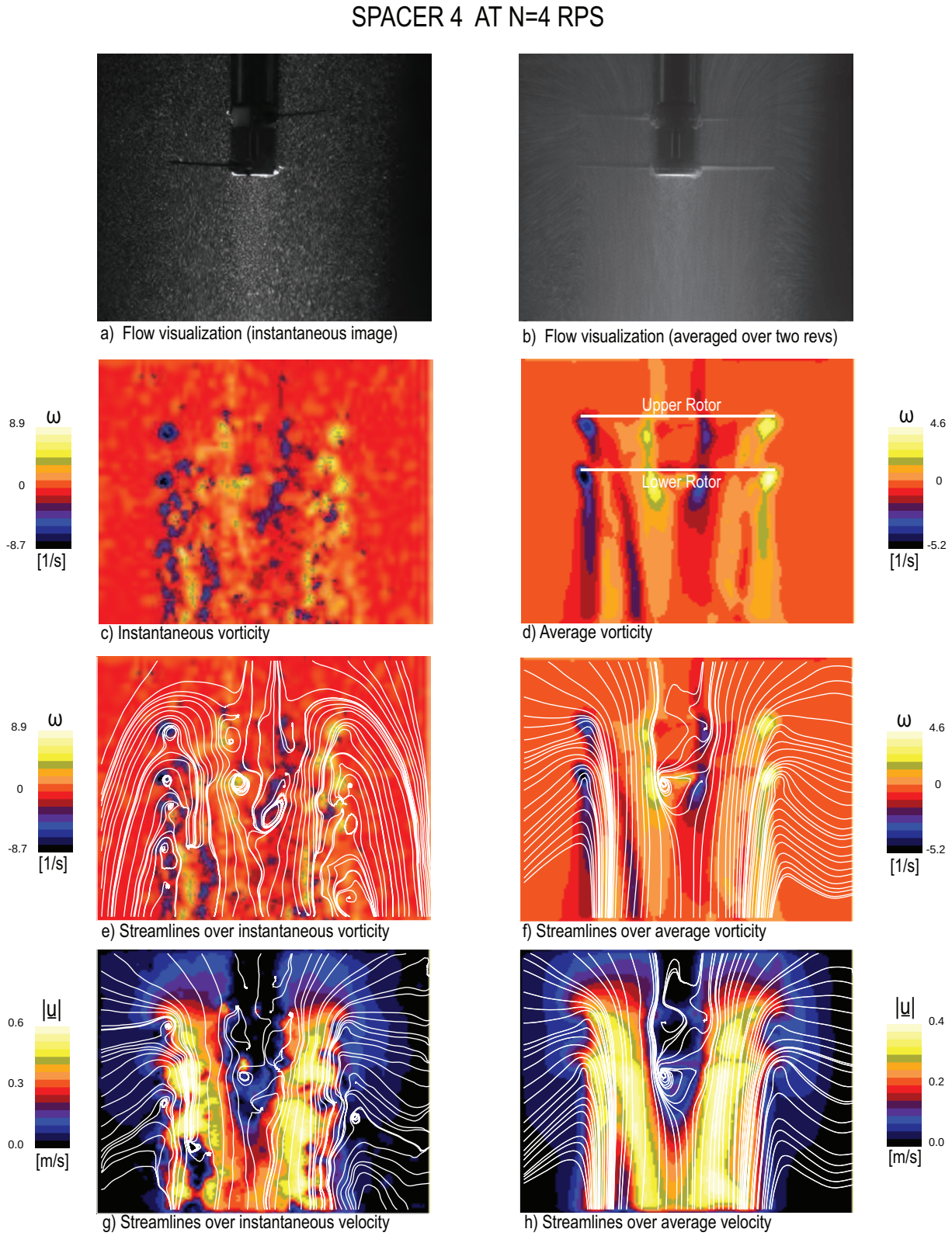

Figure A.46: Flow field of a two-bladed coaxial rotor (spacer4) at $N = 4$ rps. First row (a,b): particle flow visualization. In rows 2-4 are shown PIV measurements. Second row (c,d): vorticity fields. Third row (e,f): streamlines over vorticity. Fourth row (g,h): streamlines over speed. Streamlines in frame (e) are drawn from a moving reference frame and streamlines in frames (f-h) are drawn from a stationary reference frame.

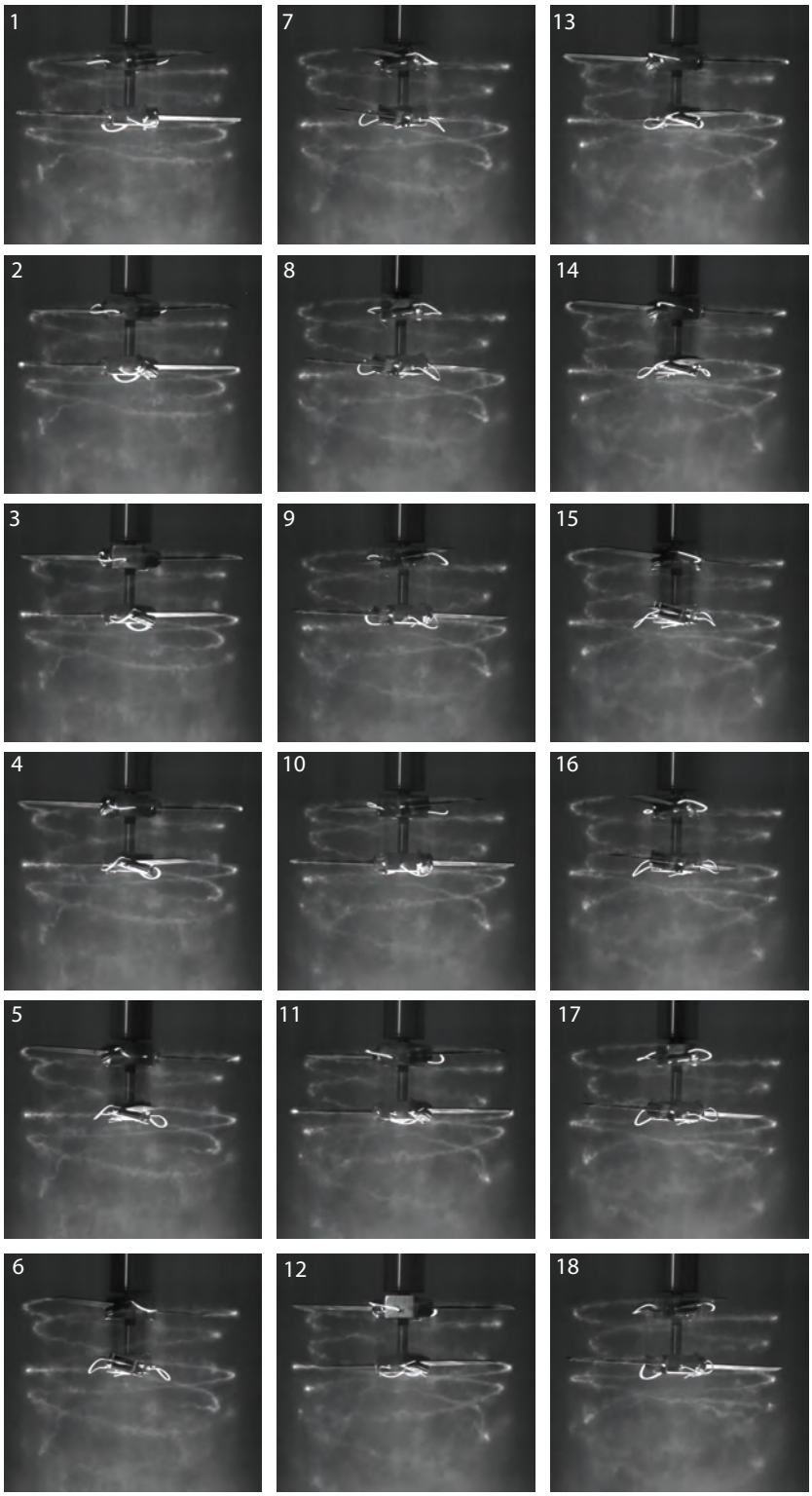

Figure A.47: Vortex wake evolution of the coaxial rotors with axial spacing of H/R=0.5 during one complete rotor revolutions at 2 rps. Images are 20° ($\pi/9$ rad) apart. Time separation between successive images is 27.78 ms.

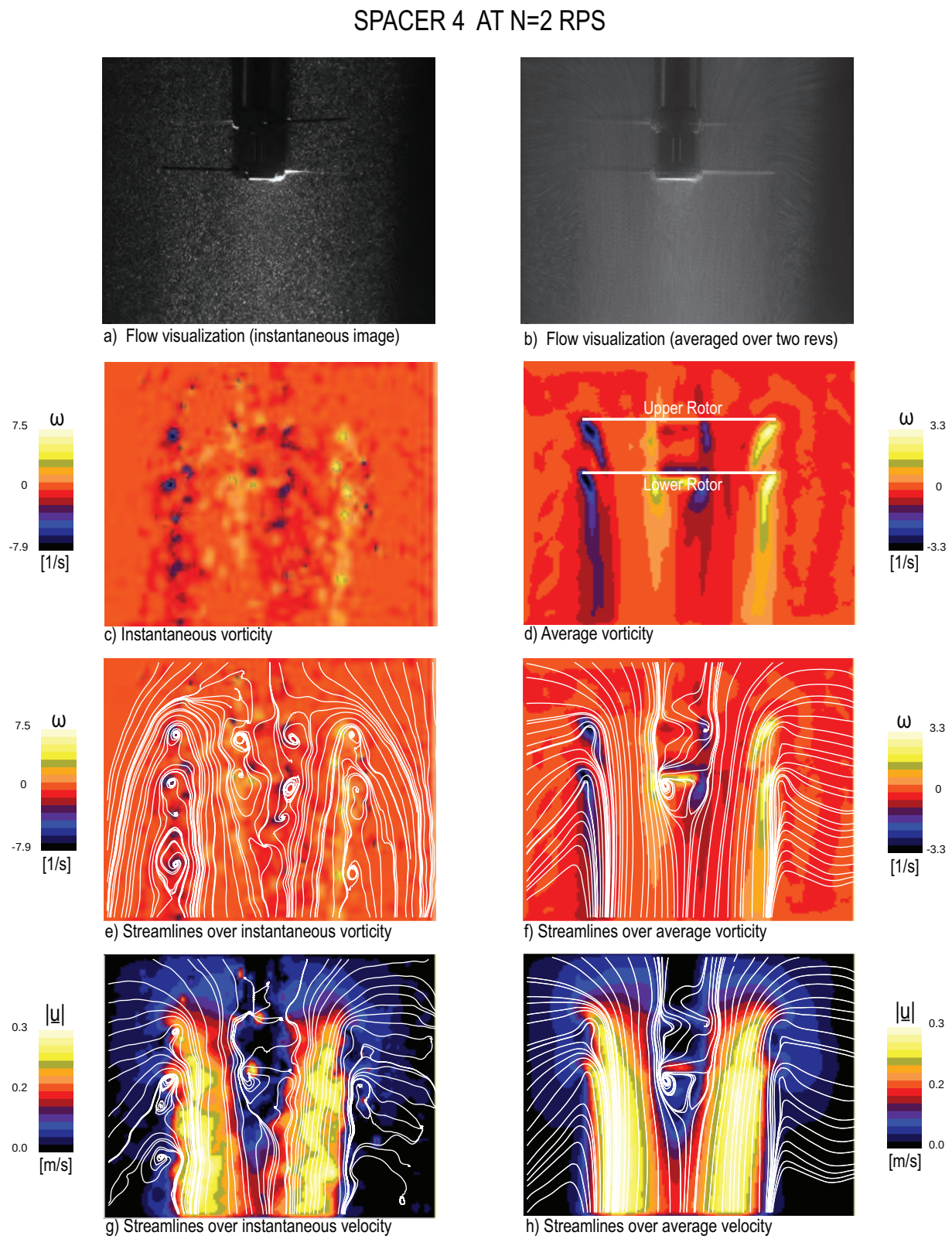

Figure A.48: Flow field of a two-bladed coaxial rotor (spacer4) at $N = 2$ rps. First row (a,b): particle flow visualization. In rows 2-4 are shown PIV measurements. Second row (c,d): vorticity fields. Third row (e,f): streamlines over vorticity. Fourth row (g,h): streamlines over speed. Streamlines in frame (e) are drawn from a moving reference frame and streamlines in frames (f-h) are drawn from a stationary reference frame.

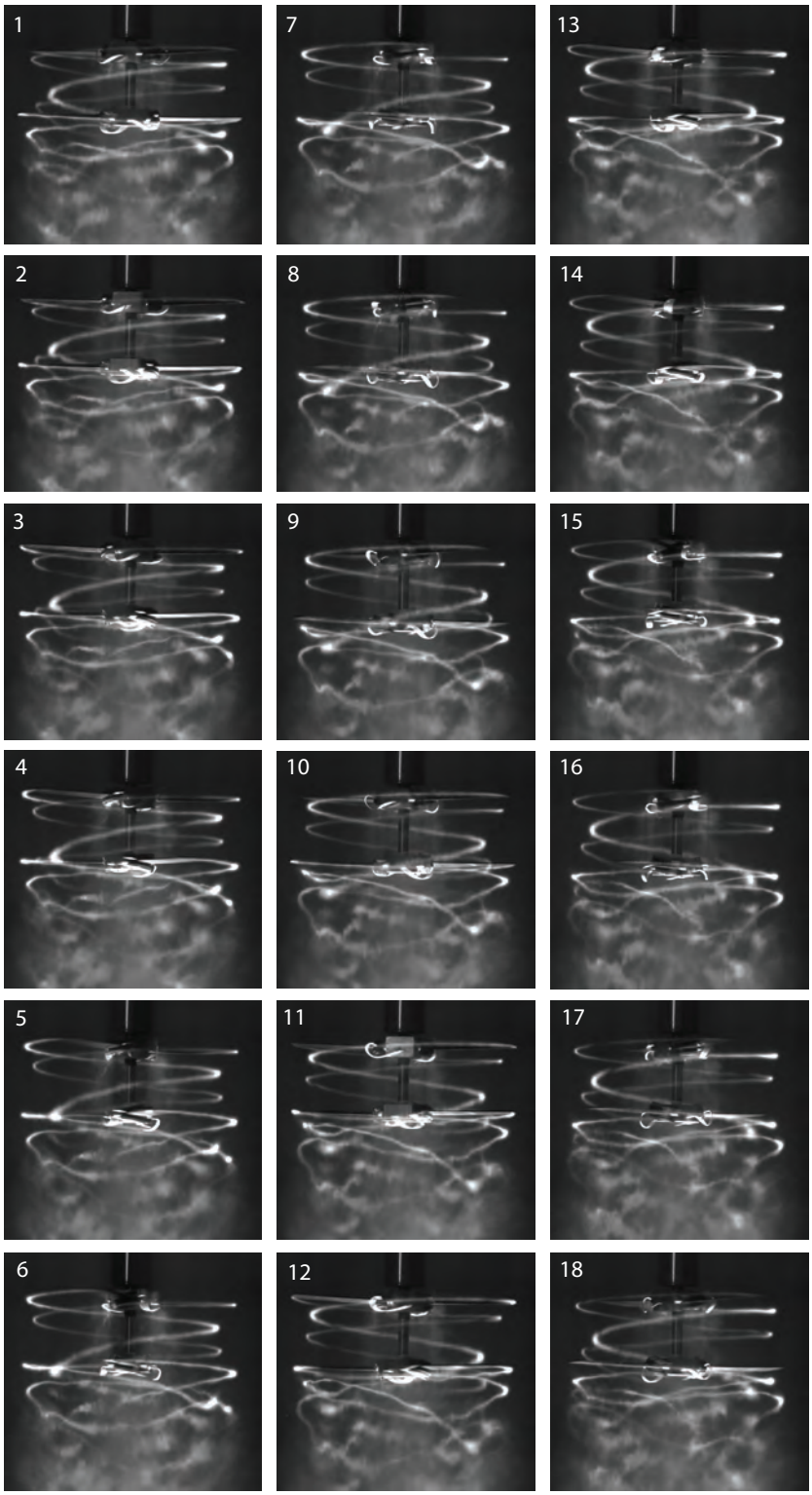

Figure A.49: Vortex wake evolution of the coaxial rotors with axial spacing of H/R=0.625 during one complete rotor revolutions at 6 rps. Images are 20° ($\pi/9$ rad) apart. Time separation between successive images is 9.26 ms.

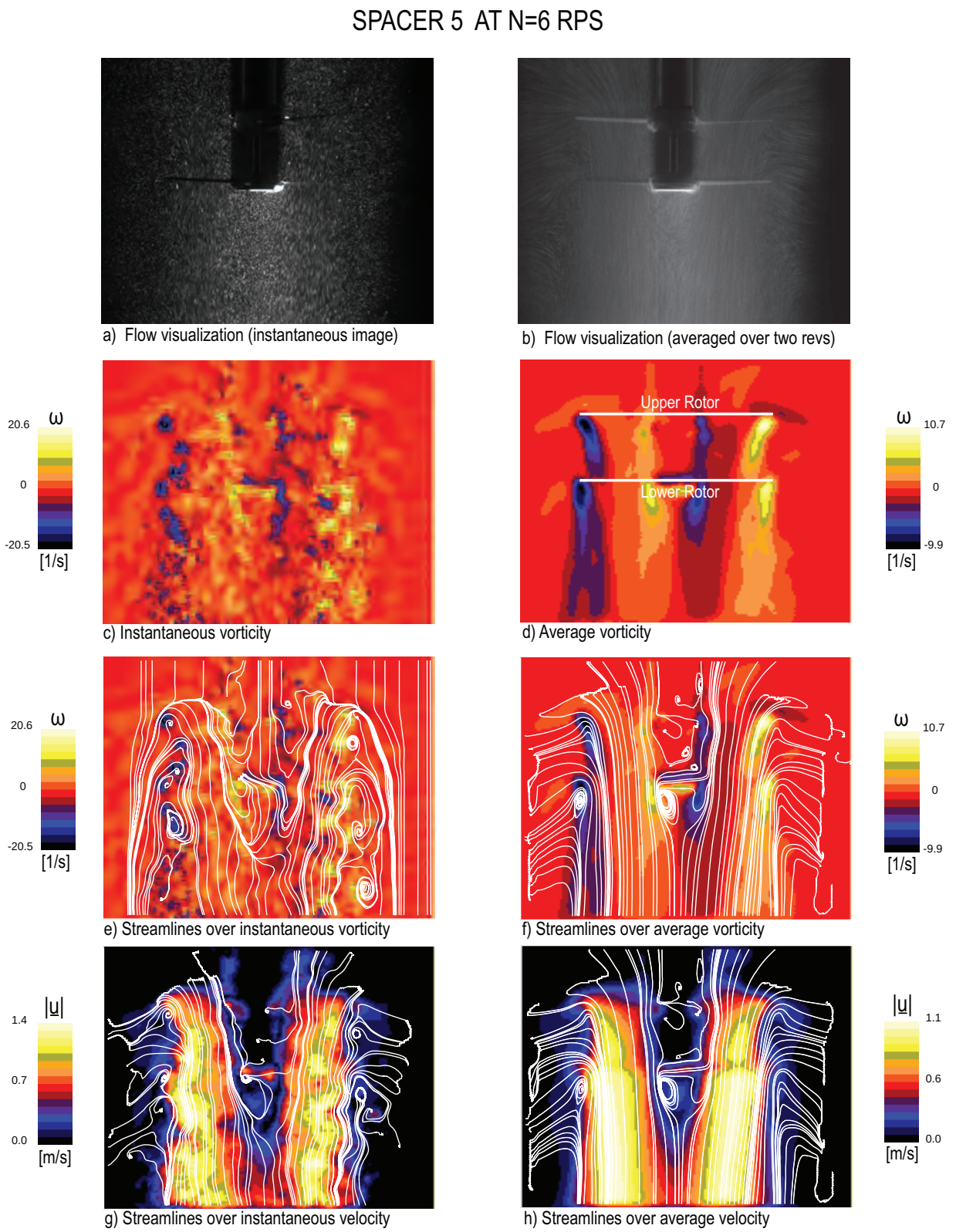

Figure A.50: Flow field of a two-bladed coaxial rotor (spacer5) at $N = 6$ rps. First row (a,b): particle flow visualization. In rows 2-4 are shown PIV measurements. Second row (c,d): vorticity fields. Third row (e,f): streamlines over vorticity. Fourth row (g,h): streamlines over speed. Streamlines in frame (e) are drawn from a moving reference frame and streamlines in frames (f-h) are drawn from a stationary reference frame.

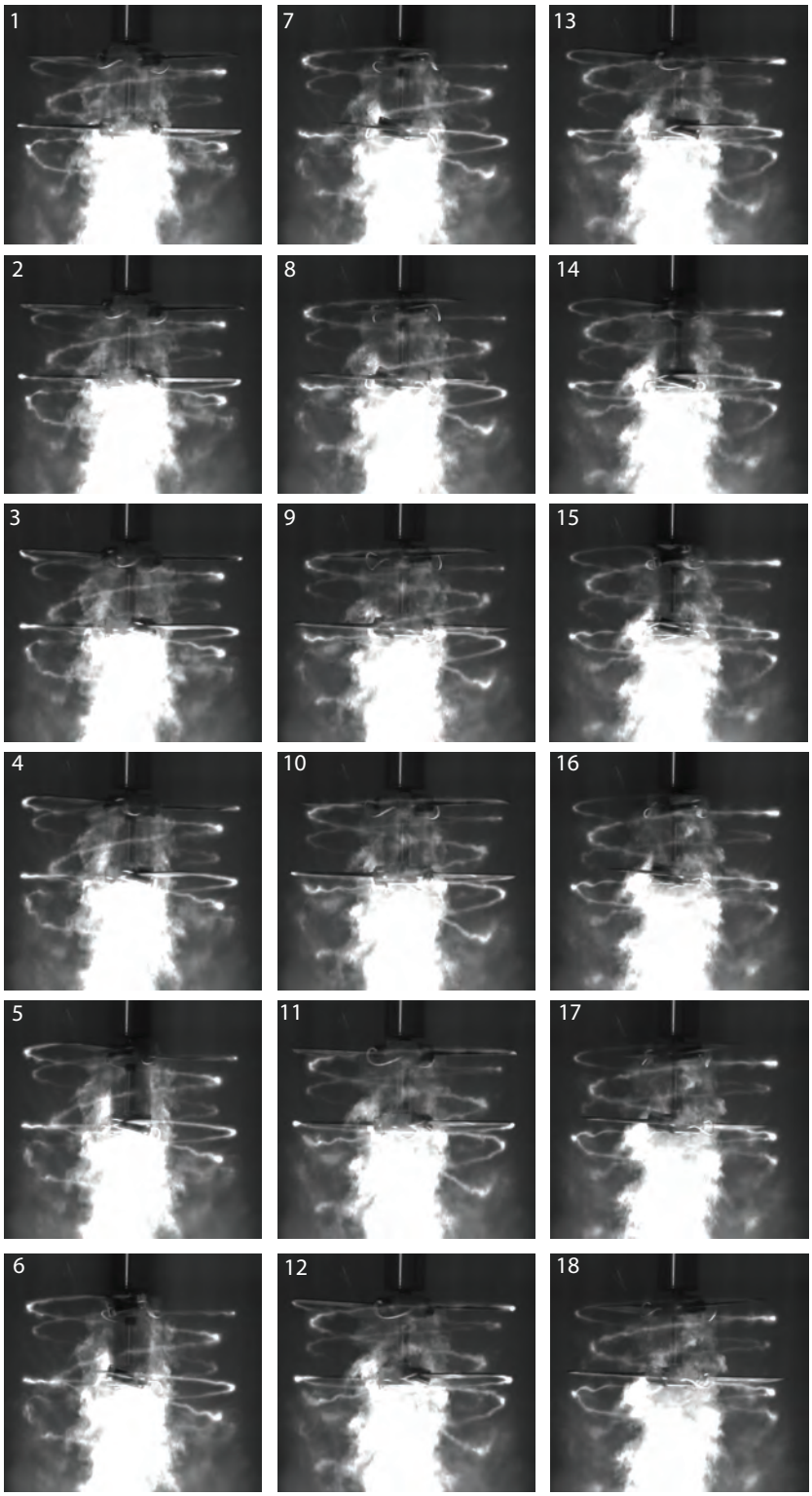

Figure A.51: Vortex wake evolution of the coaxial rotors with axial spacing of H/R=0.625 during one complete rotor revolutions at 4 rps. Images are 20° ($\pi/9$ rad) apart. Time separation between successive images is 13.89 ms.

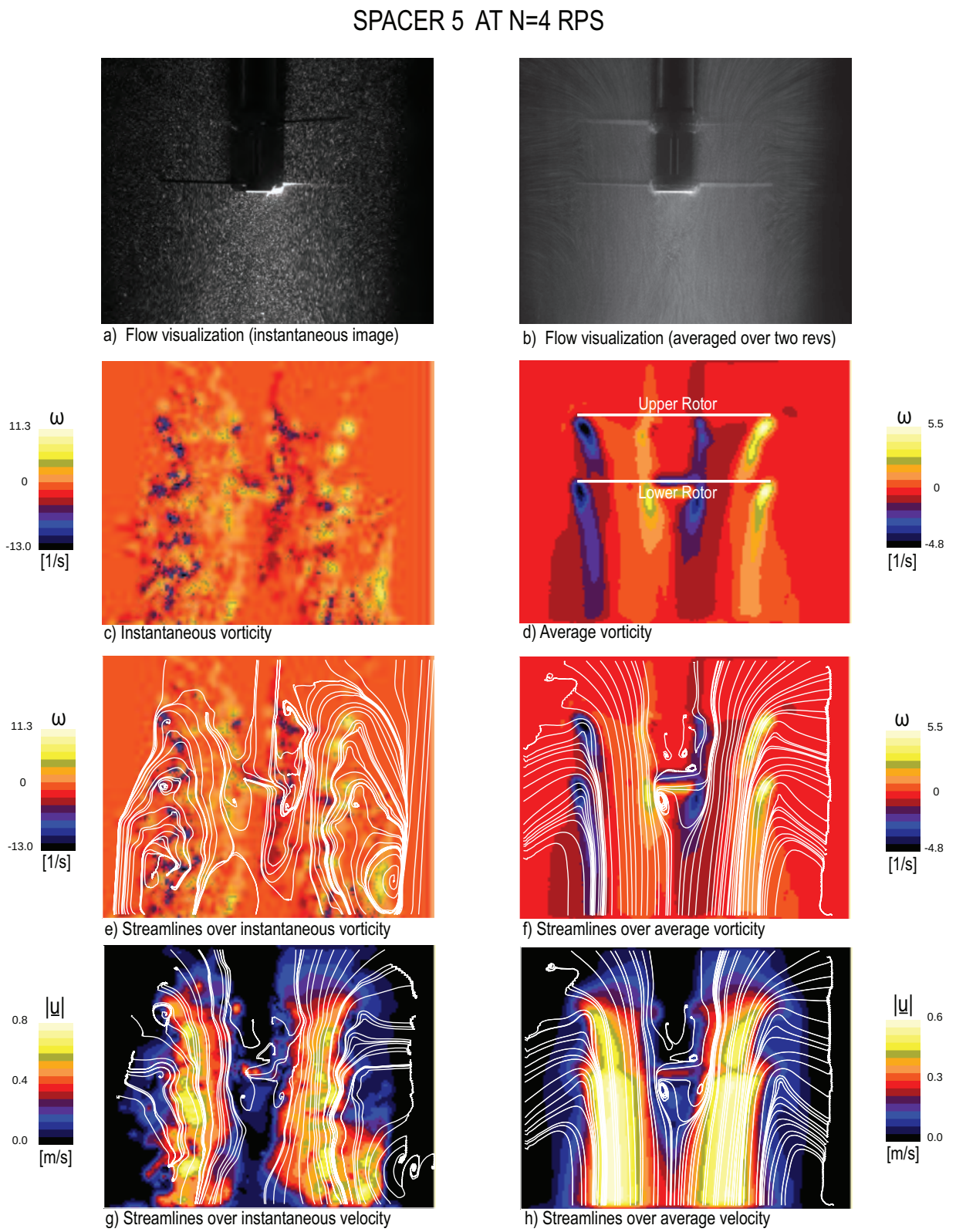

Figure A.52: Flow field of a two-bladed coaxial rotor (spacer5) at $N = 4$ rps. First row (a,b): particle flow visualization. In rows 2-4 are shown PIV measurements. Second row (c,d): vorticity fields. Third row (e,f): streamlines over vorticity. Fourth row (g,h): streamlines over speed. Streamlines in frame (e) are drawn from a moving reference frame and streamlines in frames (f-h) are drawn from a stationary reference frame.

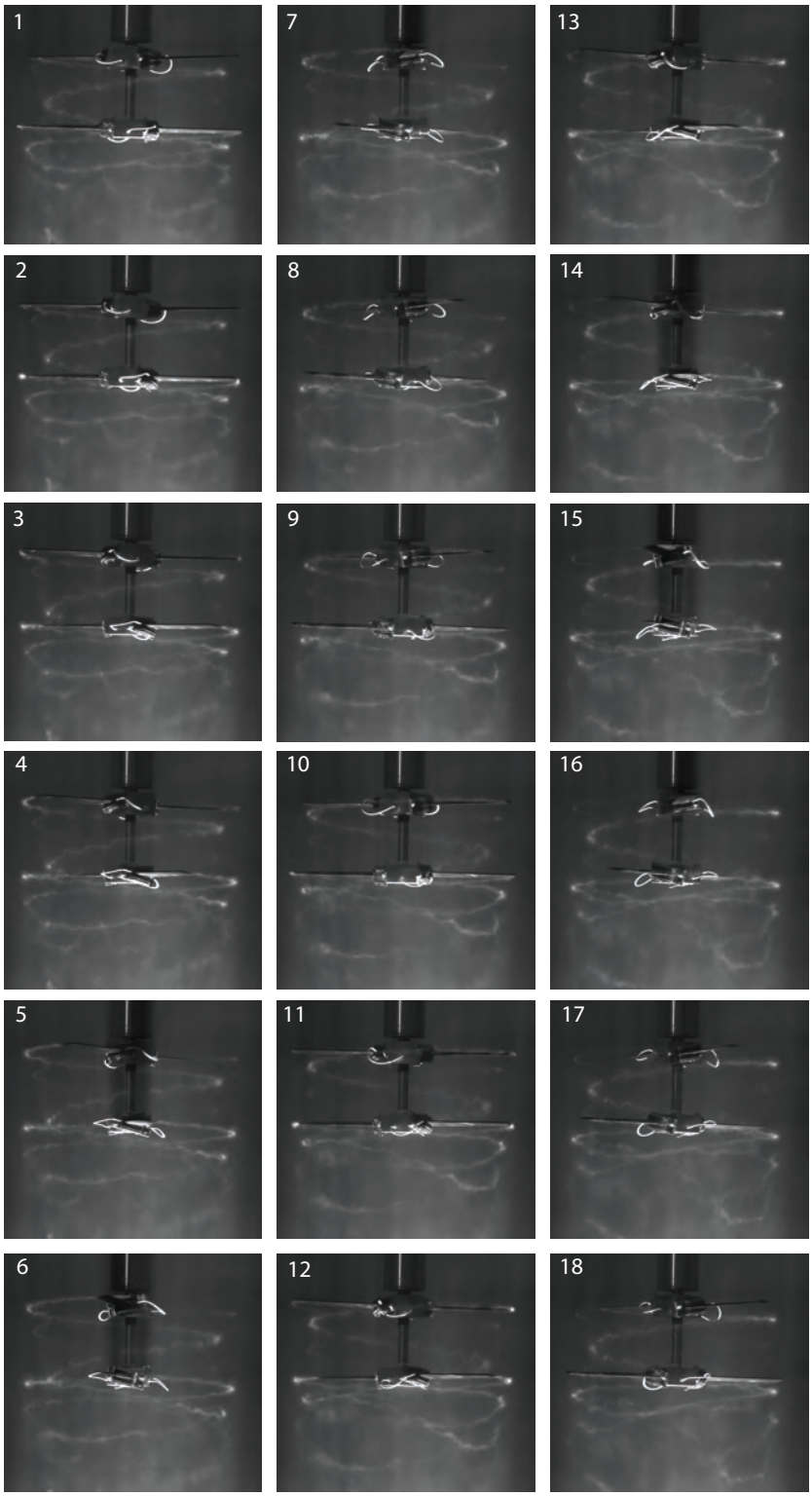

Figure A.53: Vortex wake evolution of the coaxial rotors with axial spacing of H/R=0.625 during one complete rotor revolutions at 2 rps. Images are 20° ($\pi/9$ rad) apart. Time separation between successive images is 27.78 ms.

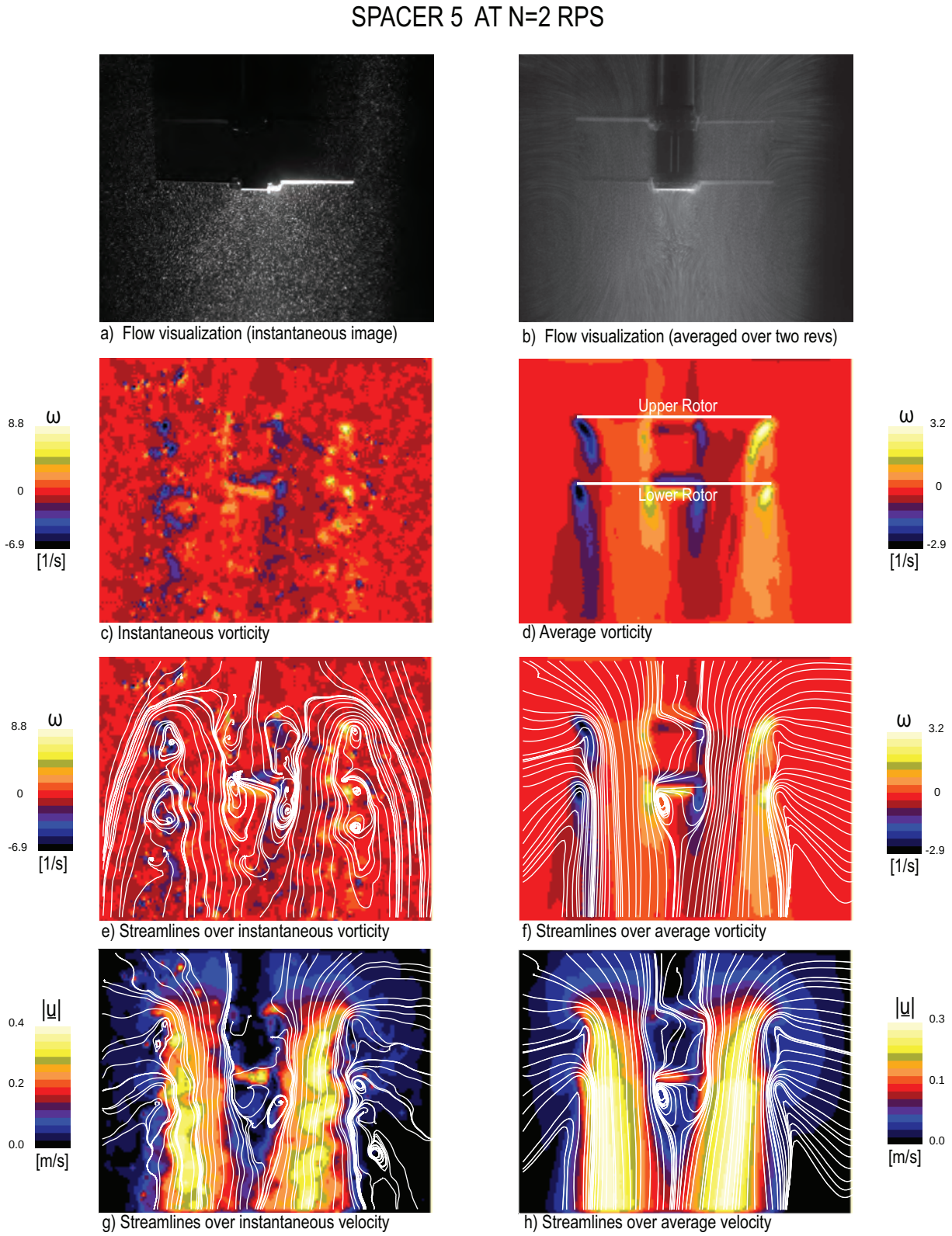

Figure A.54: Flow field of a two-bladed coaxial rotor (spacer5) at $N = 2$ rps. First row (a,b): particle flow visualization. In rows 2-4 are shown PIV measurements. Second row (c,d): vorticity fields. Third row (e,f): streamlines over vorticity. Fourth row (g,h): streamlines over speed. Streamlines in frame (e) are drawn from a moving reference frame and streamlines in frames (f-h) are drawn from a stationary reference frame.

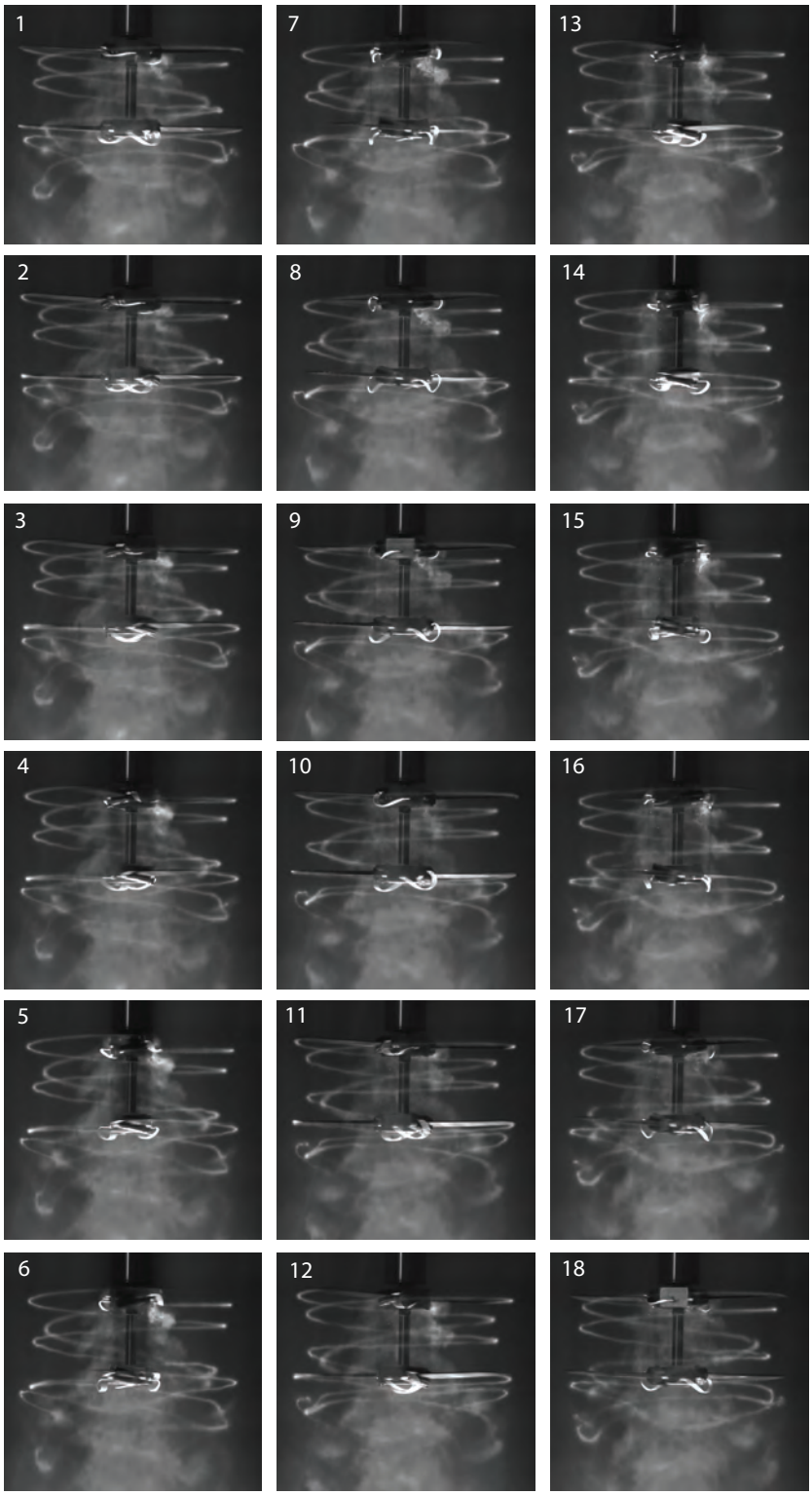

Figure A.55: Vortex wake evolution of the coaxial rotors with axial spacing of H/R=0.75 during one complete rotor revolutions at 6 rps. Images are 20° ($\pi/9$ rad) apart. Time separation between successive images is 9.26 ms.

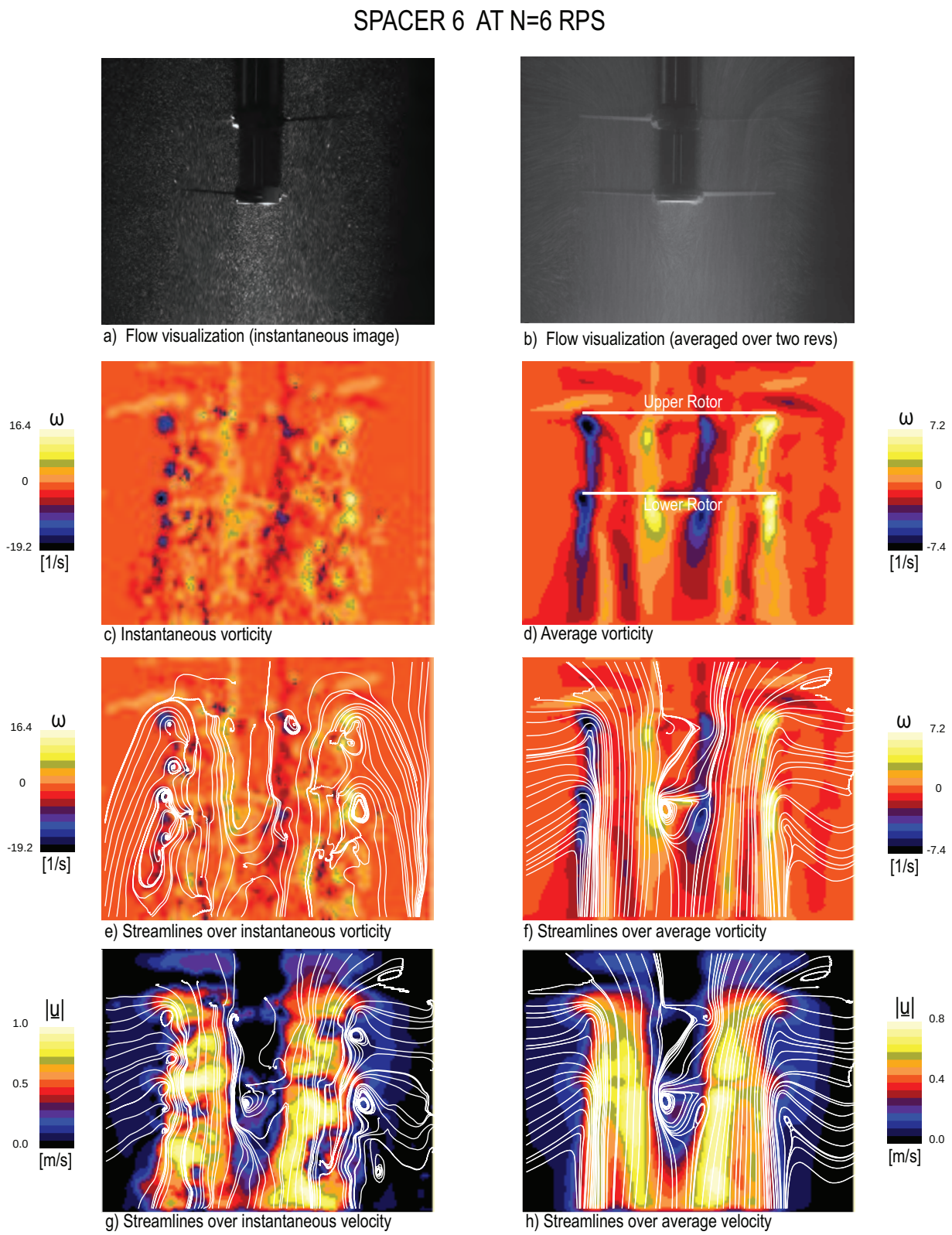

Figure A.56: Flow field of a two-bladed coaxial rotor (spacer6) at $N = 6$ rps. First row (a,b): particle flow visualization. In rows 2-4 are shown PIV measurements. Second row (c,d): vorticity fields. Third row (e,f): streamlines over vorticity. Fourth row (g,h): streamlines over speed. Streamlines in frame (e) are drawn from a moving reference frame and streamlines in frames (f-h) are drawn from a stationary reference frame.

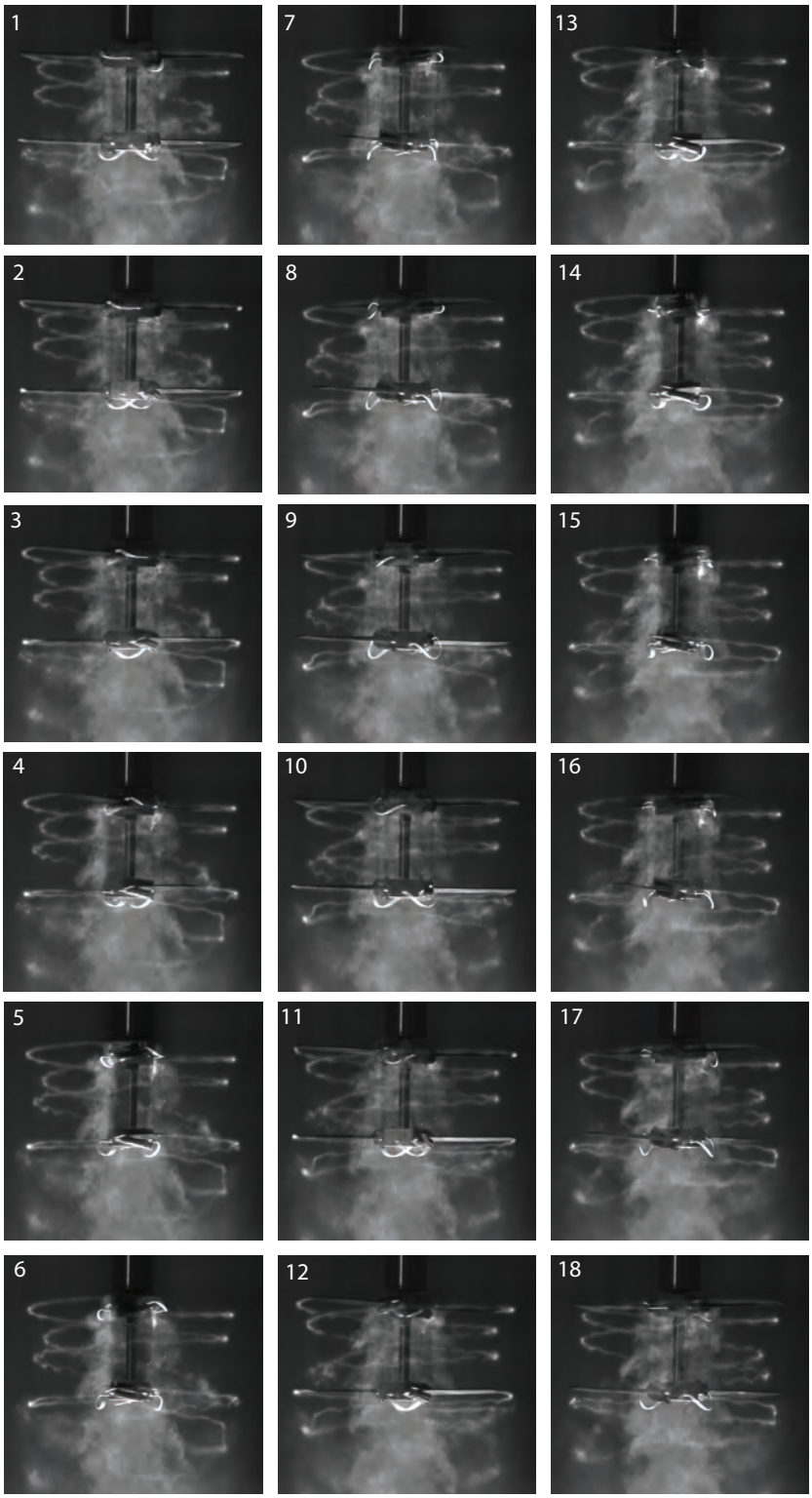

Figure A.57: Vortex wake evolution of the coaxial rotors with axial spacing of H/R=0.75 during one complete rotor revolutions at 4 rps. Images are 20° ($\pi/9$ rad) apart. Time separation between successive images is 13.89 ms.

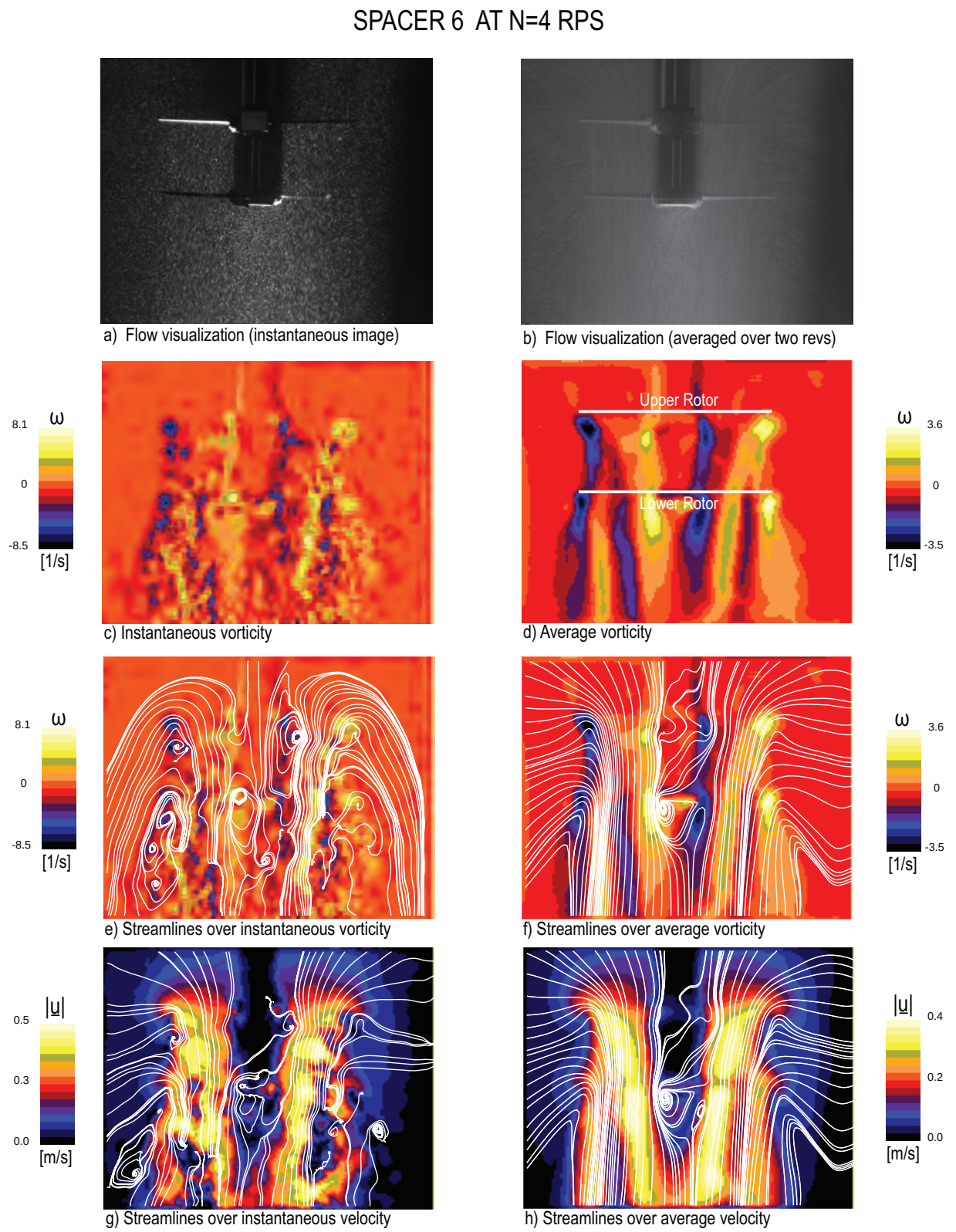

Figure A.58: Flow field of a two-bladed coaxial rotor (spacer6) at $N = 4$ rps. First row (a,b): particle flow visualization. In rows 2-4 are shown PIV measurements. Second row (c,d): vorticity fields. Third row (e,f): streamlines over vorticity. Fourth row (g,h): streamlines over speed. Streamlines in frame (e) are drawn from a moving reference frame and streamlines in frames (f-h) are drawn from a stationary reference frame.

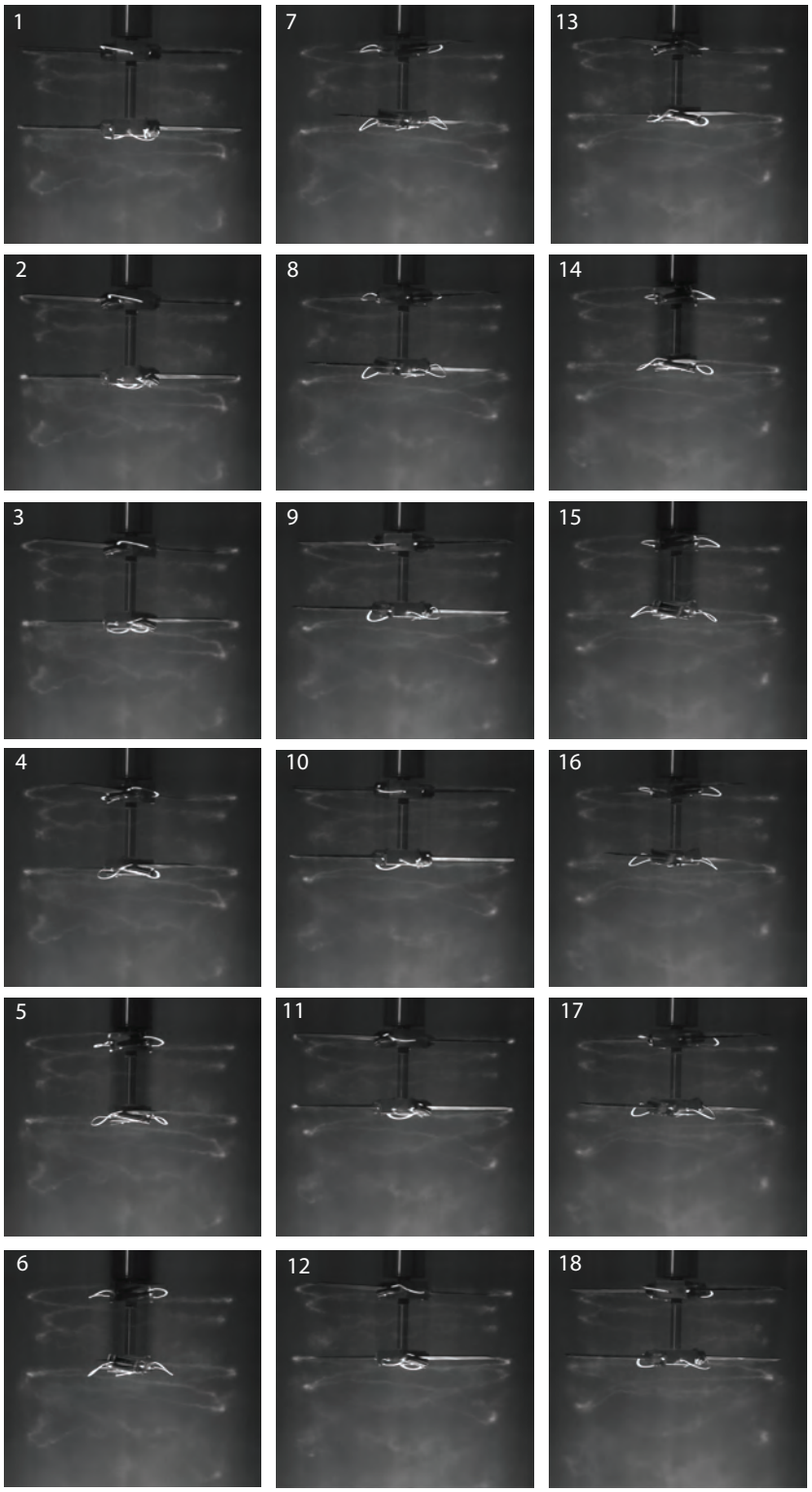

Figure A.59: Vortex wake evolution of the coaxial rotors with axial spacing of H/R=0.75 during one complete rotor revolutions at 2 rps. Images are 20° ($\pi/9$ rad) apart. Time separation between successive images is 27.78 ms.

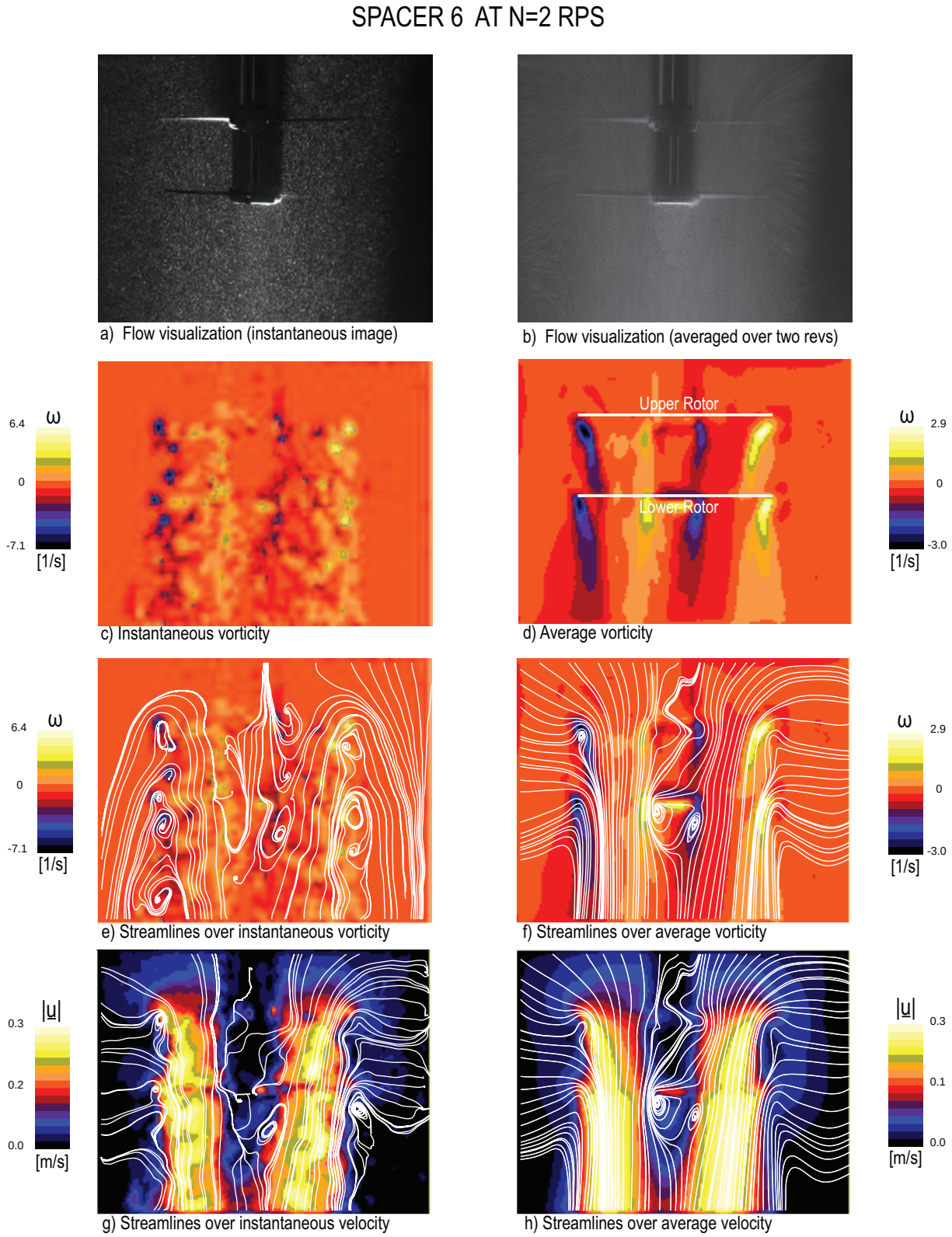

Figure A.60: Flow field of a two-bladed coaxial rotor (spacer6) at $N = 2$ rps. First row (a,b): particle flow visualization. In rows 2-4 are shown PIV measurements. Second row (c,d): vorticity fields. Third row (e,f): streamlines over vorticity. Fourth row (g,h): streamlines over speed. Streamlines in frame (e) are drawn from a moving reference frame and streamlines in frames (f-h) are drawn from a stationary reference frame.

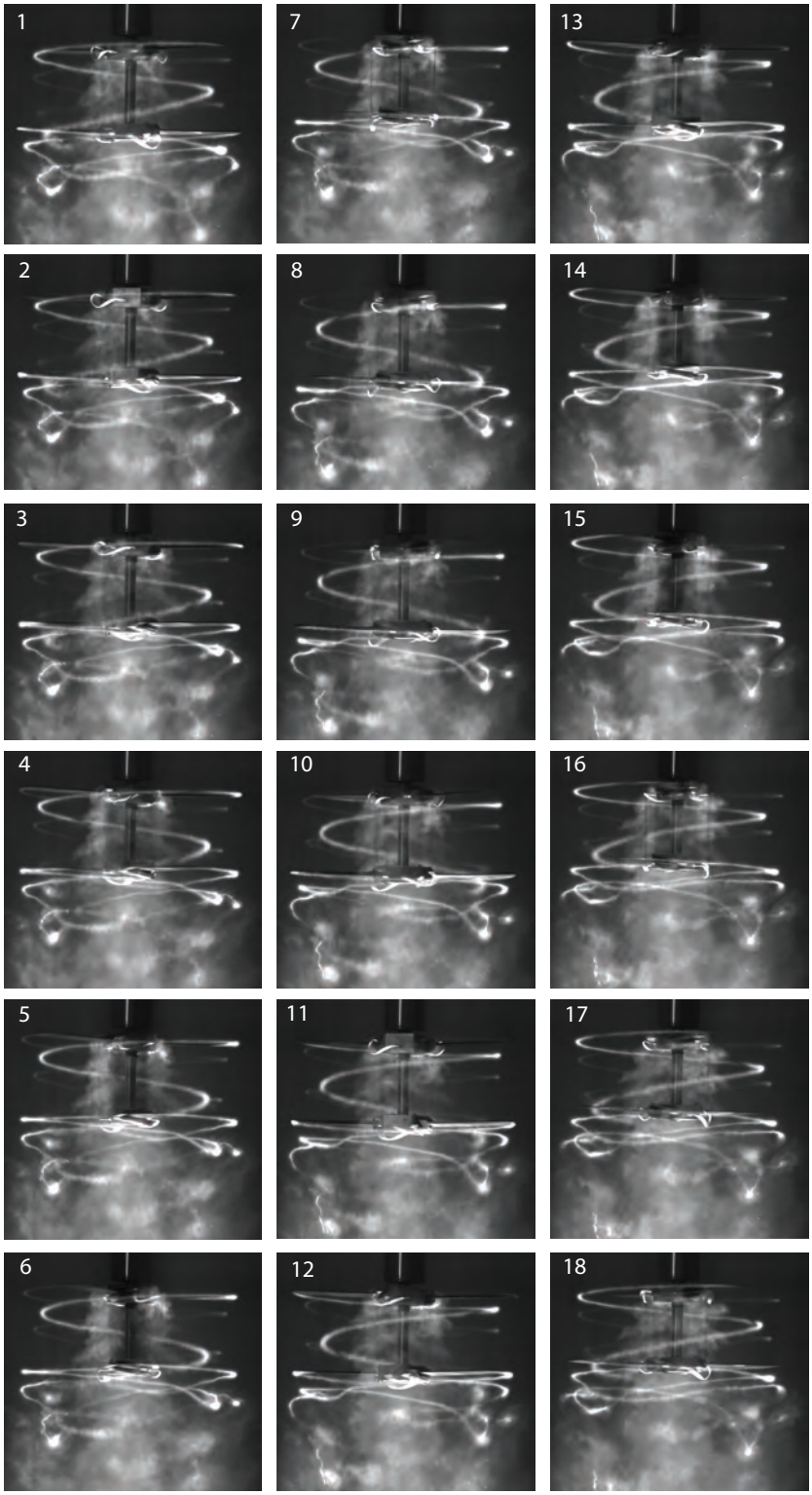

Figure A.61: Vortex wake evolution of the coaxial rotors with axial spacing of H/R=0.8 during one complete rotor revolutions at 6 rps. Images are 20° ($\pi/9$ rad) apart. Time separation between successive images is 9.26 ms.

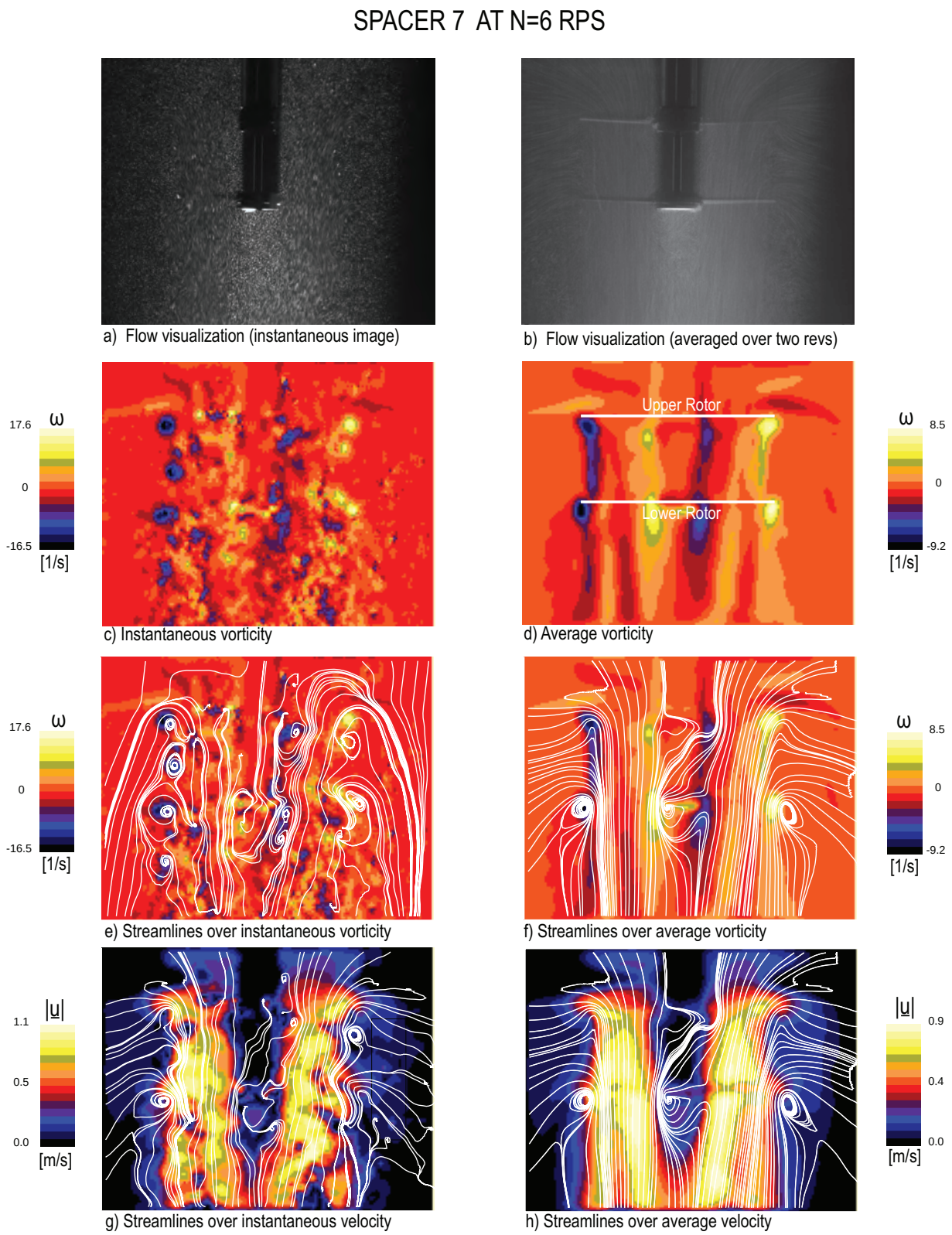

Figure A.62: Flow field of a two-bladed coaxial rotor (spacer7) at $N = 6$ rps. First row (a,b): particle flow visualization. In rows 2-4 are shown PIV measurements. Second row (c,d): vorticity fields. Third row (e,f): streamlines over vorticity. Fourth row (g,h): streamlines over speed. Streamlines in frame (e) are drawn from a moving reference frame and streamlines in frames (f-h) are drawn from a stationary reference frame.

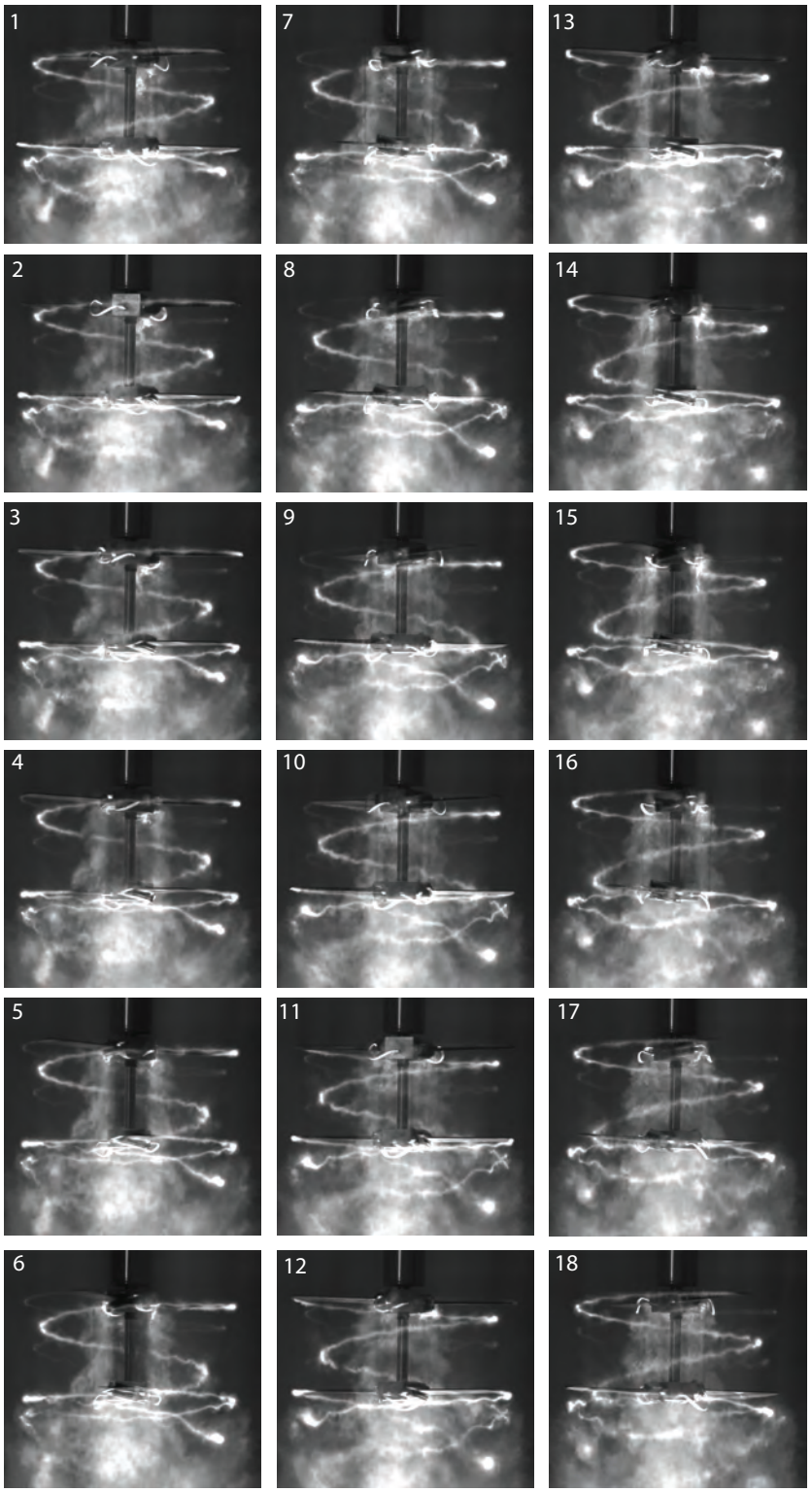

Figure A.63: Vortex wake evolution of the coaxial rotors with axial spacing of H/R=0.8 during one complete rotor revolutions at 4 rps. Images are 20° ($\pi/9$ rad) apart. Time separation between successive images is 13.89 ms.

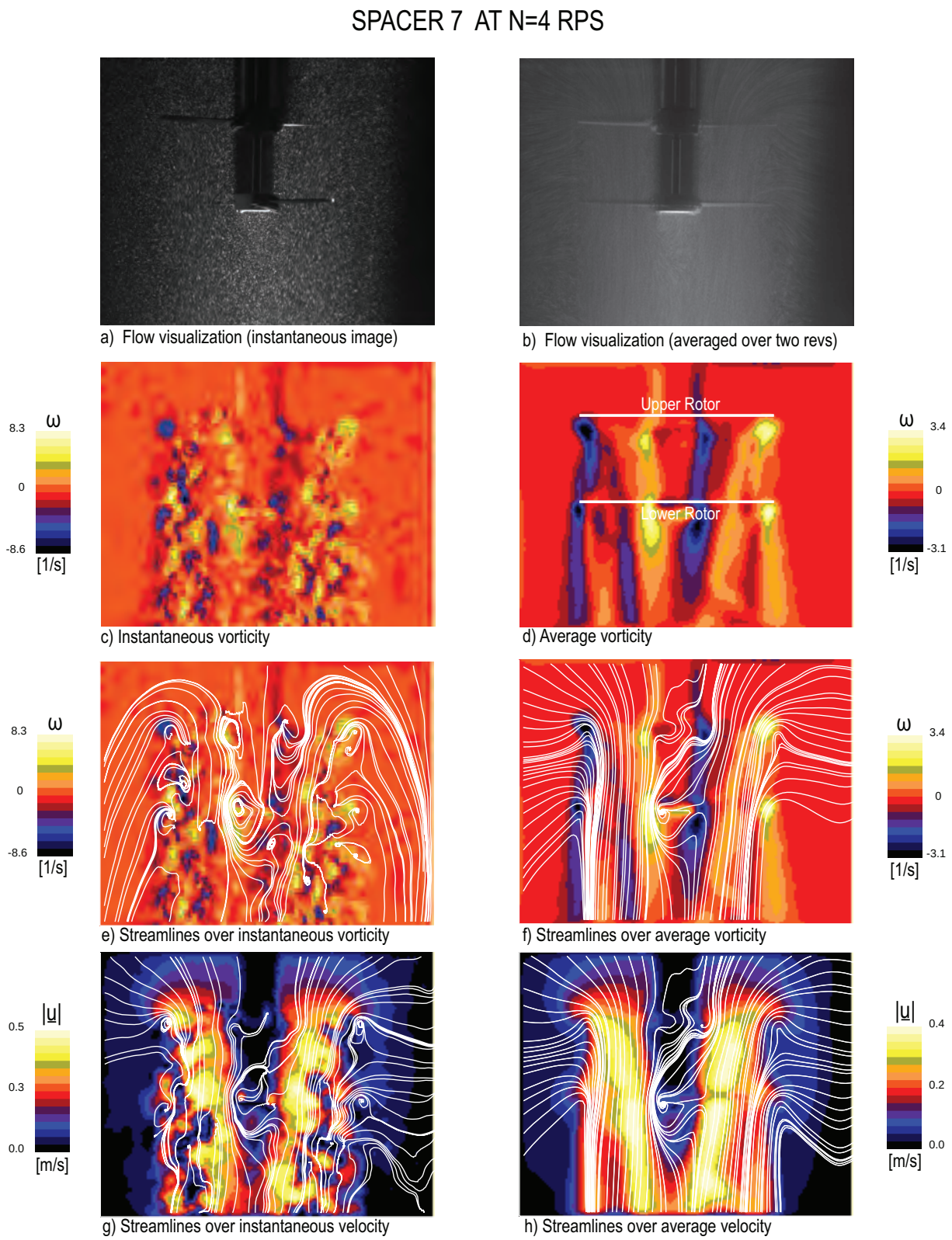

Figure A.64: Flow field of a two-bladed coaxial rotor (spacer7) at $N = 4$ rps. First row (a,b): particle flow visualization. In rows 2-4 are shown PIV measurements. Second row (c,d): vorticity fields. Third row (e,f): streamlines over vorticity. Fourth row (g,h): streamlines over speed. Streamlines in frame (e) are drawn from a moving reference frame and streamlines in frames (f-h) are drawn from a stationary reference frame.

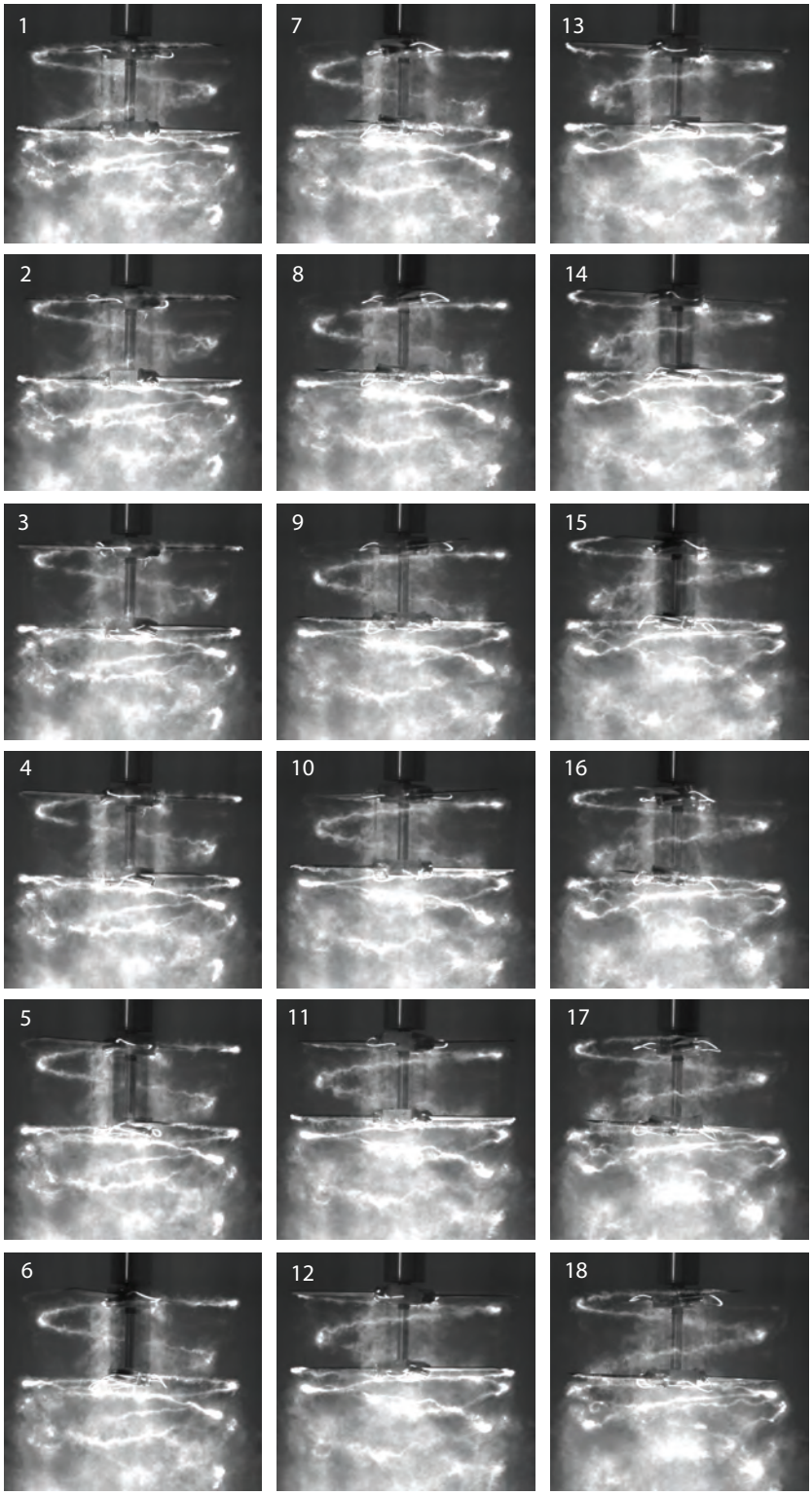

Figure A.65: Vortex wake evolution of the coaxial rotors with axial spacing of H/R=0.8 during one complete rotor revolutions at 2 rps. Images are 20° ($\pi/9$ rad) apart. Time separation between successive images is 27.78 ms.

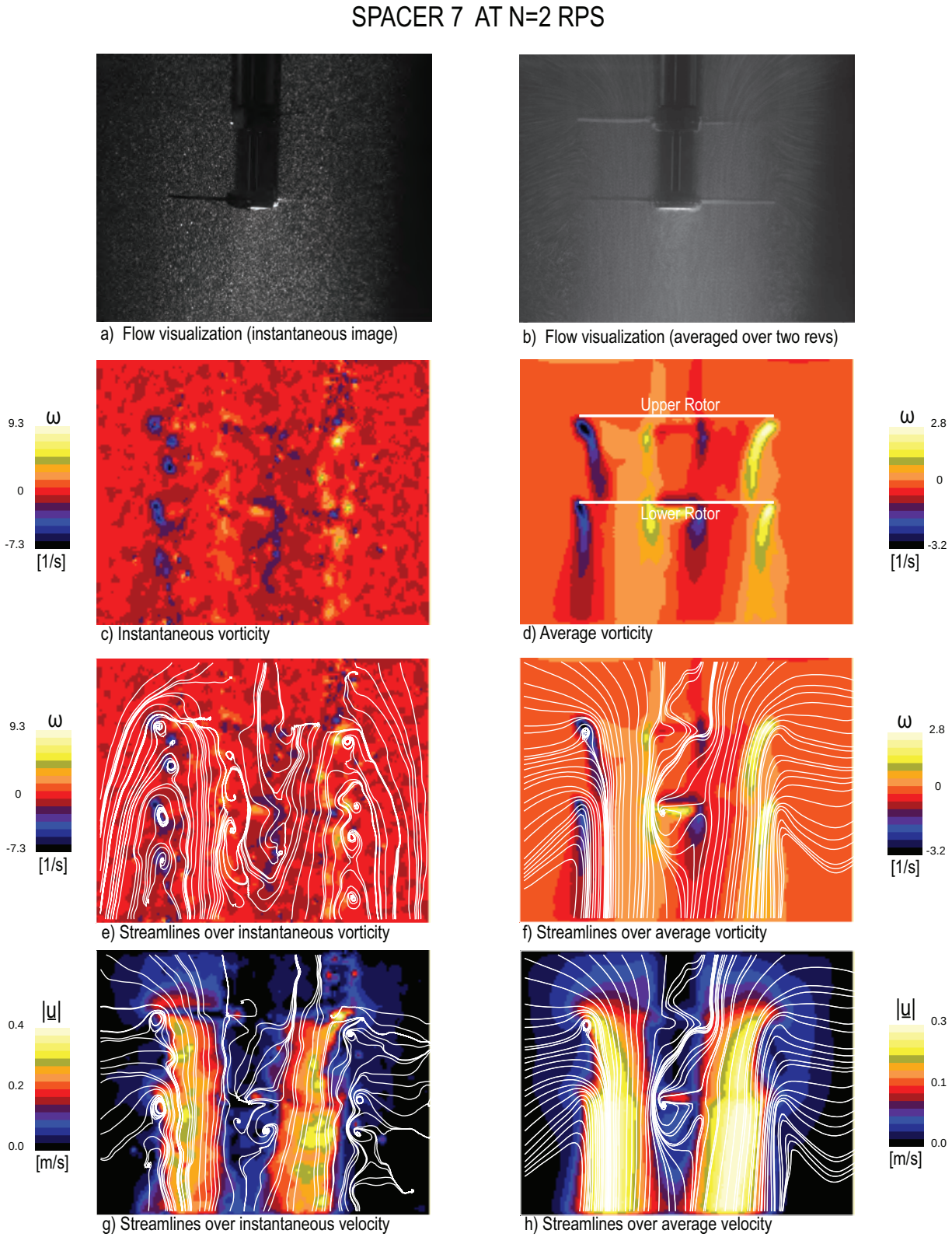

Figure A.66: Flow field of a two-bladed coaxial rotor (spacer7) at $N = 2$ rps. First row (a,b): particle flow visualization. In rows 2-4 are shown PIV measurements. Second row (c,d): vorticity fields. Third row (e,f): streamlines over vorticity. Fourth row (g,h): streamlines over speed. Streamlines in frame (e) are drawn from a moving reference frame and streamlines in frames (f-h) are drawn from a stationary reference frame.

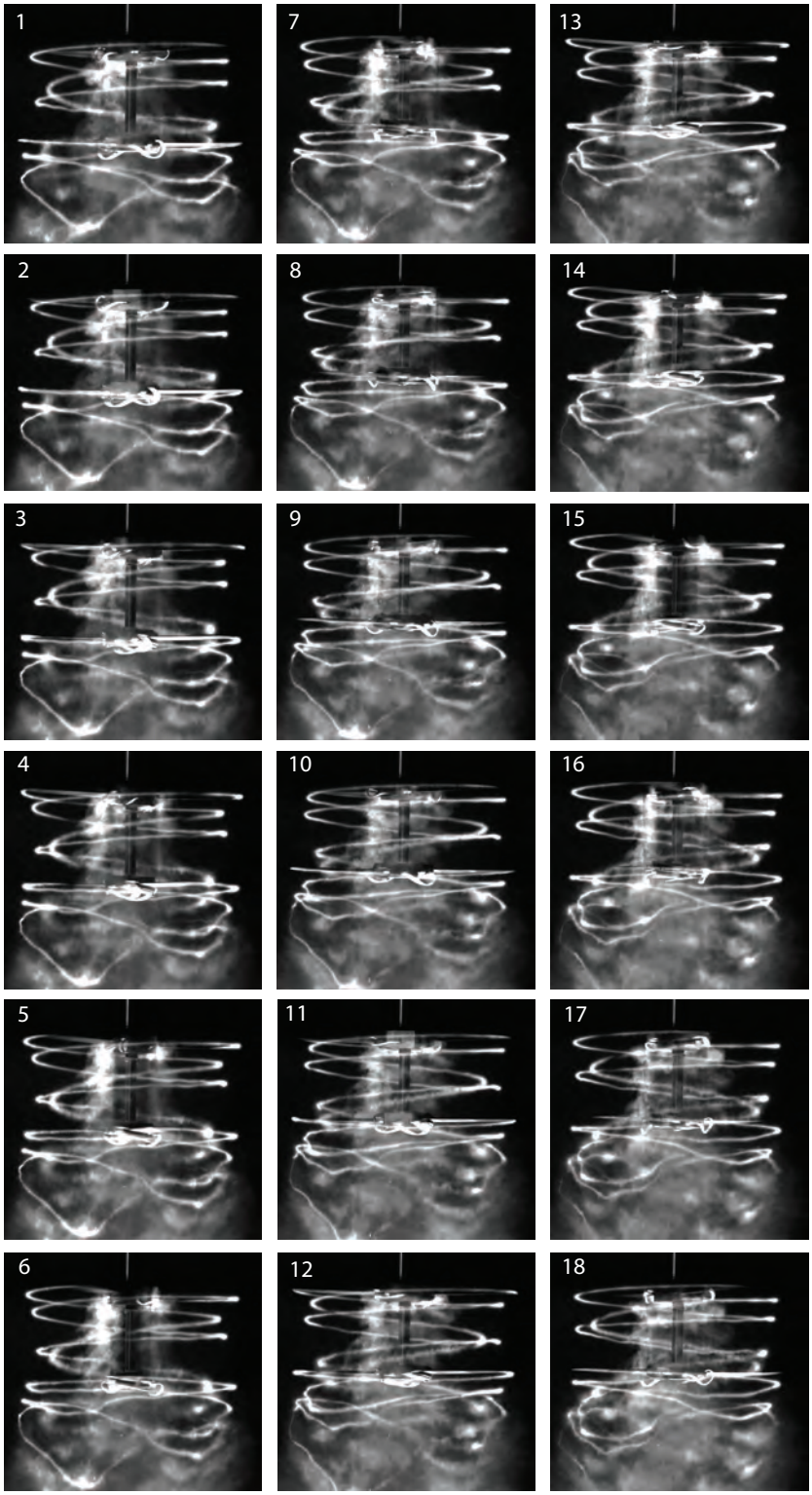

Figure A.67: Vortex wake evolution of the coaxial rotors with axial spacing of H/R=0.875 during one complete rotor revolutions at 6 rps. Images are 20° ($\pi/9$ rad) apart. Time separation between successive images is 9.26 ms.

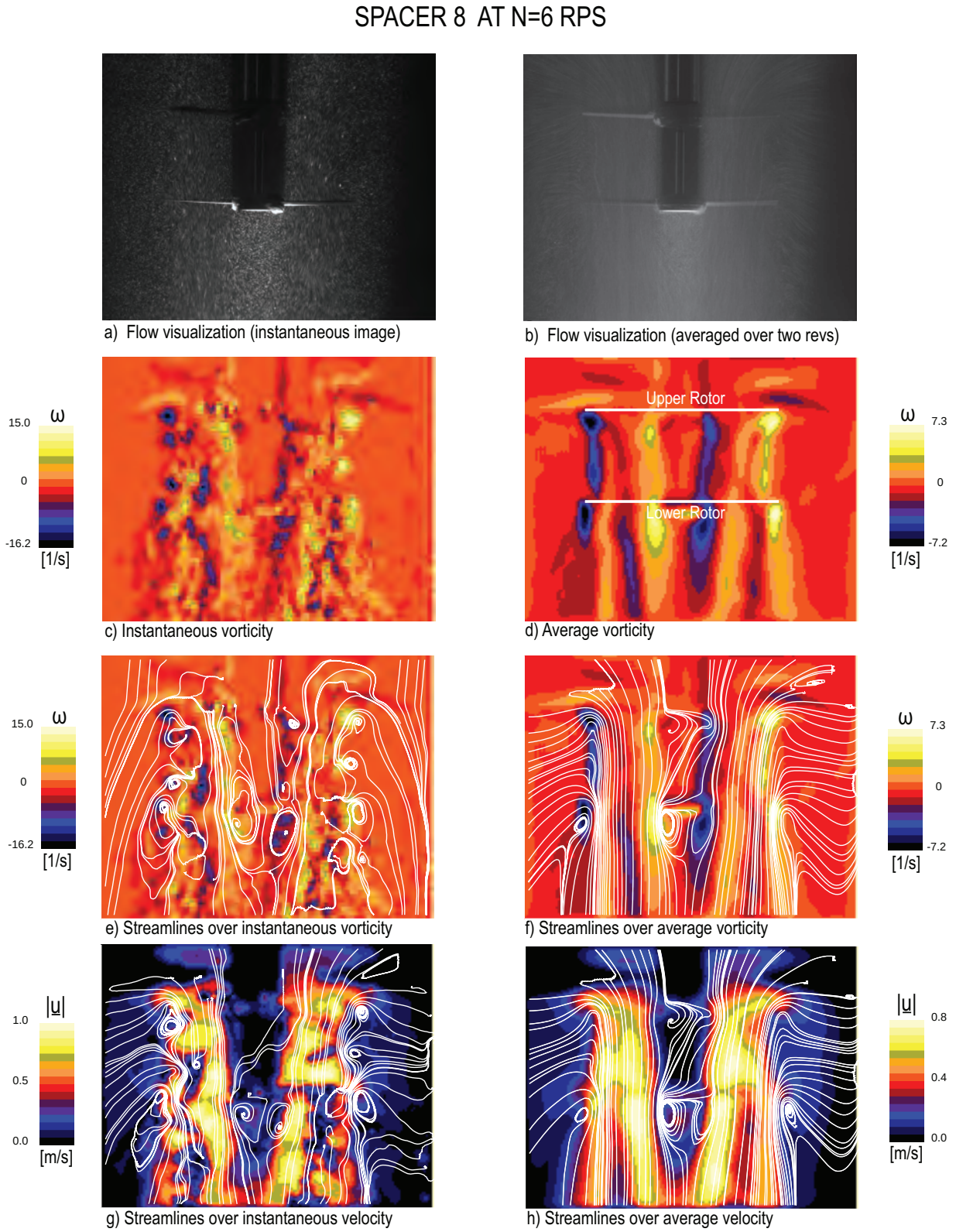

Figure A.68: Flow field of a two-bladed coaxial rotor (spacer8) at $N = 6$ rps. First row (a,b): particle flow visualization. In rows 2-4 are shown PIV measurements. Second row (c,d): vorticity fields. Third row (e,f): streamlines over vorticity. Fourth row (g,h): streamlines over speed. Streamlines in frame (e) are drawn from a moving reference frame and streamlines in frames (f-h) are drawn from a stationary reference frame.

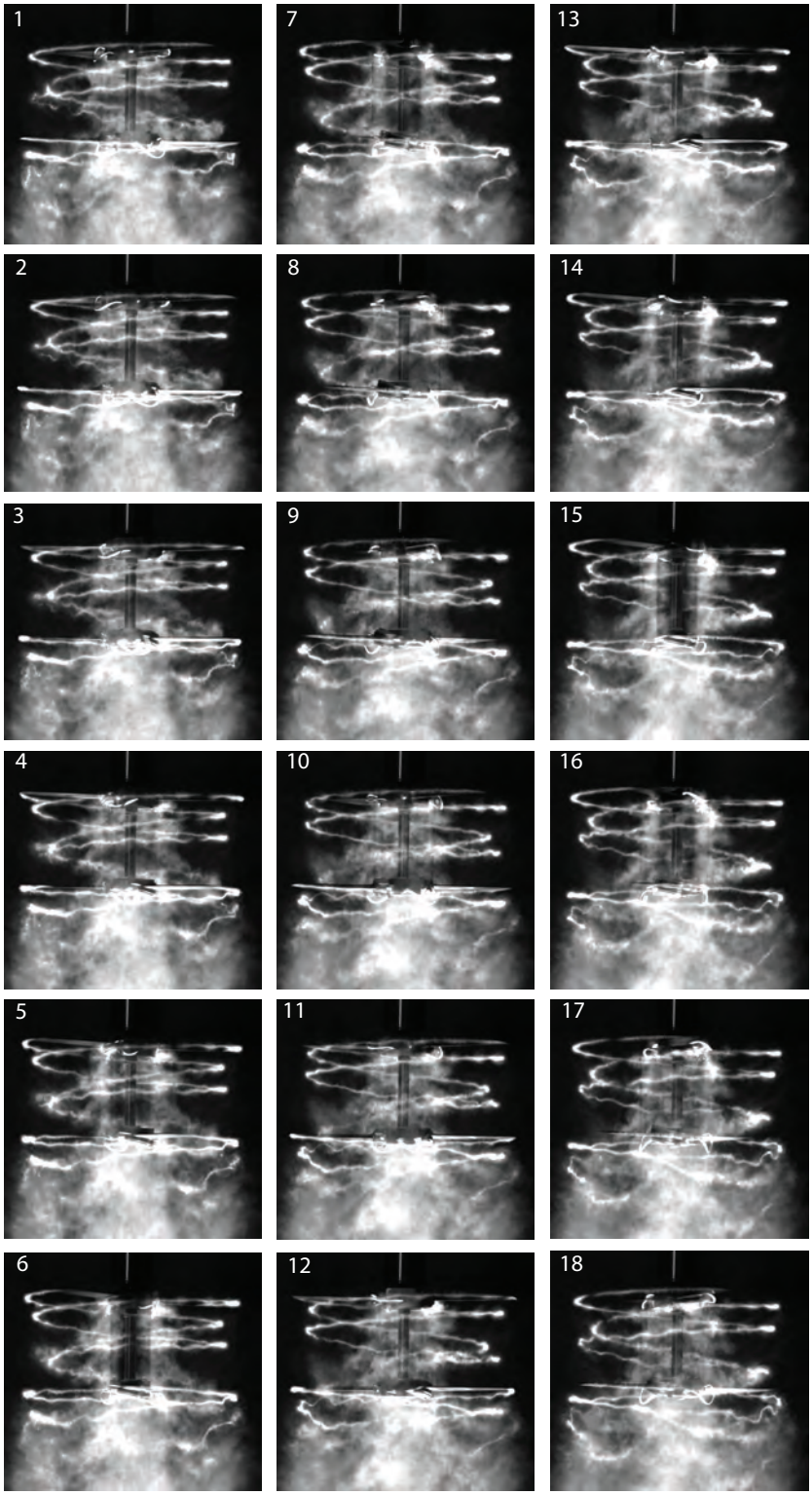

Figure A.69: Vortex wake evolution of the coaxial rotors with axial spacing of H/R=0.875 during one complete rotor revolutions at 4 rps. Images are 20° ($\pi/9$ rad) apart. Time separation between successive images is 13.89 ms.

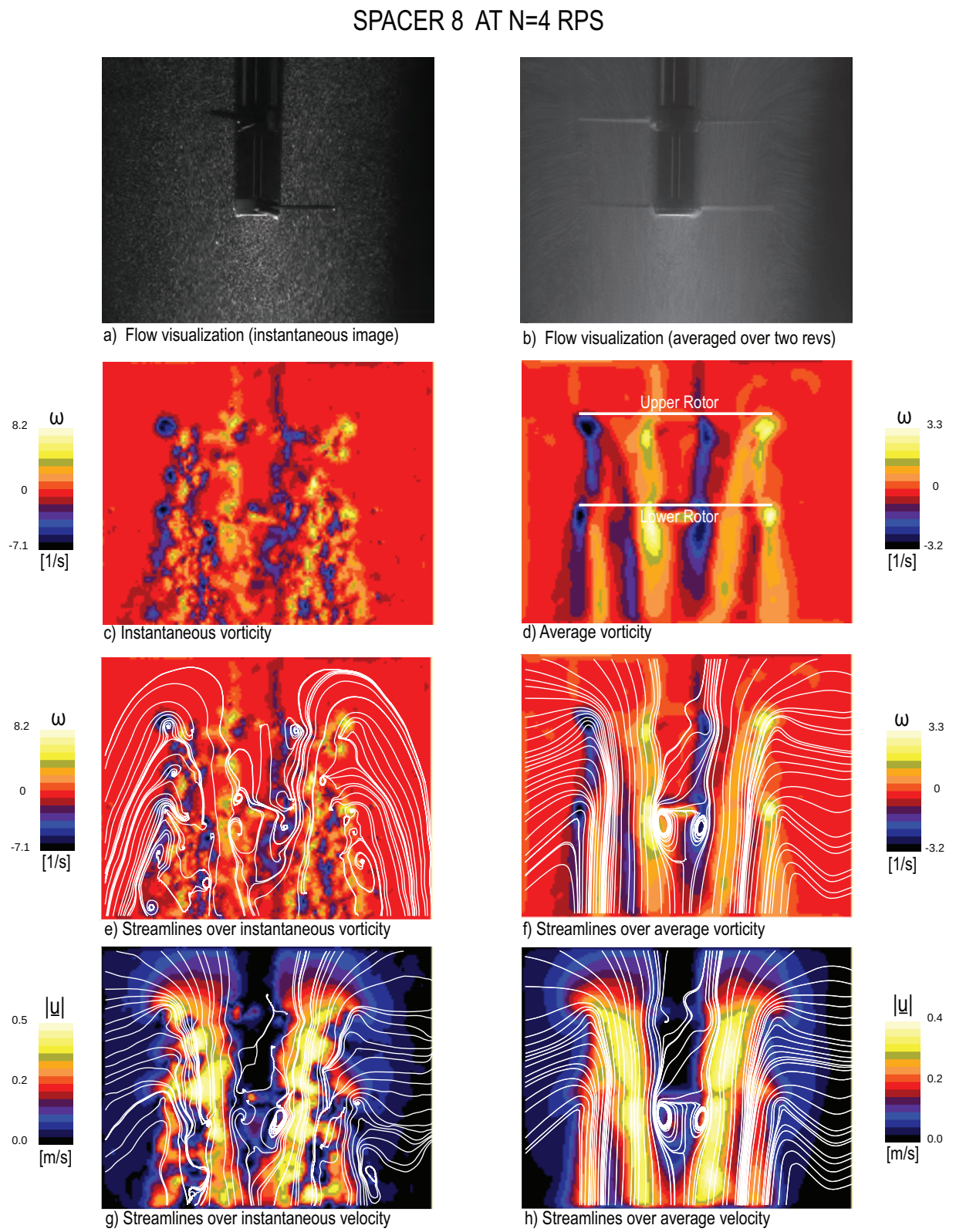

Figure A.70: Flow field of a two-bladed coaxial rotor (spacer8) at $N = 4$ rps. First row (a,b): particle flow visualization. In rows 2-4 are shown PIV measurements. Second row (c,d): vorticity fields. Third row (e,f): streamlines over vorticity. Fourth row (g,h): streamlines over speed. Streamlines in frame (e) are drawn from a moving reference frame and streamlines in frames (f-h) are drawn from a stationary reference frame.

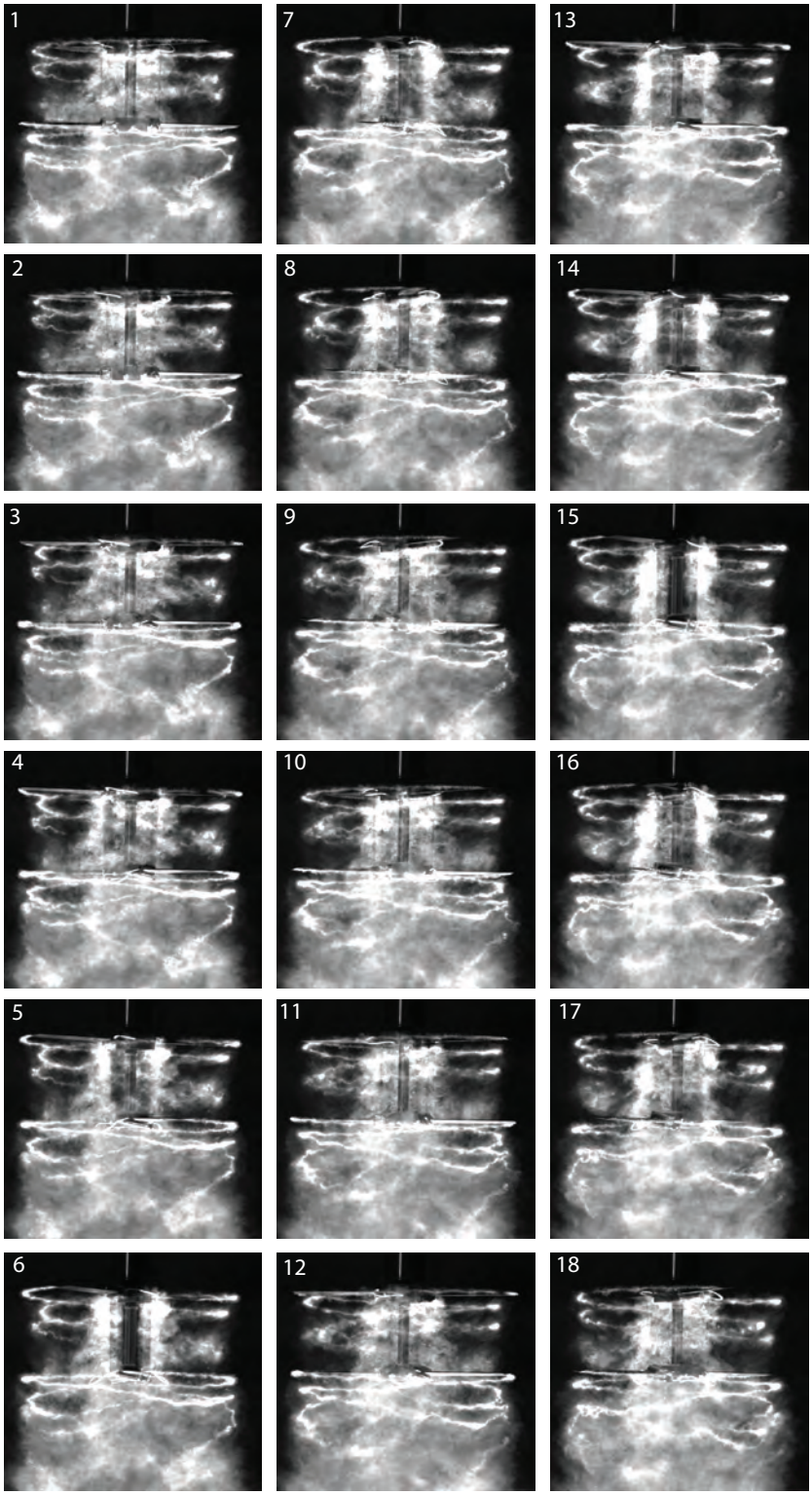

Figure A.71: Vortex wake evolution of the coaxial rotors with axial spacing of H/R=0.875 during one complete rotor revolutions at 2 rps. Images are 20° ($\pi/9$ rad) apart. Time separation between successive images is 27.78 ms.

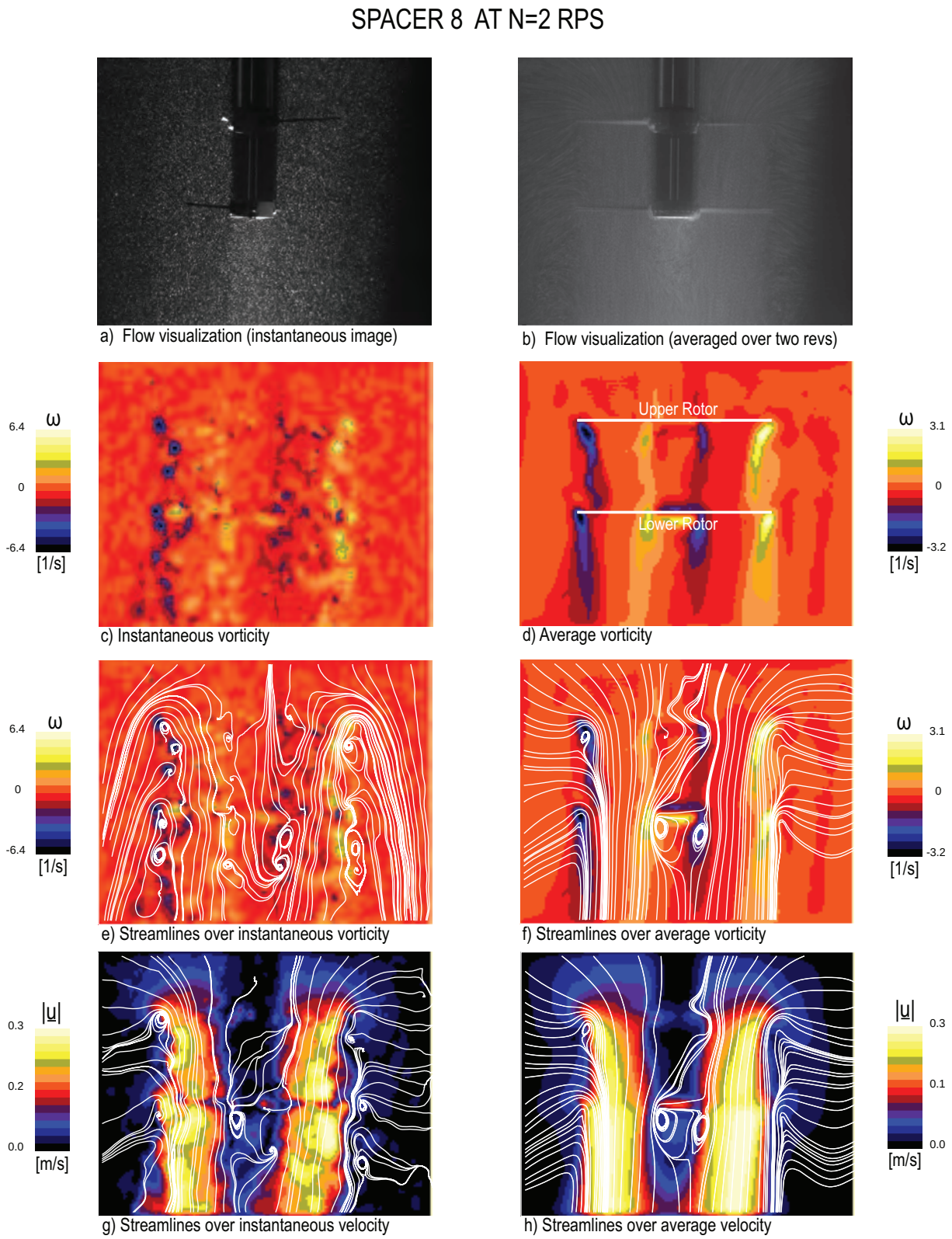

Figure A.72: Flow field of a two-bladed coaxial rotor (spacer8) at $N = 2$ rps. First row (a,b): particle flow visualization. In rows 2-4 are shown PIV measurements. Second row (c,d): vorticity fields. Third row (e,f): streamlines over vorticity. Fourth row (g,h): streamlines over speed. Streamlines in frame (e) are drawn from a moving reference frame and streamlines in frames (f-h) are drawn from a stationary reference frame.

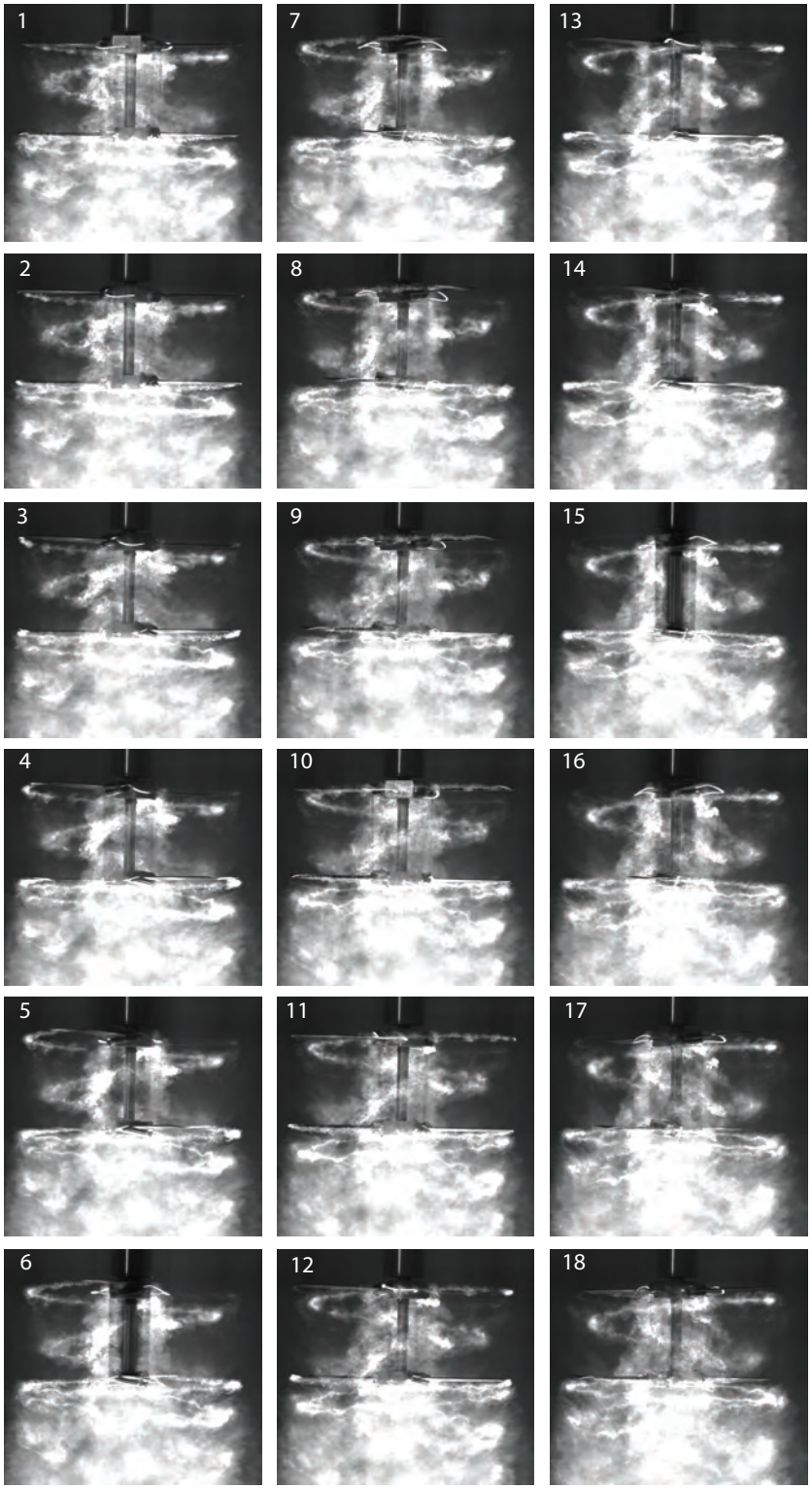

Figure A.73: Vortex wake evolution of the coaxial rotors with axial spacing of H/R=1.0 during one complete rotor revolutions at 6 rps. Images are 20° ($\pi/9$ rad) apart. Time separation between successive images is 9.26 ms.

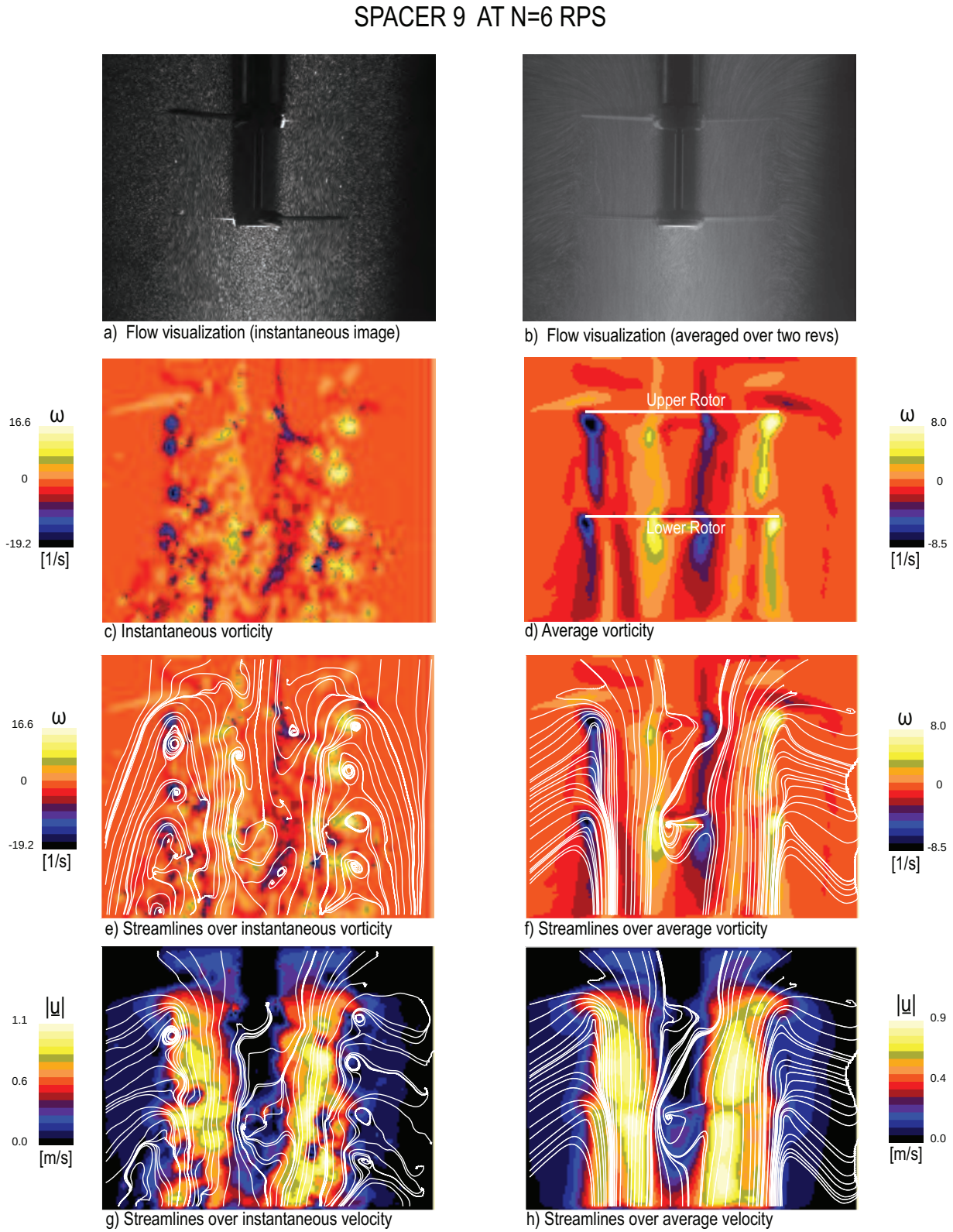

Figure A.74: Flow field of a two-bladed coaxial rotor (spacer9) at $N = 6$ rps. First row (a,b): particle flow visualization. In rows 2-4 are shown PIV measurements. Second row (c,d): vorticity fields. Third row (e,f): streamlines over vorticity. Fourth row (g,h): streamlines over speed. Streamlines in frame (e) are drawn from a moving reference frame and streamlines in frames (f-h) are drawn from a stationary reference frame.

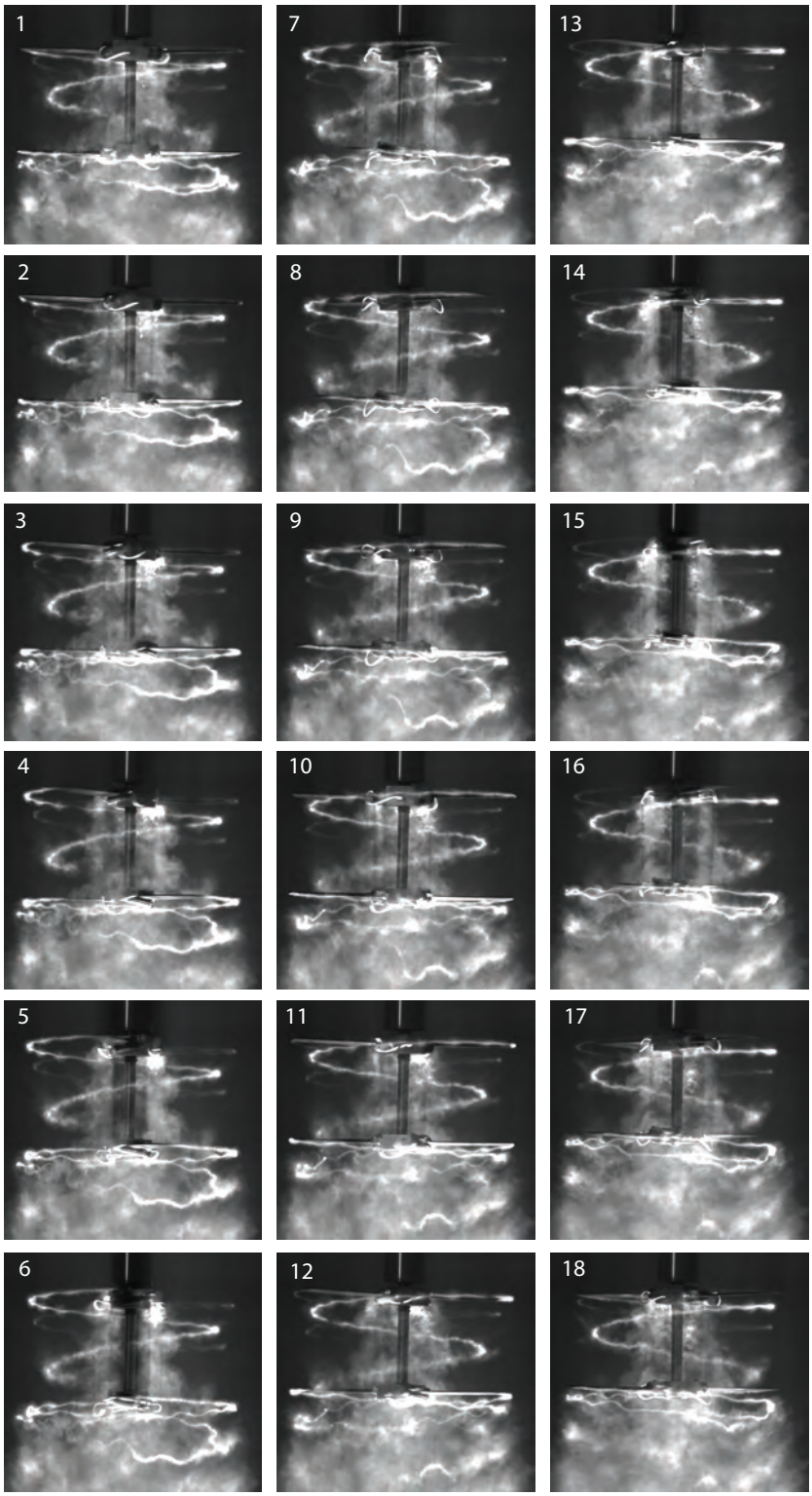

Figure A.75: Vortex wake evolution of the coaxial rotors with axial spacing of H/R=1.0 during one complete rotor revolutions at 4 rps. Images are 20° ($\pi/9$ rad) apart. Time separation between successive images is 13.89 ms.

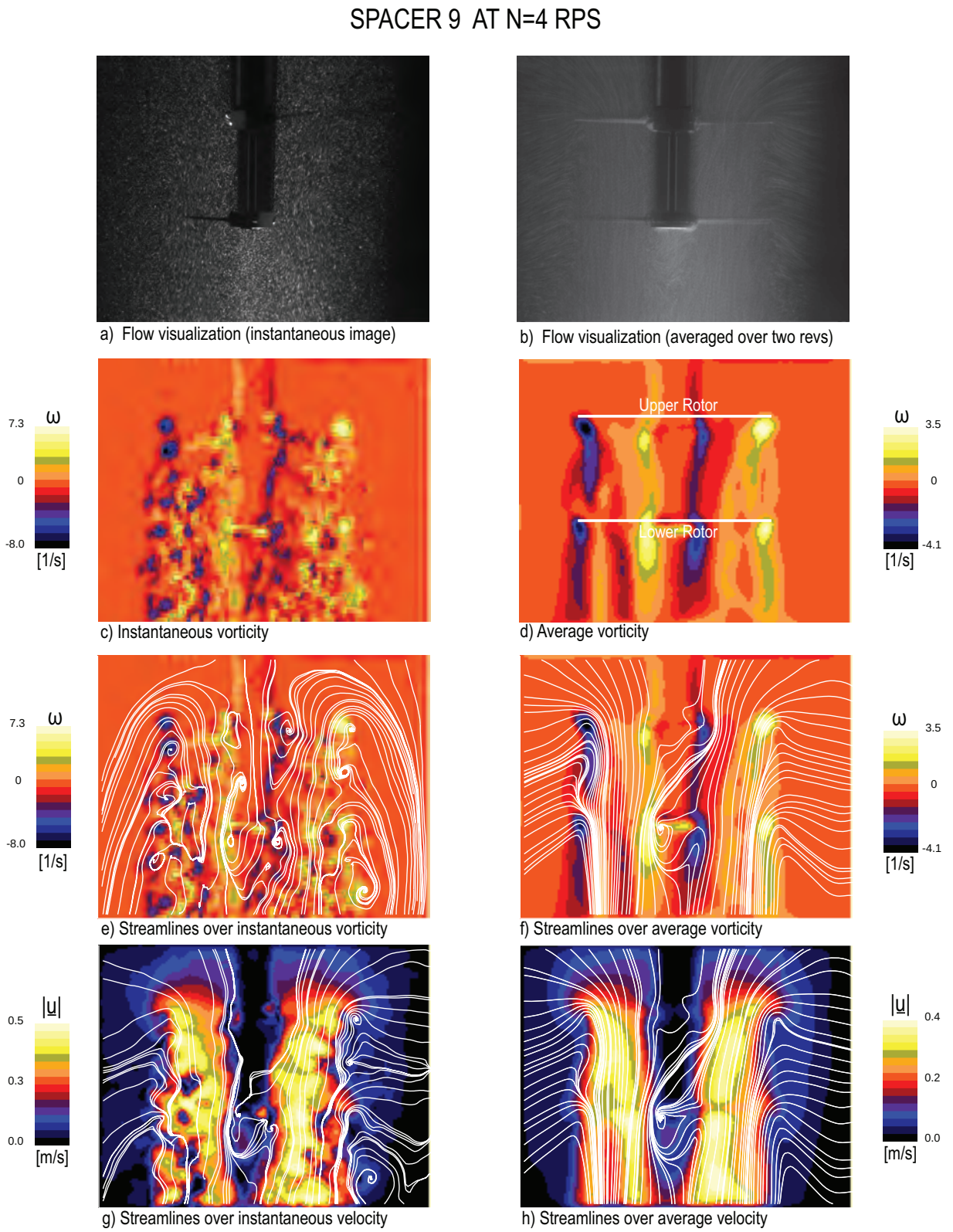

Figure A.76: Flow field of a two-bladed coaxial rotor (spacer9) at $N = 4$ rps. First row (a,b): particle flow visualization. In rows 2-4 are shown PIV measurements. Second row (c,d): vorticity fields. Third row (e,f): streamlines over vorticity. Fourth row (g,h): streamlines over speed. Streamlines in frame (e) are drawn from a moving reference frame and streamlines in frames (f-h) are drawn from a stationary reference frame.

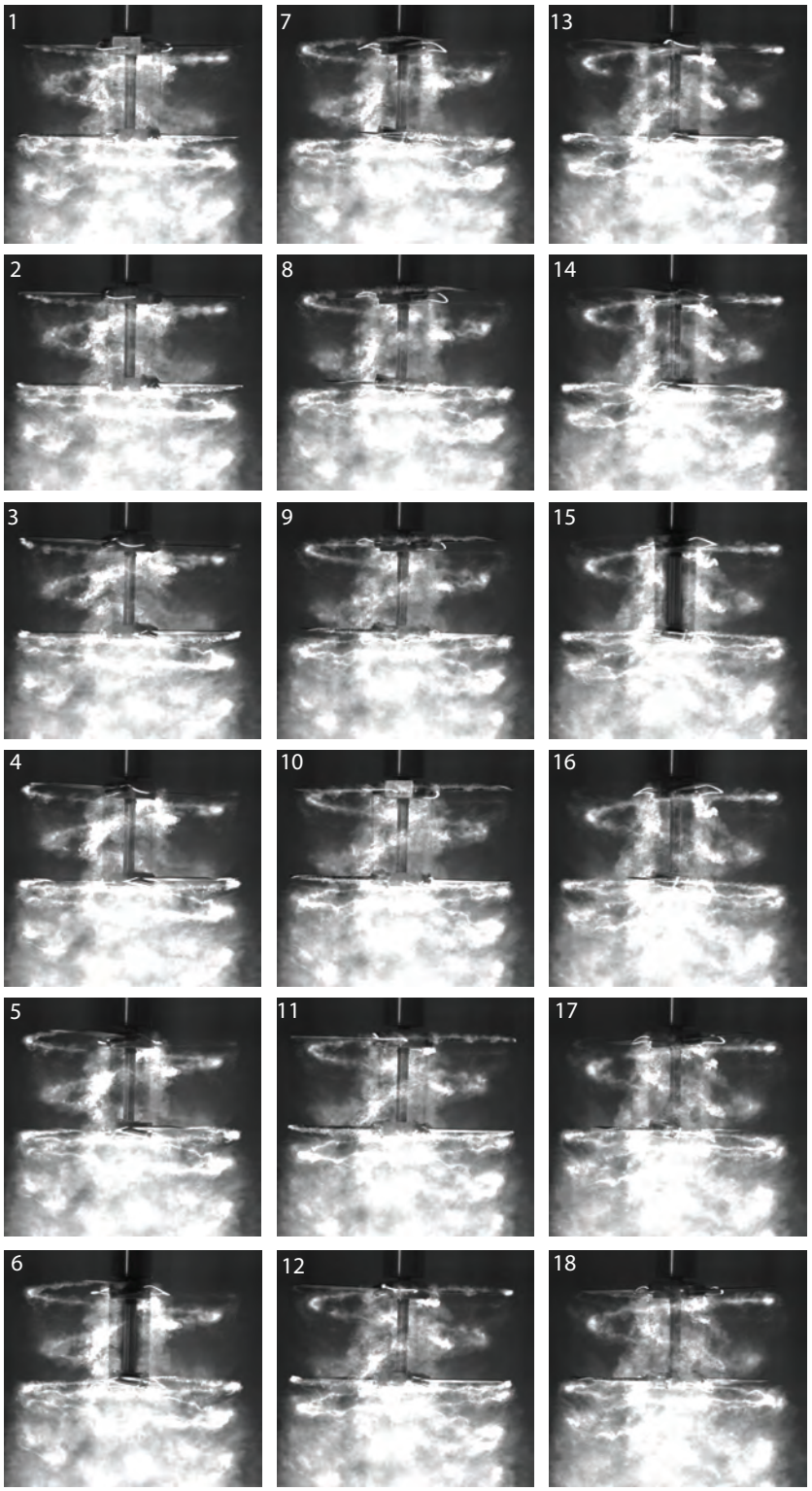

Figure A.77: Vortex wake evolution of the coaxial rotors with axial spacing of H/R=1.0 during one complete rotor revolutions at 2 rps. Images are 20° ($\pi/9$ rad) apart. Time separation between successive images is 27.78 ms.

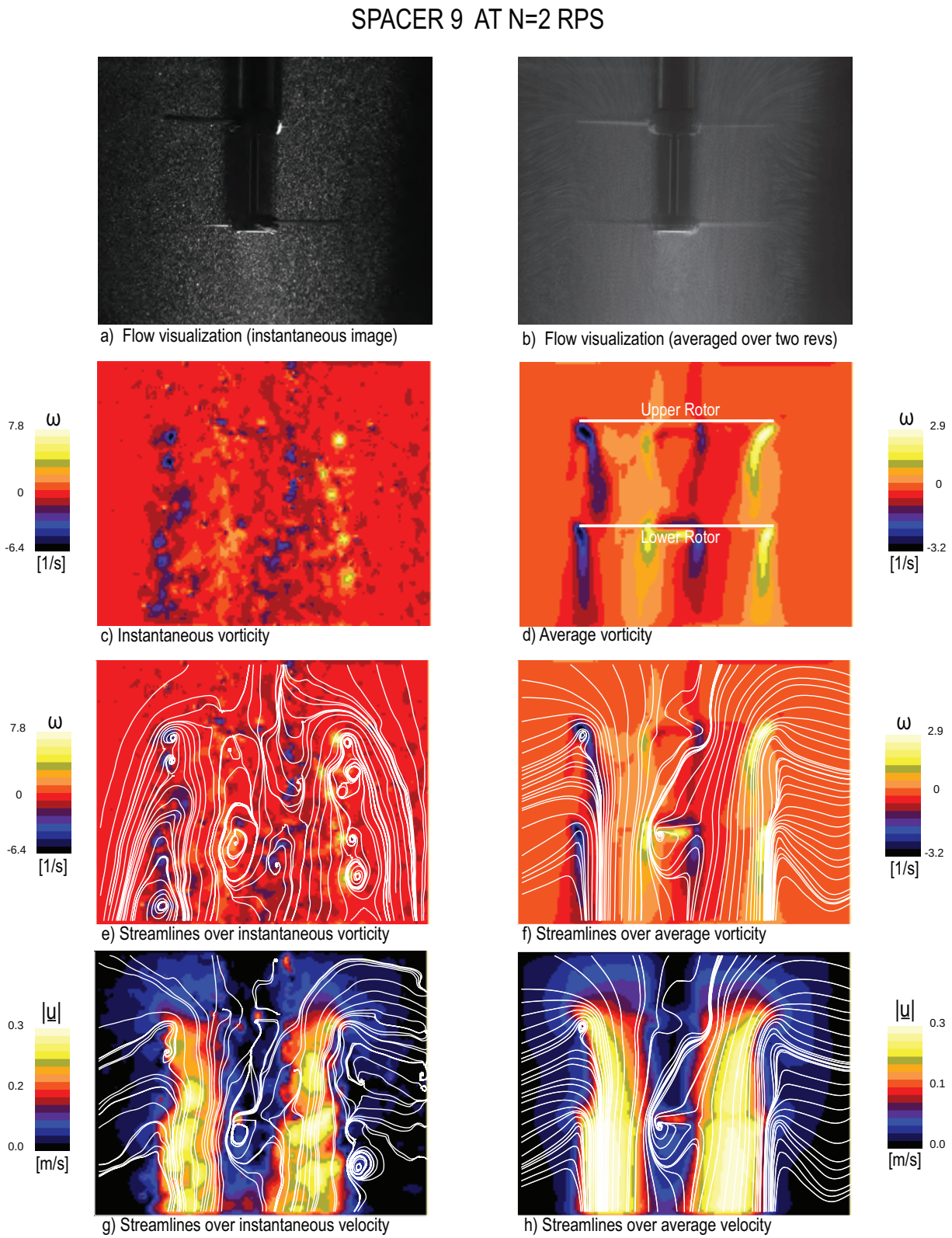

Figure A.78: Flow field of a two-bladed coaxial rotor (spacer9) at $N = 2$ rps. First row (a,b): particle flow visualization. In rows 2-4 are shown PIV measurements. Second row (c,d): vorticity fields. Third row (e,f): streamlines over vorticity. Fourth row (g,h): streamlines over speed. Streamlines in frame (e) are drawn from a moving reference frame and streamlines in frames (f-h) are drawn from a stationary reference frame.

Appendix B

SolidWorks Drawings and Pictures of the Parts

B.1 SolidWorks drawings

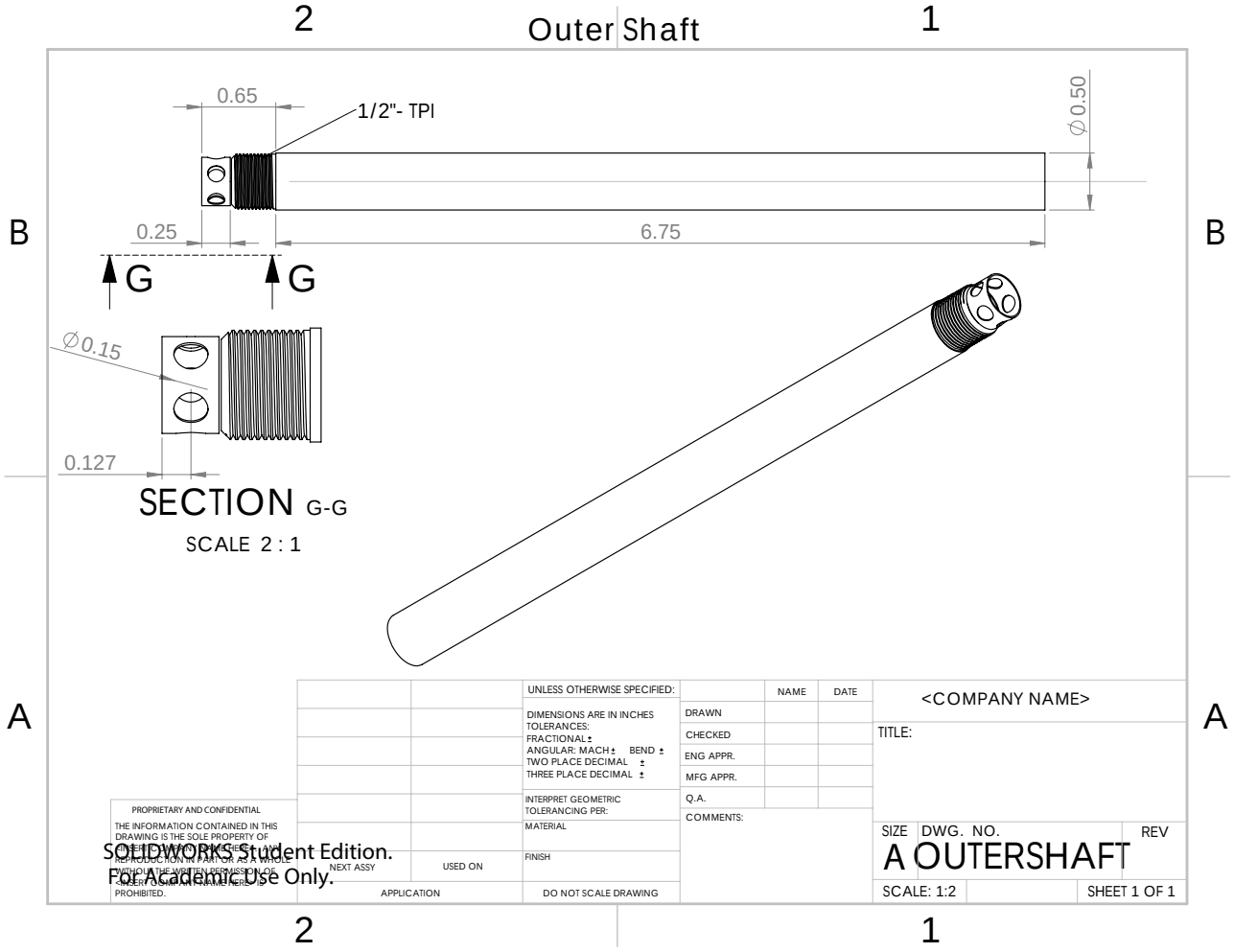
2
Outer Shaft
1
0.65
1/2"- TPI
∅0.50
B
0.25
6.75
B
G
G
∅0.15
0.127
SECTION G-G
SCALE 2 : 1
A
A
UNLESS OTHERWISE SPECIFIED:
DIMENSIONS ARE IN INCHES
TOLERANCES:
FRACTIONAL ±
ANGULAR: MACH ± BEND ±
TWO PLACE DECIMAL ±
THREE PLACE DECIMAL ±
INTERPRET GEOMETRIC TOLERANCING PER:
MATERIAL
FINISH
NEXT ASSY
USED ON
APPLICATION
DO NOT SCALE DRAWING
NAME
DATE
DRAWN
CHECKED
ENG APPR.
MFG APPR.
Q.A.
COMMENTS:
<COMPANY NAME>
TITLE:
SIZE
DWG. NO.
REV
A
OUTERSHAFT
SCALE: 1:2
SHEET 1 OF 1
PROPRIETARY AND CONFIDENTIAL
THE INFORMATION CONTAINED IN THIS DRAWING IS THE SOLE PROPERTY OF
REPRODUCTION IN PART OR AS A WHOLE
WITHOUT THE WRITTEN PERMISSION OF
USER'S NAME HERE IS
PROHIBITED.
SOLIDWORKS Student Edition.
For Academic Use Only.
2
1

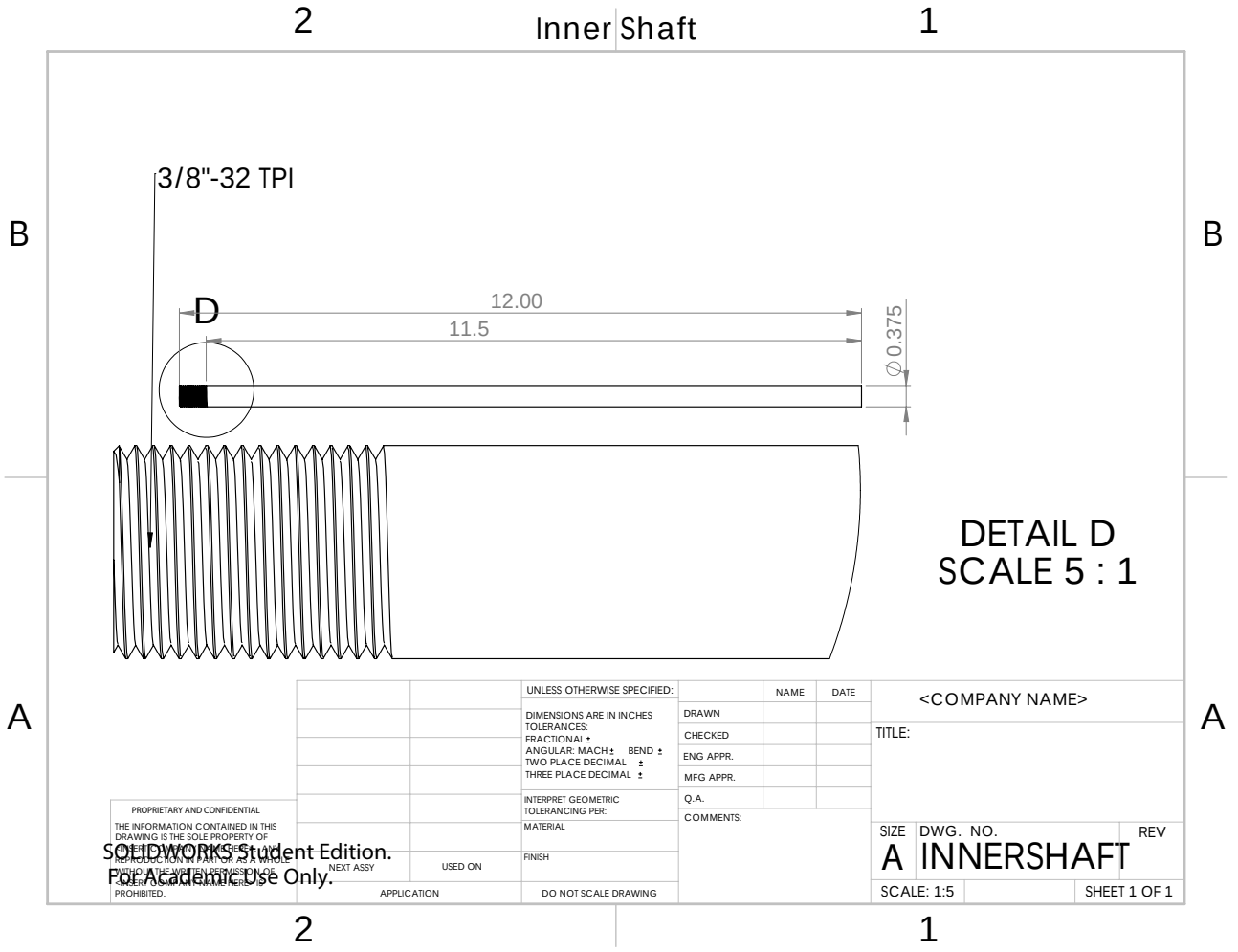
2
Inner Shaft
1
3/8"-32 TPI
B
B
D
12.00
11.5
∅0.375
DETAIL D
SCALE 5 : 1
A
A
UNLESS OTHERWISE SPECIFIED:
DIMENSIONS ARE IN INCHES
TOLERANCES:
FRACTIONAL ±
ANGULAR: MACH ± BEND ±
TWO PLACE DECIMAL ±
THREE PLACE DECIMAL ±
INTERPRET GEOMETRIC TOLERANCING PER:
MATERIAL
FINISH
DO NOT SCALE DRAWING
NAME
DATE
DRAWN
CHECKED
ENG APPR.
MFG APPR.
Q.A.
COMMENTS:
<COMPANY NAME>
TITLE:
SIZE
DWG. NO.
REV
A
INNERSHAFT
SCALE: 1:5
SHEET 1 OF 1
NEXT ASSY
USED ON
APPLICATION
PROPRIETARY AND CONFIDENTIAL
THE INFORMATION CONTAINED IN THIS DRAWING IS THE SOLE PROPERTY OF
REPRODUCTION IN PART OR AS A WHOLE
WITHOUT THE WRITTEN PERMISSION OF
PROHIBITED.
SOLIDWORKS Student Edition.
For Academic Use Only.
2
1

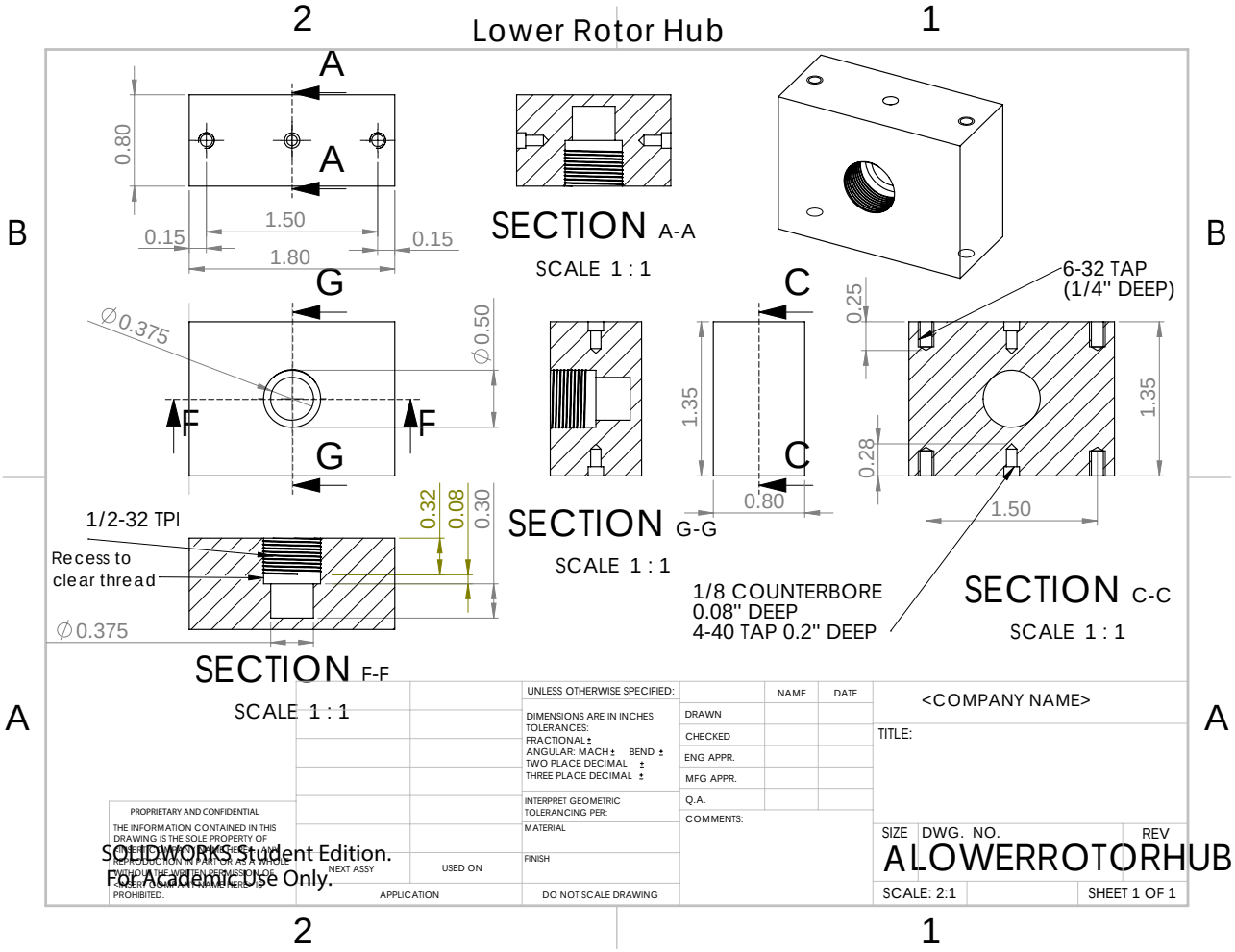
Lower Rotor Hub
SECTION A-A
SCALE 1 : 1
SECTION G-G
SCALE 1 : 1
SECTION F-F
SCALE 1 : 1
SECTION C-C
SCALE 1 : 1
6-32 TAP
(1/4" DEEP)
1/2-32 TPI
Recess to
clear thread
1/8 COUNTERBORE
0.08" DEEP
4-40 TAP 0.2" DEEP
<COMPANY NAME>
TITLE:
ALOWERROTORHUB
SCALE: 2:1
SHEET 1 OF 1
SOLIDWORKS Student Edition.
For Academic Use Only.

2 LOWER ROTOR HUB SHOWING DYE TRANSFER HOLES 1

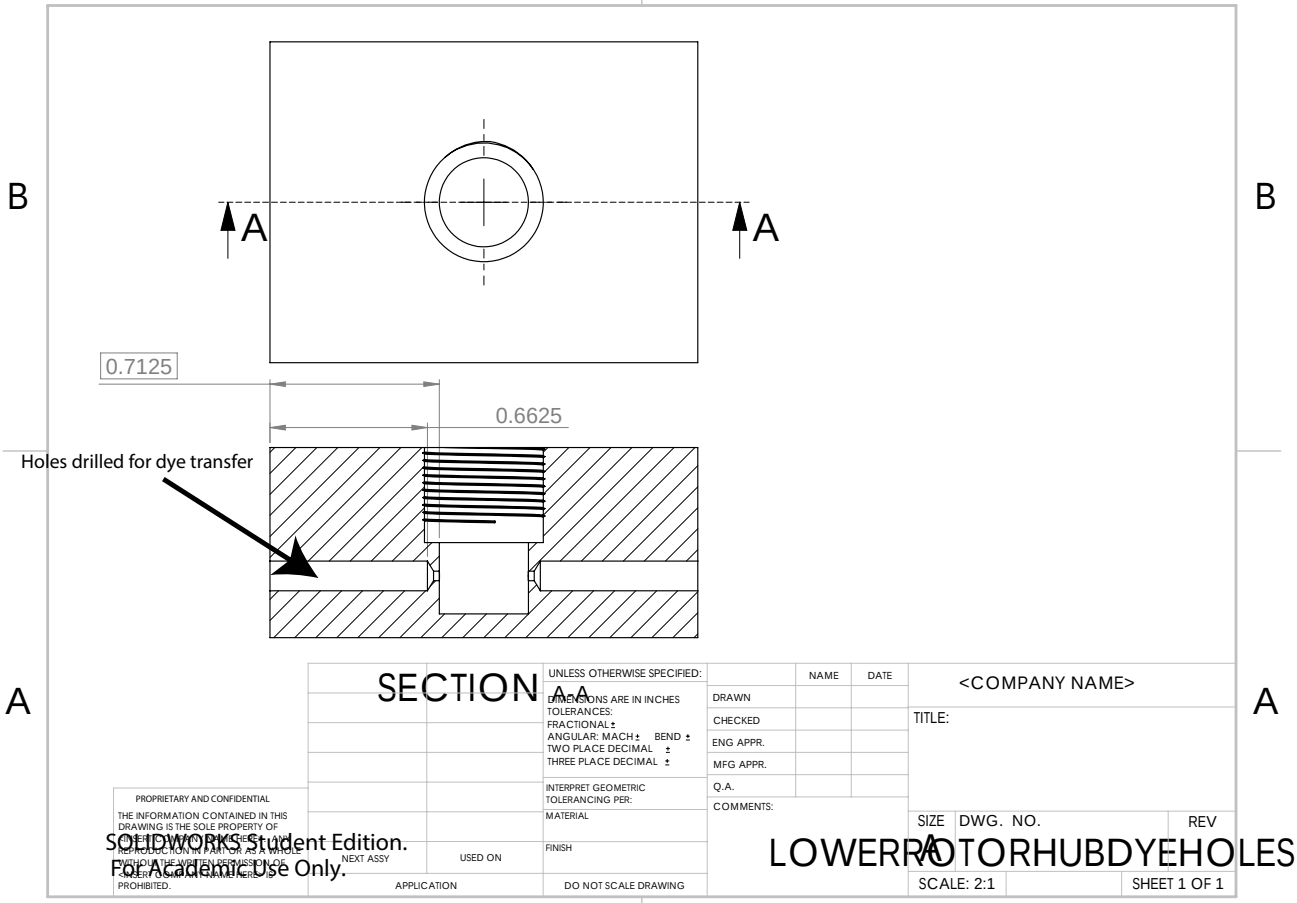

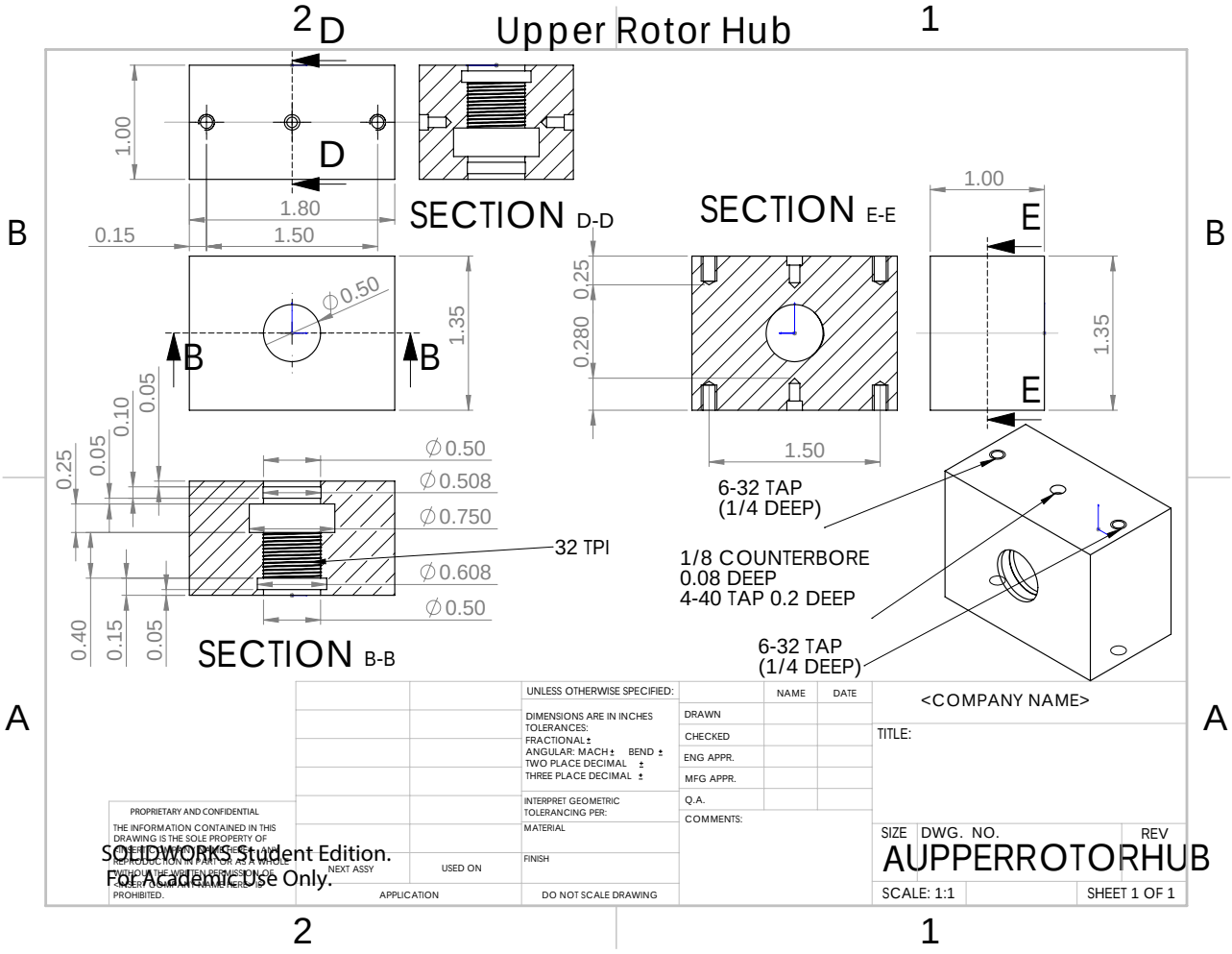

2 UPPER ROTOR HUB SHOWING DYE TRANSFER HOLES 1

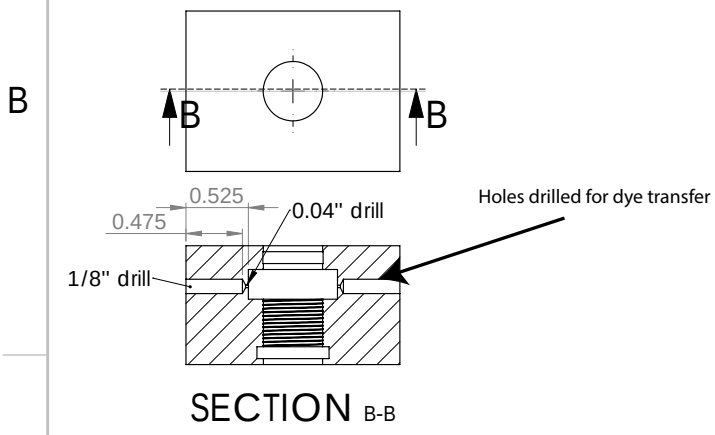

		UNLESS OTHERWISE SPECIFIED:		NAME	DATE
		DIMENSIONS ARE IN INCHES TOLERANCES: FRACTIONAL ± ANGULAR: MACH ± BEND ± TWO PLACE DECIMAL ± THREE PLACE DECIMAL ±	DRAWN		
			CHECKED		
			ENG APPR.		
			MFG APPR.		
		INTERPRET GEOMETRIC TOLERANCING PER:	Q.A.		
		MATERIAL	COMMENTS:		
NEXT ASSY	USED ON	FINISH			
APPLICATION		DO NOT SCALE DRAWING			

<COMPANY NAME>

TITLE:

SIZE A | DWG. NO. UPPERROTORHUBDYEHOLES | REV

SCALE: 1:1 | SHEET 1 OF 1

2 1

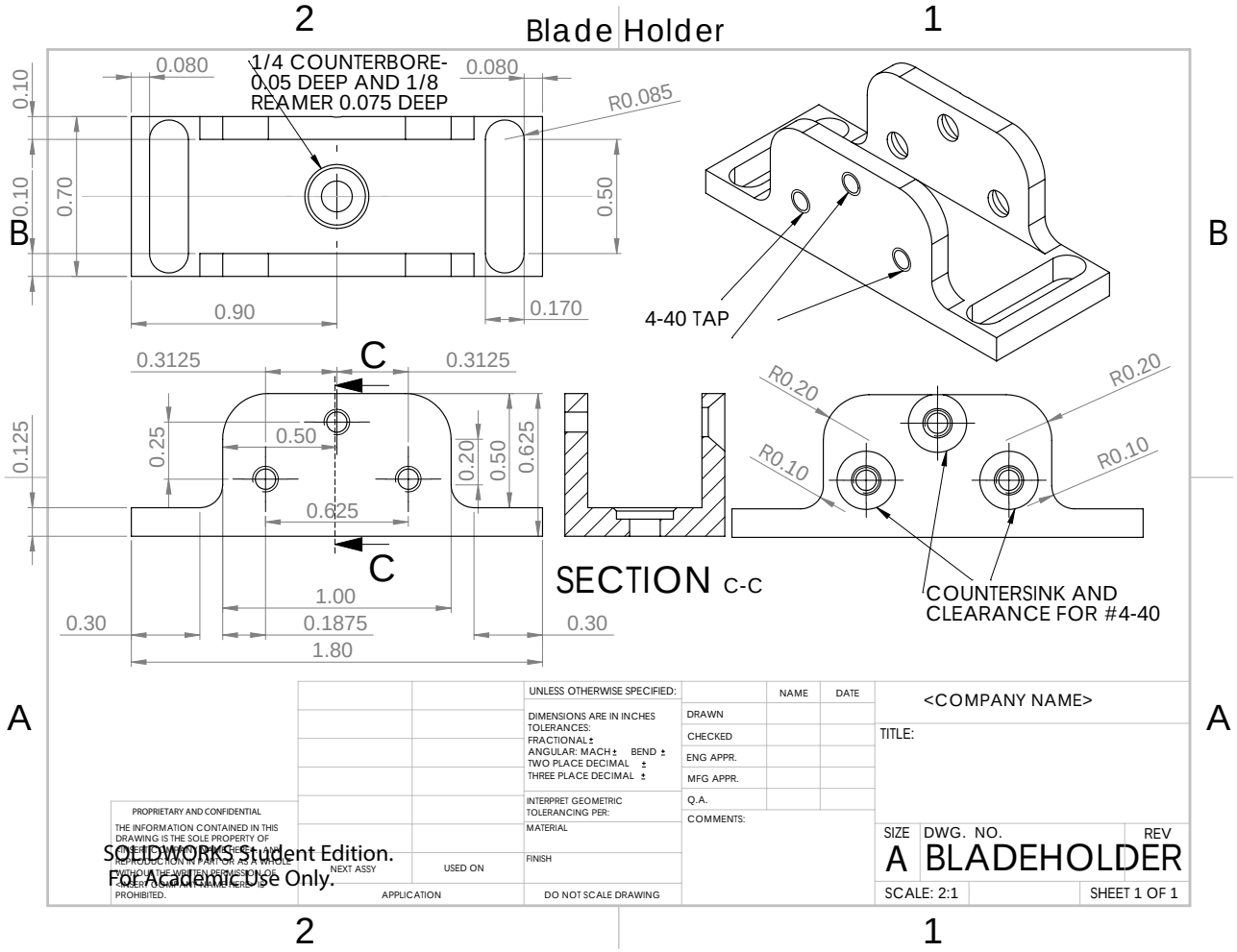
Blade Holder
1/4 COUNTERBORE-
0.05 DEEP AND 1/8
REAMER 0.075 DEEP
0.080
0.080
R0.085
0.10
0.10
0.70
0.50
0.90
0.170
4-40 TAP
0.3125
0.3125
C
C
0.125
0.25
0.50
0.20
0.50
0.625
0.625
SECTION C-C
R0.20
R0.20
R0.10
R0.10
COUNTERSINK AND
CLEARANCE FOR #4-40
1.00
0.30
0.1875
0.30
1.80
UNLESS OTHERWISE SPECIFIED:
DIMENSIONS ARE IN INCHES
TOLERANCES:
FRACTIONAL ±
ANGULAR: MACH ± BEND ±
TWO PLACE DECIMAL ±
THREE PLACE DECIMAL ±
INTERPRET GEOMETRIC TOLERANCING PER:
MATERIAL
FINISH
NEXT ASSY
USED ON
APPLICATION
DO NOT SCALE DRAWING
NAME
DATE
DRAWN
CHECKED
ENG APPR.
MFG APPR.
Q.A.
COMMENTS:
<COMPANY NAME>
TITLE:
SIZE
DWG. NO.
REV
A
BLADEHOLDER
SCALE: 2:1
SHEET 1 OF 1
PROPRIETARY AND CONFIDENTIAL
THE INFORMATION CONTAINED IN THIS DRAWING IS THE SOLE PROPERTY OF
REPRODUCTION IN PART OR AS A WHOLE
WITHOUT THE WRITTEN PERMISSION OF
PROHIBITED.
SOLIDWORKS Student Edition.
For Academic Use Only.

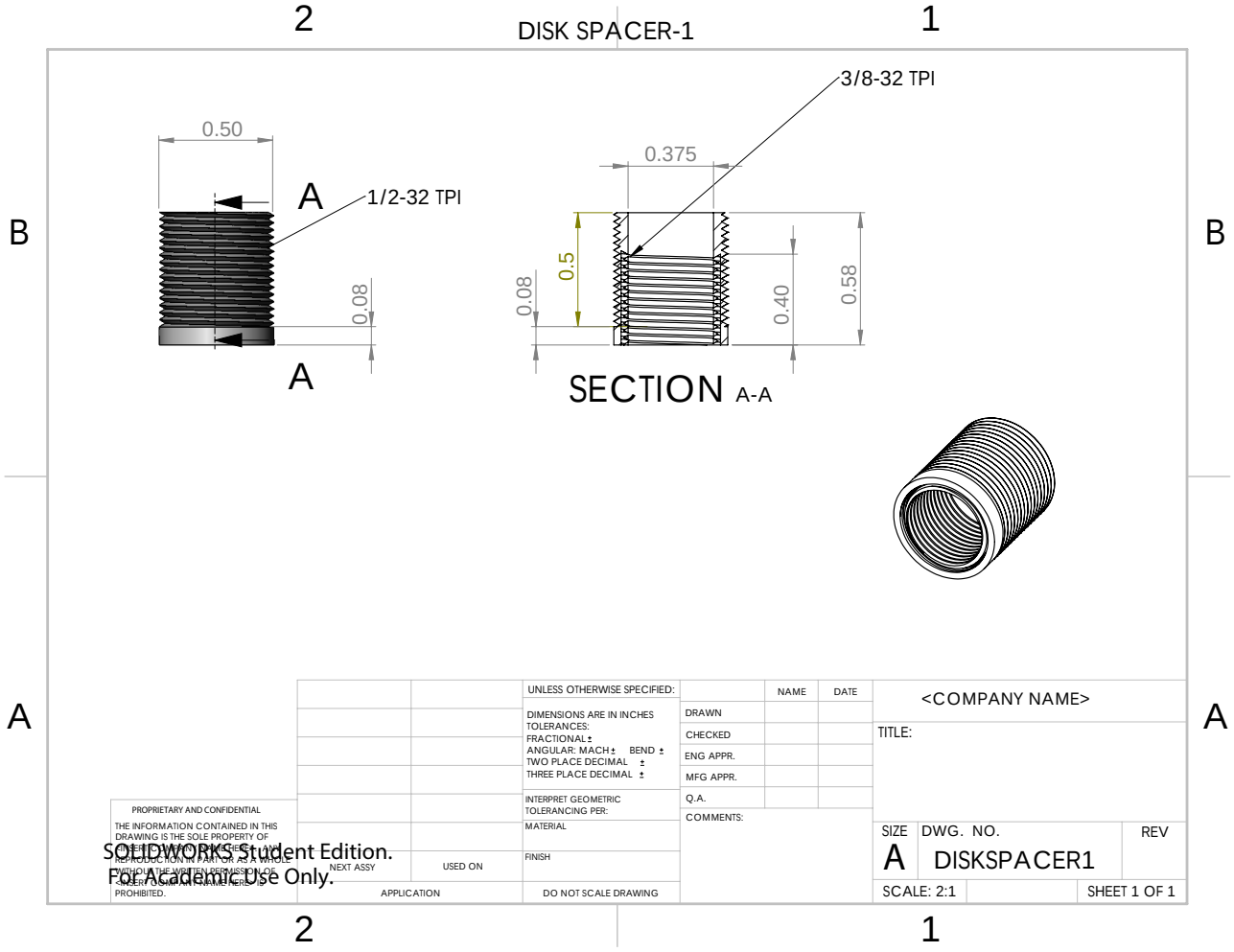
2
DISK SPACER-1
1
B
B
A
A
0.50
A
1/2-32 TPI
0.08
A
3/8-32 TPI
0.375
0.5
0.08
0.40
0.58
SECTION A-A
UNLESS OTHERWISE SPECIFIED:
DIMENSIONS ARE IN INCHES
TOLERANCES:
FRACTIONAL ±
ANGULAR: MACH ± BEND ±
TWO PLACE DECIMAL ±
THREE PLACE DECIMAL ±
INTERPRET GEOMETRIC TOLERANCING PER:
MATERIAL
FINISH
NEXT ASSY
USED ON
APPLICATION
DO NOT SCALE DRAWING
NAME
DATE
DRAWN
CHECKED
ENG APPR.
MFG APPR.
Q.A.
COMMENTS:
<COMPANY NAME>
TITLE:
SIZE
A
DWG. NO.
DISKSPACER1
REV
SCALE: 2:1
SHEET 1 OF 1
PROPRIETARY AND CONFIDENTIAL
THE INFORMATION CONTAINED IN THIS DRAWING IS THE SOLE PROPERTY OF
REPRODUCTION IN PART OR AS A WHOLE
WITHOUT THE WRITTEN PERMISSION OF
PROHIBITED.
SOLIDWORKS Student Edition.
For Academic Use Only.
2
1

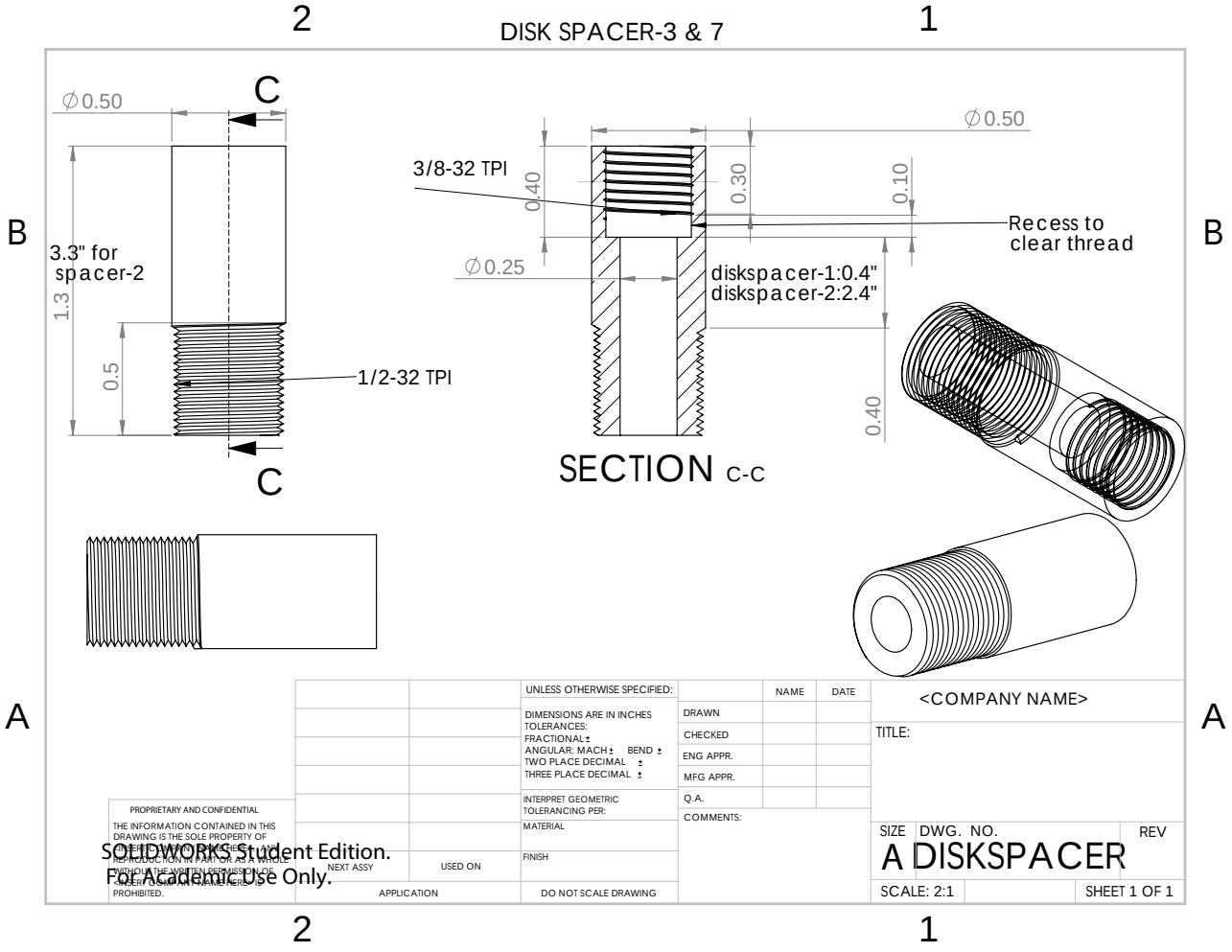
DISK SPACER-3 & 7
∅0.50
3.3" for spacer-2
1.3
0.5
1/2-32 TPI
3/8-32 TPI
0.40
0.30
0.10
Recess to clear thread
∅0.25
diskspacer-1:0.4"
diskspacer-2:2.4"
SECTION C-C
UNLESS OTHERWISE SPECIFIED:
DIMENSIONS ARE IN INCHES
TOLERANCES:
FRACTIONAL ±
ANGULAR: MACH ± BEND ±
TWO PLACE DECIMAL ±
THREE PLACE DECIMAL ±
INTERPRET GEOMETRIC TOLERANCING PER:
MATERIAL
FINISH
NEXT ASSY
USED ON
APPLICATION
DO NOT SCALE DRAWING
NAME
DATE
DRAWN
CHECKED
ENG APPR.
MFG APPR.
Q.A.
COMMENTS:
<COMPANY NAME>
TITLE:
SIZE
DWG. NO.
REV
A DISKSPACER
SCALE: 2:1
SHEET 1 OF 1
PROPRIETARY AND CONFIDENTIAL
THE INFORMATION CONTAINED IN THIS DRAWING IS THE SOLE PROPERTY OF
REPRODUCTION IN PART OR AS A WHOLE
WITHOUT THE WRITTEN PERMISSION OF
PROHIBITED.
SOLIDWORKS Student Edition.
For Academic Use Only.

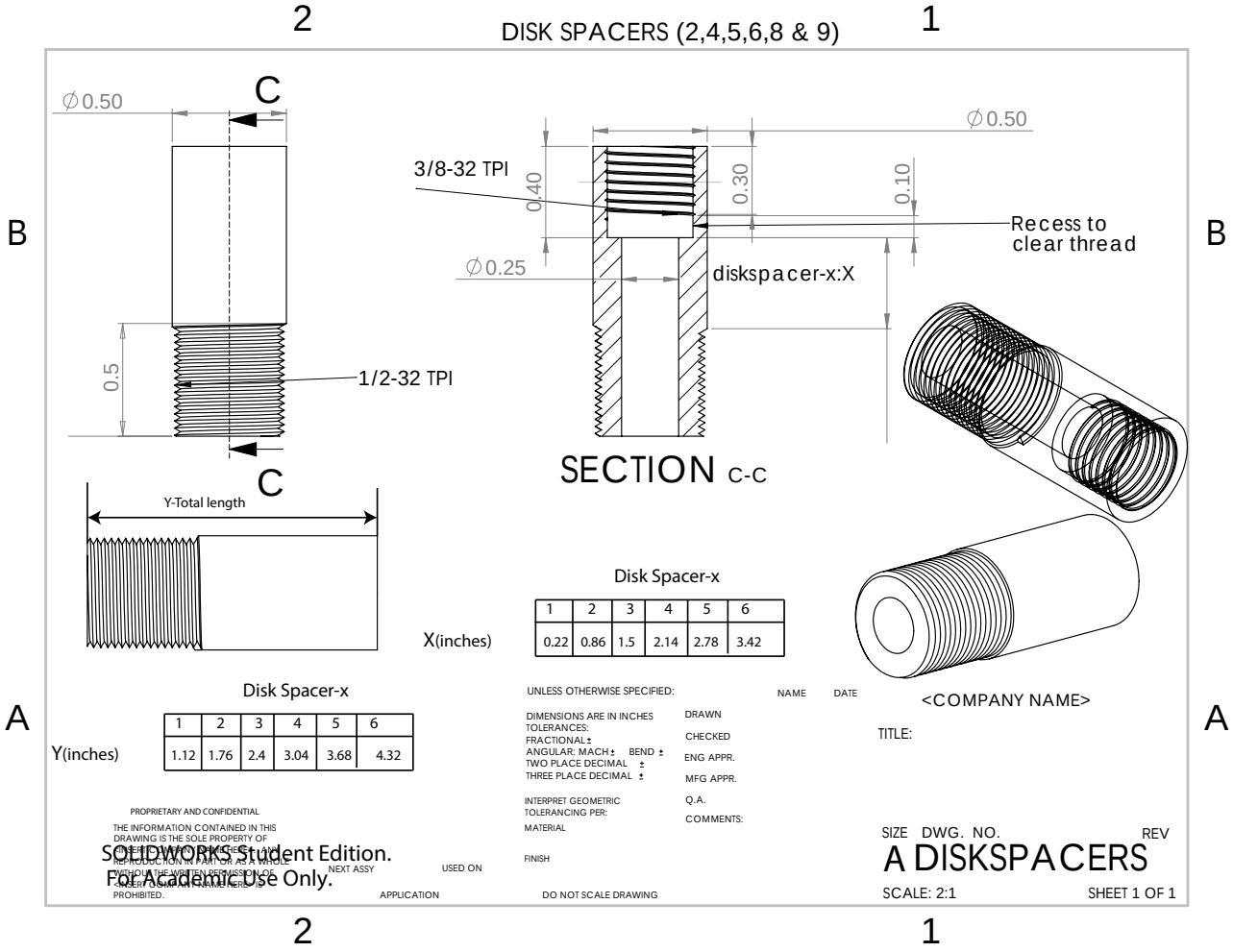

B.2 Pictures of the parts

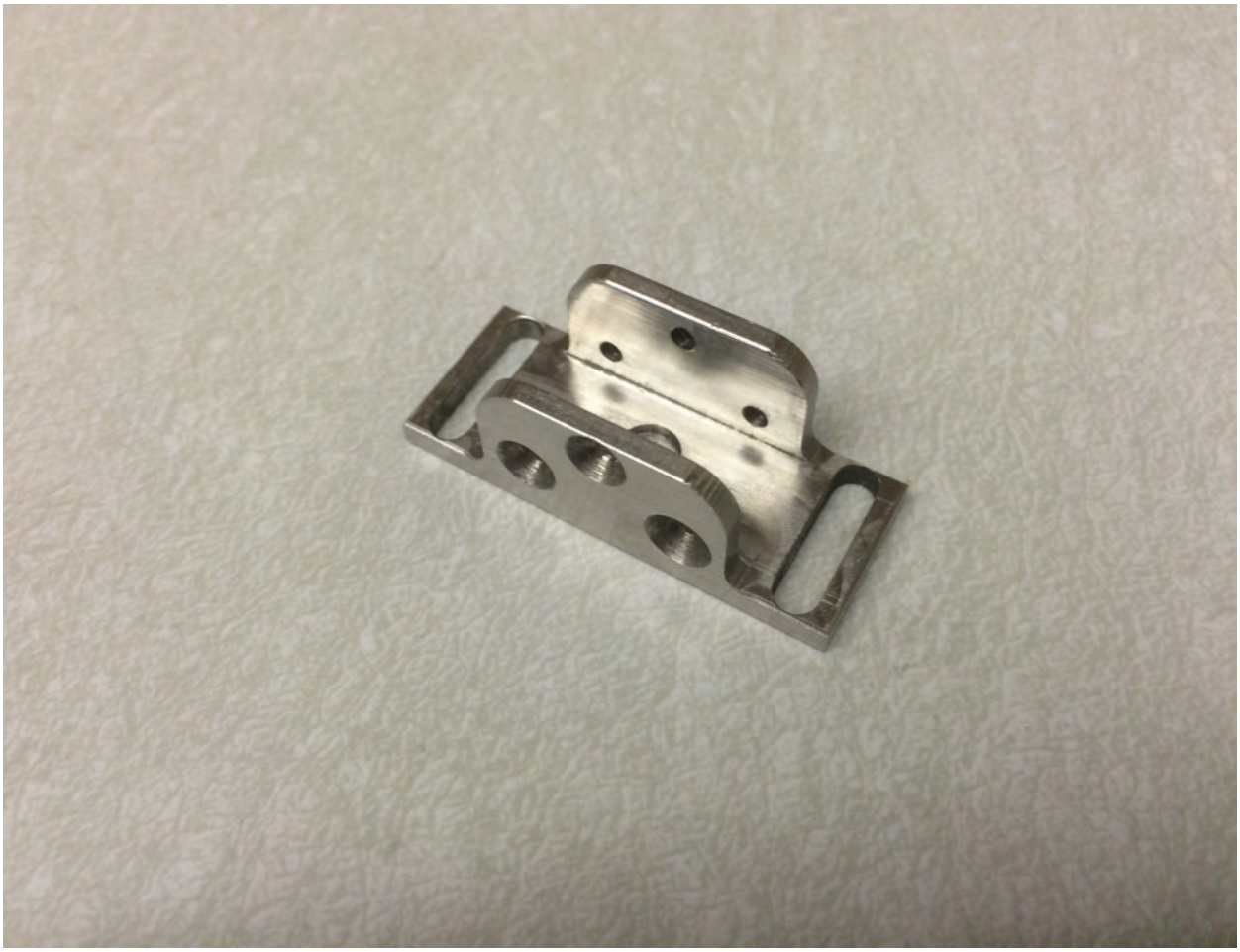

Figure B.1: Blade holder

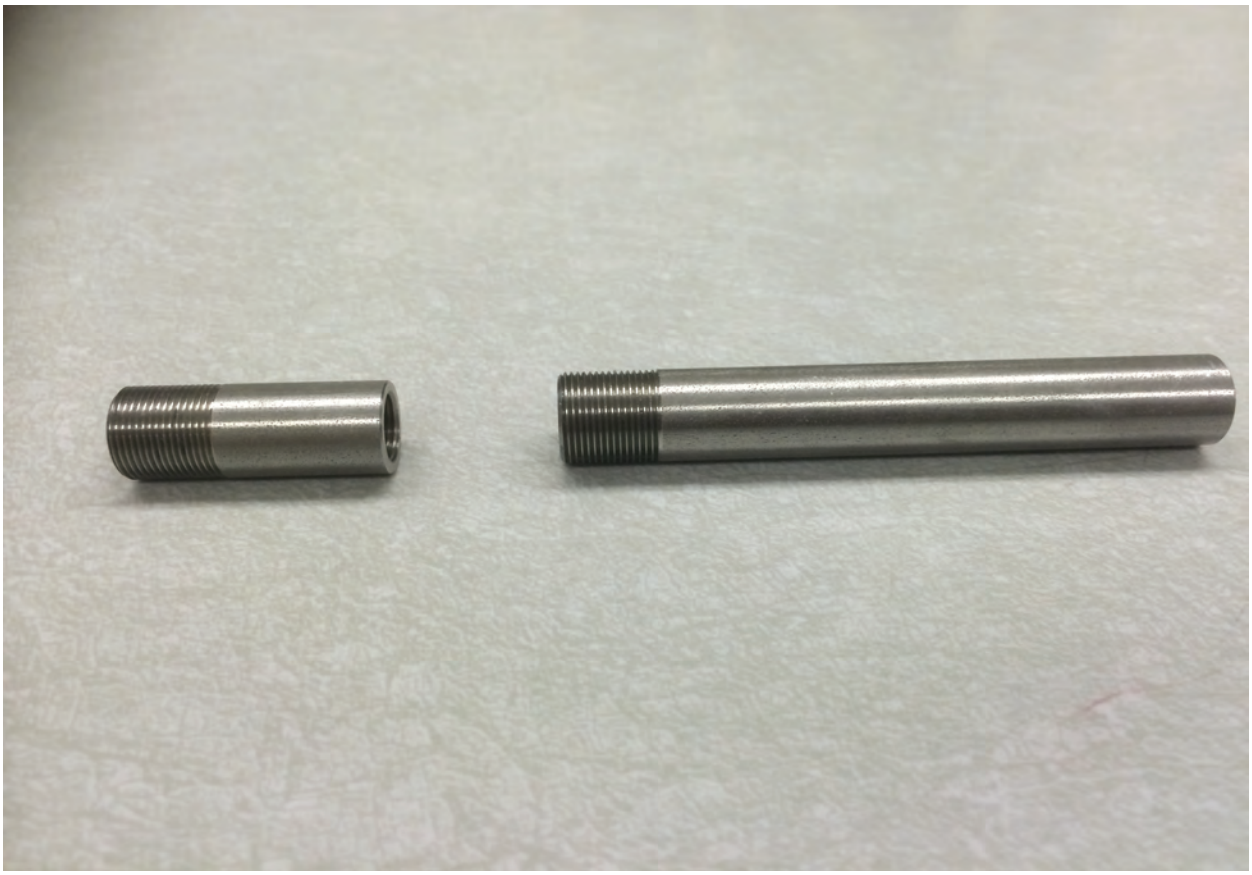

Figure B.2: Disk spacers 3 (left) and 7

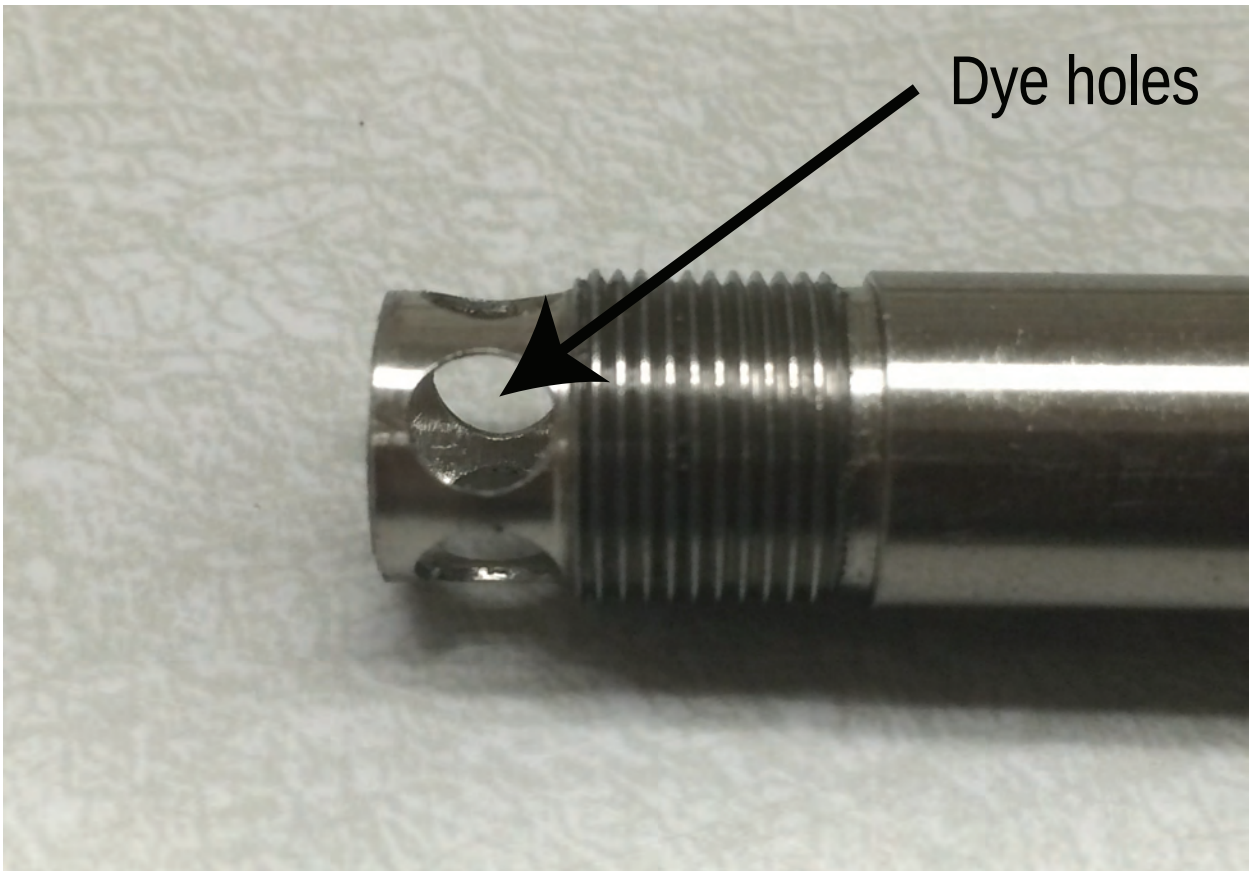

Figure B.3: Dye holes on outer shaft

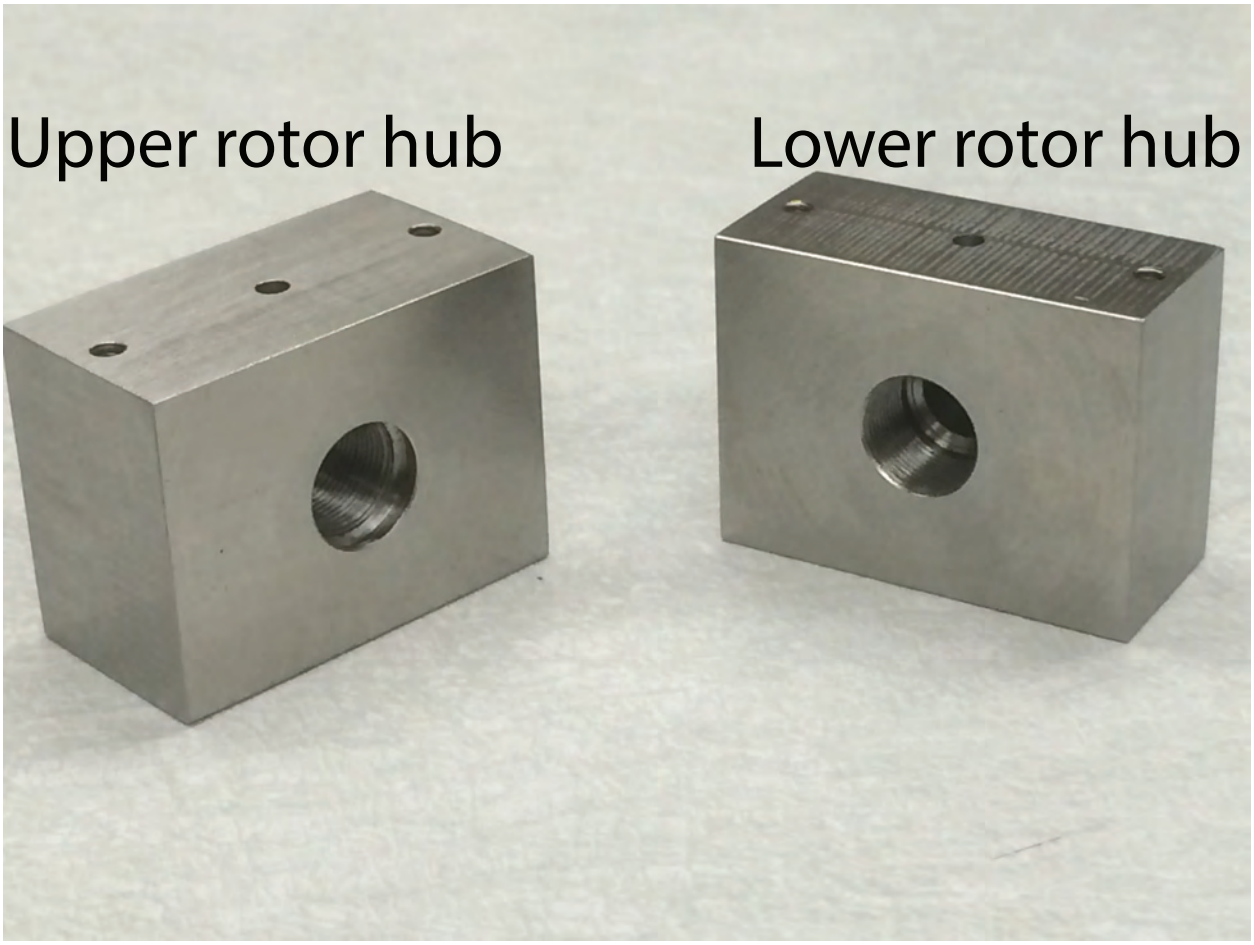

Figure B.4: Upper (left) and lower rotor hubs

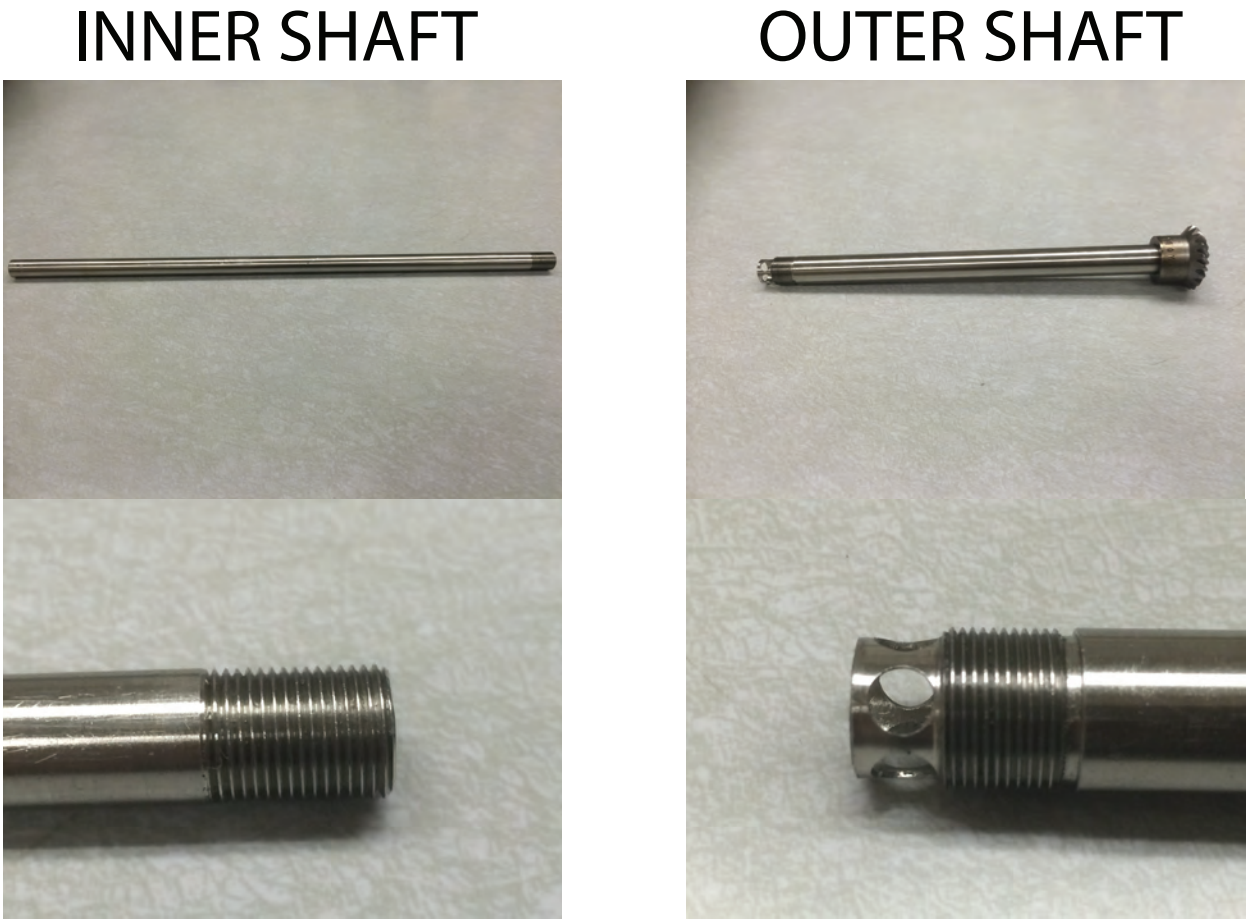

Figure B.5: Inner (left) and outer shafts